Chemically Stable, Crystalline, Porous Covalent Organic Frameworks as Proton Transport and Energy Storage Materials

Thesis Submitted to AcSIR for the Award of the Degree of

DOCTOR OF PHILOSOPHY

In Chemical Sciences

(Academy of Scientific and Innovative Research)

By

Suman Chandra

(Registration No: 10CC12A26027)

Under the guidance of

Dr. Rahul Banerjee

CSIR-National Chemical Laboratory
Pune, Maharashtra, India– 411008

August 2017

सीएसआईआर - राष्ट्रीय रासायनिक प्रयोगशाला
(वैज्ञानिक तथा औद्योगिक अनुसंधान परिषद)
डॉ. होमी भाभा मार्ग, पुणे - 411 008, भारत
CSIR - NATIONAL CHEMICAL LABORATORY
(Council of Scientific & Industrial Research)
Dr. Homi Bhabha Road, Pune - 411 008, India

Certificate

*This is to certify that the work incorporated in this Ph.D. thesis entitled **"Chemically Stable, Crystalline, Porous Covalent Organic Frameworks as Proton Transport and Energy Storage Materials"** submitted by **Mr. Suman Chandra** to **Academy of Scientific and Innovative Research (AcSIR)** in fulfillment of the requirements for the award of the Degree of Doctor of Philosophy, embodies original research work under my supervision. I further certify that this work has not been submitted to any other University or Institution in part or full for the award of any degree or diploma. Research material obtained from other sources has been duly acknowledged in the thesis. Any text, illustration, table etc., used in the thesis from other sources, have been duly cited and acknowledged.*

Chandra.

Mr. Suman Chandra

(Student)

Rahul Banj.

Dr. Rahul Banerjee

(Supervisor)

Communication Channels
☎
NCL Level DID : 2590
NCL Board No. : +91-20-25902000
EPABX : +91-20-25893300
: +91-20-25893400
FAX
Director's Office : +91-20-25902601
COA's Office : +91-20-25902660
SPO's Office : +91-20-25902664
WEBSITE
www.ncl-india.org

DECLARATION

I hereby declare that the matter embodied in this thesis entitled ***"Chemically Stable, Crystalline, Porous Covalent Organic Frameworks as Proton Transport and Energy Storage Materials"*** *is the result of investigations carried out by me in the Physical & Materials Chemistry Division, CSIR-National Chemical Laboratory, Pune, India under the supervision of Dr. Rahul Banerjee.*

In keeping with the general practice of reporting scientific observations due acknowledgments have been made wherever the work described is based on the findings of other investigators.

SChandr.

Pune,
August 2017

Suman Chandra

Dedicated to
My Maa, Baba & Bhai

ACKNOWLEDGEMENT

I would take this opportunity to express my sincere gratitude to my supervisor **Dr. Rahul Banerjee***. My heartfelt thanks go to him for introducing me to the wonders of scientific research, for his persistent guidance, encouragement, inspiration and support during every stage of my doctoral research work. Again I warmly thank him for his precious advice, analysis, criticism and discussions on my research work. I am very much thankful to him for his pursuance for improving me as a person as well as my scientific skills. I would also like to sincerely thank my DAC committee members* **Dr. C.P.Vinod**, **Dr. Jayaraj Nithyanandhan** *and* **Dr. Prakash P. Wadgaonkar** *for their constructive, innovative suggestion and comments throughout my Ph.D. work period at CSIR-NCL, Pune.*

I extend my sincere thanks to the Director of CSIR-NCL **Prof. Ashwani Kumar Nangia***, former Directors* **Dr. Vijayamohanan K. Pillai** *and* **Dr. Sourav Pal***, Head of Physical and Materials Chemistry Division* **Dr. P. A. Joy** *and* **Dr. Anil Kumar** *(Ex-HoD) for their kind help and encouragement during the course of this work. I must earnestly acknowledge the collaborative assistance, valuable scientific discussions and suggestions that I received from* **Dr. Amit Paul**, **Dr. K. Sreekumar, Dr. Joytisman Dasgupta, Dr. Manjusha V. Shelke, Ajay Jha, Indrapal Kharbal** *and* **Debarati Roy Choudhari***. I also thank* **Dr. Thomas Heine** *and* **Dr. Matthew Adddicoat***, School of Engineering and Science, Jacobs University, Germany, for their help in theoretical calculations in few projects.*

I am very grateful to UGC, New Delhi for fellowship support to carry out my research work and **AcSIR** *for allowing me to submit my work in the form of thesis. I thank all the non-teaching staff of CSIR-NCL for their assistance on various occasions. I wish to thank all my friendly and cooperative labmates* **Tamas Da, Pradip da, Chandan da, Subhadeep da, Arijit, Tanay, Sharath, Bishnu, Harshitha, Bikash, Mohitosh, Saibal, Arjun, Suvendu, Jayshri di, Gobinda da, Digambar ji, Manas da, Shouvik da, Sujit da, Kaushik, Himadri, Abdul, Shebeeb, Kanhu, Amit da, Srinu anna, Arghya da, Tapan da, Sushil ji** *and* **Gargi di** *for creating a cheerful and enjoyable working atmosphere in the lab. They were extremely supportive as well as helpful during my tenure. I also thank all the project students' especially* **Bidhan** *and* **Amarjith***, who helped in various projects.*

My stay on this campus has been pleasant with the association of all the research scholars at CSIR-NCL. I am thankful to **Anupda, Santi, Pravat da, Partha da, Kanak da,**

Achintya da, Susanta da, Arpan da, Arya da, Saikat da, Shyam da, Chandan da, Himadri da, Krishanu da, Arijit da, Tamas da, Prathit da, Tanaya di, Munmun di, Soumen da *for their support, guidance, and advice.*

I would also like to thankful to all my juniors ***Siba, Subhrasis, Tapas, Tamal, Pronob, Manzoor, Saibal, Subrata, Avijit, Pranoy, Sandipan, Mohitosh, Indrwadeep, Sutanu, Anirban, Argha, Milan.***

My sincere thanks to new hostel saturday night group. My pune stay would have been boring without you people, ***Atanu, Manik, Santanu, Sudip, Chayanika, Monalisa, Bittu, Atryee, Manoj, Gablu, Munna.***

I would also like to thanks my previous mentor **Dr. U.P.Singh** *and all my seniors and friends from IIT, Roorkee, specially* **Malayda**, **Chanchalda**, **Tapasda**, **Kuntalda**, ***Sujata mam, Rajesh sir, Nidhi mam, Sandip sir, Kapil sir, Raman sir, Shikha, Neetu.***

I am grateful to all my teachers and I expressed my gratitude for their encouragement in different part of my life. I thank the entire members of my family for their constant care and wishes. Last but not least, I would like to pay high regards to my father **Gourinath Chandra**, *mother* **Asha Chandra** *and brothers* **Pariman** *and* **Bittu** *for their love, prayers and support which inspired me and strengthen throughout my life. Dedicating this thesis to them is a minor recognition for their valuable support and encouragement.*

Suman Chandra

PREFACE

The over growing population in worldwide not only demands an urgent need for efficient, sustainable and clean sources of energy but also new technologies associated with energy conversion and storage. The use of fossil fuel greatly increases the environment pollution. Therefore, modern research focuses on the developments of novel materials and technologies. Porous materials have been extensively used for gas storage, separation, catalysis and also recently for electrochemical energy conversion and storage. Fine tuning in their structures and morphologies greatly improved efficiency for electrochemical energy conversion and storage.

Covalent organic frameworks are the emerging class of crystalline organic porous materials formed by reversible covalent bond formation reaction between light elements like C, H, N, O, S etc. By the virtue of reticular chemistry, COFs can be rationally designed by judicious choice of monomers, which is very important to develop novel materials. But the low chemical stability of COFs largely prevents their uses in many fields including energy production and storage.

Chapter 2 represents the synthesis of a series of isoreticular chemically stable two-dimensional COFs by Schiff base condensation reaction. The high chemical stability originates due to the enol-keto tautomerization. Further, we were successfully delaminated all COFs into covalent organic nanosheets (CONs) by safe, and environmentally friendly mechanical grinding route. These exfoliated CONs are also highly chemically stable and have graphene-like layered morphology.

Chapter 3 will present the synthesis of two new chemically stable functional crystalline covalent organic frameworks (**Tp-Azo** and **Tp-Stb**). Both COFs show the expected keto-enamine form, and high stability toward boiling water, strong acidic, and basic media. The protonation of azo based COF (**Tp-Azo**) by H_3PO_4 shows its potential as proton conducting materials. The extension of the azobenzene monomeric unit in higher dimensions with a 1D channel facilitates unidirectional proton transport. H_3PO_4 doping in **Tp-Azo** leads to immobilization of the acid within the porous framework, which shows proton conduction in both the hydrous ($\sigma = 9.9\times10^{-4}$ S cm^{-1}) and anhydrous state ($\sigma = 6.7\times10^{-5}$ S cm^{-1}). This report constitutes the first emergence of COFs as proton conducting materials.

Chapter 4 describes the synthesis of a sulfonic-acid-based covalent organic framework (**TpPa-SO_3H**) that exhibits intrinsic proton conductivity under anhydrous conditions. The sulfonic acid groups are aligned on the two-dimensional (2D) layers at periodic intervals and promote the proton hopping inside the hexagonal one-dimensional channel. The intrinsic proton conductivity of **TpPa-SO_3H** was measured as 1.7×10^{-5} S cm^{-1} at 120 °C under anhydrous conditions. To enhance the proton conductivity, we have synthesized a hybrid COF **TpPa-(SO_3H-Py)** by a ligand-based solid-solution approach that contains sulfonic acid as the acidic site, as well as pyridine as the basic site, in order to immobilize acidic proton carrier molecules. Impregnation of phytic acid molecules inside the framework increases the anhydrous proton conductivity up to 5×10^{-4} S cm^{-1} at 120 °C. Such an approach highlights the advantage and first-time use of hybrid COF for interplaying intrinsic to extrinsic proton conductivity.

Chapter 5 describes the synthesis of two redox-active covalent organic frameworks [**TpPa-$(OH)_2$** and **TpBD-$(OH)_2$**] and their pseudocapacitor application. Of these COFs, TpPa-$(OH)_2$ exhibited the highest specific capacitance of 416 F g^{-1} at 0.5 A g^{-1} current density in three electrode configuration while the highest specific capacitance was 214 F g^{-1} at 0.2 A g^{-1} current density in two electrode configuration. Superior specific capacitance was due to the emergence of excellent pseudocapacitance by virtue of precise molecular level control over redox functionalities present in the COF backbone. The exceptionally high specific capacitance of **TpPa-$(OH)_2$** was due to the reversible proton-coupled electron transfer ($2H^+/2e^-$) of hydroquinone/benzoquinone (H_2Q/Q) moieties wherein H_2Q and Q had comparable chemical stabilities during redox cycling that originated from H-bonding, which was supported by calculated structures.

Finally, Chapter 6 will describe the summary of the overall work presented in this thesis. The future direction based on the understanding of this thesis work also presented in the last section of this chapter.

Suman Chandra

CONTENTS **PAGE**

CHAPTER 1

Covalent Organic Frameworks: Concept, Construction and Applications

CHAPTER 2

Mechanical Delamination of Chemically Stable Isoreticular 2D Layer Covalent Organic Frameworks (COFs) into Covalent Organic Nanosheets (CONs) 41-82

CHAPTER 3

CHAPTER 4

CHAPTER 5

Redox Active Covalent Organic Frameworks as Pseudocapacitor and the Role of Hydrogen Bonding in Capacitance **151-206**

LIST OF FIGURES

LIST OF TABLES

CHAPTER 1

Covalent Organic Frameworks: Concept, Construction, and Applications

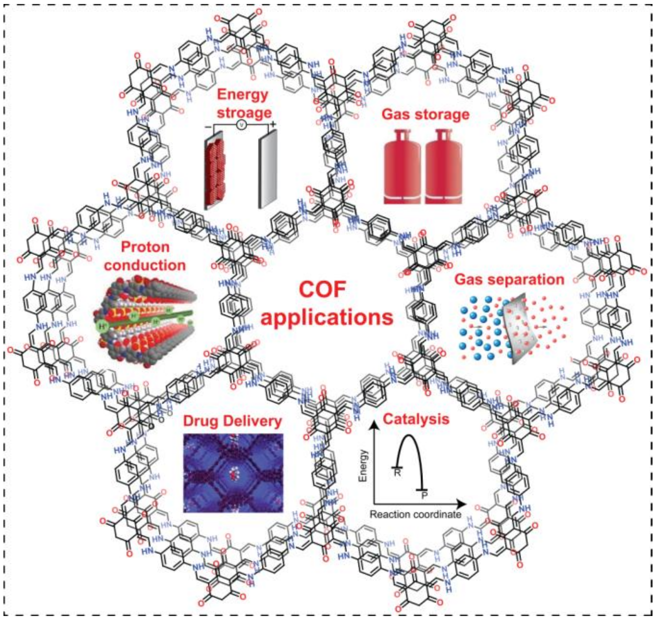

Abstract: *The ever increasing demands of energy and the worst effect of green house gases (like* CO_2 *etc) in environment concern scientist to develop new materials for sustainable energy conversion and storage. In this respect, Covalent Organic Frameworks, a class of emerging crystalline organic porous frameworks with predetermined topologies and functionalities, are ideal materials for gas storage and separation (such as* H_2*,* CH_4*,* CO_2*), proton conduction (in fuel cell), photoconduction (in solar cell), capacitive energy storage (in supercapacitor and battery), heterogeneous catalysis, separation, drug delivery and many others field. Despite these promising applications, the utilization of this porous COF material towards real life application has not recognized yet, due to complex problems such as chemical instability and scalability. So scientists are looking for the methodologies to stabilize these COFs and use it for practical application.*

1.1 General Background

The over growing world population demands a huge amount of sustainable energy source and their storage medium [1.1]. The diverse effect of global warming due to the CO_2 emission restricts the uses of fossil fuels and search for alternative non-emissive renewable energy sources like solar, wind, wave and another natural source [1.2]. Scientists are not only searching for alternative energy production sources like nuclear power, hydrogen power, electrochemical etc, but also focusing on the storage of the energy to use it conveniently [1.3]. So huge amount of research is going on the development of porous materials to store different gases for clean energy production like (H_2, CH_4 etc) as well as the storage of ions (like in fuel cell, battery, and supercapacitor) and their conduction [1.4]. The prime development of novel material is mainly based on their stability, cheapness (easy to synthesize) and high efficiency towards energy production and storage

Porous materials can play a pivotal role in the area of sustainable energy since they were already been used for an application such as gas storage, separation, catalysis, energy storage, sensing, water purification etc [1.5]. Activated carbons, zeolites, mesoporous silica are some of the examples of porous materials [1.6]. Due to their high surface area and tailored pore size, they have used as ion exchange membranes and electrode materials in fuel cell. The efficiency of a cell depends on the electrode/electrolyte interaction, which mainly depends on the surface area and the conductively of the materials. So research has been focused to develop novel porous materials with high surface area, high stability, high conductivity and optimum pore size [1.7].

Designing porous materials with controlled pore size and selective functionality is one of the main challenges for improving performance in the area of gas storage, energy storage, electronic properties etc [1.8]. In 1998, Yaghi and coworkers discovered a new type of inorganic-organic hybrid porous materials, termed as metal organic frameworks (MOFs) [1.9]. Metal organic frameworks (MOFs) are an open porous framework with single crystalline structure, constructed from the metal ions clusters and organic linkers. Their ultra high porosity and controlled pore size make them better materials for adsorption, catalysis, and separation [1.9]. Due to the reversible nature of the coordinate bond generated during the MOF synthesis, their low physicochemical stability limits their practical applicability [1.10]. One of the ways to improve the thermochemical stability of the porous frameworks is replaced the weak coordinate bond with strong covalent bonds. However, connecting organic building blocks (monomers) through covalent bonds into periodically ordered frameworks structure is a great challenge for researchers. Even though scientists were able to impart crystallinity in 1D polymers, attempts to build 2D or 3D crystalline organic framework with order periodic structure with covalent bonds often results in the formation of amorphous cross linked polymers [1.11]. In 2005, Yaghi and coworkers were able to solve this long standing problem by synthesizing the first covalent organic framework (COF) using the basic rule of reticular chemistry and following the Dynamic Covalent Chemistry (DCC) [1.12].

1.2 Classification of the porous materials

According to IUPAC, depending upon the size of the pore, porous materials have been divided into three categories, (a) Microporous materials having pore diameter less than 2 nm; (b) Mesoporous materials having pore diameter in between 2-50 nm and (c) Macroporous materials having pore diameter more than 50 nm (Figure 1.1). On the other hand, depending upon the constituted framework material type, porous materials have been divided into three categories, (i) Purely inorganic; (ii) Inorganic-organic hybrid and (iii) Purely organic (Figure 1.2).

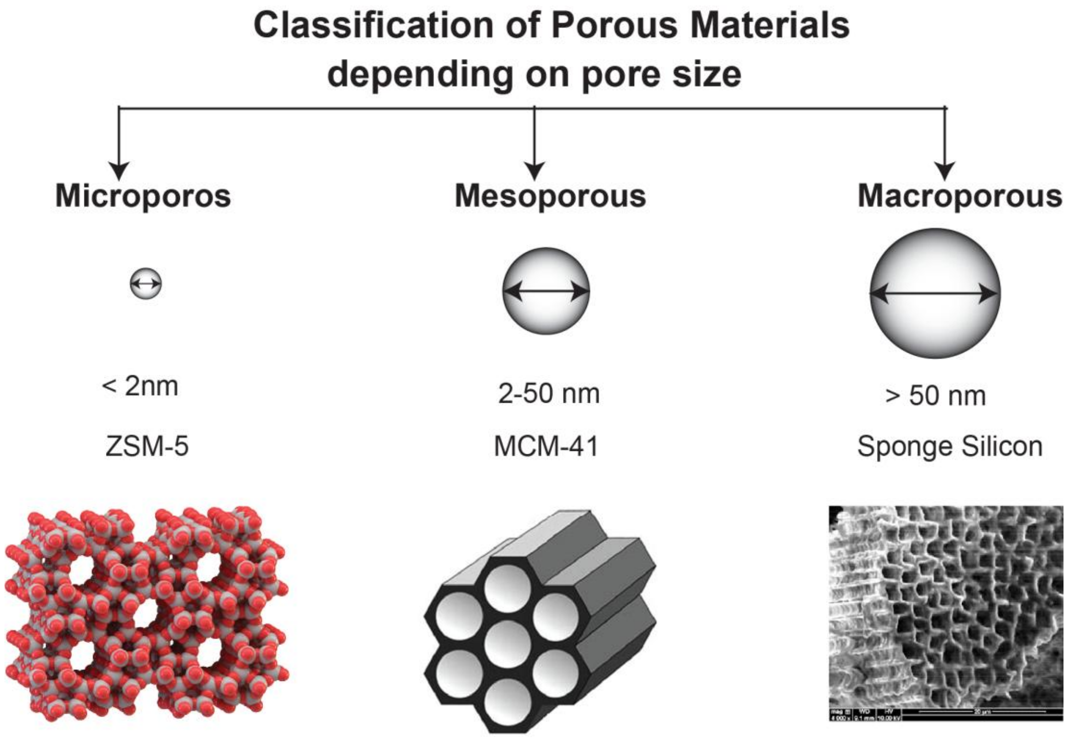

Figure 1.1: *Classification of porous materials based on the pore size.*

1.2.1 Inorganic porous Frameworks

Zeolites, aluminophosphates, germanosilicates, titanosilicates and metal phosphates (copper, zinc, gallium, iron phosphates, etc.) are the common examples of inorganic porous frameworks materials. Zeolites are crystalline aluminosilicates, primarily constructed from the tetrahedral corner sharing TO_4 (T = Si, Al) species. The general formula for zeolites is $M_{n+x/n}[(AlO_2)_x(SiO_2)_y]_x \cdot wH_2O$ (M= metal). [1.13a]. Pure silica frameworks are formed from SiO_4 tetrahedral units and are electrically neutral. When some of the SiO_4 units are replaced by aluminium, a charge imbalance is created, and as a result, framework becomes anionic in nature. To balance the charge, the framework also occupies metal cations such as Na^{+1}, K^{+1}, Ca^{+1}. The presence of these metal cations helps to induce ion exchange characteristics to zeolites. The ratio of the silicon to aluminium (Si/Al) in zeolites varies from zero to one. Most of the zeolites are strong Bronsted acid due to the presence of bridging hydroxyl group. Zeolite framework structure contains cavities or pores in the range of 3 to 15 Å [1.13b]. Replacement of the silicon atoms in zeolites with aluminium and phosphorus results in another class of inorganic porous framework materials called aluminophosphates (AlPOs) [1.14]. Aluminophosphates are usually formed as neutral, due to the presence of octahedral aluminium sites in the framework.

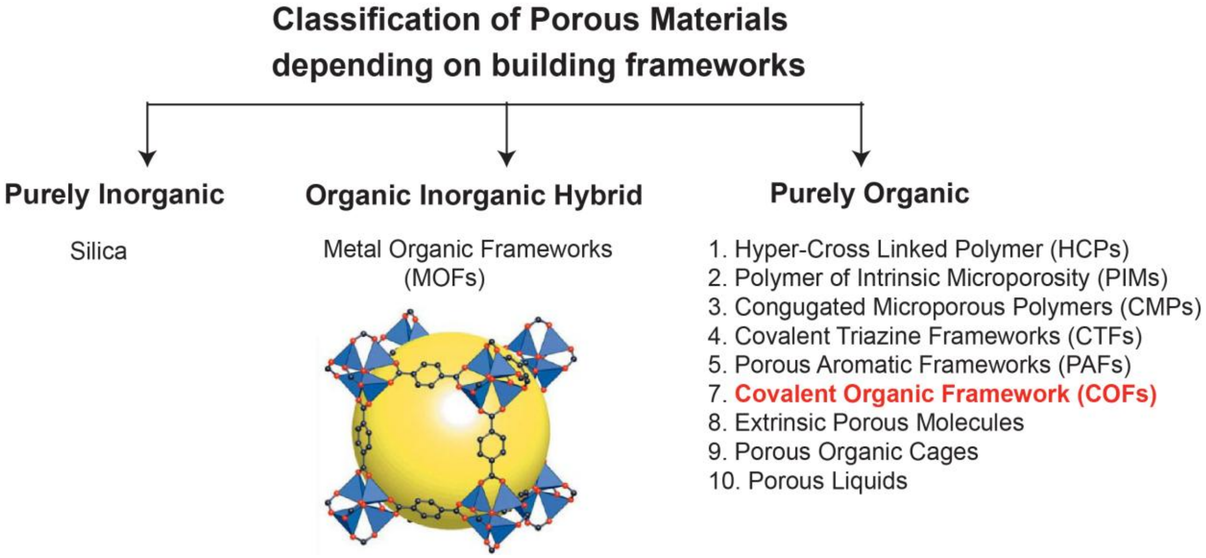

Figure 1.2: *Classification of porous materials based on the framework material type.*

Replacement of aluminium by bivalent metal ions such as copper, gallium or zinc will lead to the formation of anionic metal phosphate frameworks [1.15]. Due to the low production costs, high chemical and thermal stability zeolites were widely employed as industrial adsorbents and catalyst. Some of the important applications of zeolites are shaped selective catalysts, water purifiers or softeners, dehydrating and dehumidification agent and heat storage materials [1.16].

1.2.2 Inorganic-organic hybrid porous frameworks

It is very difficult to functionalize inorganic porous frameworks and therefore limits the structural diversity of the frameworks. The bonding between organic and inorganic units with proper arrangement leads to a discovery of novel unprecedented crystalline structures. Metal organic frameworks (MOFs) are a common example of inorganic-organic hybrid porous frameworks [1.9]. MOFs possess a three-dimensional framework structure with metal ion clusters at the nodes separated by organic ligands spacers. The metal ions used in MOF synthesis varies from transition metals (e.g. Cu, Zn), alkaline earth elements (e.g. Sr, Ba), p-block elements (e.g. In, Ga), actinides (e.g. U, Th) [1.17]. The commonly used organic spacers in the MOF construction are di, tri, tetra or poly carboxylate, imidazolate or phosphate anions and bipyridine ligands [1.17]. MOFs follow basic rules of reticular chemistry and it is easy to predesign the framework structure and porosity. Functional variation and pore size tuning of MOFs can be controlled by interchanging the organic spacers in iso-reticular structures. Based on the nature of the frameworks, MOFs are classified in three groups namely 1) 1st generation, 2) 2nd generation, 3) 3rd generation [1.18]. 1st generation MOF frameworks only retain their framework structure in presence of guest/ solvent molecule. After the removal of the guest molecules framework structure usually get collapsed. 2nd generation MOFs are stable and robust. They retain their 3D framework structure even after the solvent removal. 3rd generation MOFs are flexible and their porosity and surface area changes in a response to the external stimuli [1.18c]. MOFs are usually crystallized by the solvothermal reaction, with solvents/guest molecule trapped inside pores. Removal of these solvent/guest molecules generates open framework structures in MOF with ultra high porosity. MOFs were tested for different gas storage application (H_2, CO_2, CH_4, acetylene etc). Selective adsorption/ separation of gas molecules was also performed in MOFs with precise pore channels. The other important applications of MOFs are catalysis, proton conductivity, drug delivery etc. [1.19]. Despite the interesting properties, MOFs also suffer from some disadvantages. It is difficult to extend the porosity of MOF to the mesoporous region, thus storage of bigger sized guest molecules (e.g. biomolecules) is found to be difficult. MOFs also lack sufficient chemical and thermal stability, since they are constructed from weak coordinate bonds [1.10].

1.2.3 Organic porous frameworks

Scientists are always searching for porous materials which are totally composed of organic building units [1.20]. Organic porous framework materials are a kind of porous frameworks exclusively constructed from organic building blocks, with the strong covalent bond connection. These organic frameworks showed high chemical and thermal stability due to the formation of strong inter connected covalent bonds. Unlike metal organic frameworks (MOFs) and zeolites, these organic frameworks consist of only light weight elements which significantly reduce their framework density and finds application gravimetric gas storage purpose. Depending on the crystallinity, organic porous frameworks are divided into two categories, (1) porous polymeric frameworks (POPs) [1.20a-b] and (2) covalent organic frameworks (COFs) [1.20e-f]. Porous polymeric frameworks (POPs) are amorphous in nature while covalent organic frameworks (COFs) possess a crystalline framework structure and ordered pore channels.

Porous Polymeric Frameworks: Porous polymeric frameworks (PPFs) are a class of highly cross-linked microporous polymers with disordered (amorphous) structure. PPFs are usually synthesized by irreversible C-C coupling reaction (like Suzuki coupling [1.21a-b], Sonogashira-Hagihara [1.21c], Yamamoto coupling [1.21d-e]), acetyl cyclotrimerization [1.21f], oxidative coupling reaction [1.21g-h], Friedel–Crafts reaction [1.21i] and phenazine ring fusion reaction [1.21j]. Although irreversible nature of the bond formation resulted in disorder structure which limits the pre-designed based reticular synthesis (like COFs), these frameworks showed high physicochemical stability for real life practical applications. Cooper and coworkers reported the first PPFs (CMP-0 and CMP-5) with surface areas ranging from 1018 m^2 g^{-1} (CMP-0) to 512 m^2g^{-1} (CMP-5) [1.21l].

1.3 Covalent organic frameworks

The formation of the molecule from the atoms through covalent bond formation had well documented by G.N. Lewis in the long back. In addition, organic chemists have introduced "Retrosynthesis" method for the synthesis of targeted new molecules from easily available small organic compounds. Polymer chemists also have been able to successfully link the organic molecules in a linear chain to form macro molecular structures (1D polymer) by covalent bonds. Supramolecular chemists were able to form well defined extended (2D and 3D) organized structures from the self-assembling of small molecules by weak interactions like H bond and Van der Waals forces. But, their limited thermal and chemical robustness hinder to modify these supramolecular structures for the applications. In 2005, Yaghi and coworkers have shown that organic molecules can be linked periodically precise manner by strong covalent bonds in two or three dimensions maintaining their molecular integrity [1.22a]. They introduced Covalent Organic Frameworks (COFs), which holds the chemistry of dynamic covalent bond formation (also known as Dynamic Covalent Chemistry, DCC) and synthesized predicted rigid porous crystalline frameworks through reticular synthesis [1.22b]. By the virtue of strong covalent bonds, COFs are thermally and chemically robust. Their structures can be modified without the destruction of the frameworks and in addition, their pore can be functionalized and tuned through the proper selection of the building blocks. As a result, COF materials open up a new direction in materials chemistry [1.22]. By virtue of their high surface area, low density, robustness and predesigned functionality, COFs have been used in many applications like gas storage, gas separation, catalysis, sensing, energy storage and many other fields [1.23].

1.3.1 Reticular approaches to generate COFs:

As the synthesis of targeted large organic molecule can be visualized by the retrosynthesis approaches in organic chemistry, the frameworks can also be synthesized by using reticular approaches in supramolecular chemistry [1.24]. In step-1, we chose a target network topology and deconstruct it to its building blocks. In step-2, we evaluated these building blocks as per their connectivity (like tetrahedral vs square planar for the connectivity of four) and geometry. In step-3, we search for organic molecules that are equivalent to the geometric units and used them as a linker for COF synthesis (Figure 1.3).

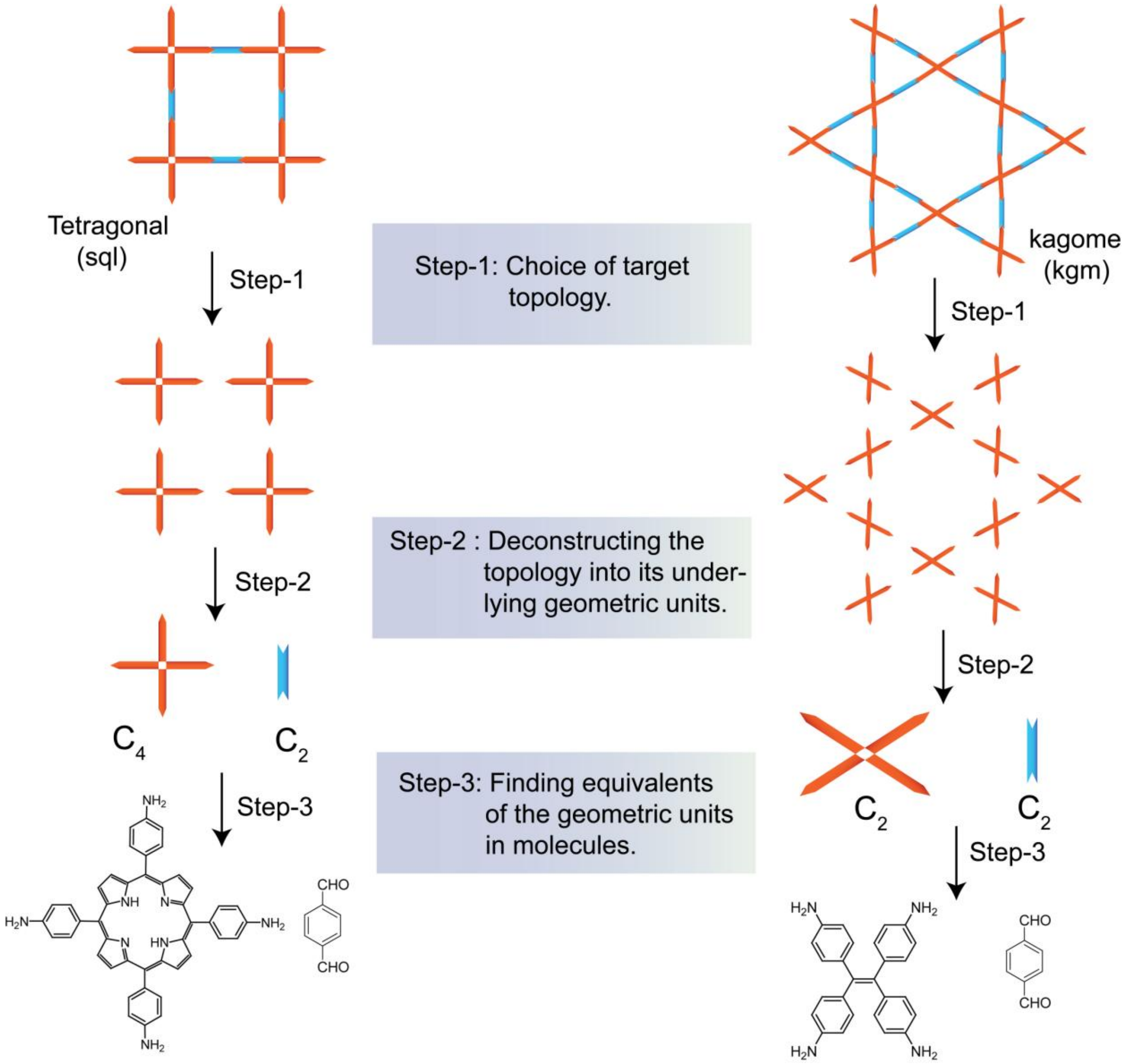

Figure 1.3: *Reticular synthesis of COFs. Shown are the steps involved in choosing the topology, deconstructing it into its fundamental geometric units, finding the equivalents of these in molecules.*

1.3.2 Mechanism studies and approaches used to improve the quality of COF materials

In the case of two-dimensional polymerization, there are two distinct approaches (i) thermodynamic approaches where the building blocks are simultaneously assembled and polymerized by the dynamic covalent bond formation reaction to form 2D-covalent organic frameworks; (ii) kinetic approaches where building blocks are pre-organized prior to the polymerization by irreversible bond formation [1.22b].

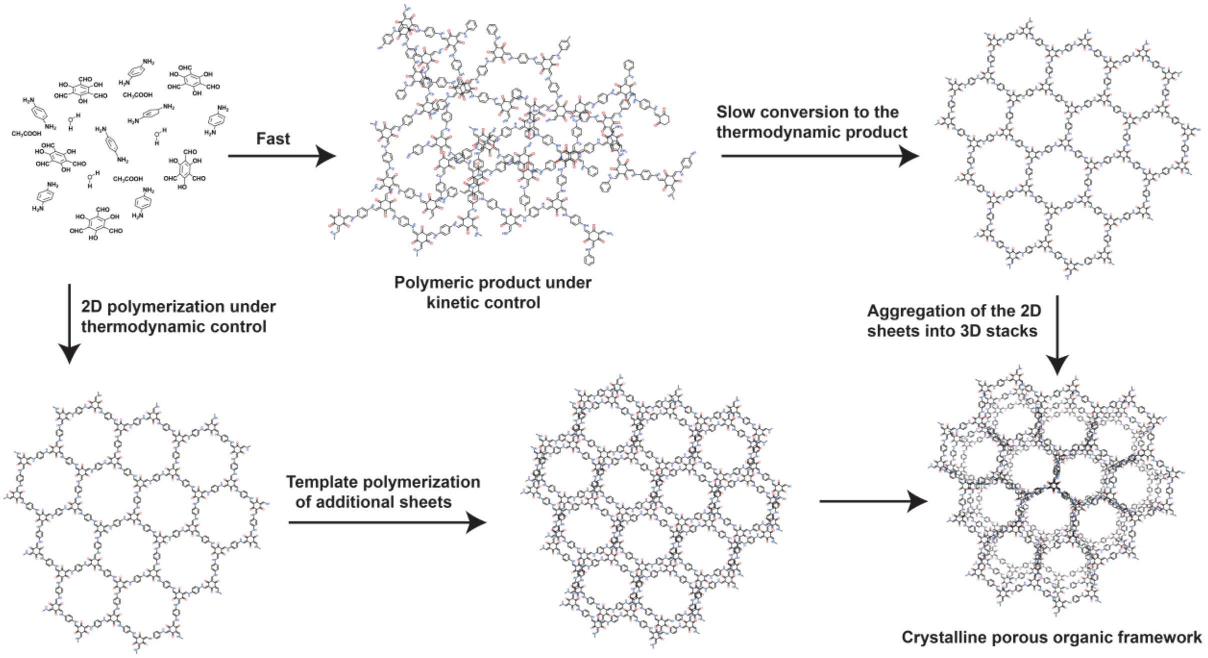

Figure 1.4: *Possible mechanistic steps during the formation of imine based 2D COF.*

In general, the formation of amorphous materials by irreversible covalent bond formation is thermodynamically favorable. Therefore, microscopic reversibility during the covalent bond formation is a necessary condition for the formation of extended crystalline solid. In addition, the reaction rates should be such that it permits the self-correction of defects generated by initial polymerization. So, the finding of optimized reaction conditions (solvents, temperature, pressure, time, catalyst, modulator etc) for the reversibility is a challenge for COF researchers. This has been realized by choosing reversible condensation reactions like boronic acid trimerization [1.22], boronated ester formation [1.25], nitrile group trimerization [1.26] and Schiff base reaction [1.27] for COF synthesis. By controlling the concentration of the by-product (generally water) and pressure, it is possible to control the microscopic reversibility of the reaction.

In order to improve the COF materials quality i.e. crystallinity, porosity, surface area, crystallite size etc, it is necessary to understand the nucleation and growth process during the COF synthesis. The better understanding of the kinetics of polymerization and crystallization process will help for the improvement of the quality of COFs materials. Dichtel and coworkers, first time, studied the formation of boronate ester based COF from their completely soluble monomers by optical turbidity measurements and showed the effect of water addition in the improvement of crystallinity by hydrolyzing the initially formed oligomers precipitate to its parent building blocks [1.28a]. Also, they showed that the addition of monofunctional catechol as a competitor during the polymerization reaction slows down the rate of COF formation but unable to increase the crystallite size. Bein and coworkers, first time, successfully exhibited the role of a modulator (competitor, here mono-functionalized boronic acid) to increase the crystallinity of COFs and further functionalize the COF surface [1.28b]. In another report, Banerjee and coworkers also showed the role of monohydrate p-toulenesulfonic acid (PTSA.H_2O) as a modulator to form highly crystalline COFs via the mechanochemical method in a few minutes [1.28c]. Here, monohydrate PTSA not only acts as a solid Bronsted acid catalyst for the Schiff base reaction but also acts as a water reservoir to gain the reversibility by controlling the amount of water in the reaction. Dichtel and coworkers also synthesized highly crystalline COFs at room temperature within a few minutes (10-30 min) by using metal triflates especially, $Sc(OTf)_3$ as water resistant Lewis acid catalyst [1.28d]. Another approach to improve the COF crystallinity has been to design monomers which will pre-organize to form periodic order structures. In this respect, Banerjee and coworkers used 2,5-dihydroxy terephthaldehyde for the Schiff based COF synthesis where the H-bonding between the newly formed imine N and the –OH group co-planarized the whole structure, and hence enhanced the stacking of 2D layers resulting improved crystallinity and surface area [1.28e]. Similarly, Lotsch and coworkers also able to minimize the dihedral angle by introducing N atom of the central ring of 1,3,5-triphenyl benzene based COFs to planarized the whole structure for better stacking and therefore better crystallinity [1.28f]. Jiang and coworkers also showed the improve COFs crystallinity by minimizing the repulsion caused by the same polarity of imine bonds (C=N) between the pi-pi stacking layers via introducing methoxy groups in the building blocks [1.28g]. Here oxygen lone pairs are conjugated with the imine bond causing less charge separation in imine bond, which helps in stacking the 2D layers, resulting in good crystallinity. In another way, the same group minimized the repulsion between the layers by using terephthaldehyde and its perfluorinated analogs for mix link COF synthesis [1.28h]. They suggested that the pi-pi stacking force was greatly improved between the electron rich benzene in one layer and electron deficient benzene in another. Salonen and co-workers also showed that the cancellation of dipole moments in the building blocks can help to get better crystalline COF materials [1.28i]. Recently, Bein and coworkers introduced propeller like monomer (tetraphenyl ethylene units) which stack in a distinct way to give a better chance of fusion between grain boundaries of COFs resulting good crystalline COF materials [1.28j].

1.4 Types of reversible reaction used for the synthesis of COFs

1.4.1 Boronic acid trimerization reaction:

In 2005, Yaghi and coworkers introduced a new class of emerging materials, known as Covalent Organic Frameworks, by synthesizing first COF (COF-1) from the self condensation reaction of 1,4-benzene diboronic acid to form boronic acid anhydride (boroxine) based crystalline two dimensional frameworks (Figure 1.5a). After that many boroxine based COFs have been synthesized e.g COF-102, COF-103, PPy-COF [1.22]. Due to the high reversibility of this self-condensation reaction, boroxine based COFs exhibit high crystallinity and porosity, but at the same time low chemical stability.

1.4.2 Boronate ester formation reaction:

Yaghi and coworkers, for the first time, showed that the condensation esterification reaction between boronic acid and aromatic diols was reversible and used it for the synthesis of boronate ester based COFs (Figure 1.5b) like COF-5, COF-8, COF-10 etc [1.25]. The generated boronate ester five member ring (C_2O_2B) is completely planar with the building block motif. These frameworks exhibit high crystallinity and surface area due to the high reversibility of the esterification reaction. The major drawback of these kinds of frameworks is its low chemical stability.

1.4.3 Aminoborane trimerization reaction:

El-Kaderi and coworkers have successfully synthesized crystalline borazine based polymer BLP-2(H) by the thermal decomposition of 1,3,5-(p-aminophenyl)-benzene-borane in solvothermal condition (Figure 1.5c). The borazine based COFs exhibit high thermal stability (~420 ºC) and high surface area (SA_{BET} = 1178 m^2g^{-1}). It also showed high hydrogen uptake of 2.4 wt% at 77 K and 15 bar along with isosteric heat of adsorption of 6.8 kJ mol^{-1} [1.29].

1.4.4 Schiff base reaction:

One of the major breakthrough in early COF chemistry was the introduction of the reversible Schiff base reaction (Figure 1.5d) in the synthesis of COFs by Yaghi *et al*. They successfully synthesized first three dimensional COF-300 by the Schiff base reaction between

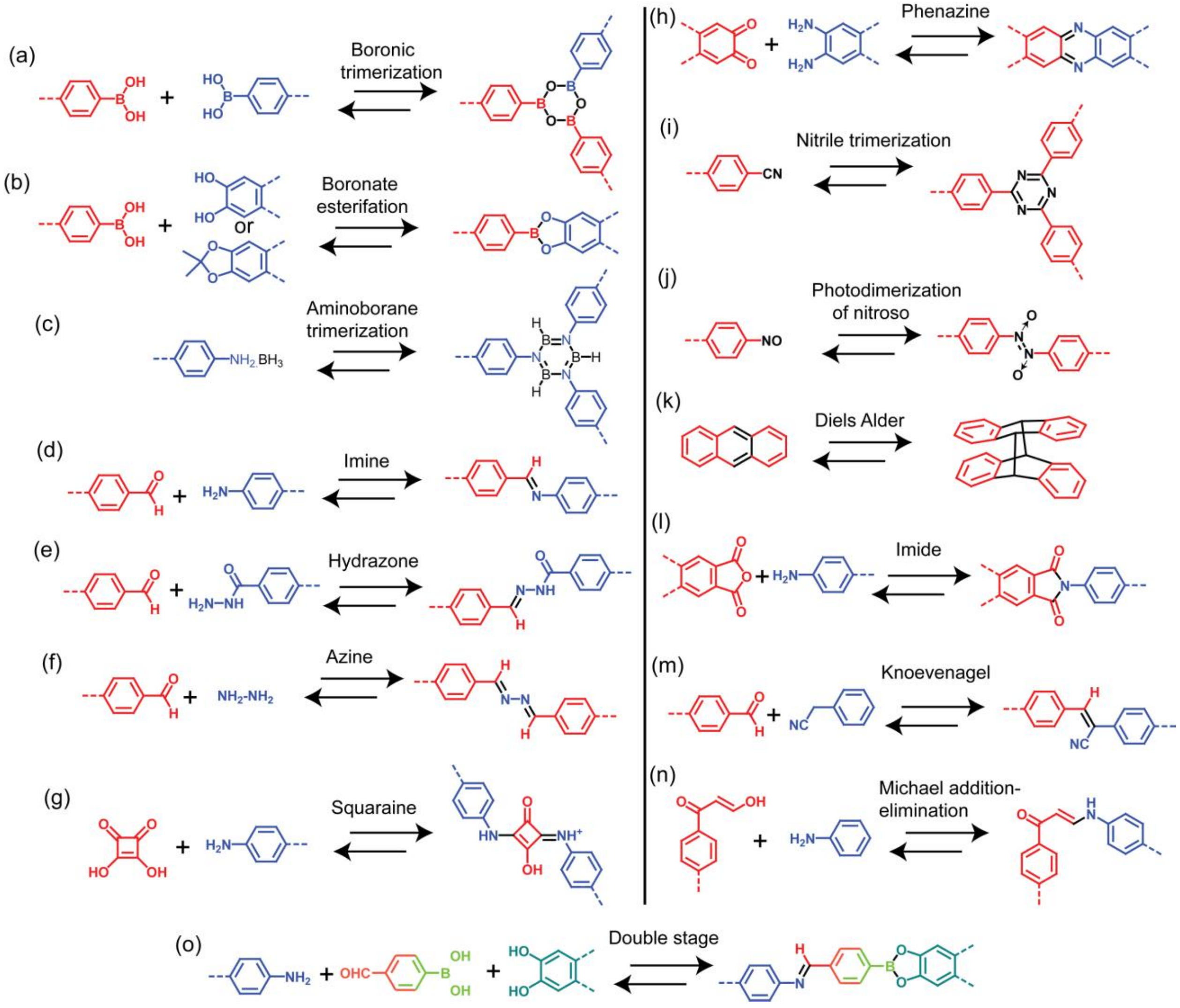

Figure 1.5*: Different reversible organic reaction used for the synthesis of COFs.*

tetra-(4-anilyl) methane (Td) and terephthaldehyde (C2) [1.27]. After this seminal works, many Schiff based 2D COFs (e.g COF-42, COF-43, COF-366, COF-LZU-1 etc) have been synthesized by using symmetry combination like C3 + C2 or C3 + C2. Many acid catalysts [aqueous acetic acid, $BF_3.Et_2O$, $Sc(OTf)_3$, PTSA] have been used for the complete reversibility of the Schiff based reaction. As these imine based COFs have moderately high hydrolytic stability than other boron based COFs, they were found more practical applications like catalysis, gas storage and separation, energy application and others. However, at very high acidic or basic condition the imine based COFs decomposed into its monomers.

1.4.5 Hydrazone Reaction:

After the synthesis of imine based COFs by Yaghi *et al.*, the same group explored hydrazone reaction for the synthesis of hydrazone link COFs (COF-42 and COF-43) from their respective monomers (Figure 1.5e). This new linkage reaction generates crystalline COFs with high surface area, and high chemical stability [1.30a]. Due to its high chemical stability towards solvents, Dichtel and coworkers exfoliated these 2D layered hydrazone based COFs into few layer 2D polymer in bulk [1.30b].

1.4.6 Azine Reaction:

Jaing and coworkers explored new linkage reaction by synthesizing azine based COFs via the condensation of hydrazine and 1,3,6,8-tetrakis(4-formylphenyl)pyrene (Figure 1.5f) [1.31]. The reaction condition is similar like imine based COF synthesis. Due to the periodically order pyrene columns and one dimensional porous channel structure, this COF showed highly luminescent properties and used as sensor for explosive like 2,4,6-trinitrophenol detection. After this seminal work, many azine based COFs have been synthesized by using hydrazine and C_3-symmetric trialdehydes. These azine based frameworks showed good crystallinity, high porosity and high chemical stability. Synergetic effect of chemical stability and order porous structure make them better materials for practical application in sensing, catalysis and other field.

1.4.7 Phenazine Reaction:

Jiang and coworkers were able to synthesize phenazine based 2D covalent organic frameworks by the condensation of triphenyl heaxamine (TPHA) and *tert*-butyl pyrene tertalone (PT) in solvothermal condition (Figure 1.5h) [1.32]. The *tert*-butyl groups increase the solubility of the monomer to maintain the chemical reversibility during the polymerization. Unlike imine based COFs, these phenazine based COFs were chemically robust and at the same time fully conjugated and permanently porous. Unlike conjugated microporous polymer (CMP), phenazine based COFs are crystalline in nature and can be used as molecular motif for designing ordered fully conjugated polymeric system. By the virtue of their high chemical stability, extended pi conjugation and permanently porous structures, these phenazine based frameworks can be used in organic electronics, energy storage, and fuel cell.

1.4.8 Trimerization of nitriles:

Thomas and coworkers in 2008, were able to synthesize first Covalent triazine based frameworks (CTF-1) ionothermally from the trimerization of aromatic nitrile in presence of molten $ZnCl_2$ at 400 ˚C (Figure 1.5i) [1.33]. The molten $ZnCl_2$ used not only acts as solvent but also as Lewis catalyst for this reaction. Due to the high chemical and thermal stability and high concentration of basic nitrogen, CTFs found many practical applications like CO_2 uptake, energy storage and conversion etc. However, the harsh reaction condition (400 ºC) for CTF synthesis limits the uses of the organic molecules as building blocks.

1.4.9 Polymerization of Nitroso Compounds:

Wuest and coworkers have described the polymerization of nitroso compounds in mild condition to form monocrystalline azodioxy frameworks e.g. NPN-1, NPN-2 and NPN-3 (Figure 1.5j) [1.34]. The azodioxy bond is quite ionic in character and its bond dissociation energy is in between 20-30 kcal/mole, which is quite less than pure covalent bonds. This gives the opportunity to self correct the initially formed polymeric networks into order crystalline frameworks. Oxidizing the initially synthesized hydroxyamines into nitroso compounds by Feriton’s reagent followed by filtering and keeping the solution at room temperature gives large crystals of azodioxy networks.

1.4.10 Cycloaddition Reaction:

Both Schlüter and King groups successfully synthesized two-dimensional polymeric crystal by photochemical reversible [4 + 4] cycloaddition reactions of properly designed anthracene based monomers (Figure 1.5k) [1.35]. These 2D crystalline frameworks are also easily exfoliated into nano-meter thin sheets which can be used as membrane and optoelectronic application.

1.4.11 Imidization Reaction:

In general imidization reaction is irreversible and it generates amorphous polyimide polymer of high thermal and mechanical stability. With proper choice of reaction condition, imide bond formation reaction can also become reversible. Yan and coworkers synthesized a series of 2D and 3D polyimide COFs (PI-COFs) via imidization reaction and showed their ability to dye absorption for temperature sensitive luminescent property and drug delivery (Figure 1.5l) [1.36].

1.4.12 Knoevenagel Condensation Reaction:

Feng and coworkers, for the first time, synthesized 2D fully conjugated olefinic linkage (C=C) frameworks by Knoevenegal polycondensation reaction of 1,4-phenylene diacetonitrile and C_3 symmetric aldehyde (Figure 1.5m) [1.37]. The generated carbanion intermediate partly stabilized by cyano groups making the Knoevenegal reaction quasi reversible. The synthesized layered crystalline 2D poly(phenylenevinylene) framework (2DPPV) have an optical band gap of 2.10 eV, less than the non-conjugated counterpart. These COFs further used for the preparation of porous carbon nanosheets for supercapacitor and electrocatalysis (ORR) applications.

1.4.13 Michel Addition-Elimination Reaction:

Perepichka and coworkers introduced dynamic polymerization based on Michel addition and elimination reaction between β-ketoenols and aromatic amines for the synthesis of novel 2D conjugated COFs (Figure 1.5n) [1.38]. The synthesized COFs having chemically robust olefinic (C==C) bond which is extended conjugated with the aromatic system. Unlike imine (C=N) bond, the olefinic (C=C) bond has low polarity and enable efficient π-delocalization between connecting molecular units. These β-ketoenamine based COFs showed good chemical stability due to the intramolecular C=O····HN hydrogen bonding as mentioned by Banerjee and coworkers. Additionally, the π-conjugation significantly reduced the band gap (1.8-2.2) and showed solid state luminescence. These COFs have been used to directly detect the triacetone triperoxide (TATP) explosive via fluorescence quenching.

1.4.14 Orthogonal reaction:

Zhao and coworkers, for the first time, introduced the idea of orthogonal reaction for the synthesis of double stage COFs. They were able to do two different reactions e.g. imine and boroxine parallelly to synthesized NTU-COF1 and NTU-COF-2 (Figure 1.5o) [1.39]. The main challenge was the design of the monomers and finding the proper reaction conditions where both the reactions will be reversible. They simultaneously used 4-formyl phenyl boronic acid (FPBA), a C_3 symmetric amine (TAPB) and a C_3 symmetric diols (HHTP) to form three components NTU-COF-2 in solvothermal condition. At high temperature, boronic acid reacts with diols to form boroxine ring and aldehyde reacts with amine to form imine bond. This strategy shows the synthetic feasibility for generating complicated COF based system using multi-component reaction in near future.

1.5 Basic symmetric rules of combination

MOFs and COFs are the ideal examples of materials whose topology can be designed from the symmetry of the building blocks. In order to build a rigid crystalline frameworks from

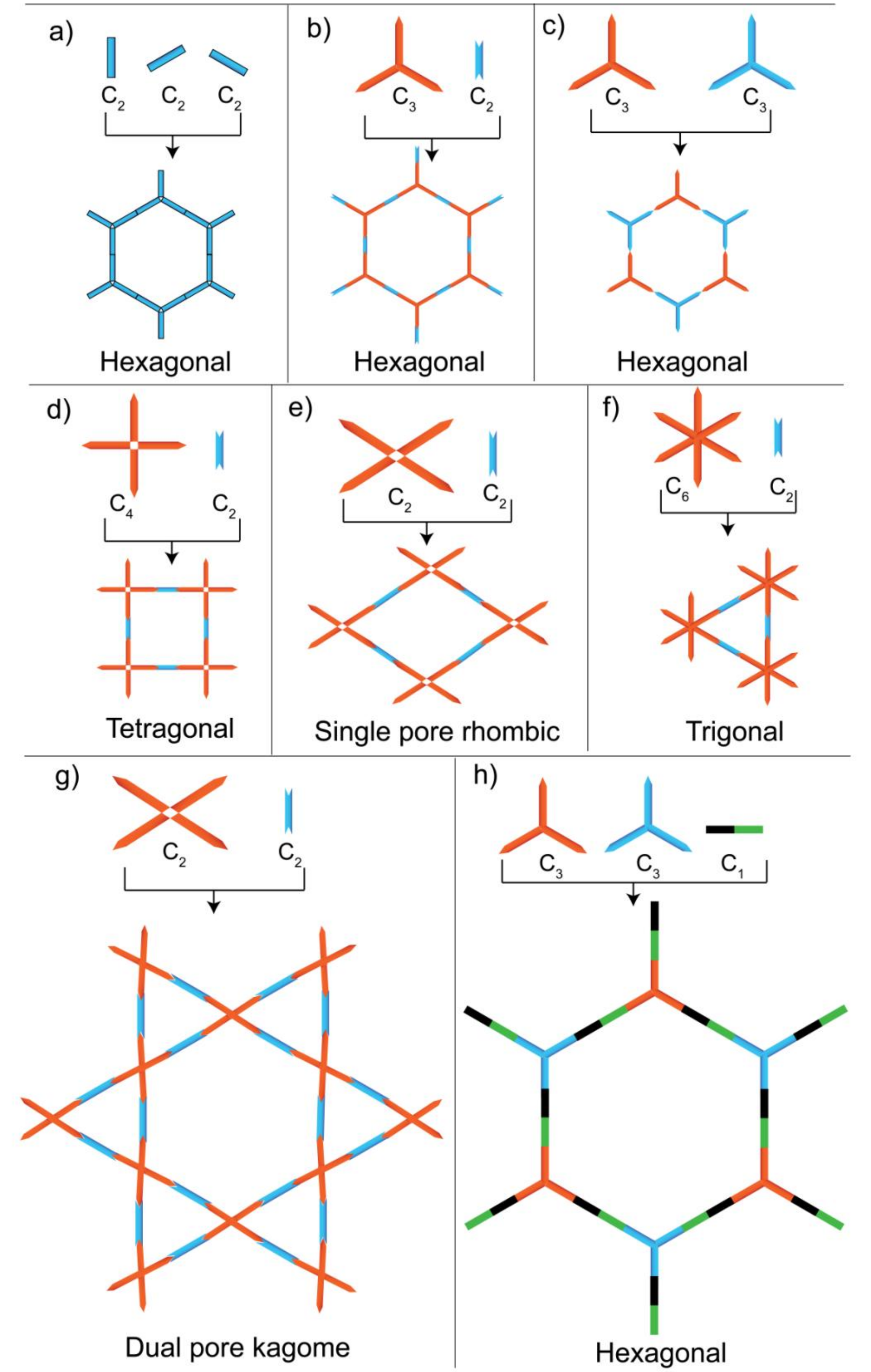

Figure 1.6: *Schematic representation of different organic symmetric combination used in COF framework construction.*

their building blocks (linkers and knots), it is necessary that the building blocks should maintained their rigidity during the polymerization. In addition, to make close porous structures, the building blocks should follow some basic symmetric rules of combination. According to the direction of reactive groups, they were classified different symmetric groups like 2D-C_2, 2D-C_3, 2D-C_4, 3D-T_d and 2D-C_6. Only some combinations are possible to generate a closed pore with

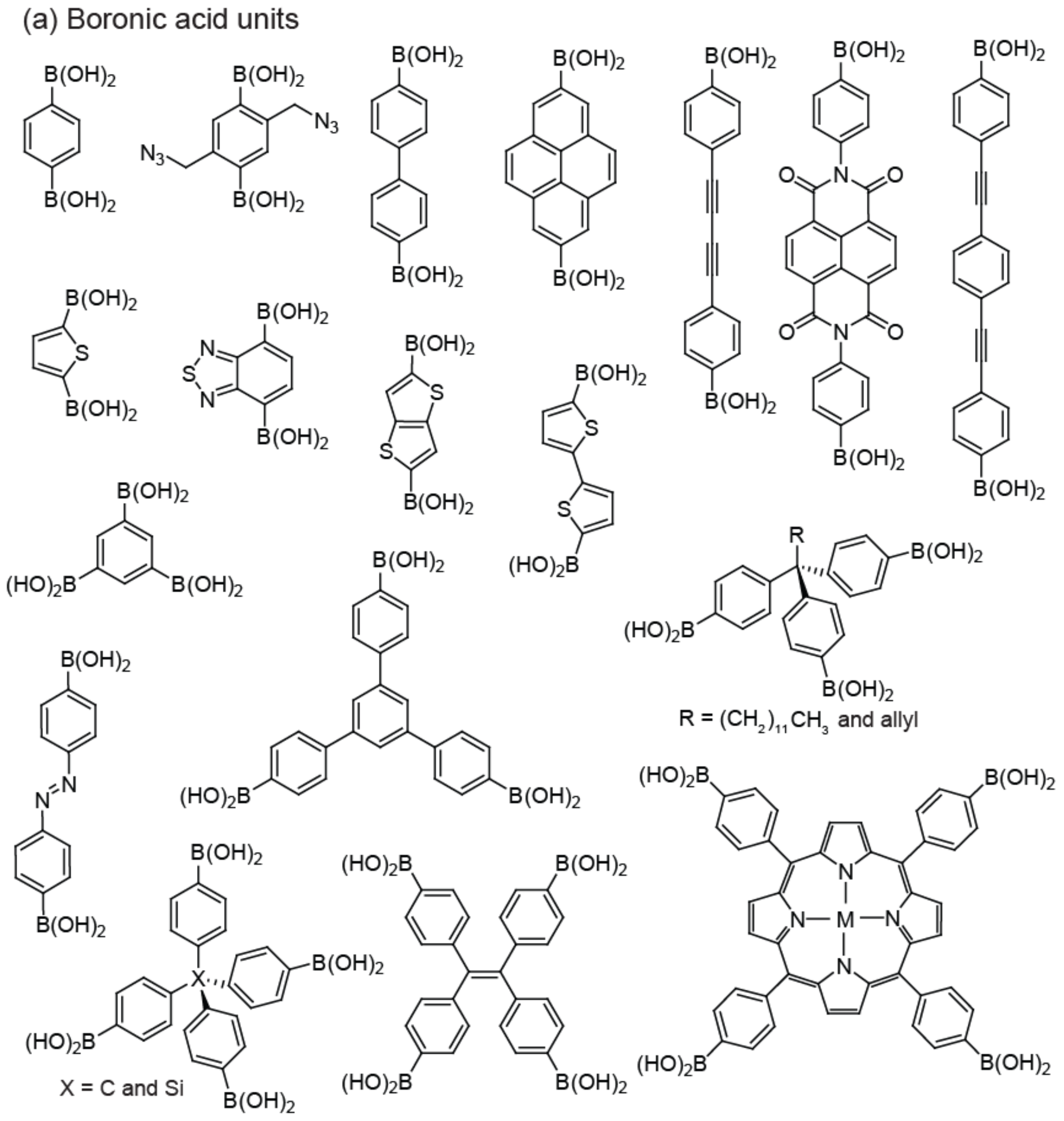

Figure 1.7: *Different boronic acid based building blocks used for the synthesis of boron based COFs.*

2D or 3D extended structure. For example, (2D-C_2 + 2D-C_2), (2D-C_2 + 2D-C_3) and (2D-C_3 + 2D-C_3) can lead to 2D-COFs with hexagonal pores (Figure 1.6a-c). Again, (2D-C_4 + 2D-C_2) can lead 2D-COFs with rectangular pore (Figure 1.6d). On the other hand, (2D-C_6 + 2D-C_2) will give 2D-

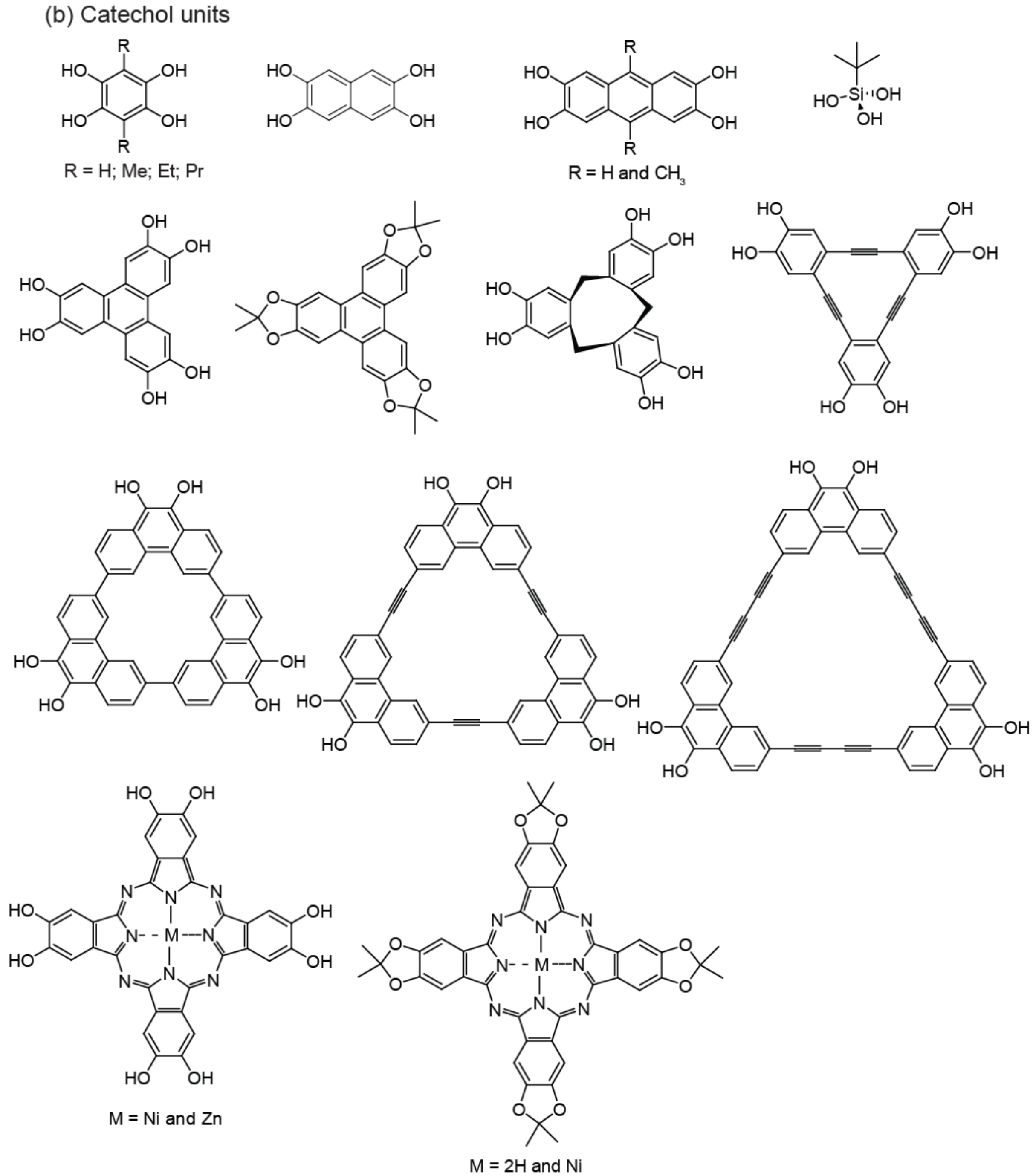

Figure 1.8: *Different catechol based linkers used for the synthesis of boron based COFs.*

COFs with triangular pores (Figure 1.6f). Moreover, (3D-T_d + 2D-C_2) can also generate 3D-COFs with diamondoid structures. Other combinations like (3D-Td + 2D-C3), (3D-Td +3D-Td) will give 3D-COFs with different crystalline space groups which are hard to ascertain. Also, the combination of four armed C_2 (D_{2h}) and two armed C_2 can lead to the 2D-COFs with dual pore kagome structure or rhombic-shaped skeletons (Figure 1.6e, g). Some asymmetric building blocks can also lead to the hexagonal structure with the dual pore. Recently, triple pore with kagome structure has been derived from C2 + C2 combination of one knot and two different linkers [1.40].

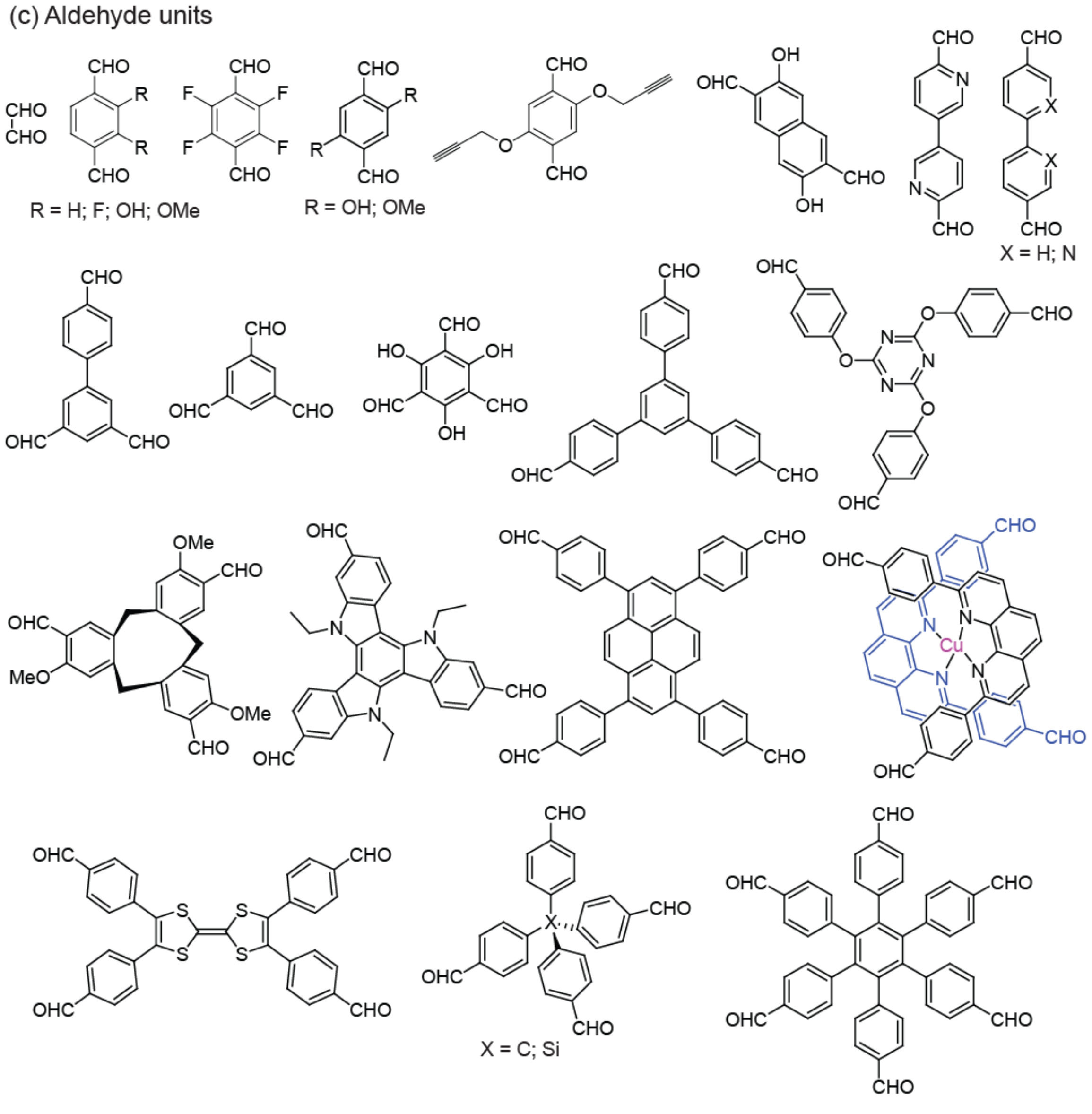

Figure 1.9: *Different aldehyde building units used for the synthesis of imine based COFs.*

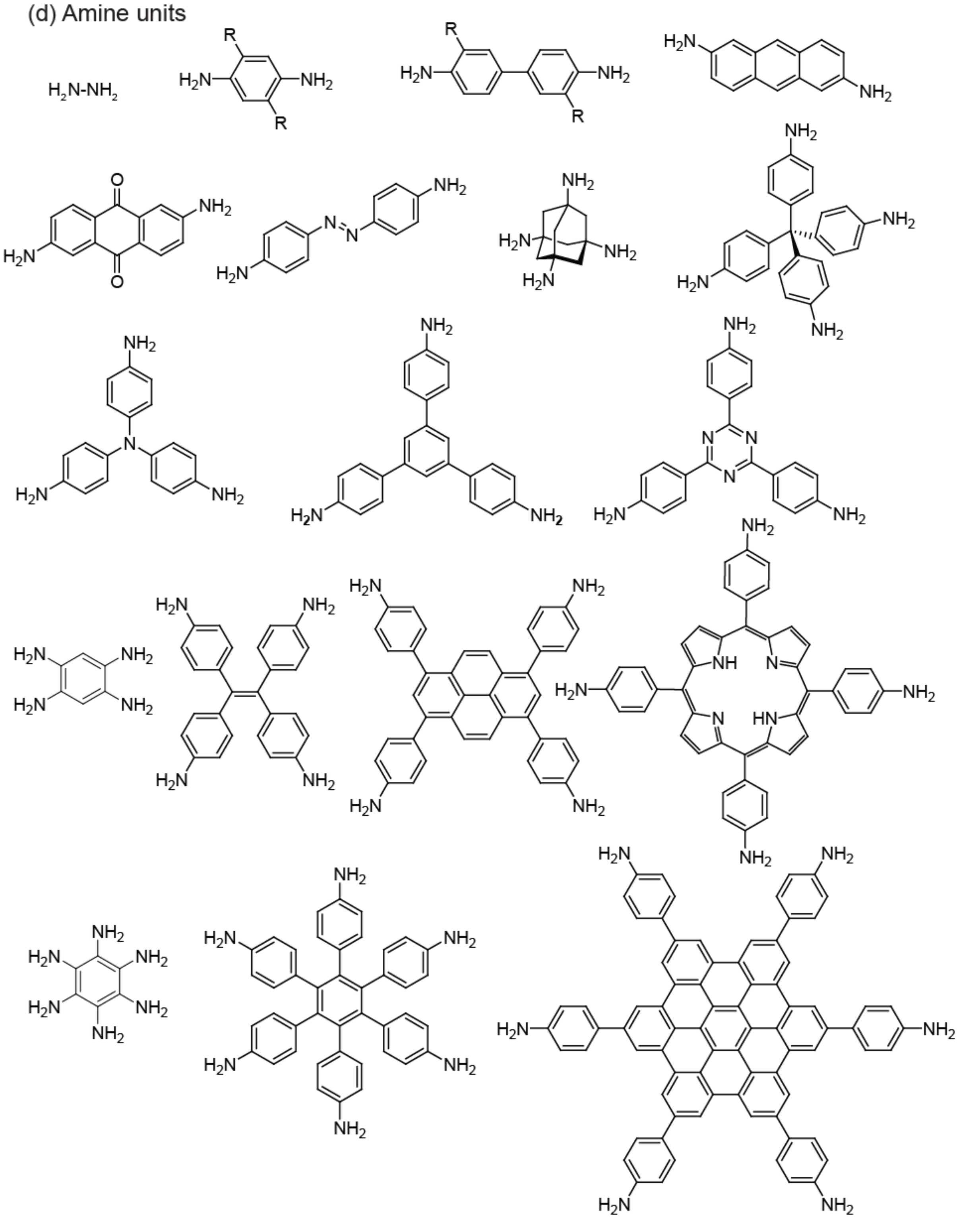

Figure 1.10: *Different amine linkers used for the synthesis of imine based COFs.*

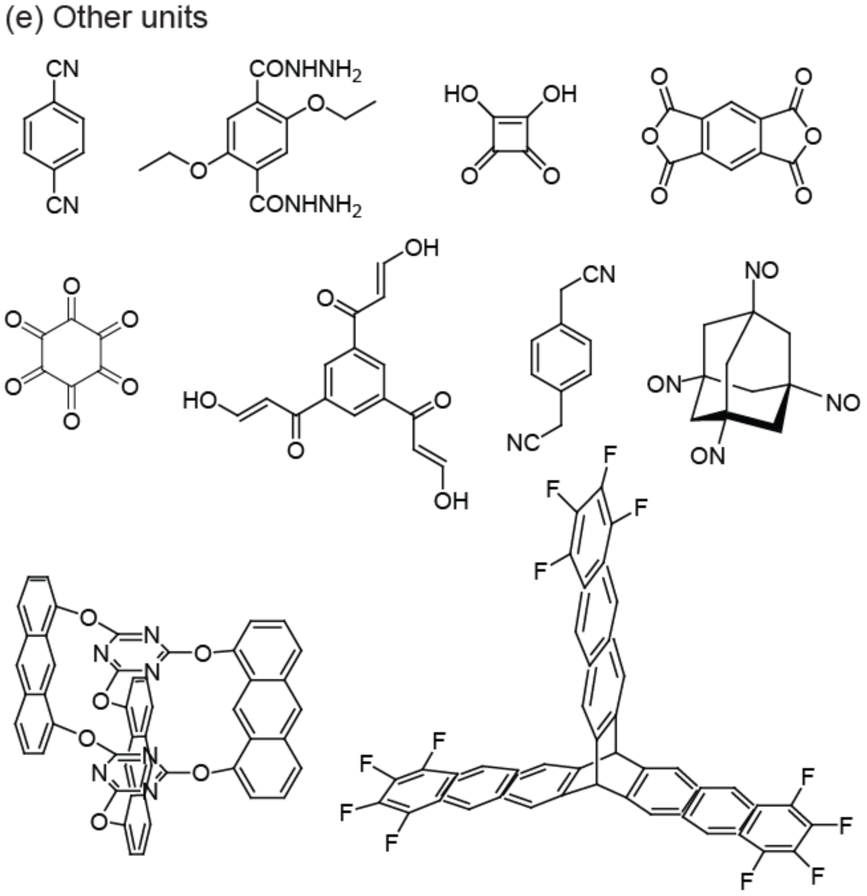
(e) Other units

Figure 1.11: *Other linkers used for the synthesis of COFs.*

1.6 Synthetic methods

Most of the amorphous organic polymers were synthesized by the irreversible reaction through the kinetically control medium. So the structural characterization is difficult for these amorphous polymers. On the other hand, COFs are synthesized by reversible covalent bond formation reactions through thermodynamic control condition [1.22b]. To attain the thermodynamic reversibility, researchers utilized diffident reaction conductions for a different type of COFs. Finding the proper conditions for a specific reaction is a trial and error method, by changing the concentration of the reactants, solvent combination and ratio, temperatures, catalysts, templates, modulator and others. Here, we discussed six different methods largely used for the COF synthesis; a) Solvothermal, b) Microwave, c) Ionothermal, d) Mechanochemical, e) Growth on the surface and f) Room temperature (Figure 1.12). Other than these, air-liquid interfacial [1.41 and 1.42] and continuous flow synthesis [1.43] of COF has been recently reported.

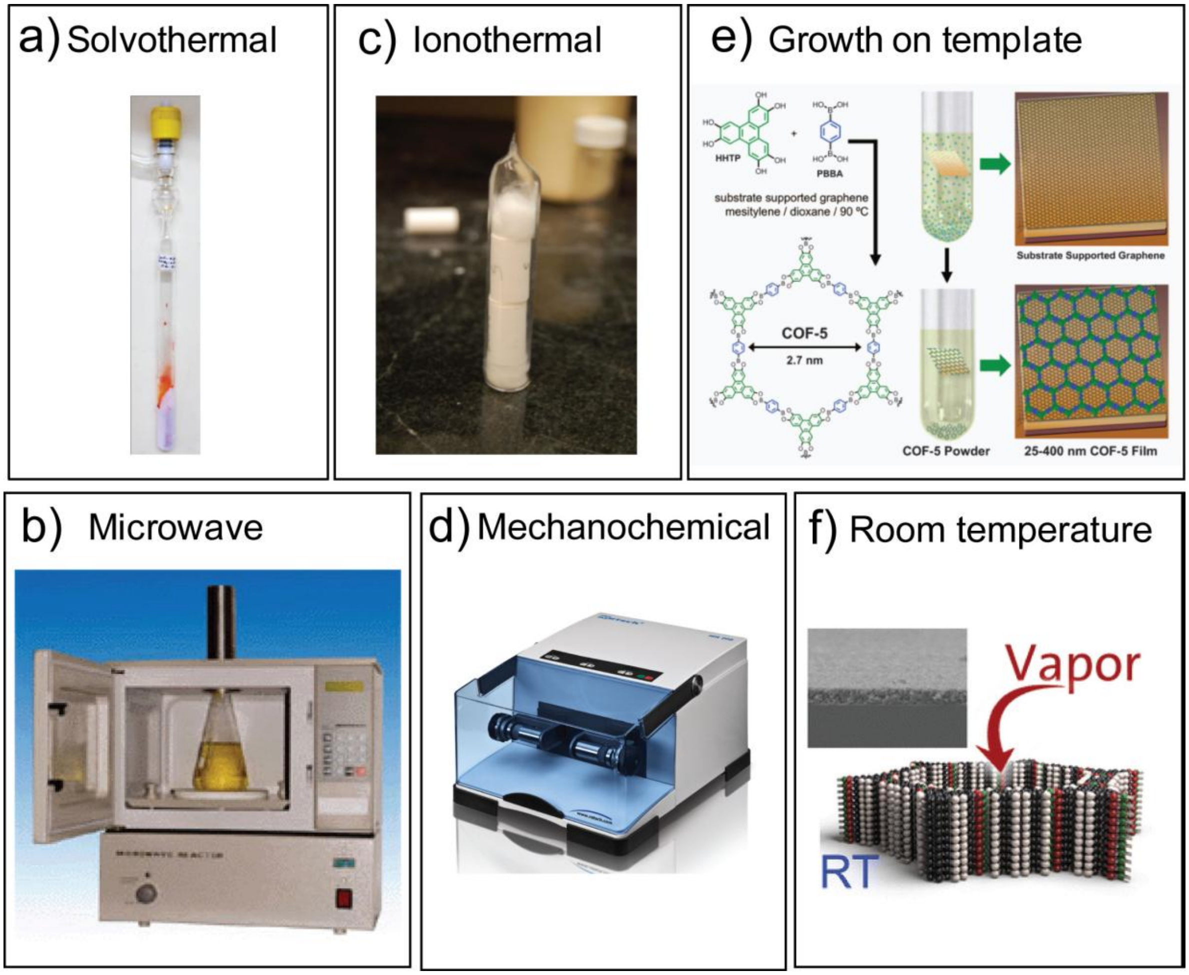

Figure 1.12: *Different synthetic methods used for the synthesis of COFs.*

1.6.1 Solvothermal Synthesis

The solvothermal reaction was widely utilized for COFs synthesis. Yaghi and coworkers, for the first time, introduced the solvothermal synthesis of boroxine (COF-1) and boronated ester (COF-5) based COF synthesis [1.22a]. The microscopic reversibility is controlled by the choice of the solvents and their ratios, temperature, pressure, catalyst, time and presence of the template. In general, a combination of polar and non-polar high boiling solvents used to optimize the solubility of the reactants to control the equilibrium. Completely soluble and completely insoluble reaction medium always give amorphous polymers. In most of the COF reactions, the side product is water and its amount determines the reversibility of the reaction. Due to this, the pressure inside the reaction tube maintains very low (50 to 150 mbar) and at least two-third of the reaction tube remains vacant. The whole reaction is done in a closed sealed tube, so the water cannot remove from the reaction medium (Figure 1.13). Generally, most of the COF reactions were carried out at high temperature (80 - 200 ºC) and long time (3-7 days), depending on the type of reactions. The high temperature and long reaction time favored the formation of the more stable crystalline product (thermodynamic control product) rather than cross linked amorphous polymer (kinetic control product). In order to attain the equilibrium faster, depending upon the reaction types, few catalysts like aqueous acetic acid, pTSA.H_2O; $BF_3.Et_2O$; $Sc(OTf)_3$; isoquinoline etc. have been used in COFs synthesis. The main disadvantages of the solvothermal method are i) long reaction time and ii) the powder form of COFs which hinder its use in device applications.

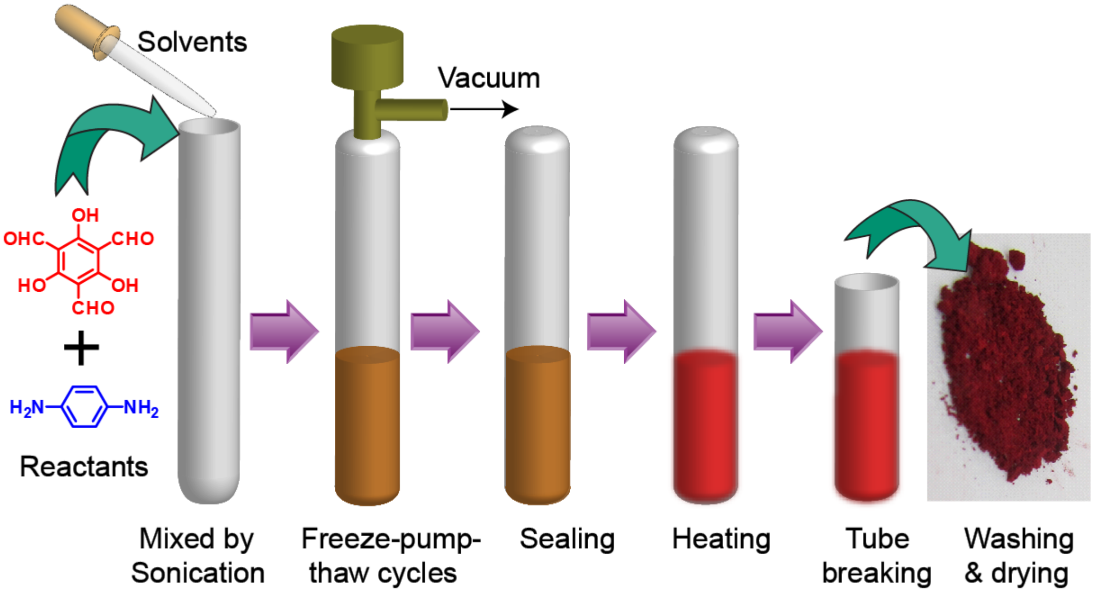

Figure 1.13: *Different steps involved in the Solvothermal COF synthesis.*

1.6.2 Microwave Synthesis

Cooper and coworkers, for the first time, introduced the microwave synthesis for the boronate ester based COFs [1.44a]. It has many advantages over solvothermal, (i) it's reduced the reaction time, so large scale synthesis is possible; (ii) improved yield and porosity due to the complete reaction and efficient removal of the impurities and residue trapped inside the frameworks respectively, (iii) No need of sealed tube which simplified the COF synthesis [1.44].

1.6.3 Ionothermal Synthesis

Thomas and co-workers have introduced ionothermal method for the synthesis of covalent triazine frameworks (CTFs) [1.45]. They used cyclotrimerization of aromatic nitrile compounds (1,4-dicyanobenzene) in presence of molten $ZnCl_2$ at high temperatures (400 ºC). At this high temperature, $ZnCl_2$ has been melted and acts as a solvent as well as Lewis acid catalyst. This reaction is partially reversible and therefore it gives less crystalline products compared to Schiff based and boronic acid based COFs [1.45]. Due to the use of very high temperature, very limited organic building blocks are available for the COF synthesis.

1.6.4 Mechanochemical Synthesis

The mechanochemical method has also been used for the COFs synthesis. Banerjee and coworkers, first time, have synthesized keto-enamine based COFs (TpPa-1, TpPa-2, and TpBD) via mechanochemical (or liquid assisted) grinding method [1.46]. Although it has many advantages (like solvent free, less reaction time, scalable large production, cost effective) over solvothermal, the COFs quality (crystallinity and porosity) is not good compared to solvothermal synthesized COFs.

1.6.5 Room temperature Synthesis

Bein and coworkers have synthesized 2D COFs (COF-5 and BDT-COF) as thin film via room temperature vapour assisted conversion technique [1.47]. They used acetone and/or ethanol solution of the reactants and drop cast on to a glass subtracts. Then, the glasses subtracts were kept into a desiccator along with a vial containing (1:1) volumetric mixture of mesitylene and 1,4-dioxane. The slow diffusion of the solvents into the reaction medium lead to the complete coverage of the glass subtract by COFs after 72 h. The thickness of the films controlled by the concentration of the reactants. Recently, Dichtel and co-workers also showed that imine linked COFs can be synthesized at room temperature (20 ºC) in presence of metal triflates (especially, $Sc(OTf)_3$] as Lewis acid water tolerant catalyst [1.47]. Zhao and coworkers, very recently, reports the synthesis of imine based COFs by continuous flow method at room temperature [1.48]. This method opens up the large scale synthesis of COFs.

1.6.6 Growth of mono and multilayer COFs on surface

Bulk synthesis of COFs as powder form has limited its application in many fields like optoelectronics, energy storage, and conversion etc. So researchers have developed techniques to synthesize a single layer COF on support like HOPG and metal surfaces [Ag(111)] by the condensation of the building blocks in UHV condition at high temperature [1.49a]. In this method, building blocks were either solubilized and deposited on support for further heating in an autoclave or sublimated in presence of a water reservoir ($CuSO_4.5H_2O$) under ultra high vacuum. The surface morphologies pore structures and defects were characterized by scanning tunneling microscopy (STM).

It is also possible to grow a thin film of COFs on conducting substrate by in-situ solution based synthesis of COF thin films on supporting subtract. Dichtel and coworkers able to synthesized oriented 2D COF films on single layer graphene supported by SiO_2 (SLG/SiO_2) (Figure 1.14). During the solvothermal synthesis of COFs, they kept SLG/SiO_2 support in the reaction medium to grow COF films onto it. Finally, highly crystalline vertically aligned COF films were found by grazing incidence X-ray diffraction studies [1.49b].

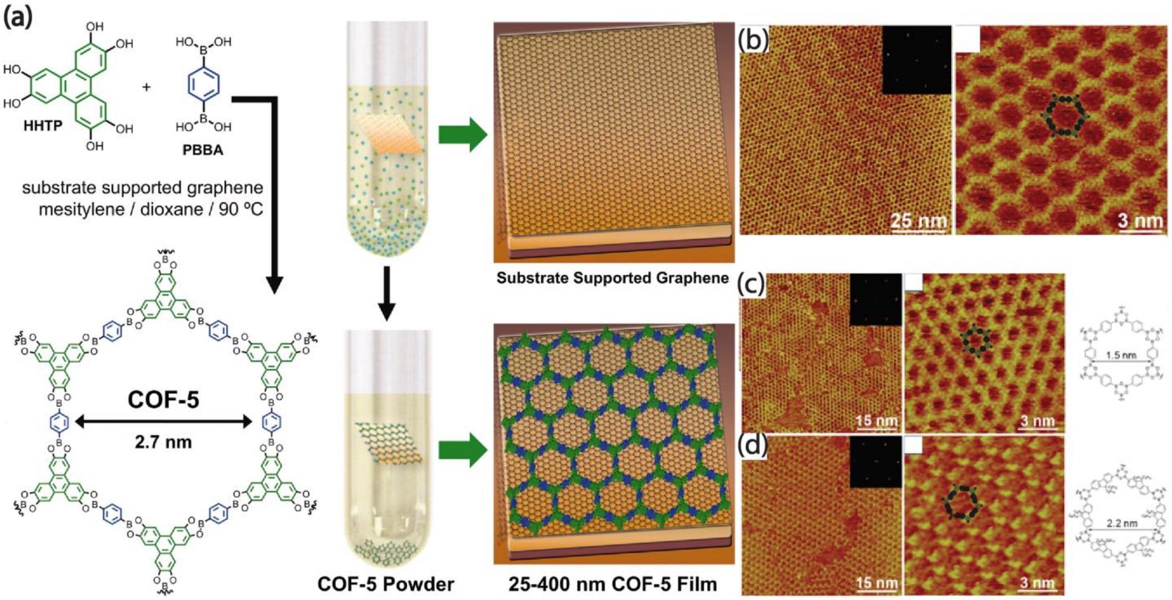

Figure 1.14: *(a) Synthesis of COF-5 on the surface of few layer graphene. (b) & (c) STM images of COF-1 and (d) STM images of COF 10 on HOPG surface. [Reprinted with permission from Ref. [1.49b], Copyright Science, 2010].*

1.7 Applications of COFs

By virtue of its high porosity, order predesigned structure, and easy functionalization, COFs have found many applications in gas storage, gas separation, catalysis, energy storage, photoconduction, sensing and many others (Figure 1.15). Due to its robust porous structure with low density, COFs have been widely used in gas storage purpose. Many gases like H_2, CH_4, CO_2 and NH_3 etc can be stored in COFs. The control over the pore sizes, high chemical stability, and good mechanical stability makes them better materials for membrane based gas/molecules/ions separation. The easy pre or post functionalization of COFs with catalytic sites makes them better heterogeneous catalysts or electrocatalyst by incorporating redox active functionality or metal ions. Also the high surface area, tunable pore size (micro or meso) and extended π-conjugated structure make them better materials for energy storage purpose such as supercapacitor and battery. In addition, the 1D porous channel structure of COFs helps to transport ions (like H^+, Li^+, Na^+, OH^- etc) and can be used as solid electrolytes in fuel cell and battery. Moreover, the 2D layer columnar structure of COFs offers a good platform for photoconduction and semiconduction applications. Among many applications of COF, some selected important applications of are listed below.

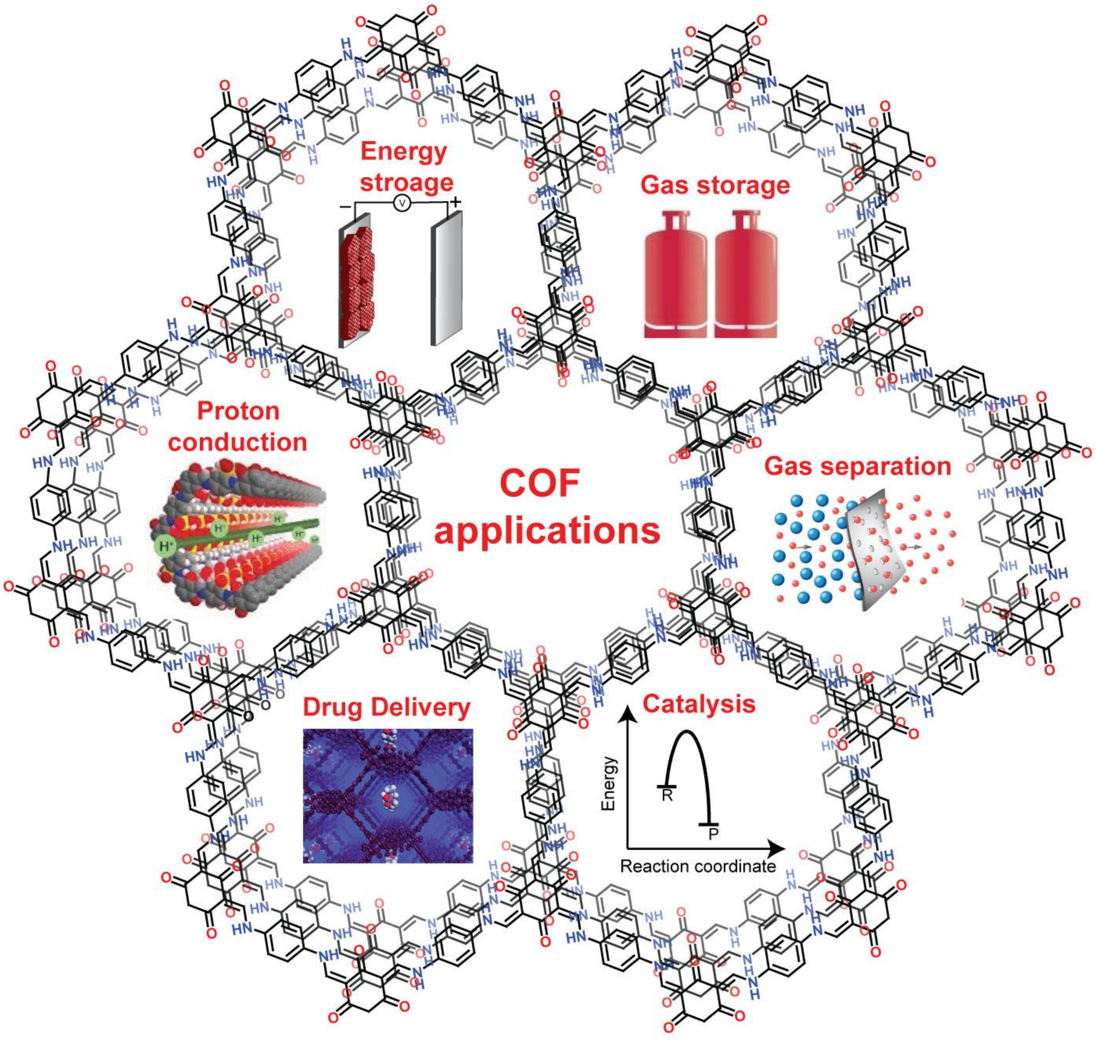

Figure 1.15: *Various applications of COFs such as gas storage, photo-conducting materials, heterogeneous catalysis, energy storage, separation and drug/bio molecules storage.*

1.7.1 Gas storage application

COFs are considered as ideal nanoporous materials for gas storage application due to its low density, high surface area, high pore volume and comparable pore size with guest gas molecules. Especially 3D COFs showed high gravimetric gas uptake capacities due to its exceptionally low mass density. Moreover, the pore can be functionalized by suitable groups (like acidic or basic) for better interaction with gas molecules. Theoretical studies suggest that COFs doped with alkali metals could improve the gas uptake capacity significantly. Gases like H_2, CH_4, CO_2, and NH_3 were adsorbed in COFs are summarized below.

1.7.2 Hydrogen storage:

To reduce the uses of fossil fuel, scientists have searched for clean energy sources with high energy density. Hydrogen is one of the alternatives for that and it is also environment-friendly. The US Department of Energy (DOE) has set the target of H_2 storage for 2017 to be 5.5 wt% at a temperature of -40 to 60 ˚C and a maximum pressure of 100 atm. Till now, many porous materials have been tested for H_2 storage. There are two ways to increased H_2 uptake in COFs; (i) Increasing the surface area and pore volume without changing the optimum pore size and (ii) metallation of the COFs by ions like Li^+, Ca^{2+}, Sc^{3+}, Pd^{2+} etc. Therefore, COFs having a very high surface area (> 3000 m^2g^{-1}), optimized pore size (in between 0.7-1.2 nm) and high density of metal ion (like Li^+, Ca^{2+}, Sc^{3+}, Pd^{2+} etc) can reach the DOE target. In this regards, 3D COFs like COF-102 and COF-103 showed the highest H_2 uptake of 7.24 and 7.05 wt% at 77K and 85 bar, which is comparable to MOF-5, MOF-177 and PAF-1 [1.50a]. Among 2D COFs, COF-10 (S_{BET} = 1760 m^2g^{-1}) showed the highest H_2 uptake of 3.9 wt% at 77K and 85 bar [1.50b]. Various theoretical and experimental studies show that metal ion (like Li^+, Ca^{2+}, Sc^{3+}, Pd^{2+} etc) doped COFs can exceptionally increase the H_2 uptake and meet the DOE target at ambient temperature. As for example, lithium ion intercalated COF-105 and COF-108 exhibit H_2 uptake of 6.84 and 6.73 wt% respectively at 100 bar and 298 K [1.51]. The reason for the high H_2 uptake might be the dative bond formation between the lithium ion and hydrogen molecules. In another similar report, Pd-doped COF, COF-301-$PdCl_2$, can exceed the DOE target at room temperature.

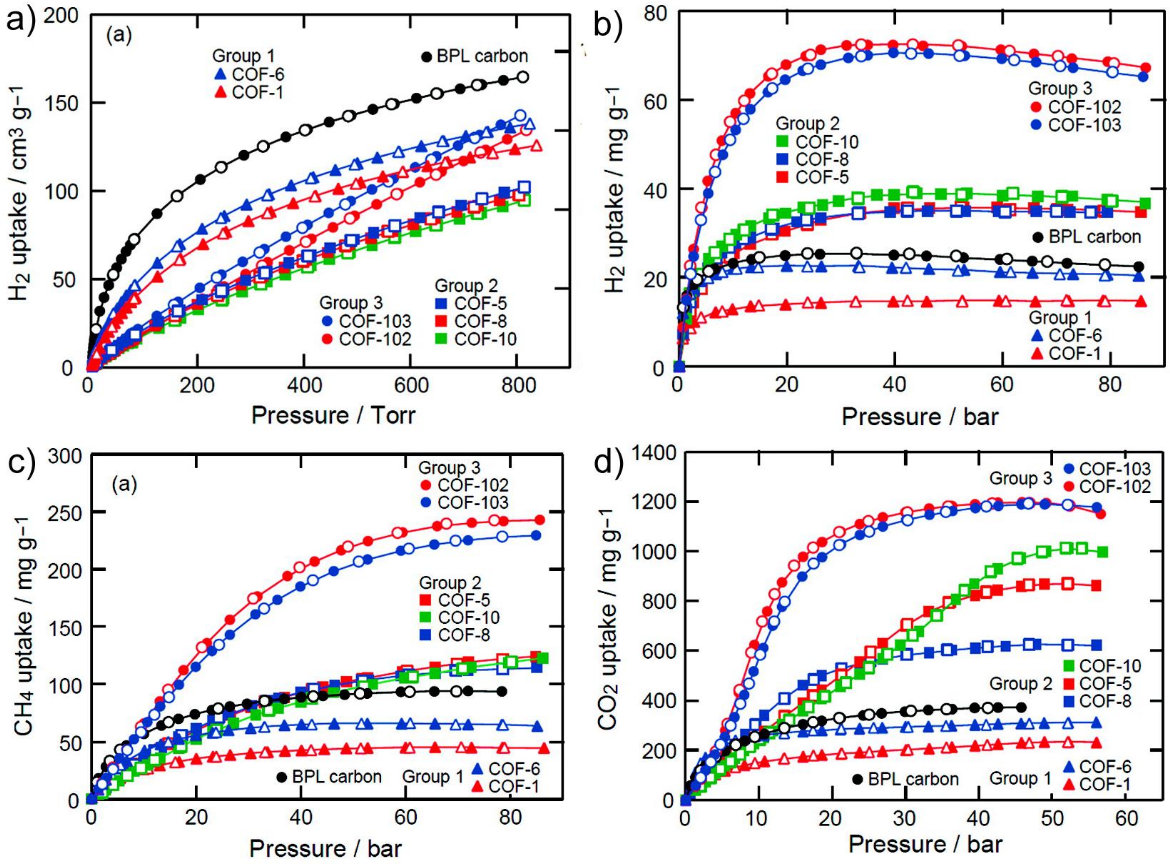

Figure 1.16: *Comparison of excess hydrogen uptake of different COFs (a) at 1 bar and (b) high pressure (open symbols represent experimental results, filled symbols simulated results). (c) Methane adsorption isotherms of COFs at high pressure. (d) Carbon dioxide adsorption isotherms of COFs at high pressure. [Reprinted with permission from Ref. [1.37], Copyright American Chemical Society, 2009].*

Table 1.1*: Hydrogen, carbon dioxide and methane storage properties of COFs of different surface areas reported in the literature.*

COF Name	BET Surface area (m^2g^{-1})	H_2 uptake (wt%)	CO_2 uptake (mg g^{-1})	CH_4 uptake (mg g^{-1})	References
COF-102	3620	7.24	1200	187	1.23
COF-103	3530	7.05	1190	175	1.23
COF-10	1760	3.92b	1010	80	1.37
CTC-COF	1710	1.12	—	—	1.38
COF-5	1670	3.58b	870	89	1.37

COF-8	1350	3.50b	630	87	1.37
COF-18A	1263	1.55 (1 bar)	—	—	1.28e
COF-14A	805	1.23 (1 bar)	—	—	1.28e
COF-16A	753	1.40 (1 bar)	—	—	1.28e
COF-6	750	2.26	310	65	1.37
COF-1	628	1.28 (1 bar)	—	—	1.37
COF-11A	105	1.22 (1 bar)	—	—	1.28e

1.7.3 Methane storage:

Methane, major component of natural gases, is abundant, cheap and an alternative to the fossil fuel for clean energy. But finding a safe and effective storage medium for methane storage at ambient temperature and pressure is a challenge for researcher. The current US DOE target for methane storage is 180 (v/v) at 298K and 35 bar. The basic criteria for high methane uptakes in porous materials are (i) High sorption capacity, (ii) Good adsorption enthalpy and (iii) An efficient charge–discharge rate. Many porous materials like zeolites, MOFs etc have been widely tested for methane storage. Like H_2 uptake, CH_4 uptake also depends on the surface area and the density of the metal ions (like Li^+ etc) doped inside COFs. Among COFs, 3D COF-102 and COF-103 showed the highest gravimetric methane uptake of 187 mg g^{-1} and 175 mg g^{-1} respectively at 35 bar and 298K [1.52]. Wang and coworkers, theoretically, shown that the lithiated 3D COF-102 and COF-103 exhibited gravimetric methane uptake of 303 and 295 v(STP)/v respectively at 298K and 35 bar, which is more than double from their parents COF-102 (127 v(STP)/v) and COF-103 (108 v(STP)/v). These improvement of the uptakes attributed to the increased induced dipole interaction and London dispersion forces between methane molecules and doped lithium ions.

1.7.4 Carbon dioxide removal:

Carbon dioxide (CO_2) is considered as major contributor to the global warming. Scientists are developing porous materials for their storage and sequestration. Various porous materials such as porous carbon, silicas, zeolites, MOFs have been widely used for CO_2 uptake. Yaghi and coworkers, first time, used a series of COFs for CO_2 uptake and found that COF-102 exhibits the highest uptake of 27 mmol g^{-1} at 298 K and 35 bar, which is higher than the uptake of both zeolites (5-8 mmol g^{-1}) and MOF-5 (22 mmol g^{-1}) [1.52]. Calculation shows that the lithium ion doping can increased significantly the CO_2 uptakes e.g. lithium doped COF-102 and COF-105 showed a CO2 storage capacity of 409 and 344 mg g^{-1} respectively, which is eight and fourfold increase of CO_2 uptake than their pristine COFs [1.53]. Further improvement of CO_2 uptake done by Thomas group by synthesizing triazine based COFs such as CTF-1 by ionothemal method. The high CO_2 uptake capacity for triazine based, azine based and imine based COFs arises due to the dipole-induced dipole interaction of polar functional groups and the CO_2 molecules inside the frameworks and their sub-nanometer (< 1 nm) pore which selectively adsorbed CO_2 over N_2 and CH_4 [1.54]. Further, Jiang and coworkers successfully post synthetically modify the COFs for enhancing the CO_2 uptake capacities [1.55].

1.7.5 Ammonia storage:

Ammonia is widely used for the production of fertilizer and therefore suitable storage medium is necessary for safe storage and transportation purpose of both liquid and gaseous ammonia. As the handing of liquid NH_3 is very risky due to its toxicity and corrosive nature, scientists have searches for various porous materials to reversibly adsorbed gaseous ammonia for safe storage and transportation. Yaghi and coworkers have successfully synthesized boroxine and boronated ester based COFs for better storage of gaseous ammonia. The boronate ester COF-10, synthesized by the condensation of 2,3,6,7,10,11-hexahydroxytriphenylene (HHTP) and 4,4‘-

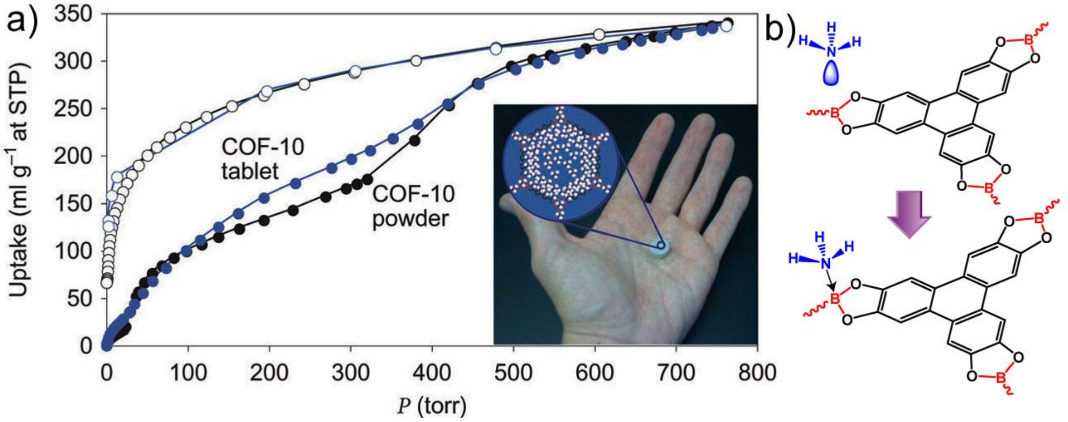

Figure 1.17: *(a) Ammonia adsorption isotherms of COF-10 powder (black) and tablet (blue). (b) Lewis adducts formation between ammonia and boronate ester. [Reprinted with permission from Ref. [1.56], Copyright Nature Chemistry, 2010].*

biphenyldiboronic acid (BPDA), exhibited the highest ammonia uptake of 15 mol kg^{-1} at 1 bar and 298K [1.56]. The electron deficient Lewis acidic boron center strongly binds with the basic ammonia molecules via Lewis acid-base interactions. Due to the reversible nature of these interactions, the adsorbed ammonia can easily be recovered by heating of the porous materials.

1.7.6 Heterogeneous catalysis

Being a part of porous crystalline solid framework family and its insolubility, COFs are ideal materials for the heterogeneous catalyst. Its modular nature enables us to design COFs with suitable catalytic sites with tunable pore size. Their high surface area and an optimized pore size can control the reactivity and selectivity of a catalysis reaction. But to use these COFs as a heterogeneous catalyst, it should be chemically robust. Wang and coworkers synthesized imine based COF-LZU1 and loaded Pd(II) in between the adjacent layer and bonded to the imine nitrogen. The Pd/COF-LZU1 tested for the Suzuki-Miyaura C-C coupling reaction. The broad scope of the reactants, high yields (96-98 %), short reaction time, less catalyst loading, high stability and easy to recycle makes it better heterogeneous catalyst than other porous materials [1.57a]. Zhang and coworkers also synthesized metal free porphyrin based H_2P-Bph-COF from Schiff base reaction of 5,10,15,20-tetra(p-aminophenyl)porphyrine and 4,4'-biphenyldialdehyde. This porphyrin based COF showed high yield for Suzuki coupling reaction in mild condition [1.57b]. Banerjee and coworkers showed the use of chemically stable Pd(0)/TpPa-1 and Pd(II)/TpPa-1 in Heck and Suzuki coupling reaction [1.57c]. In another report, this keto-enamine based COF (TpPa-1) was loaded with ($AuCl_4$. $3H_2O$) precursor by simple stirring and incubation process and subsequent reduction with sodium borohydride ($NaBH_4$) to afford Au nanoparticles doped TpPa-1(Au/TpPa-1) [1.57d]. This (Au/TpPa-1) showed good catalytic activity towards the reduction of 4-nitrophenol. Again they have synthesized bifunctional 2,3-DhaTph COF for cascade reaction which involved the hydrolysis of dimethyl ketal to afford the corresponding aldehyde which further reacts with malononitrile through Knoevenegal condensation reaction to give the final product [1.57e]. Yan and co-workers have successfully synthesized base functionalized BF-COF-1 and BF-COF-2 from Schiff base reaction between 1,3,5,7-tetraaminoadamantane (TAA) and 1,3,5-triformylbenzene (TFB) for (BF-COF-1) or triformylphloroglucinol (TFP) (for BF-COF-2) respectively. These COFs showed high conversion yields, efficient size selectivity, and good recyclability for Knoevenegal condensation reaction [1.57f]. More recently, Jiang and coworkers were able to synthesized alkyne functionalized $[HC\equiv C]_X$-H_2P-COFs and reacted it with pyrrolidine azide to give $[Pyr]_X$-H_2P-COFs which contain hanging chiral pyrrolidine moieties and used as chiral organocatalysts for asymmetric Michael addition reaction [1.57g]. In another report, the same group also synthesized mix link $[HC\equiv C]_X$-TPB-DMTP-COF by three component reaction of 1,3,5-tris(4-aminophenyl)-benzene (TPB), 2,5-bis(2-propynyloxy)terephthalaldehyde (BPTA) and 2,5-dimethoxyterephthalaldehyde (DMTA) in solvothermal condition. Further modification of the pore through click reaction with pyrrolidine azide give $[(S)\text{-Py}]_X$-TPB-DMTP-COFs [(S)-Py, (S)-pyrrolidine] where hanging chiral pyrrolidine moieties are responsible for asymmetric C-C coupling reaction in neat water at ambient condition (25 ˚C and 1 bar) [1.57h].

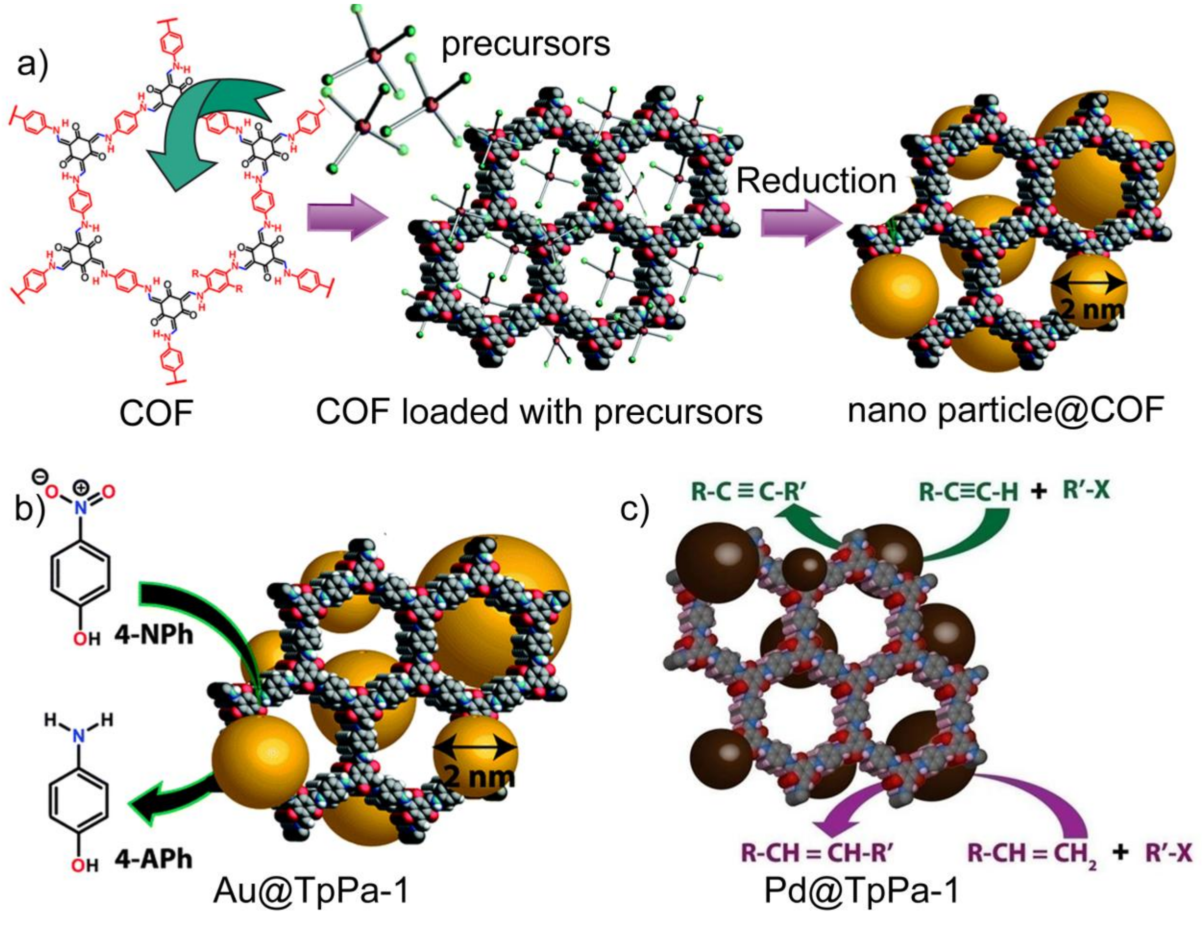

Figure 1.18: *(a) Schematic representation of synthesis of nano particle loaded COFs. (b) and (c) Catalysis performed by nano particle immobilized COF-TpPa-1. [Reprinted with permission from Ref. [1.57(c-d)], Copyright Royal Society of Chemistry, 2014-15].*

1.7.7 Photoelectric and semi conduction applications

The efficient π-π stacking, order pore for high mobility of charge carriers (hole or electron) and the molecular control of the arrangement of donor and acceptor moieties make 2D COFs good materials for the organic solar cell. Jiang and coworkers synthesized PPy-COF from the self-condensation of pyrene diboronic acid and shown its ability towards photoconductivity upon irradiation with visible light (Figure 1.19) [1.58a]. Similarly, TP-COF, formed by the condensation of 2,3,6,7,10,11-hexahydroxytriphenylene (HHTP) and pyrene diboronic acid (PDBA), showed luminescent property and p-type semiconductive behavior because of the eclipsed arrangement of pyrene and triphenylene units. Yaghi and coworkers synthesized porphyrin based p-type semiconductor COF-366, formed by the Schiff base reaction between tetra(p-amino-phenyl)porphyrin and p-phenylenediamine, which showed highest charge carrier mobility value of 8.1 $V^{-1} s^{-1} cm^2$ among all the 2D-COFs [1.27d]. Donglin Jiang *et al.* have also formed three porphyrins containing COFs, with different metal ions (Zn^{2+} and Cu^{2+}) at the porphyrin system via boronate esterification reaction (Figure 1.19c) [1.58c]. These COFs were highly crystalline with tetragonal pore structure created by the eclipsed stacking. Due to the different electron densities, the flash photolysis time resolved microwave conductivity measurement shows different charge transport behavior in these three COF. The metal ions present in the COF layers significantly affect the charge transfer properties. The metal free porphyrin COF (H_2P-COF) shows hole transport capabilities, where as the Cu^{2+} doped porphyrin COF (CuP-COF) shows electron transport ability (Figure 1.19c). The Zn^{2+} doped porphyrin COF (ZnP-COF) showed ambipolar characteristics [1.58c]. Bein and coworkers have synthesized thiophene based TT-COF by co-condensing thieno[3,2-b]thio-phene-2,5-diyldiboronic acid (TTBA) and hexahydroxytriphenylene (HHTP) [1.58d]. These TT-COF infiltrated with PCBM used to make a photovoltaic cell ITO/TT-COF: PCBM/Al with an efficiency of 0.053 and open circuit voltage of 0.62 V. Later on Jiang and coworkers integrate donor and acceptor building blocks in COF to form layered periodic structure of donor and acceptor molecules (D-A COFs). They synthesized D-A COF by condensation of 2,1,3-benzothiadiazole-4,7-diboronic acid (BTDADA) and hexahydroxyterphenylene (HHTP) [1.58e]. The vertically ordered p–n heterojunctions with large donor–acceptor interface significantly increase the photoconductivity of the material. The flash photolysis time-resolved microwave conductivity measurement of this D-A COF showed both holes and electrons mobilities of 0.04 and 0.01 $V^{-1}s^{-1}cm^2$ respectively.

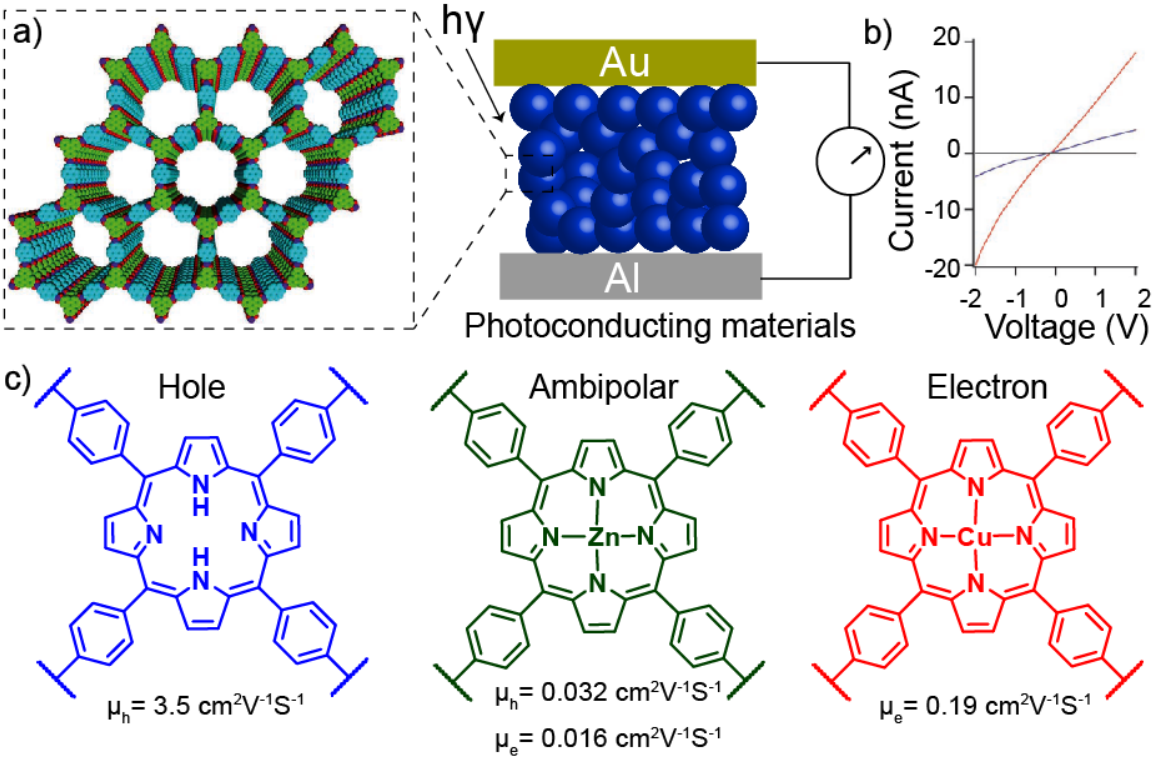

Figure 1.19: *(a) Schematic representation of device set up used for the measurement of the photocurrent of TP-COF.(In the device COF powders (blue) were sandwiched between two electrodes). (b) I-V profiles as-synthesized TP-COF (blue) and iodine doped TP-COF (red). (c) Hole (μ_h) and electron (μ_e) carrier mobilities of H_2P-COF (blue), ZnP-COF (green) and CuP-COF (red). [Redrawn with permission from Ref [1.58b,c], Copyright with permission from Wiley-VCH Verlag GmbH & Co. KGaA, Weinheim, 2009 and 2012].*

1.7.8 *Energy storage*

Owing to the high surface area, tunable pore size and ability to control the functionality, COFs are regarded as ideal electrode materials for energy storage purpose. They have been used as both active electrode materials for battery and electrochemical capacitor (Supercapacitor). Dichtel and co-worker introduced redox active anthraquinone moieties into the keto-enamine based DAAQ-TFP COF and used as capacitive energy storage materials [1.59a]. Due to the high chemical stability, high surface area and the presence of redox active groups, it shows specific capacitance of 40±9 Fg^{-1} after 5000 cycle. The low capacitance arises due to the low conductivity of the COF materials which significantly decrease the electrochemical accessibility of the redox active groups (3%). When the same COF synthesized in orientated thin films of thickness up to 200 nm on the gold surface to enhance the conductivity, it shows an increased areal capacitance of 3.0 mF cm^{-2} compared to 0.4 mF cm^{-2} for powder COF modified electrode at a current density of 150 mA cm^{-2} [1.59b]. Further, the same group improved the capacitance through the electropolymerization of 3,4-ethylenedioxythiophene (EDOT) inside the porous DAAQ-TFP COF to give a composite of COF and conductive poly(3,4-ethylenedioxythiophene) (PEDOT) polymer [1.59c]. This PEDOT-COF composite shows an enhanced volumetric capacitance of 350 Fg^{-1} and stable performance after 10000 charge cycles. Shengbin Lei and co-workers synthesized the imine based DAAQ-TFA on graphene surface to improve the conductivity and the electrochemical accessibility of redox groups [1.59d]. Tang, Li, and coworkers synthesized pyridine functionalized TaPa-Py COF and showed redox activity of pyridine groups with a specific capacitance value of 209 Fg^{-1} along with high capacitance retention (92%) after 6000 cycles [1.59e]. Jiang and coworkers were post synthetically modified the alkyne based $[HC{\equiv}C]_{X\%}$-NiP COF (where X = 0, 50, 100) into organic radical based redox active $[TEMPO]_{(100-X)\%}$-NiP-COF through click reaction. The TEMPO modified COF i.e. $[TEMPO]_{100\%}$-NiP-COF showed a specific capacitance of 167 Fg^{-1} at a current density of 100 mA g^{-1} [1.59f].

1.7.9 *Proton conduction*

The channel structure of COFs has been used for loading and transporting of proton carrier molecules inside COFs. Banerjee and coworkers, for the first time, showed the proton conductivity in COFs [1.60a]. They synthesized azo (N=N) functionalized chemically stable Tp-Azo COF for phosphoric acid loading. The high chemical stability and Lewis basic azo groups in Tp-Azo COF help to bind phosphoric acid and proton hopping inside the nanochannel. The H_3PO_4@Tp-Azo COF exhibit proton conductivity of 9.9 x 10^{-4} Scm^{-1} in hydrous condition. To know the role of the azo groups in proton conductivity, they also synthesized ethylene-based Tp-Stb COF where azo groups are replaced by ethylene (C=C) groups. The Tp-Stb COF shows very low proton conductivity after loading with phosphoric acid suggest the importance of azo groups in proton conduction. They also synthesized sulfonic acid based COF (TpPa-SO_3H) for intrinsic proton conduction [1.60b]. The sulfonic acid groups are aligned on the two-dimensional (2D) layers at periodic intervals and promote the proton hopping inside the hexagonal one-dimensional channel. The intrinsic proton conductivity of TpPa-SO_3H was measured as 1.7×10^{-5} Scm^{-1} at 120 °C under anhydrous conditions. To enhance the proton conductivity, they have also synthesized a hybrid COF TpPa-(SO_3H-Py) by a ligand-based solid-solution approach that contains sulfonic acid as the acidic site, as well as pyridine as the basic site, in order to immobilize acidic proton carrier molecules. Impregnation of phytic acid molecules inside the framework increases the anhydrous proton conductivity up to 5×10^{-4} Scm^{-1} at 120 °C. Such an approach highlights the advantage and first-time use of hybrid COF for interplaying intrinsic to extrinsic proton conductivity. In another work, Banerjee and coworkers synthesized bipyridine based TpBpy-COF via mechanochemically and used as proton exchange membrane [1.60c]. It showed proton conductivity of 1.4×10^{-2} Scm^{-1} at 120 ºC and an open circuit voltage of 0.93 V. This clearly indicates the potential of COFs as solid electrolytes in hydrogen fuel cell. Later on, Jiang and coworkers also synthesized chemically stable imine linked TPB-DMTP-COF by the Schiff base reaction of 1,3,5-tri(4-aminophenyl)benzene (TPB) and 2,5-dimethoxyterephthalaldehyde (DMTP). The high loading (up to ~160 wt%) of N-heterocyclic proton carrier molecules (like triazole, imidazole) into the one-dimensional mesoporous channel afforded trz@TPB-DMTP-COF and im@TPB-DMTP-COF; which exhibited proton conductivity of 1.1×10^{-3} and 4.37×10^{-3} Scm^{-1} at 130 ºC respectively [1.60d].

1.7.10 *Separation*

By virtue of the designing frameworks shape and their pore size, COFs have been widely used for selective gas adsorption and separation. The order channel and functionalities of COFs open the door of adsorption based gas separation. Gao and coworkers successfully synthesized COF-320 on porous alumina ceramic support and used as a membrane for H_2/CH_4 and N_2/H_2 separation [1.61a]. The membrane fabrication is done by the functionalization of porous α-Al_2O_3 support with 3-aminopropyltriethoxysilane and reacts with 4,4'-biphenyldicarboxaldehyde to form covalent linkage followed by the synthesis of COF-320 on an alumina support. The surface synthesized COF-320 hold by the grafted α-Al_2O_3 support by imine linkage. Although they were able to synthesized thin film COF membrane the presence of a large number of inter crystallite voids hamper the overall selectivity performance of the membrane. Banerjee and coworkers also synthesized COF based hybrid membrane with PBI polymers [1.61b]. These hybrid membranes were highly flexible, thermally and chemically stable and showed moderate selectivity for CO_2 $/N_2$ and CO_2 $/CH_4$. Recently, the same group has developed a method to synthesized highly porous, crystalline, free standing Covalent Organic Framework Membranes (COMs) over a large scale length [1.61c]. Due to the high order pore of these membranes (M-TpBD and M-TpTD) it does not only show very high permanence for acetonitrile, water but also reject dyes, bacteria, APIs, organic pollutants, food additive from both aqueous as well as organic solvents.

1.7.11 *Drug delivery*

Mesoporous materials have widely been used as drug storage and delivery due to its large pore size (2-50 nm) to incorporate the large drug/bio molecules. Similarly, mesoporous COFs also can be synthesized by proper choosing of the building blocks. Yan and co-workers used porous polyimide based 3D-COF (PI-COF-4), formed by pyromellitic dianhydride and 1,3,5,7-tetraaminoadamantane, for drug loading and control delivery [1.62a]. Due to its high surface area ($SA_{BET} = 2403 m^2 g^{-1}$) with sufficient thermal and chemical stability, it had been used for high (20 wt %) ibuprofen loading and good release control. From UV-Vis spectroscopy, it was observed that 95 wt % of IBU have been released within six days. Recently, Zhao and coworkers also able to synthesized biocompatible imine based COFs with different pore sizes and shown the influence of the pore size to the release of the anti-cancer drug (5-Fluorouracil) *in vitro* [1.62b].

1.8 Chemical stability of COFs

Real time applications of COFs depend on its stability, processability, easy synthesis, porosity and other factors. Some practical applications such as (i) gas storage/separation from natural gases, (ii) CO_2 removal from flue gases, (iii) H_2 adsorption for a fuel cell, for that the chemical stability of the frameworks is essential.

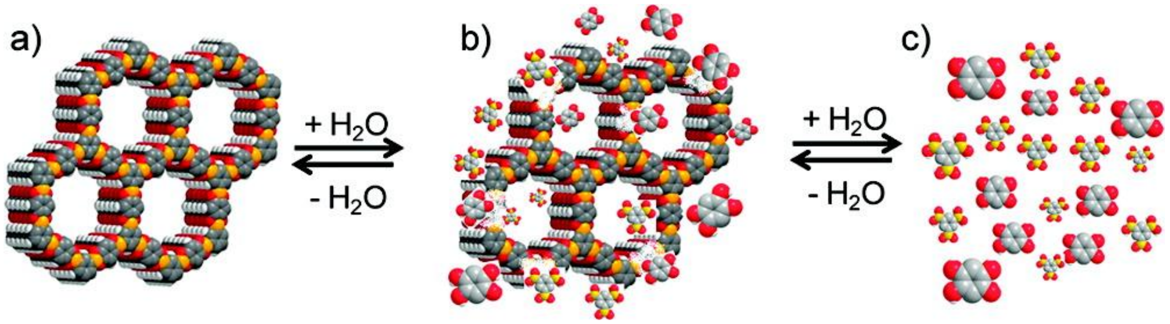

Figure 1.20: *Schematic representation of (a) as-synthesized COF (b) partial hydrolysis and release of monomers into solution upon submersion in water (c) completely hydrolyzed COF. [Reprinted with permission from Ref. [1.63a], Copyright American Chemical Society, 2011].*

On the other hands, reversible condensation reactions were used for the synthesis of COFs (Boronic acid, Schiff base etc) and therefore there is always remains a possibility of backward reaction to generate its parent components (building blocks) in presence of nucleophiles or electrophiles (like H_2O, acid, and base) (Figure 1.20) [1.63a]. For this reason, most of the boronic acid based COFs are hydrolytically unstable and limited their practical uses.

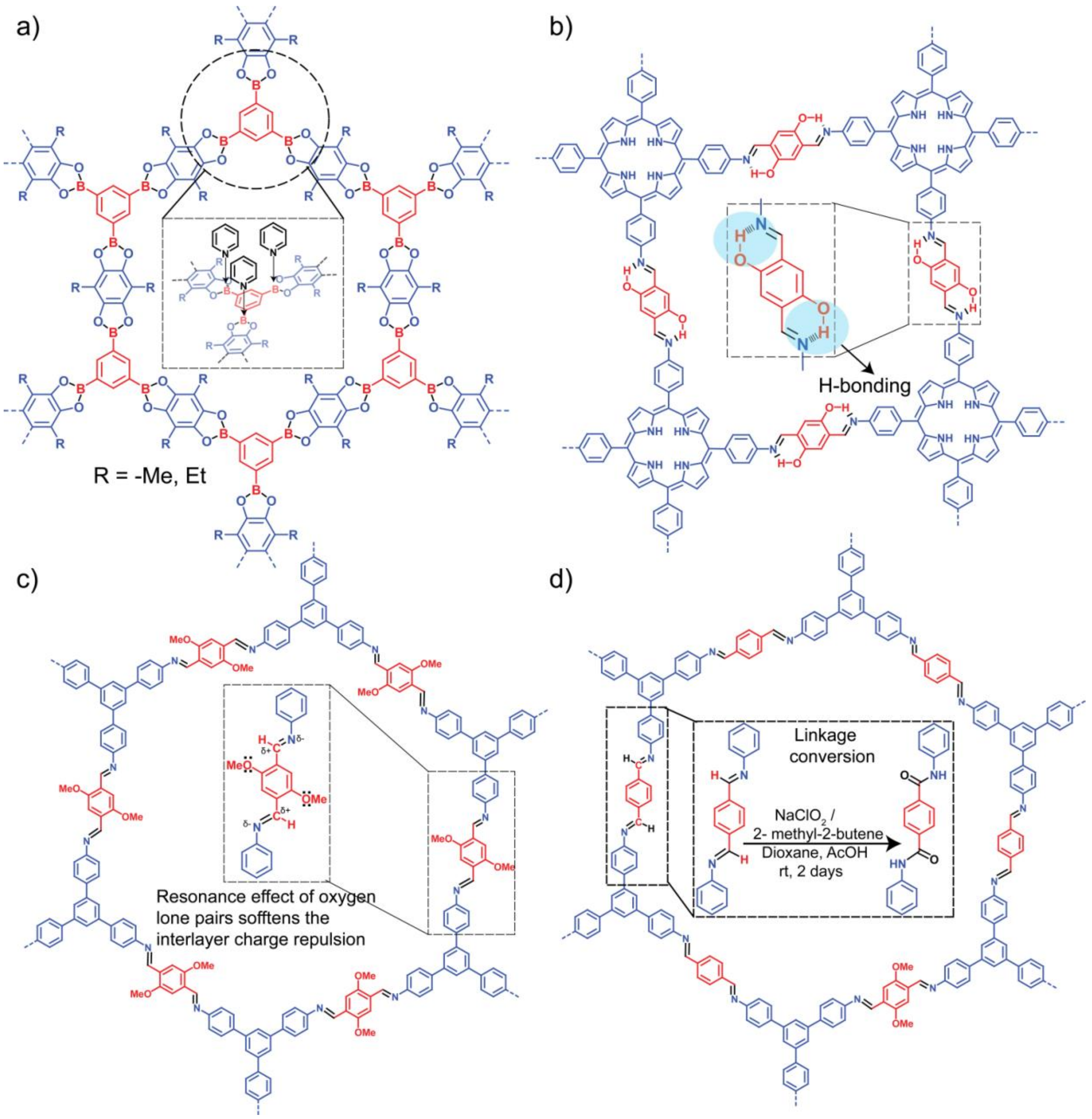

Figure 1.21: *Attempts done to improve the chemical stability in COFs (a) alkylation and doping of pyridine, (b) Intralayer hydrogen-bonding interaction in DhaTph COF, (c) Resonance effect in TPB-DMTP-COF, and (d) Conversion of imine TPB-TP-COF to amide TPB-TP-COF under oxidative reaction conditions [inset showing the reaction condition used for the oxidation]. [Redrawn with permission from Ref [1.63(a-e)], Copyright American Chemical Society, 2011 and 2016; Wiley-VCH Verlag GmbH & Co. KGaA, Weinheim, 2013 and Royal Society of Chemistry, 2012].*

Although Schiff base COFs are relatively more stable in water, their low chemical stability in acidic and basic medium also limited their application. There are two methods used to enhance the hydrolytic stability of boronic acid based COFs; (i) via pore functionalized with alkyl chain by Lavigne and coworkers in 2011 [1.63a] and (ii) by pyridine vapors doping by David Calabro and coworkers (Figure 1.21a) [1.63b]. Although these modifications increase the frameworks stability towards humid air to some extent, the porosity and surface area of the resulting materials have been decreased. Moreover, direct treatment of these COFs with water decomposed its framework. To improve the chemical stability of imine based COFs, Banerjee and coworkers have introduced the intramolecular H-bonding in hydroxyl functionalized imine based frameworks (Figure 1.21b) [1.63c]. These H-bonding not only increases the crystallinity but also increases the π- π stacking forces, which boots the chemical stability of the frameworks. Jiang and coworkers also introduced methoxy (-OMe) substitutes in the phenyl ring and increased the stability of imine based COFs. The inter-layer charge repulsion generated due to the imine bond (C=N) polarity largely diminished by the delocalization of the lone pair of oxygen into the phenyl ring (Figure 1.21c) [1.28g]. Recently, Yaghi and coworkers also stabilize the imine based COFs via linkage conversion. They post-synthetically modified the imine linkage into amide one and therefore stabilized the COFs (Figure 1.21d) [1.63d]. COFs synthesized by semi-reversible reactions such as Imide reaction, Triazine reaction, Knoevenegal reaction, Micheal addition-elimination reaction etc have shown improved chemical stability due to the formation of new linkage with high chemical stability. To use the modular COF materials in a wide verity of applications there is a high demand for developing a new methodology which could make COFs stable in extreme condition (water, acid etc) without affecting the porosity and crystallinity.

Banerjee and coworkers also introduced a new protocol for the synthesis of highly acid and base stable COFs by a combination of reversible imine reaction and irreversible tautomerization of imine to keto-enamine (Figure 1.22) [1.63e]. They used 1,3,5-triformylphloroglucinol as aldehyde and p-phenylene diamine (for TpPa-1 COF) or 2,5-dimethyl-p-phenylenediamine (for TpPa-2 COF) as amine. Initially formed imine based enol form very quickly tautomerizes to keto form. Due to the three hydroxyl groups conjugated to the three imine bond in the enol form, the hydroxyl proton quickly transfers to imine nitrogen through σ bond (i.e. tautomerizes) to form β-keto-enamine COF. Crystallinity gained by the reversible imine reaction will not hamper by the fast tautomerization process because tautomerization did not change any atomic position (except hydrogen). Although during this tautomerization phenyl aromaticity is lost, the gaining of three new carbonyl bond makes this conversion thermodynamically feasible. As a result, without any post-synthetic modification, they were able to synthesize more stable β-keto-enamine COF containing carbonyl and secondary amine functionality in one step.

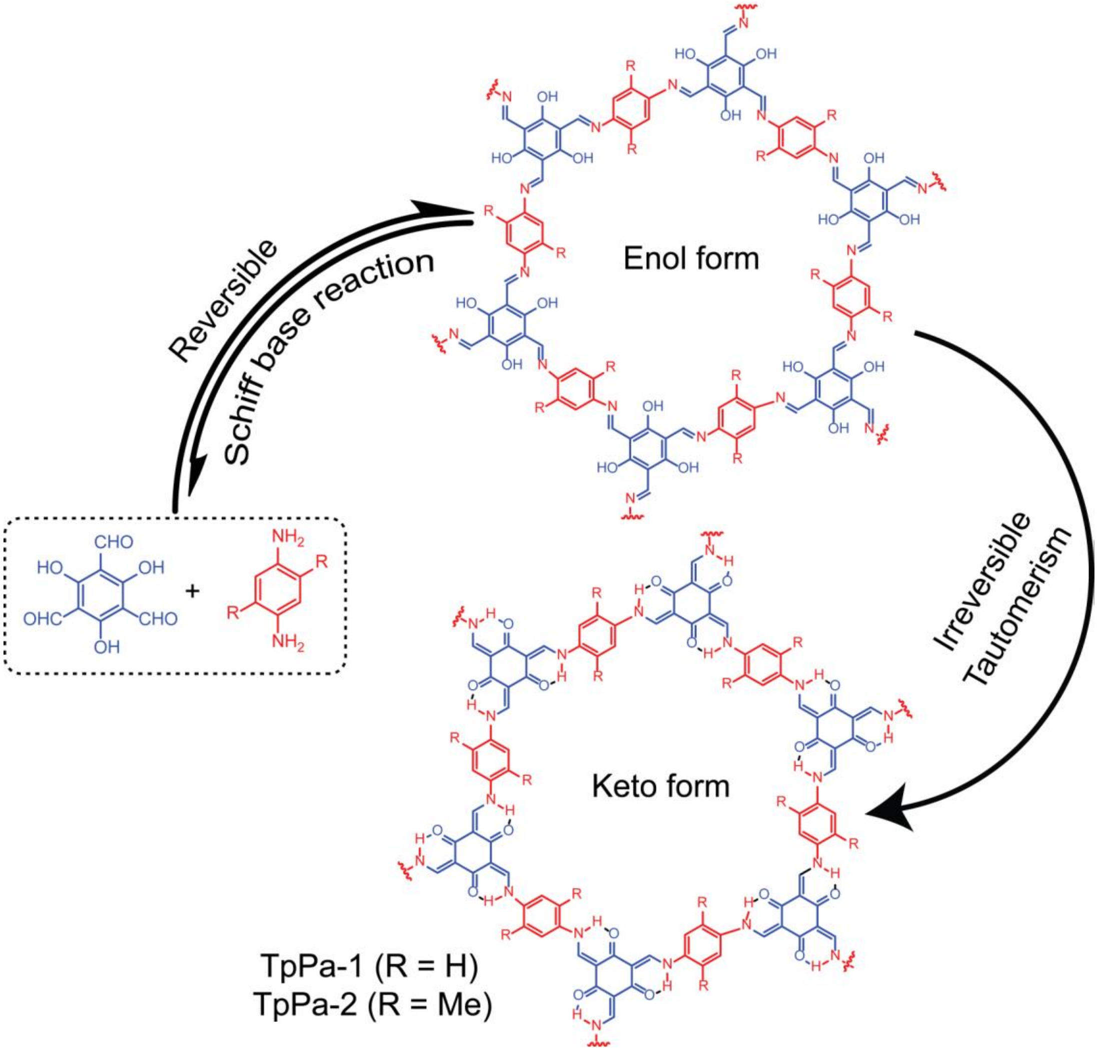

Figure 1.22: *Schematic representation of the synthesis of TpPa-1and TpPa-2 by the combined reversible and irreversible reaction of 1,3,5-triformylphloroglucinol with p-phenylenediamine and 2,5-dimethyl-p-phenylenediamine, respectively. The total reaction proceeds in two steps: (1) reversible Schiff-base reaction and (2) irreversible enol-to-keto tautomerism. [Redrawn with permission from Ref. [1.63e], Copyright American Chemical Society, 2012].*

CHAPTER 2

Mechanical Delamination of Chemically Stable Isoreticular 2D Layer Covalent Organic Frameworks (COFs) into Covalent Organic Nanosheets (CONs)

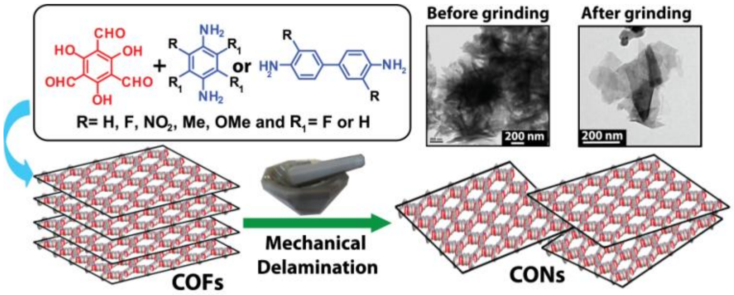

Abstract: *In this chapter, we have synthesized a series of eight thermally and chemically stable keto-enamine based covalent organic frameworks (COFs), namely,* ***TpPa-1****,* ***TpPa-2****,* ***TpPa-NO_2****,* ***TpPa-F_4****,* ***TpBD****,* ***TpBD-Me_2****,* ***TpBD-$(OMe)_2$*** *and* ***TpBD-$(NO_2)_2$*** *by employing the solvothermal aldehyde-amine Schiff base condensation reaction. All COFs were fully characterized by powder X-ray diffraction (PXRD), Fourier transform Infra red (FT-IR) spectroscopy, ^{13}C CP MAS solid-state NMR spectroscopy, and thermo gravimetric analysis (TGA). These COFs are crystalline, permanently porous, and stable in boiling water, acid (9 N HCl), and base (3 N NaOH). The synthesized COFs were successfully delaminated using a simple, safe, and environmentally friendly mechanical grinding route to transform into covalent organic nanosheets (CONs) and were well characterized via transmission electron microscopy (TEM) and atomic force microscopy (AFM). Further PXRD and FT-IR analyses confirm that these CONs retain their structural integrity throughout the delamination process and also remain stable in aqueous, acidic, and basic media like the parent COFs. These exfoliated CONs have graphene-like layered morphology (delaminated layers), unlike the COFs from which they were synthesized.*

2.1 Introduction

It has been observed that with the size of the materials properties can change drastically [2.1a]. Nanomaterials, having at least one dimension in nanometer scale, could differ from its bulk form in many physicochemical properties [2.1b]. Not only the size, but the dimensionality plays a vital role to determine the properties of the materials. It is clearly observed in the different properties of 0D fullerenes, 1D nanotube, 2D graphene and 3D graphite, all form of sp^2 carbon materials. Graphene, a single atom thick two-dimensional nanomaterial and recently isolated from the layered 3D graphite, showed outstanding properties which are completely different from their bulk graphite materials [2.1c]. Huge amounts of research have been performed for basic understanding and controlling their properties [2.1d]. Inspired by the development of the graphene chemistry, scientists are also interested in other inorganic based 2D materials like metal dichalcogenides [2.2 (a-d)], oxides [2.2 (e, f)], hydroxides [2.2 (f, g)], hexagonal boron nitride [2.2 (h-j)] etc. However, the less control over structural architectures and physicochemical properties drive the scientists to find alternative materials with fine control of the properties and architectures. In this aspect, reticular materials like metal organic frameworks (MOFs) and covalent organic frameworks (COFs) open up the opportunity to design a wide variety of structural architectures, cavities and chemical functionalities for tuning the property of materials**.** The structural periodicity (i.e. crystallinity) in two dimensions can be achieved by spatially confined polymerization method where the shape-persistent monomers either self-organized first and then react or follow the dynamic covalent bond formation followed by the cleavage technique to form a 2D crystalline polymer.

2.1.1 Synthetic methods for two-dimensional nanosheets

In general, the synthesis of the 2D nanosheets can be done via two approaches: i) top-down, where a bulk 2D layered polymer is delaminated into one or few atom thick monolayer. and ii) bottom-up, where the molecular building blocks react to form 2D polymeric sheet or monolayer. The top down method can be divided into two categories:

a) Micromechanical Cleavage Technique,
b) Mechanical Force-Assisted Liquid Exfoliation, which includes sonication assisted liquid exfoliation, ion intercalation-assisted liquid exfoliation, oxidation-assisted liquid

exfoliation, selective etching-assisted liquid exfoliation, and ion exchange-assisted liquid exfoliation.

Further, bottom up approaches can be divided into two categories:

a) Chemical vapor deposition (CVD),

b) The wet chemical process, which includes hydro/solvothermal synthesis, self-assembly of nanocrystals, 2D-templated synthesis, hot-injection method, interface-mediated synthesis, on-surface synthesis etc.

Bottom up approaches generates high quality 2D nanosheet materials with less number of defects and useful in electronic devices. But the low yield and expensive production techniques hinders their use in large scale production of two dimensional materials. On the contrary, top down approaches are simple and low cost effective and can be used for large scale production.

2.1.2 Advantages of mechanochemical exfoliation

Mechanochemical or mechanical exfoliation of 2D layer materials has several advantages like

i) Environmentally friendly green method i.e. use of no or less amount of solvents,

ii) Simple and efficient,

iii) Cost effective,

iv) Large scale production,

v) Control the thickness by tuning the frequency of milling and time,

vi) Introduction of defects which sometimes can improve the properties of the materials.

2.1.3 Advantages of few or single layer 2D Nanosheets

There are many unprecedented physical, chemical, electronic, optical, mechanical properties arises when one bulk 3D materials converted into 2D single layer or few layers nanosheets. The confinement of electrons in two dimensions generates new electronic and optoelectronic properties which can be useful for electronic and optoelectronic device applications [2.6]. Also, the strong in-plane covalent bond and atomic thickness of the layers ascertain good mechanical strength, optical transparency and flexibility, an important requirement for next generation device applications [2.7]. Moreover, the large lateral size along with nanometer scale thickness of these materials endowed with high specific surface area which are extremely useful for surface related applications like catalysis, supercapacitor etc [2.8]. In addition, the easy solution based processability of these nanosheets help to fabricate self standing thin film which can have some useful applications such as supercapacitor, solar cell, membrane based separation etc [2.9].

2.1.4 Applications of two dimensional nanosheet materials

Here, we discuss some of the major application of 2D nanosheet materials like electronic, optoelectronics, photocatalysis, electrocatalysis, supercapacitor, battery, sensing and solar cell.

2.1.4.1 Electronic/Optoelectronic Devices application

With the discovery of graphene in 2004, it replaces most of the 1D nanomaterial like CNT and silicon nanowires in next generation electronic devices due to its high carrier mobility and mechanical stability. Although it shows high electron mobility, the lack of band gap hinders its use in the electronic application. The band gap was generated in graphene by nitrogen or boron doping. Recently, other 2D materials like transition metal dichalcogenides (TMD) and black phosphorus (BP) have been widely used as semiconducting materials with high carrier mobility. The ultrathin/nanosheets of the semiconducting materials show intriguing mechanical and electronic properties and found application in nanoelectronics. Because of their very low thickness, it shows resistant to short-channel effects while keeping the flexibility. Also, the absence of dangling bond on the surface of 2D materials reduces the surface scattering effects. Due to these unique interesting properties, 2D semiconducting materials like MoS_2, WS_2, GaTe, BP etc. find many applications in electronics and optoelectronics.

2.1.4.2 Electrocatalysis

The ultrahigh surface area, high conductivity, tunable structures of 2D nanosheet materials open various application in electrocatalysis including HER, OER, ORR and carbon dioxide reduction.

(a) Hydrogen Evolution Reaction (HER)

In HER, the proton from solution combines with electron on electrode surface to form hydrogen gas. Scientists are constantly searching for an HER electrocatalyst with low over potential, cheap and earth abundant to replace costly Pt based HER electrocatalyst. For an good

HER catalyst, the Gibbs free energy of atomic hydrogen absorption (ΔG_H) on active catalyst should be close to zero. MoS2-2H has proposed to be a good HER catalyst due to its low ΔG_H (+0.08 eV). The catalytic activity of an active HER catalyst depends on the number of active sites and the intrinsic activity i.e. turnover frequency of each site. The edge of pristine TMD consider as an active site for HER and the activity can be increase the exposing the edge as high as possible. One of the way to increase the activity of 2D nanomaterials by reducing the size of the materials which basically increase the number of active sites per unit volume of the materials.

(b) Oxygen Evolution Reaction (OER)

During the water splitting, the slow kinetics of oxidation half reaction leads to the high over potential loss. Many transition metal oxide (TMOs) and hydroxides have been used for OER. The commonly used highly efficient catalyst IrO_2 and RuO_2. But their high cost and low earth abundant force to search for low cost, efficient OER catalyst with low over potential. Layer double hydroxides (LDHs) based on Fe, Ni, Co shows good activity towards OER. To overcome the low electronic conductivity, these LDHs are grown on conducting supports like CNTs, rGO and 3D graphene resulting high activity towards OER. The high exposed surface of 2D nanosheet materials help to absorbed the intermediate and enhanced the intrinsic activity of the electrocatalyst. Doped graphene has recently been used as OER catalyst due to its low cost and easy preparation. Further development of highly efficient and electrochemically stable catalyst needed to fulfill the full potential application in water splitting.

(c) Oxygen Reduction Reaction (ORR)

The efficiency of fuel cell and metal-air battery mainly depends on the oxygen reduction reaction. In ORR, oxygen get reduce by two ways: i) by 4-electron reduction pathway to water (in acidic medium) or hydroxide ion (in basic medium) and ii) by 2-electron reduction pathway to H_2O_2 (in acidic medium) or HO2- (in basic medium) intermediate. Pt based catalyst shows excellent activity in ORR, but their high cost and less durability forces researcher to develops low cost metal free or non-precious metal based catalyst to fasten the oxygen reduction reaction. In this aspect, metal (Fe and/or Co) doped carbon, N-doped CNT and 2D graphene sheets doped with heteroatom were tested for ORR. The heteroatom effective modulates the electronic and chemical properties of graphene, generating charged sites for favorable oxygen adsorption. Moreover, the extended pi-electron of graphene helps to reduced oxygen easily. Recently, Ni-based MOF, Ni(HITP)2 (HITP = 2,3,6,7,10,11-hexaiminotriphenylene) has also shows good activity for ORR in alkaline condition. The exposed surface area and hence activity has greatly improve by making nanosheets of the MOFs. The well defined structure and tunable pore size with functionality makes COFs an efficient electrocatalyst for ORR.

2.1.4.3 Batteries application

From last decade research has focused to develop novel porous materials for a rechargeable battery with high energy density, long cycle life, high charge rate, relatively low cost and low fire risk. Graphite is commonly used for anode materials in LIB and has a theoretical capacity of 372 mAh/g. After exfoliation of the graphite into mono/few layer graphene nanosheet, it shows double (744 mAh/g) theoretical capacity. This is because now both the sides are utilized. There are many advantages of the 2D nanosheets over graphite which includes facilitating intercalation and deintercalation of the electrolyte ions, relaxing the volume expansion of the materials due to the flexibility of 2D nanosheet materials and increasing the surface lithium storage property. Moreover, the defects generated from the exfoliation process can act as active sites for lithium storage. Due to the high conductivity and high surface area, graphene also used as the matrix material to prevent the aggregation of other active materials like metal oxides/sulfides.

2.1.4.4 Supercapacitors application

Supercapacitor is also a promising device for energy storage like battery. Unlike battery supercapacitor exhibits high power density, high life cycle, fast charge discharge rate. But their low energy density hinders its used in many power suppliers. A great amount of research has been carried out on the development of novel porous materials with high surface area and conductivity for high energy density capacitive materials. Activated carbon is widely used capacitive materials which storage charge on the electrical double layer. Although activated carbon has high surface area, their broad pore size distribution with high density of inaccessible pore results low specific capacitance. 2D nanosheets materials having high surface area and high electrical conductivity are ideal materials for supercapacitor application.

2.1.4.5. Photocatalysis application

Photocatalysis generally consists of three steps, i) generation of charge carrier by photo excitation, ii) charge separation and migration to the catalyst surface and iii) redox reaction on the catalyst surface. For a good photocatalyst, the materials should possess suitable band gap to harvest solar energy, efficient charge separation and sufficient stability. Hugh amount of research has been dedicated to develop a cost effective photocatalyst materials which can absorb sunlight and initiate catalysis for solar fuel production and pollutant remediation. In this aspect, 2D thin nanosheet materials have several advantages over bulk counterparts. Firstly, the high surface area of 2D thin nanosheet materials ensures efficient light harvesting and mass transport. Secondly, the nanosheet nature reduces the charge migration distance and enhancing charge separation. Thirdly, rational design of multicomponent photocatalyst for the requirement of various photocatalysis is possible for these 2D nanosheet materials. As a result, these materials have been widely used in photocatalytic water splitting and CO_2 reduction.

2.1.5 Covalent Organic Nanosheets as Two Dimensional Ultrathin Materials

Covalent organic nanosheets consider as a two dimensional ultrathin (few layers) materials synthesized by the top down exfoliation of 2D layer covalent organic frameworks or by the interfacial bottom up approaches. The strong in-planar covalent bond assures the good mechanical stability and robustness of the 2D crystalline polymer. But the inter layer Van der Waal interaction is weak and it can break easily to generate single layer or few layer nanosheets by thermally, sonochemically, mechanochemically etc. as the preparation of graphene from graphite. Scanning electron microscopy (SEM), transmission electron microscopy (TEM), Dynamic light scattering measurement studies revealed the exfoliation of 2D-COF stacks into ultra thin 2D-COF nanosheets. The thickness of these 2D few layers or a single layer can be measured by TEM and/or AFM. The first attempts to prepare nanosheets of COFs made by Zamora group taking 2D boronic acid based COFs as starting materials via liquid phase exfoliation [2.4]. But due to the instability of the boronic acid based COFs, they performed the experiment in an inert atmosphere using dry solvent. This hinders the large scale synthesis of 2D nanosheets of COFs in ambient condition. Also, they have used organic pure dry solvents which increases the overall cost of the exfoliation process and at the same time, it is not environment-friendly. Therefore, a green approach is highly demanding for the bulk scale synthesis of chemically stable covalent organic nanosheets (CONs) with long time stability. In this chapter, we have used a greener mechanochemical top-down exfoliation approach to exfoliate a series of layered 2D COFs with different functionalities into covalent organic nanosheets (CONs) and examined their gas as well as water uptake capacities. Also, these 2D crystalline nanosheets exhibit permanent pore with definite size and shape, moderate surface area and accessible pore volume. These features of 2D crystalline materials ascertained their use in selective separation, sensing, catalysis, optoelectronics, energy storage and many others [2.5]. Their high surface area can be used for post synthetically functionalization as well as in tune of their physicochemical properties as per the requirement. However, the one-step synthesis of pre-functionalized nanosheets with high surface area and crystallinity has not been realized until COFs have used for exfoliation. In addition, the role of functionalities in the COF nanosheets towards the enhancement of properties has not explored yet. In future, the mechanical, optical, catalytic, optoelectronic, separation, sensing and other properties of these COF nanosheets will be examined.

As previously discussed, the covalent organic frameworks (COFs) are light weight, crystalline porous materials ingeniously formed by strong covalent linkages between C, Si, B, N and O. These materials contain well-defined, predictable 2D or 3D ordered porous architectures and follow reticular chemistry protocols similar to that of metal-organic frameworks (MOFs) [2.3]. COFs are well-known for their various potential applications like gas storage, catalysis, sensing, and optoelectronics. The majority of the COFs have been synthesized utilizing selected reversible organic reactions. Reversibility in bond formation during COF synthesis is an essential condition for achieving good crystallinity. However, the possibility of reversible reactions makes the crystalline COFs prone to hydrolysis and subsequently hampers their sustainability even at ambient humidity. In order to address the stability issue in COFs, we have developed a synthetic protocol using combined reversible and irreversible Schiff base reactions [2.10] and synthesized three stable 2D COFs (**TpPa-1**, **TpPa-2** and **TpBD**), where the concept of proton tautomerism has given exceptional stability to the framework towards water, acid, and base. Moreover, we could synthesize these COFs *via* alternative solvent-free rapid mechanochemical grinding method [2.11] to substitute harsh experimental conditions (e.g., reaction in a sealed pyrex tube at high temperature and inert atmosphere) required to synthesize COFs with decent crystallinity. Interestingly, we observed some extent of delamination of the 2D COF layers during this mechanochemical synthesis, although the extent of delamination was very poor. Inspired by these observations, we altered our strategy and applied mechanical grinding to as-synthesized chemically stable COFs (**TpPa–1**, **TpPa–2** and **TpBD**) to produce thin covalent organic nanosheets (CONs) with high chemical stability. We could further extend this strategy to synthesize covalent organic nanosheets from a library of eight crystalline, porous, functionalized COFs namely **TpPa–1**, **TpPa–2**, **TpPa–NO_2**, **TpPa–F_4**, and **TpBD**, **TpBD–$(NO_2)_2$**, **TpBD–Me_2**, **TpBD–$(OMe)_2$** (Figure 2.1).

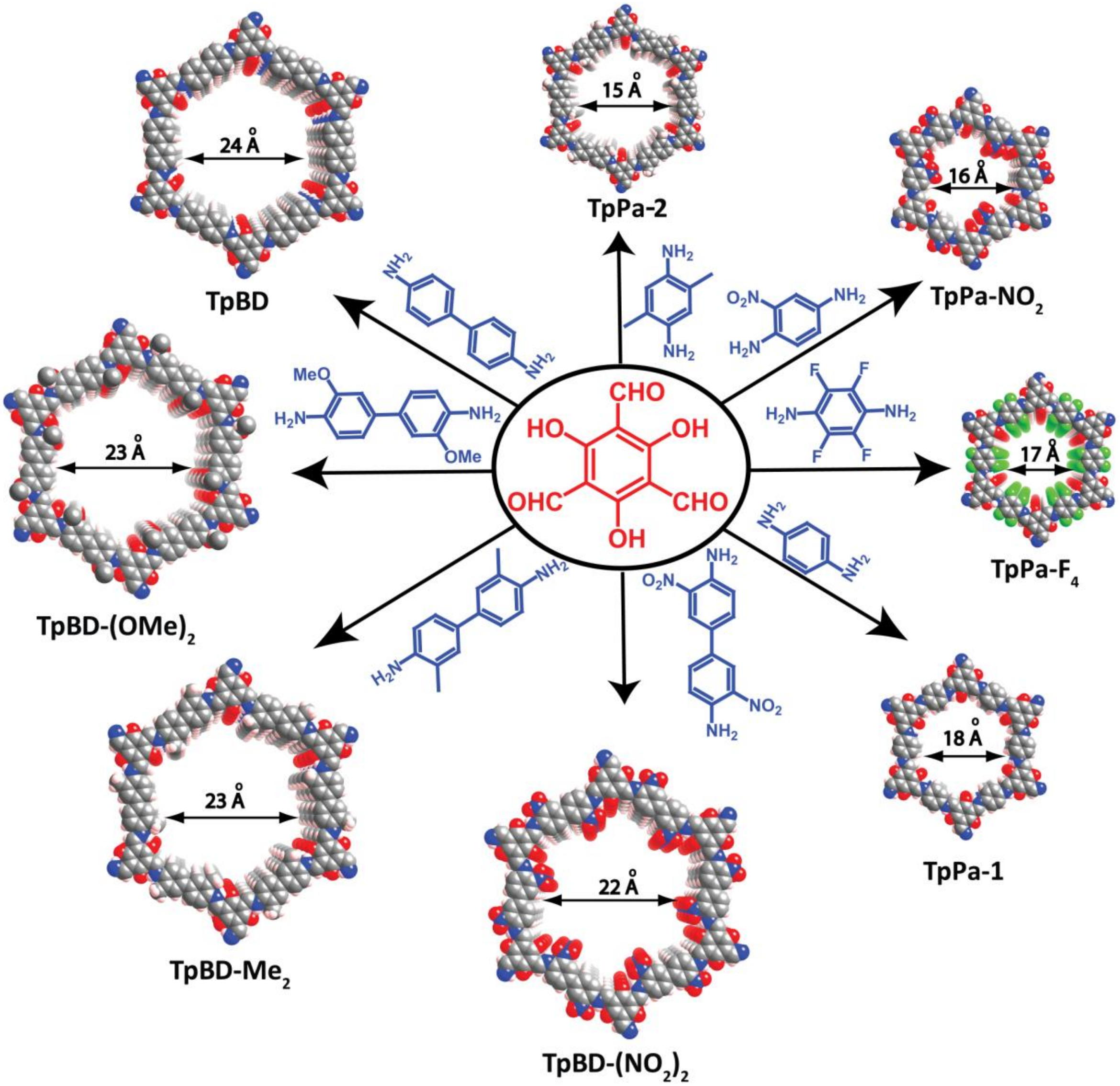

***Figure 2.1**: Schematic representation of the synthesis of highly stable β-Keto-enamine COFs from their parent compounds by Schiff base reaction along with their hexagonal pore.*

There are few reports on 2D COFs or CONs grown on surfaces [2.12] or synthesized by ultrasonication [2.4]. These processes are highly energy consuming and need special precautions, such as the usage of dry solvents, ultra high vacuum and also the need of expensive supports. Hence, a strategy to synthesize CONs by employing a simple, safe, eco-friendly and energy efficient process is highly desirable [2.13]. Although this delamination method using mechanical grinding has already been utilized to synthesize graphene from graphite [2.14], not a single effort has been made to delaminate these chemically stable COFs into nanosheets. A possible reason could be the instability of most COF materials under ambient conditions, which forbids the use of mechanical force [2.15].

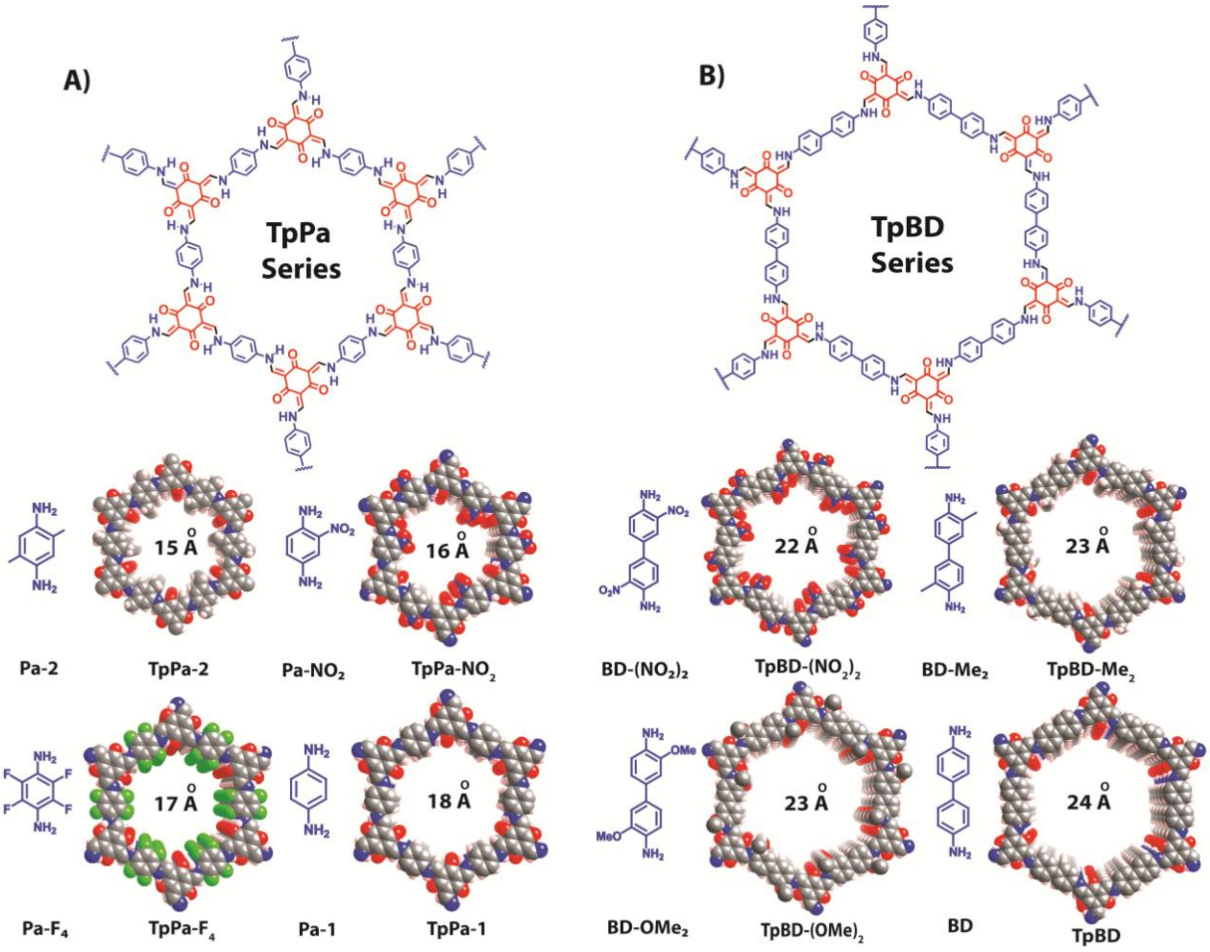

***Figure 2.2**: (A) **TpPa** series and (B) **TpBD** series COFs with the diamine linkers and models showing pore apertures (ascending order) of corresponding TpPa series (15−18 Å) and TpBD series (22−24 Å).*

Hence, we decided to apply mechanical grinding on as-synthesized stable bulk COFs in order to extensively produce CONs. These CONs retain their structural integrity throughout the delamination process and also remain stable in aqueous, acidic and basic media.

2.2 Preparative methods and characterization

2.2.1 Synthesis of COFs

The detail synthetic procedure for **TpPa–1**, **TpPa–2** and **TpBD** was described in our recent publications [2.11]. In the typical synthesis, a pyrex tube (o.d. × i.d. = 10 × 8 mm^2 and length 18 cm) is charged with Triformylphloroglucinol (**Tp**) (0.3 mmol), corresponding diamine {[2-Nitro-1,4-phenelynediamine (**Pa-NO_2**), 2,3,5,6-Tetrafluoro-1,4-phenylenediamine (**Pa–F_4**), 3,3'-Dinitrobenzidine [**BD–$(NO_2)_2$**], o-Tolidine (**BD–Me_2**), and o-Dianisidine [**BD–$(OMe)_2$**]} (0.45 mmol), 1.5 mL of mesitylene, 1.5 mL of 1,4-dioxane, 0.5 mL of 3 M aqueous acetic acid. This mixture was sonicated for 10 minutes in order to get a homogeneous dispersion. The tube was then flash frozen at 77 K (liquid N_2 bath) and degassed by three freeze-pump-thaw cycles. The tube was sealed off and then heated at 120 °C for 3 days. A dark red (few COFs are yellow) coloured precipitate was collected by centrifugation or filtration and washed with acetone/THF thrice. The powder collected was then solvent exchanged with acetone 5-6 times and dried at 180 °C under vacuum for 12 hours to get corresponding COFs in ~80 % isolated yield.

FT-IR (**TpPa–NO_2**, powder, cm^{-1}): 1586 (s), 1518 (s), 1444 (m), 1228 (s), 1098 (w), 987 (w), 814 (m). **Elemental Analysis;** Anal. Calcld. For $C_{36}O_{12}N_9H_{21}$: C, 56.03; H, 2.72; N, 16.34; found: C, 53.26; H, 3.09; N, 13.98. **FT-IR** (**TpPa–F_4**, powder, cm^{-1}): 1586 (s), 1555 (s), 1426 (s), 1247 (s), 1012 (w), 987 (m), 845 (w). **Elemental Analysis;** Anal. Calcld. For $C_6F_2H_2ON$: C, 50.67; H, 1.40; N, 9.85; found: C, 51.9; H, 1.83; N, 11.29. **FT-IR** (**TpBD–$(NO_2)_2$**, powder, cm^{-1}): 1580 (s), 1512 (s), 1432 (m), 1333 (m), 1209 (m), 981 (w), 809 (m). **Elemental Analysis;** Anal. Calcld. For $C_9O_3N_2H_5$: C, 57.14; H, 2.64; N, 14.81; found: C, 54.06; H, 3.09; N, 11.93. **FT-IR** (**TpBD–Me_2**, powder, cm^{-1}): 2921 (s), 1617 (w), 1580 (s), 1450 (s), 1247 (s), 1117 (w), 987 (m), 802 (s). **Elemental Analysis;** Anal. Calcld. For $C_{10}H_8ON$: C, 75.96; H, 5.06; N, 8.86; found: C, 73.26; H, 5.27; N, 10.25. **FT-IR** (**TpBD–$(OMe)_2$**, powder, cm^{-1}): 1574 (s), 1438 (m), 1271 (s), 1254 (s), 1123 (w), 987 (w), 796 (m). **Elemental Analysis;** Anal. Calcld. For $C_{10}O_2H_8N$: C, 68.96; H, 4.59; N, 8.04; found: C, 63.65; H, 4.51; N, 9.09.

2.2.2 Synthesis of covalent organic nanosheets (CONs) from COFs by mechanical grinding approach

50 mg of as-synthesized COF was placed in a mortar (inner diameter = 3 inch or 75 mm) and with 1–2 drop of methanol, ground using pestle at room temperature for 30 minutes (Figure 2.3). The dark red colour (some COFs are yellow) powder collected after 30 minutes of grinding was then dispersed in 100 mL of methanol; the resulting suspension was centrifuged at 8000 rpm for 5 min, obtaining a clear solution. The concentration of the material transferred from the settled solids to the solution as a result of mechanical grinding was calculated as 0.04 mg mL^{-1} (~8 wt %) from the dry residue obtained after the complete evaporation of solvent as CONs. The dry powdered samples of CONs were used as such for characterization like PXRD, TGA, FT-IR etc. to ensure their structural stability after grinding. Similar experiments of COF delamination was also performed in a ball mill (Restch MM 400) operating at 25 Hz, for 30 minutes, which also produces the same CONs in high isolated yield. For TEM and AFM imaging, we used 1 mg of CONs in 10 mL of isopropanol, sonicated for 5 minutes and subsequently coated on the carbon-coated copper grid (TEM) and Si-wafer or mica (AFM), and dried at room temperature prior to imaging.

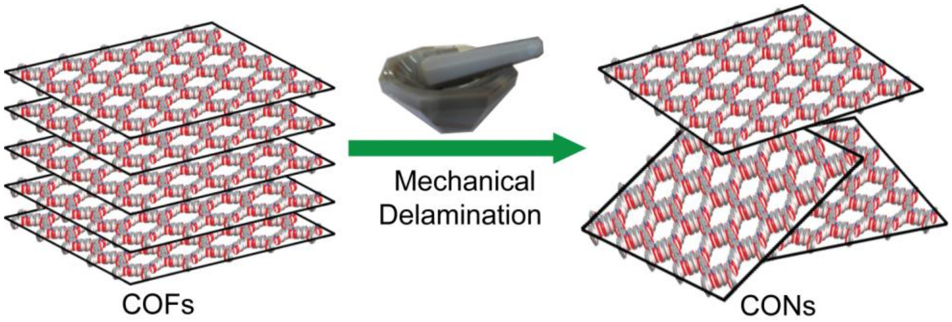

***Figure 2.3**: Schematic representation of the formation of CONs from as-synthesized COFs via mechanical grinding.*

2.2.3 *Structural simulation and characterization*

Since COFs are synthesized as polycrystalline powder, powder X-ray diffraction (PXRD) is used for determining the crystallinity and investigating the structural details of the material. As revealed by PXRD analysis, COFs belonging to **TpPa**–series (**TpPa–1, TpPa–2, TpPa–NO_2, TpPa–F_4)** show high crystallinity, exhibiting the first intense peak at low angle ~4.7° (2θ), which corresponds to the (100) reflection plane, along with the minor peaks at ~8.1, ~11.1 and ~27°

(2*θ*), attributed to the (200), (210) and (001) reflection planes, respectively (Figure 2.4). Similarly, for the COFs belong to **TpBD**–series [**TpBD, –Me$_2$, – (OMe)$_2$, –(NO$_2$)$_2$**], the first and most intense peak corresponding to the (100) reflection plane appears at ~3.3° (2*θ*), with other minor peaks at ~6.3, ~11.7 and ~25° (2*θ*), attributed to the (200), (210) and (001) reflection planes respectively. The shift of the reflection (2*θ)* towards the lower value of 3.3° from 4.7° for COFs belonging to **TpBD**–series compared to **TpPa**–series COFs is due to the isoreticulation, which results in larger pore aperture. The centre-to-centre pore distance varies from ~1.5 to ~2.4 nm and the 2D sheets are stacked by a distance of ca. ~3.5 Å (Figure 2.2). Peaks at higher 2*θ* correspond to the π-π stacking between the COF layers and could be assigned to the 001 reflection planes (Figure 2.4). In order to elucidate the structure of these COFs and to calculate the unit cell parameters, a possible 2D model was built with eclipsed and staggered stacking using Self- Consistent Charge Density Functional Tight-Binding (SCC-DFTB) Method [2.16]. The experimental PXRD pattern matches well with the simulated pattern of the eclipsed stacking

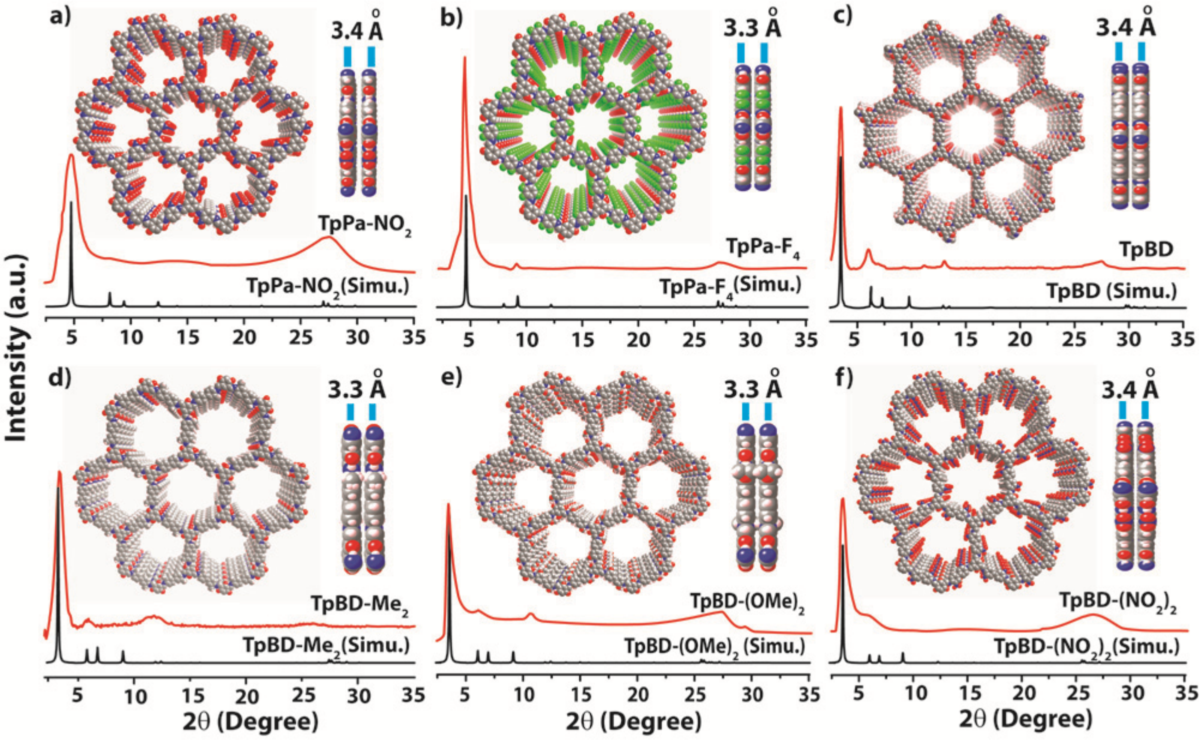

***Figure 2.4**: Comparison of PXRD spectra of solvothermal synthesized (red) with the simulated eclipsed (black) stacking models for (a) **TpPa-NO$_2$**, (b) **TpPa-F$_4$**. (c) **TpBD**, (d) **TpBD-Me$_2$**, (e) **TpBD-(OMe)$_2$** and (f) **TpBD-(NO$_2$)$_2$** (Inset showing the hexagonal porous structure and π-π stacking distance of all the COFs.)*

model (Figure 2.4). Hence, we propose a structure close to the hexagonal space group (*P*6/m) for both the **TpPa** and the **TpBD**–series COFs. In order to find out the unit cell parameters, Pawley refinements were done for all the COFs (Figure 2.5) using Reflex module of Material studio [2.17]. The proposed 2D models and the detailed structural description of **TpPa–1** (*a* = *b* = 22.1 Å, *c* = 3.3 Å), **TpPa–2** (*a* = *b* = 22.1 Å, *c* = 3.3 Å) and **TpBD** (*a* = *b* = 22.1 Å, *c* = 3.3 Å) were presented in our previous publications [2.11]. However, the unit cell parameters for other COFs such as **TpPa–NO_2** were found to be *a* = *b* = 21.8 Å, *c* = 3.2 Å and for **TpPa–F_4** the values obtained were *a* = *b* = 22.1 Å, *c* = 3.3 Å. Similarly, the unit cell parameters have been obtained for **TpBD–$(NO_2)_2$** (*a* = *b*=31.5 Å, *c* = 3.5 Å), **TpBD–Me_2** (*a* = *b* = 29.3 Å, *c* = 3.2 Å), and **TpBD–$(OMe)_2$** (*a* = *b* = 29.3 Å, *c* = 3.2 Å) (***Table 2.1-2.3***).

Atomic positions and cell sizes of modeled COF layers were optimized using Self-Consistent Charge Density Functional Tight-Binding (SCC-DFTB) Method. Stacking of layers is affected by the Coulomb repulsion between the partial atomic charges in adjacent layers [2.18]. Hence, we performed Mulliken population analysis for the charges. The adjacent layers were shifted with respect to each other in different directions in order to avoid Coulomb repulsion from charges alike. Several possibilities were considered, however, the best was taken from the comparison of simulated PXRD pattern with the experimental. Interlayer separation was also determined from the comparison of PXRD patterns. The fractional coordinates of **TpPa-NO_2** and **TpPa-F_4** are given in **Table 2.1** and **2.2**. Similarly, the fractional coordinates of **TpBD-Me_2**, **TpBD-$(OMe)_2$** and **TpBD-$(NO_2)_2$** are given in **Table 2.2** and **2.3**.

Table 2.1: Fractional atomic coordinates for the unit cell of **TpPa-NO_2**.

TpPa-NO_2 Triclinic *P*1 *a* = *b* = 21.8 Å, *c* = 3.24 Å α = 90, β = 90, γ = 119.03							
Atom	*x*	*y*	*z*	Atom	*x*	*y*	*z*
O	0.02829	0.76093	0.48167	C	0.9691	1.67864	0.48167
O	0.83835	0.98147	0.48167	C	0.89799	1.6626	0.48167
O	0.56757	1.27332	0.48167	C	0.84191	1.59228	0.48167

O	0.54522	1.16495	0.48167	C	0.85912	1.53755	0.48167
O	0.94546	1.50211	0.48167	C	0.511	0.91811	0.48167
O	0.77822	1.57789	0.48167	C	0.92993	1.5511	0.48167
O	0.52554	1.03133	0.48167	C	0.80523	1.47008	0.48167
O	0.72531	1.00432	0.48167	C	0.77456	1.34967	0.48167
O	0.50269	0.80708	0.48167	C	0.70336	1.32313	0.48167
O	0.37007	0.69531	0.48167	C	0.88404	1.71737	0.48167
O	0.26248	0.61116	0.48167	C	0.79513	1.75025	0.48167
N	0.39688	0.82479	0.48167	C	0.83894	1.82132	0.48167
N	0.70949	0.88163	0.48167	C	0.67102	1.09096	0.48167
N	0.64708	1.13591	0.48167	C	0.68833	1.20642	0.48167
N	0.81887	1.70331	0.48167	C	0.76101	1.23523	0.48167
N	0.82055	1.41939	0.48167	C	0.55313	0.99281	0.48167
N	0.11274	0.71832	0.48167	C	0.64154	0.85903	0.48167
N	0.30638	0.67343	0.48167	C	0.73847	0.83918	0.48167
N	0.8609	0.93954	0.48167	C	0.69545	0.76661	0.48167
N	0.58607	1.22846	0.48167	C	0.81116	0.86569	0.48167
N	0.39688	0.82479	0.48167	C	0.66033	1.25206	0.48167
N	0.70949	0.88163	0.48167	C	0.80344	1.30542	0.48167
C	0.54027	0.87216	0.48167	C	0.72303	0.72298	0.48167
C	0.21035	0.69676	0.48167	C	0.6274	1.02099	0.48167
C	0.18266	0.74128	0.48167	C	0.66014	0.97777	0.48167
C	0.22589	0.81325	0.48167	C	0.61514	0.90373	0.48167
C	0.29619	0.84001	0.48167	C	0.44079	0.89255	0.48167
C	0.0628	0.65358	0.48167	C	0.32626	0.79644	0.48167

C	0.00514	0.64067	0.48167	C	0.28166	0.7239	0.48167

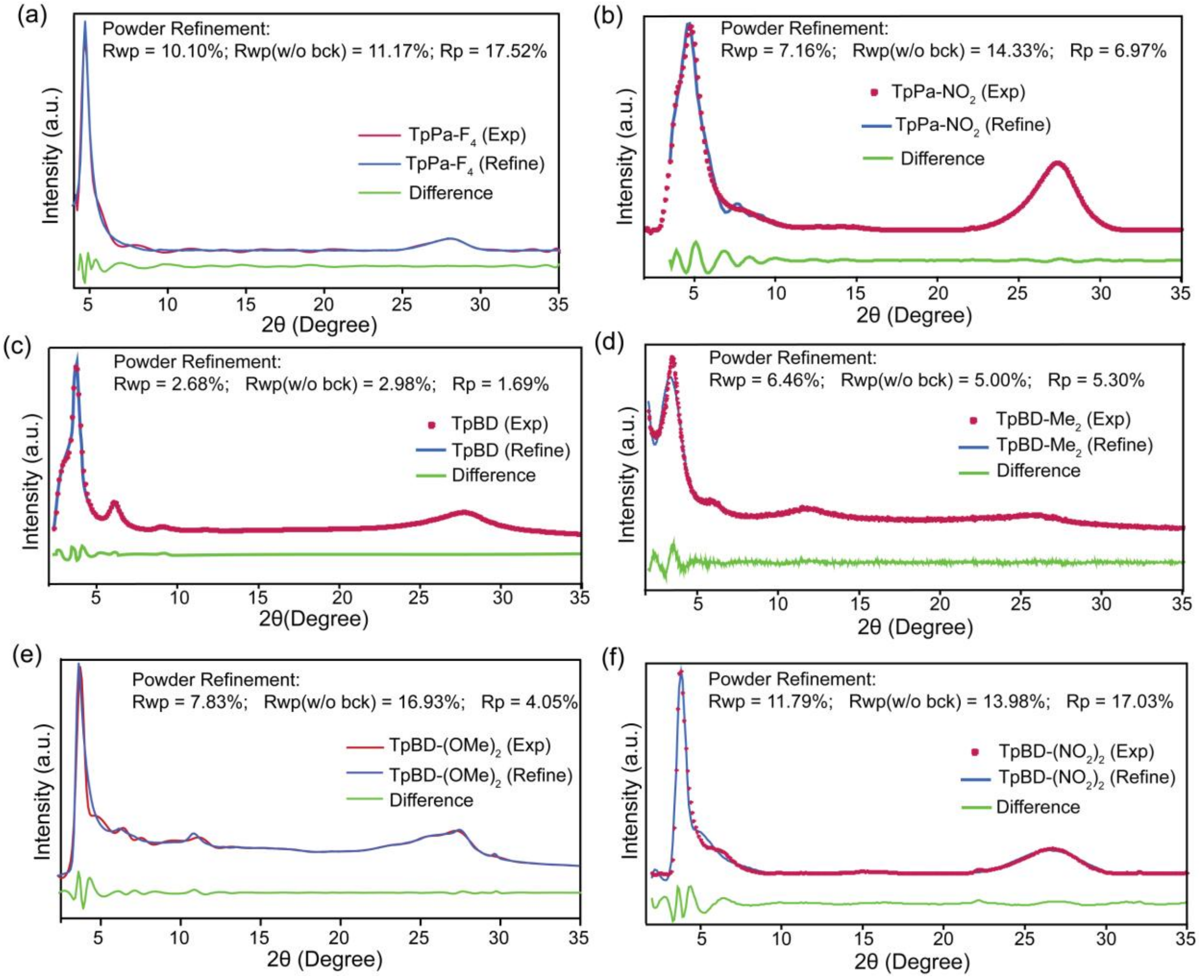

***Figure 2.5**: Experimental (Red) compared with refined (Blue) PXRD profiles of an eclipsed arrangement for (a) TpPa-F$_4$, (b) TpPa-NO$_2$, (c) TpBD, (d) TpBD-Me$_2$, (e) TpBD-(OMe)$_2$ and (f) TpBD-(NO$_2$)$_2$; difference plot is given in (Green).*

Table 2.2: Fractional atomic coordinates for the unit cell (eclipsed) of **TpPa-F$_4$** and **TpBD-Me$_2$**.

TpPa-F$_4$				**TpBD-Me$_2$**			
Hexagonal *P*6/m *a* = *b* = 20.90 Å, *c* = 3.4 Å				Hexagonal *P*6/m *a* = *b* = 33.61 Å, *c* = 3.03 Å			
Atom	*x*	*y*	*z*	Atom	*x*	*y*	*z*
F	0.42831	0.3566	0	O	0.28755	0.56179	0

F	0.35777	0.42603	0	N	0.38477	0.57293	0
O	0.70395	0.47093	0	C	0.30922	0.60977	0
N	0.57967	0.43562	0	C	0.39846	0.62504	0
C	0.68597	0.40653	0	C	0.42288	0.55812	0
C	0.61379	0.35215	0	C	0.4797	0.59233	0
C	0.5612	0.36839	0	C	0.50767	0.56659	0
C	0.5379	0.46432	0	C	0.48375	0.51191	0
C	0.42812	0.46239	0	C	0.42892	0.48087	0
C	0.46465	0.42728	0	C	0.39964	0.50379	0
				C	0.36596	0.64285	0

Table 2.3: Fractional atomic coordinates for the unit cell (eclipsed) of **TpBD-(OMe)$_2$** and **TpBD-(NO$_2$)$_2$**.

TpBD-(OMe)$_2$				**TpBD-(NO$_2$)$_2$**			
Hexagonal *P*6/m *a* = *b* = 28.36 Å, *c* = 3.25 Å				Hexagonal *P*6/m *a* = *b* = 43.9 Å, *c* = 3.70 Å			
Atom	*x*	*y*	*z*	Atom	*x*	*y*	*z*
O	0.2956	0.5612	0	O	0.30539	0.57108	0
O	0.3431	0.4714	1	N	0.40525	0.59303	0
N	0.3872	0.5781	0	C	0.31857	0.61439	0
C	0.32579	0.48675	1.22717	C	0.40982	0.64127	0
C	0.3135	0.6107	0	C	0.43874	0.57305	0
C	0.4039	0.6298	0	C	0.49214	0.59702	0
C	0.4195	0.5569	0	C	0.51373	0.56669	0
C	0.4739	0.5883	0	C	0.48726	0.51517	0
C	0.5046	0.5656	0	C	0.43624	0.4934	0

C	0.4829	0.5112	0	C	0.41338	0.52122	0
C	0.4281	0.4803	0	C	0.372	0.65149	0
C	0.3968	0.5027	0				
C	0.3684	0.6472	0				

2.2.4 *Chemical characterization*

The FT-IR spectra obtained for all these COFs clearly indicate the complete disappearance of IR bands correspond to the characteristic N–H stretching (3100–3300 cm^{-1}) of free diamine [**Pa–1**, **Pa–2**, **Pa–NO_2**, **Pa–F_4**, **BD**, **BD–$(NO_2)_2$**, **BD–Me_2**, and **BD–$(OMe)_2$**] and carbonyl stretching band (1639 cm^{-1}) of 1,3,5–triformylphloroglucinol (**Tp**) (Figure 2.6). Interestingly, the FT-IR spectrum of any COF reported in this work does not show the characteristic stretching bands of hydroxyl (–OH) or imine (C=N) functional groups, which should have been present if the compound existed in the enol form. Instead, it shows a strong peak at ~1582 cm^{-1} for both the **TpPa**–series [**TpPa–1**, **TpPa–2**, **TpPa–NO_2**, **TpPa–F_4**] and the **TpBD**–series [**TpBD**, **TpBD–$(NO_2)_2$**, **TpBD–Me_2**, **TpBD–$(OMe)_2$**], which arises due to the C=C stretching band. This C=C stretching band at 1582 cm^{-1} appears due to the enol to keto tautomerism, which has been observed in the FT-IR spectrum of the reference compound {2,4,6-tris [(phenylamino)methylene] cyclohexane-1,3,5-trione} (Figure 2.7). All eight COFs reported in this work showed similar FT-IR spectra. The little variation in the peak positions that is observed arises due to the different functional groups present at the diamine linkers. In some cases, the peak broadening was observed in the extended structures, when C=O peaks (~1616 cm^{-1}) get merged with C=C stretching bands (~1582 cm^{-1}) and appear as shoulders. This confirms the overall s-cis structure in each COF presented in this study. The appearance of two peaks at ~1445 cm^{-1} and ~1256 cm^{-1} correspond to the aromatic C=C and newly formed C–N bond in the keto form of all COFs. The FT-IR spectrum of **TpPa–2** and **TpBD–Me_2** shows an extra peak at ~2885 cm^{-1}, which is due to the C–H stretching from the methyl (–CH_3) functionality. Similarly, for **TpPa–NO_2** and **TpBD–$(NO_2)_2$** a peak appears exactly at 1506 cm^{-1}, which corresponds to the –NO_2 functionality and confirms its presence in the framework.

We carried out ^{13}C CP-MAS solid state NMR spectroscopy to verify the atomic-level construction of COFs presented in this paper. The individual spectrum obtained was compared with other members of the same series (Figure 2.8). The solid state NMR of the reference compound {2,4,6-tris-[(phenylamino)methylene]} has also been presented in (Figure 2.8**)** for comparison. All COFs reported in this work showed a signal at ~180-182 ppm, which could be ascribed as the carbonyl carbon [C=O] of the keto form. The peak at ~144 ppm confirms the

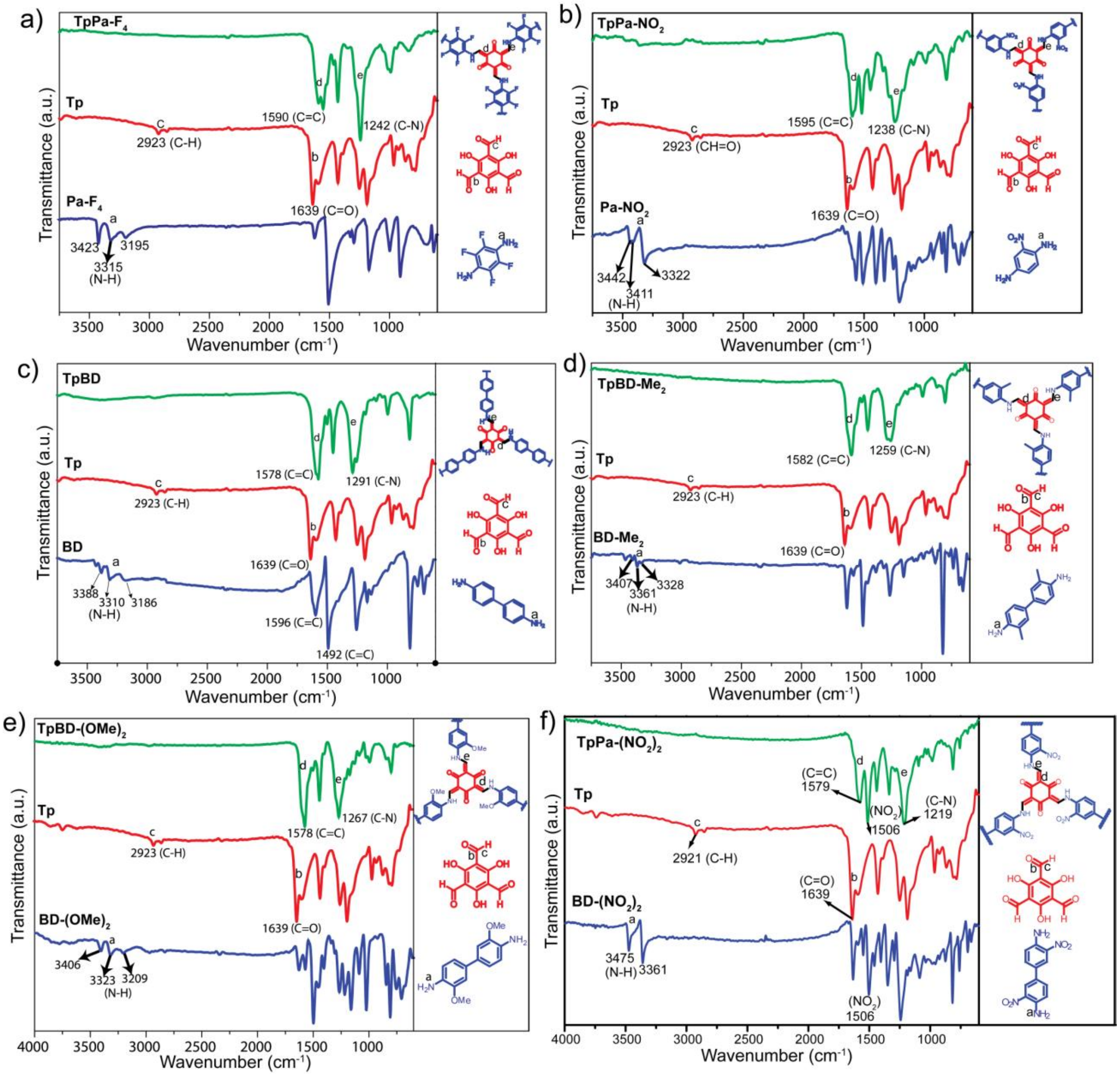

*Figure 2.6: FT-IR spectra of (a) **TpPa-NO$_2$**, (b) **TpPa-F$_4$** (c) **TpBD**, (d) **TpBD-Me$_2$**,(e) **TpBD-(OMe)$_2$**, and (f) **TpBD-(NO$_2$)$_2$** compared with triformylphloroglucinol (red) and corresponding amines (blue).*

presence of the C–N bond, instead of the C=N bond (~165 ppm), which could have been a signature peak if these COFs would have existed in the enol form. The unobserved peak at~190 ppm (for – CHO) gives clear evidence for the complete consumption of the starting material (**Tp**). The appearance of a peak at ~124 ppm is due to the carbons present at the biphenyl junction of benzidine (BD) in the **TpBD**–series. Such peak is also present in the ^{13}C spectra of **TpPa-2** and **TpPa–NO$_2$** due to unsymmetrical substitution and absent in **TpPa–1** and **TpPa-F$_4$** COFs due to the symmetrical substitution at 2,3,5,6 positions of the aromatic diamines (**Pa-1** and **Pa-F$_4$**). In the case of **TpPa-2** and **TpBD–Me$_2$** there is a ^{13}C NMR peak exactly at 14 ppm which arises due to the presence of an extra methyl (–CH$_3$) functionality, unlike the other COFs (Figure 2.8). However, for **TpBD-(OMe)$_2$**, the methyl carbon peak (52.9 ppm) gets deshielded as it is attached to the oxygen of the methoxy (–OMe) functionality.

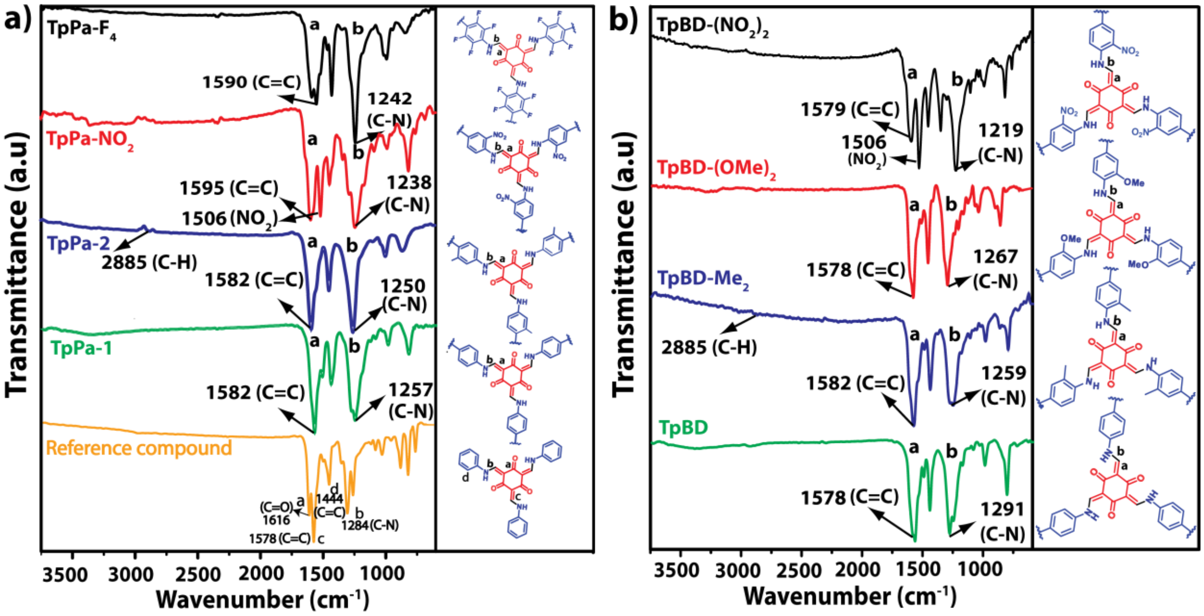

Figure 2.7: *FT-IR spectra of (a) TpPa series COFs [**TpPa-1** (green), **TpPa-2** (blue), **TpPa-NO$_2$** (red), **TpPa-F$_4$** (black)] and (b) TpBD series COFs [**TpBD** (green), **TpBD-Me$_2$** (blue), **TpBD-(OMe)$_2$** (red), **TpBD-(NO$_2$)$_2$** (black)] compared with reference compound (brown).*

External morphologies of these as-synthesized COFs were investigated by employing SEM and TEM imaging which showed that COFs belonging to the **TpPa** and **TpBD**–series crystallize with a flower like morphology (Figure 2.10). Each individual flower can be considered as a result of the aggregation of a large number of petals which have a length in the micrometer range (1–3 μm). In case of the **TpPa**–series COFs, petals (width 70–150 nm and thickness 30–40 nm) have spike shaped tips and have grown out from a core, whereas, for the **TpBD**–series COFs, petals are grown with a broader width to form plate like structures (1–5 μm length, 100–200

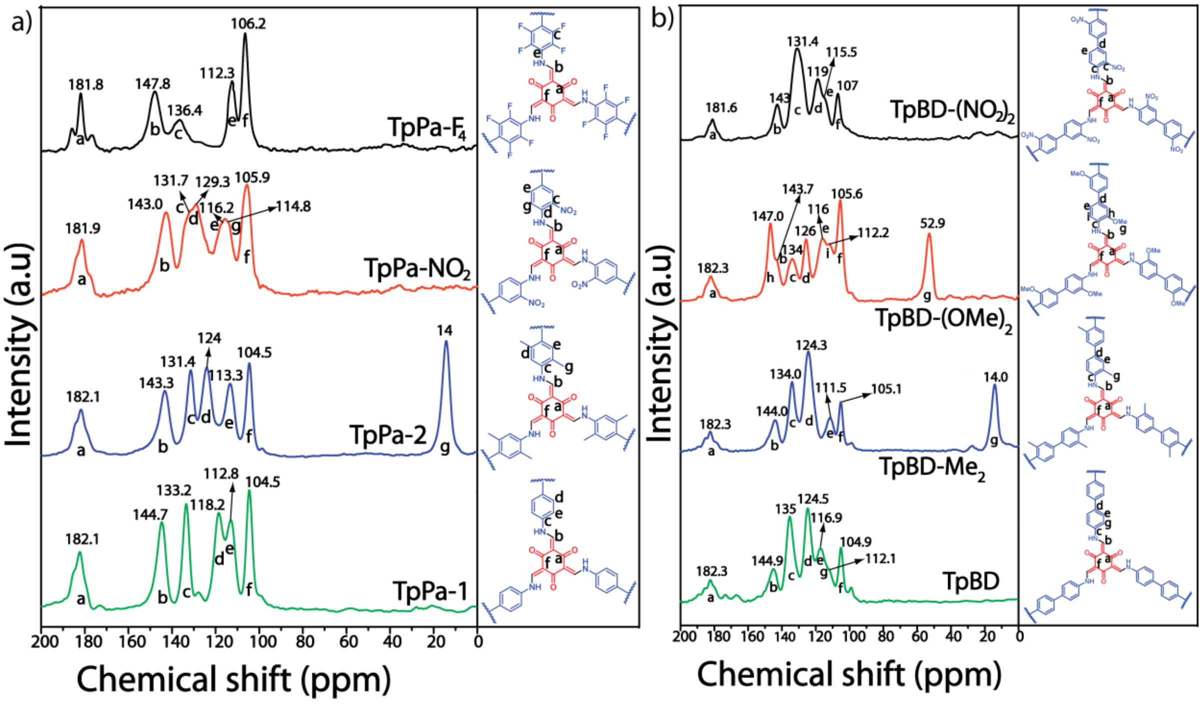

Figure 2.8: *^{13}C CP-MAS spectrum of (a) TpPa series COFs [**TpPa-1** (green), **TpPa-2** (blue), **TpPa-NO$_2$** (red), **TpPa-F$_4$** (black)] and (b) TpBD series COFs [**TpBD** (green), **TpBD-Me$_2$** (blue), **TpBD-(OMe)$_2$** (red), **TpBD-(NO$_2$)$_2$** (black)].*

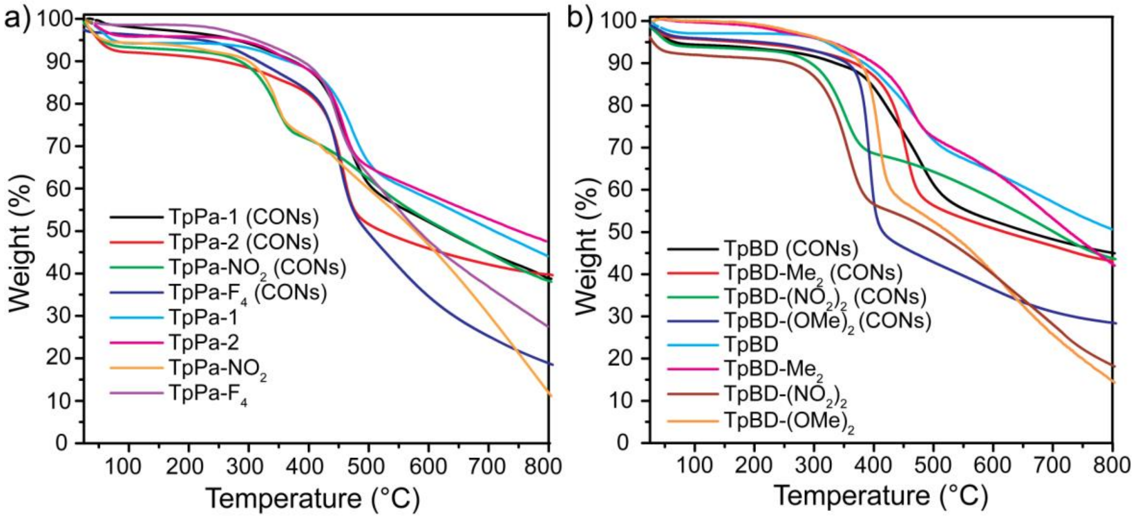

Figure 2.9: *TGA data of activated **COFs** belonging to (a)**TpPa**-series and (b) **TpBD**-series in comparison with corresponding **CONs** under N_2 atmosphere.*

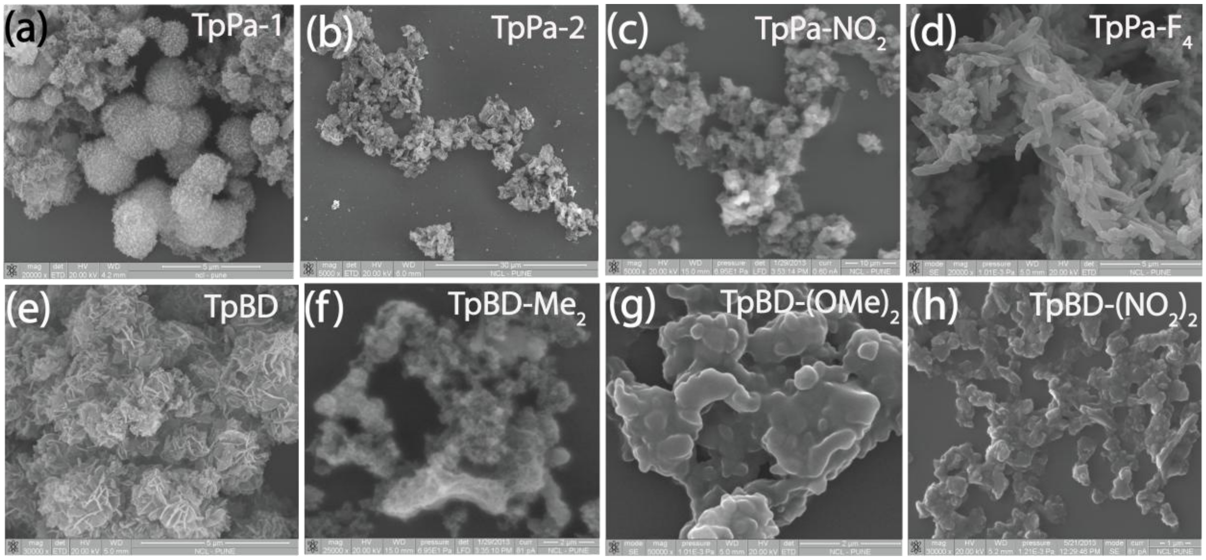

Figure 2.10: *SEM images of (a) **TpPa-1**; (b) **TpPa-2**; (c) **TpPa-NO$_2$**; (d) **TpPa-F$_4$**; (e) **TpBD**; (f) **TpBD-Me$_2$**; (g) **TpBD-(OMe)$_2$** and (h) **TpBD-(NO$_2$)$_2$**.*

width and 50–70 nm thickness). We would assume that individual petals have a sheet like structures and can be formed as a result of π-π stacking of different COF layers.

In order to check the thermal stability of all eight COFs, we have performed the TGA under a flow of N_2 gas. It has been observed from the TGA profiles that all COF pores are guest free and have almost identical thermal stabilities up to ~350 °C (Figure 2.9) except for **TpPa–NO$_2$** and **TpBD–(NO$_2$)$_2$**, where the framework is stable up to 300 °C. After 350 °C, these COFs start decomposing with gradual weight loss between 45–60 % for all COFs till 800 °C.

2.2.5 *Gas adsorption studies*

N_2 adsorption isotherms at 77 K were performed to examine the architectural rigidity and permanent porosity of all aforementioned COFs. All COFs showed typical type-I reversible isotherms (Figure 2.11a and 2.11b). The Brunauer-Emmet-Teller (BET) surface area for the activated **TpBD** was found to be 537 m^2g^{-1}, which is the highest among the **TpBD**–series COFs, whereas, for other COFs of this series, the values are 468 m^2g^{-1} [**TpBD–Me$_2$**], 330 m^2g^{-1} [**TpBD–(OMe)$_2$**] and 295 m^2g^{-1} [**TpBD–(NO$_2$)$_2$**]. **TpPa–1** possesses the highest BET surface area value of 535 m^2g^{-1}, than the other COFs of the **TpPa**–series such as **TpPa–F$_4$** (438 m^2g^{-1}), **TpPa–2**

(339 m^2g^{-1}) and **TpPa–NO$_2$** (129 m^2g^{-1}). The lower surface area values for **TpPa–NO$_2$** and **TpBD–(NO$_2$)$_2$** could possibly be due to bulkiness of the –NO$_2$ group and the poor affinity of the COFs towards N_2. Often in these kinds of porous COFs, some oligomeric impurities remain inside the pores during synthesis, which subsequently blocks the pores and impose low surface area. However, we could not find any signatures of such impurities in the COFs reported here. The pore size distributions for all COFs (both **TpPa**–series and **TpBD**–series) have been calculated on the basis of nonlocal density functional theory (NLDFT) and found to be in between 1.0–1.7 nm, (Figure 2.12). It is well-known that polar functional groups present in porous

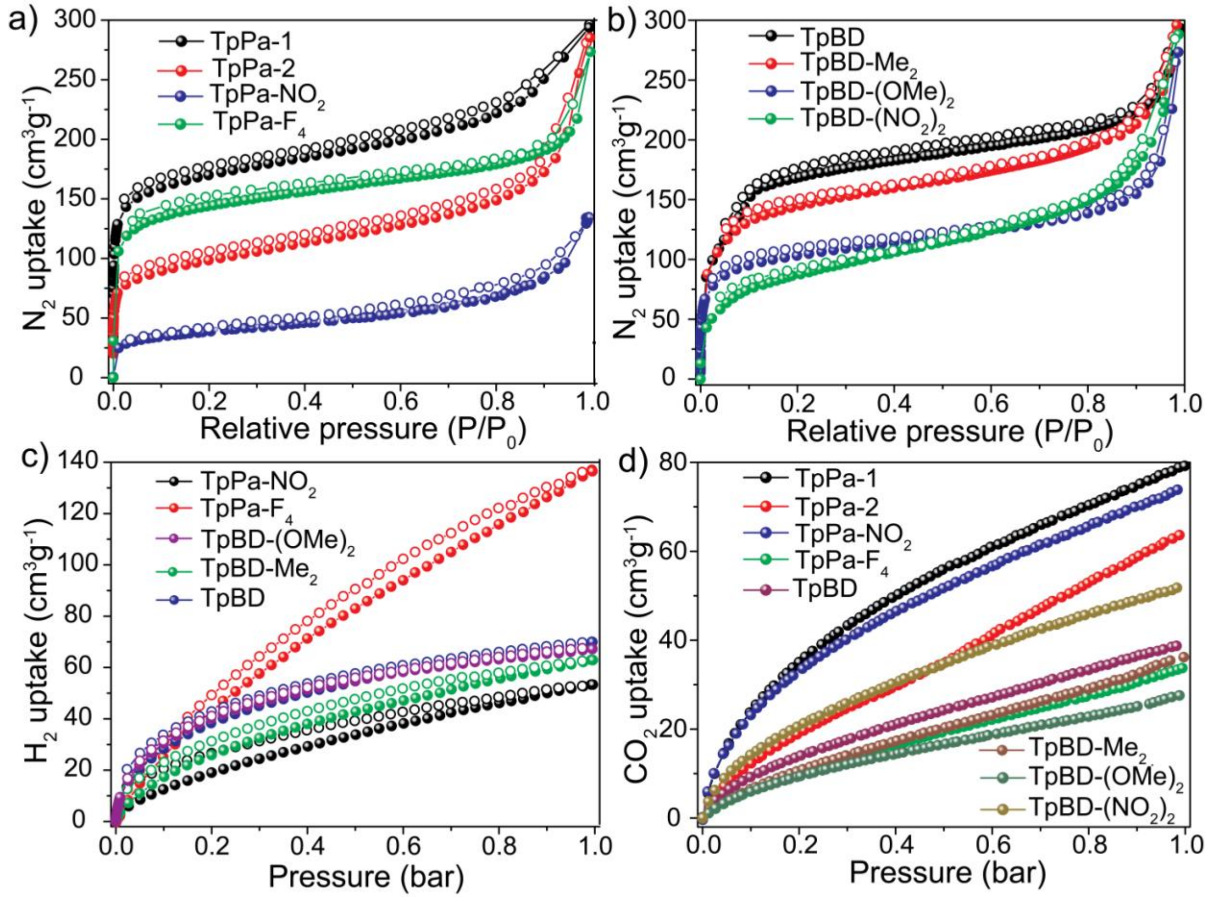

Figure 2.11: *N_2 adsorption of (a) TpPa series COFs [**TpPa-1** (black), **TpPa-2** (red), **TpPa-NO$_2$** (blue), **TpPa-F$_4$** (green)] and (b) TpBD series COFs [**TpBD** (black), **TpBD-Me$_2$** (red), **TpBD-(OMe)$_2$** (blue), **TpBD-(NO$_2$)$_2$** (green)]. (c) H_2 adsorption of **TpPa-NO$_2$** (black), **TpPa-F$_4$** (red), **TpBD-(OMe)$_2$** (violet), **TpBD-Me$_2$** (green) and **TpBD** (blue). (d) CO_2 adsorption isotherms of **TpPa-1** (black), **TpPa-2** (red), **TpPa-NO$_2$** (blue), **TpPa-F4** (green) **TpBD** (violet), **TpBD-Me$_2$** (brown), **TpBD-(OMe)$_2$** (dark green) and **TpBD-(NO$_2$)$_2$** (grey brown) . The filled symbols correspond to adsorption and empty symbols represent desorption isotherms.*

materials like MOFs and COFs have an impact on the H_2 uptake. Since these COFs contain a variety of functional groups decorated throughout the framework, we decided to perform H_2 and

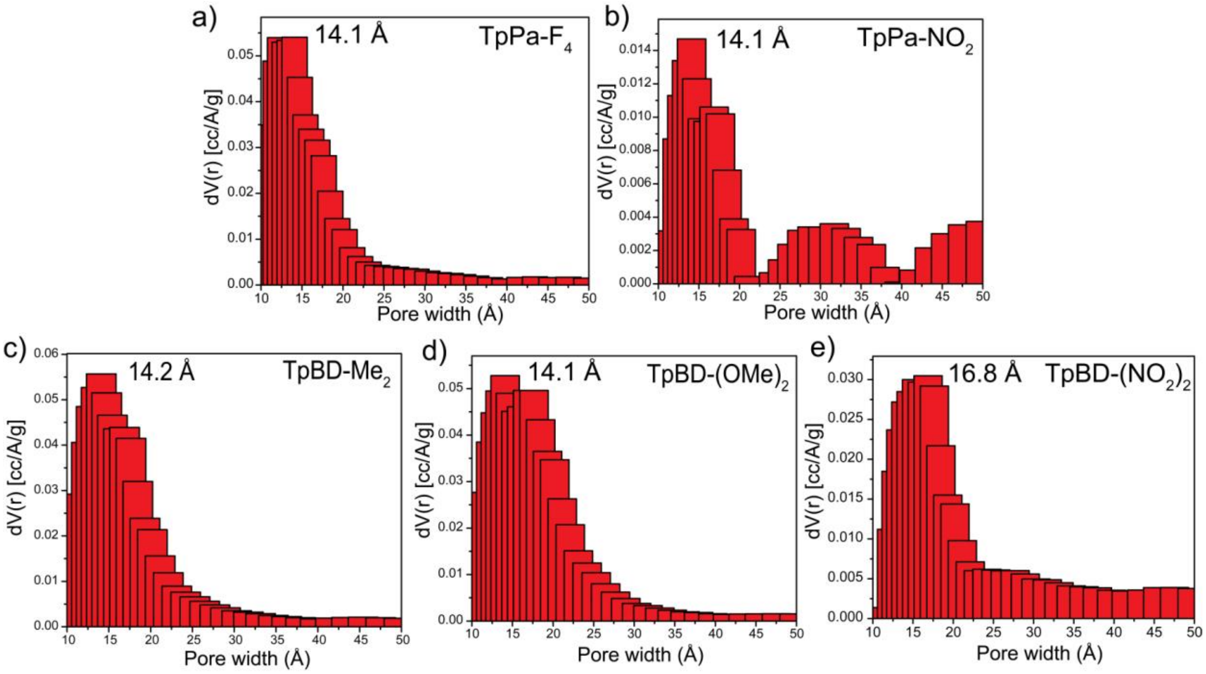

Figure 2.12: *NLDFT pore size distribution of (a)* ***TpPa-F₄****, (b)* ***TpPa-NO₂****, (c)****TpBD-Me₂****, (d)* ***TpBD-(OMe)₂*** *and (e)* ***TpBD-(NO₂)₂****.*

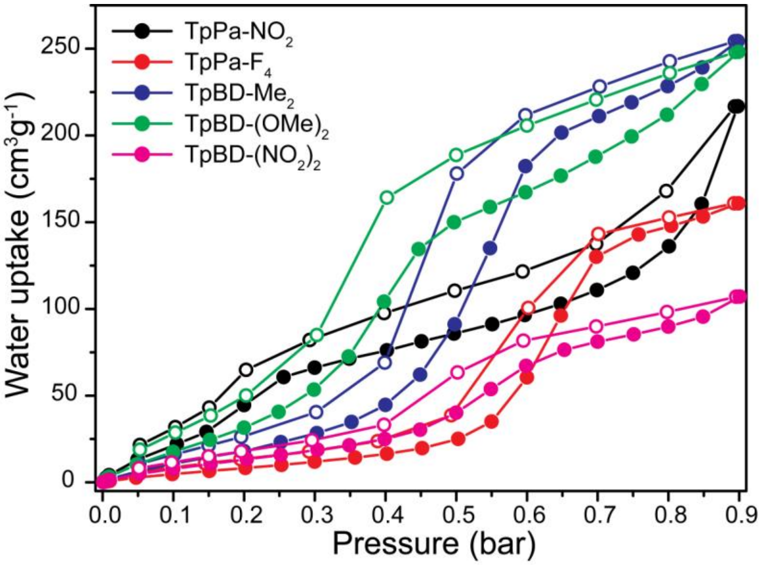

Figure 2.13: *Water adsorption isotherms of* ***TpPa–NO₂*** *(black)****,*** ***TpPa–F₄*** *(red)****,*** ***TpBD–Me₂*** *(blue)****,*** ***TpBD–(OMe)₂*** *(green) and* ***TpBD–(NO₂)₂*** *(pink) respectively collected up to P/P$_o$=0.9 (STP) at 293 K.*

CO_2 adsorption experiment at 77 K and 273 K respectively. The H_2 uptake capacity of **TpPa–F$_4$** was found to be highest (136 cm^3g^{-1}) among all the COFs presented in this paper, such as **TpPa–1** (110 cm^3g^{-1}), **TpPa–2** (89 cm^3g^{-1}), **TpBD** (69 cm^3g^{-1}), **TpPa–NO$_2$** (53 cm^3g^{-1}), **TpBD–Me$_2$** (62 cm^3g^{-1}), **TpBD–(OMe)$_2$** (67 cm^3g^{-1}) and **TpBD–(NO$_2$)$_2$** (40 cm^3g^{-1}) respectively (Figure 2.11c). The presence of fluorine functionality with polar interactions with the H_2 gas molecules could be the reason for high H_2 uptake in **TpPa–F$_4$**. Interestingly, the CO_2 uptake of **TpPa–1** (80 cm^3g^{-1} at 273 K) is the highest among all COFs presented in this work, such as **TpPa–NO$_2$** (73 cm^3g^{-1}), **TpPa–2** (63 cm^3g^{-1}), **TpBD–(NO$_2$)$_2$** (52 cm^3g^{-1}) , **TpBD** (40 cm^3g^{-1}), **TpBD–Me$_2$** (37 cm^3g^{-1}), **TpPa–F$_4$** (35 cm^3g^{-1}) and 27 cm^3g^{-1} for **TpBD–(OMe)$_2$** respectively (Figure 2.11d). We have also collected the water vapour adsorption isotherms for all COFs and found that **TpBD** possesses the highest water vapour uptake of 265 cm^3g^{-1} at 0.9 (P/P_o) and 20 °C (at STP), closely followed by **TpBD–Me$_2$** (255 cm^3g^{-1}), **TpBD–(OMe)$_2$** (250 cm^3g^{-1}) and **TpPa–NO$_2$** (223 cm^3g^{-1}) (Figure 2.13).

2.2.6 Mechanical Delamination of Covalent Organic Frameworks

Since the synthesis of 2D organic nanomaterials is currently of emerging interest in the field of nanoscience, one would assume that covalent organic nanosheets (CONs), synthesized *via* delamination of 2D COF layers, could be a potential 2D organic nanomaterial. It is noteworthy to mention that only two reports on the delamination of as-synthesized COFs, where bulk layered COFs have been exfoliated into thin flat nanostructures by ultrasonication are available in the literature [2.4]. This delamination of COFs *via* ultrasonication requires ultra-pure and absolutely dry solvents. On the other hand, 2D COFs have also been grown on expensive graphite (e.g., HOPG), single-layer graphene (SLG) or Ag support using an ultra high vacuum. Such precautions required for the delamination is mainly due to the instability of COFs under ambient conditions. Hence, in order to delaminate COFs in a more efficient manner, we used the mechanical grinding approach and applied this to all eight as-synthesized COFs [both **TpPa** and **TpBD**–series] discussed here. We anticipated that mechanical grinding will facilitate the separation of existing π-π stacking (AA) between the stable COFs layers. All these COFs have

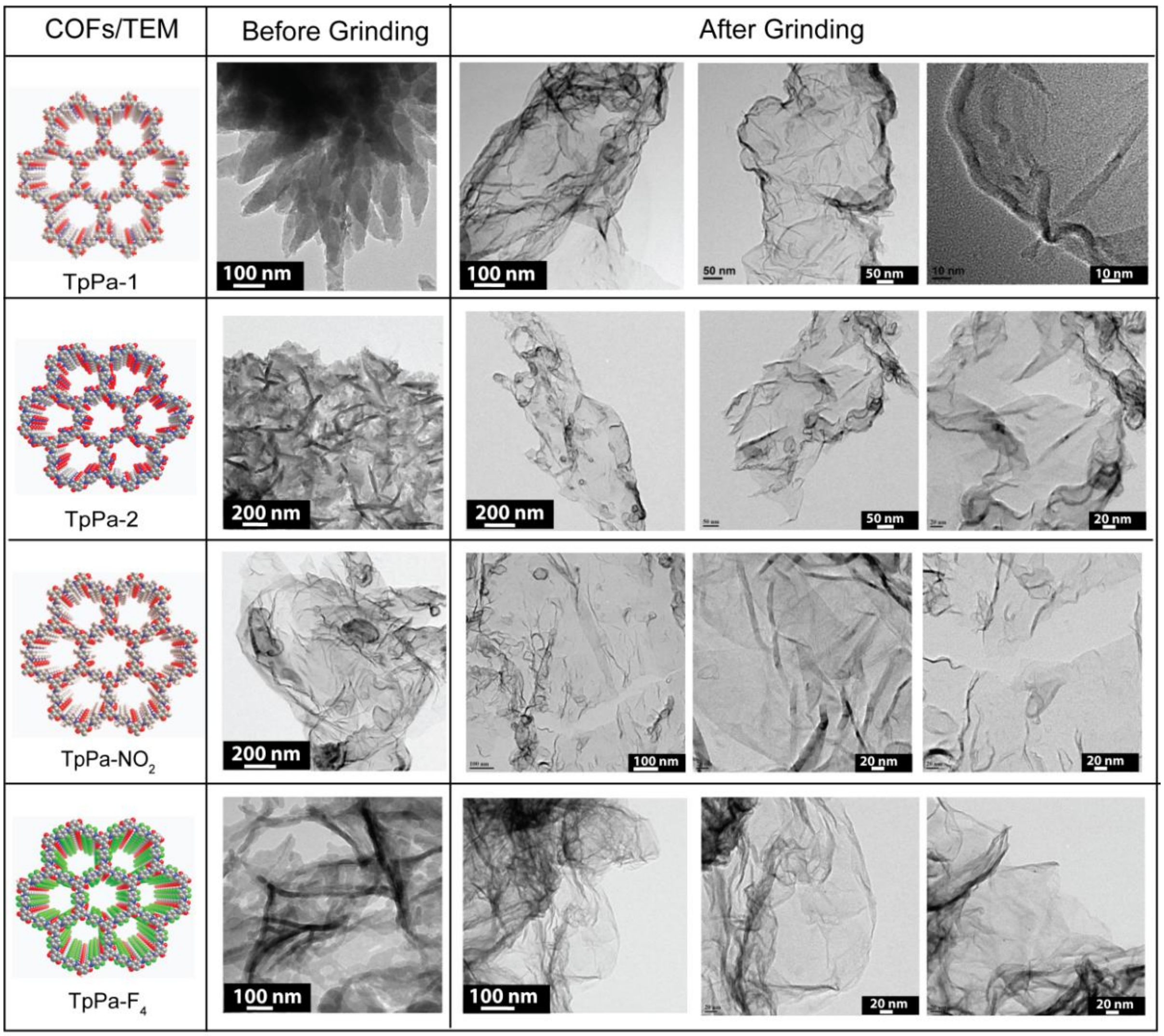

Figure 2.14: *TEM images of **COFs** (before grinding) and **CONs** (after grinding) belonging to **TpPa-**series at different magnifications.*

many similarities to graphite with respect to dimensionality, periodic, parallel lattices, along with almost identical stacking distance between consecutive layers (~3.4–3.6 Å). Like graphite, due to the presence of strong in-plane bonds and weak Van der Waals interactions between layers in COFs, there is sufficient opportunity to delaminate such materials into individual layers either by chemical or mechanical delamination. This mechanical delamination approach was found to be more effective over ultrasonication or layer growth as it does not require ultra-pure and dry solvents or expensive supports. In order to test the existence of nanosheet like structures, well dispersed mechanically ground COFs were suspended in isopropanol. This suspension has been

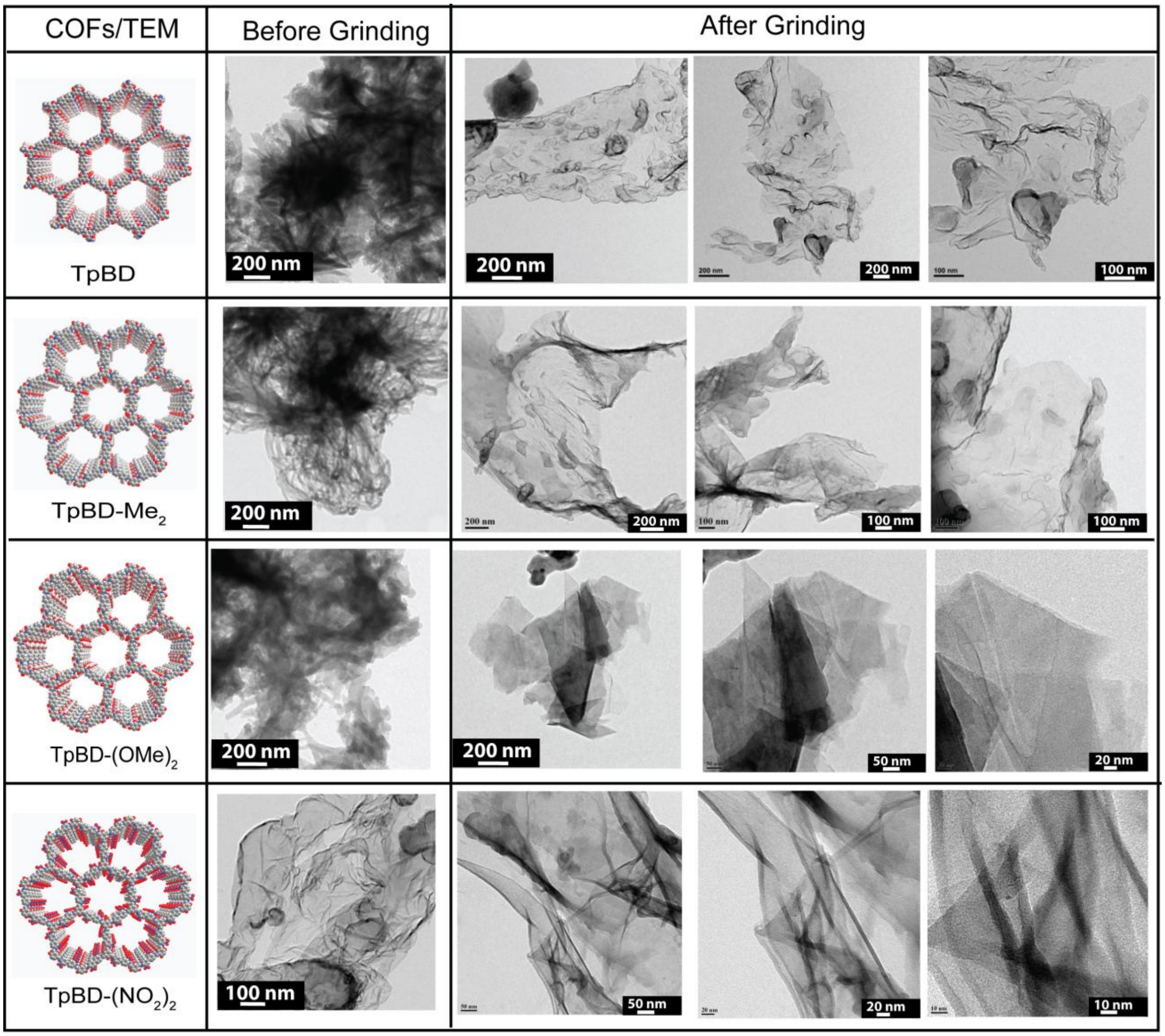

Figure 2.15: *Packing diagrams with **HR-TEM** images of **COFs** (before grinding) and delaminated COFs (after grinding i.e. **CONs**) belonging to **TpBD**-series at different magnifications.*

deposited on a carbon-coated copper grid and observed by means of TEM technique. Figure 2.14 and Figure 2.15 shows typical images observed using TEM technique. As a result of delamination, we observed very thin graphite like layered structures (100 nm to 1 µm length) from TEM images for all COFs (Figure 2.14 and Figure 2.15).

The laminar structure of the materials (CONs) obtained by mechanical grinding of as-synthesized COFs was assessed by atomic force microscopy (AFM) measurements in order to obtain precise information about the existence of single-/few-layer materials. In order to isolate a few thin layers of CONs on surfaces, the sufficiently dilute solution of CONs were drop-casted on mica and SiO_2 surfaces. These CONs show flat nanosheet like structures with lengths and widths of several micrometers and thicknesses ranging from 3 to 10 nm, which corresponds to the existence of only ~10-30 COF layers (Figure 2.16). The images obtained in some cases clearly show terraces with steps indicating distinct levels of delamination in the same nanostructures, suggesting multilayer structures.

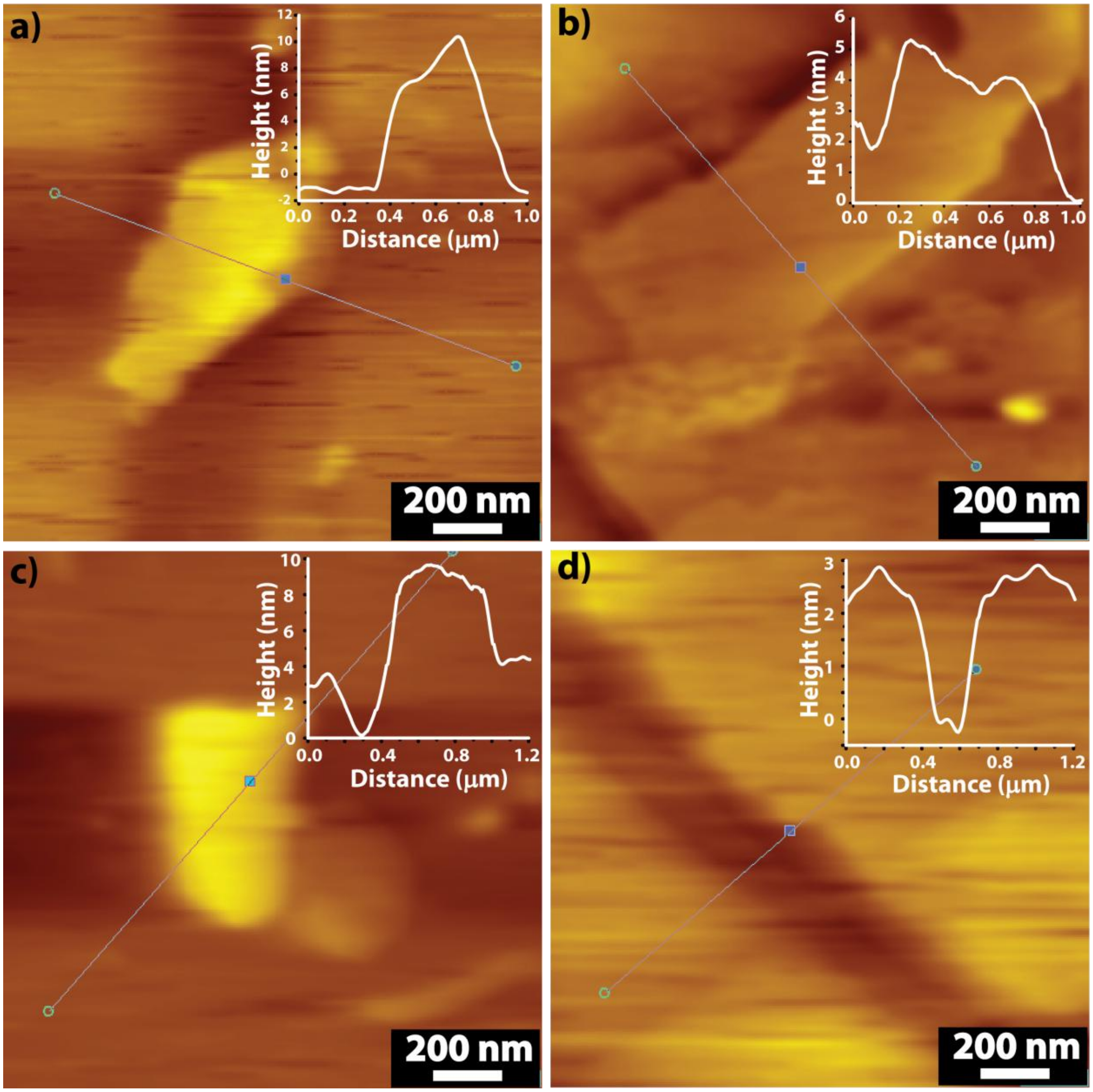

Figure 2.16: *AFM images; a)* ***TpPa-2*** *(CONs) b)* ***TpBD*** *(CONs) c)* ***TpBD-(OMe)$_2$*** *(CONs) and d)* ***TpPa-NO$_2$*** *(CONs) collected on mica support.*

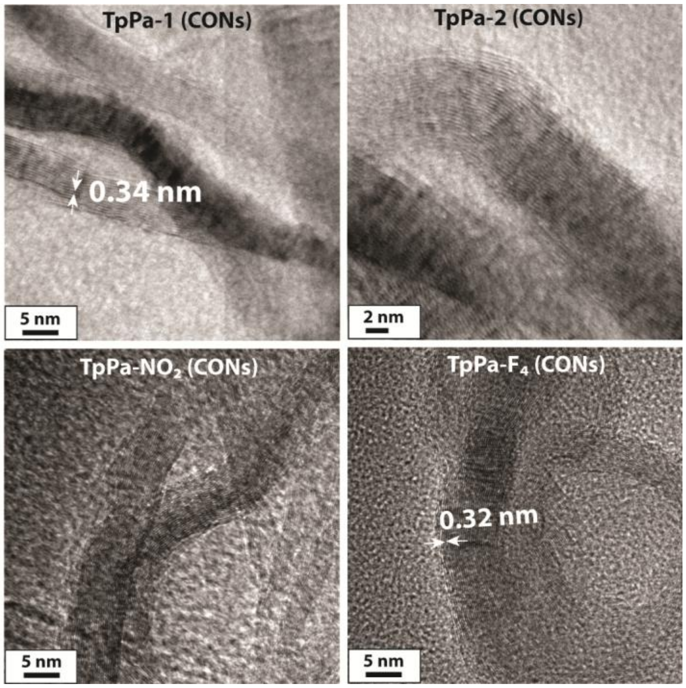

Figure 2.17: *TEM images of CONs belonging to* ***TpPa****-series showing graphite like periodic layers along one direction (fringes).*

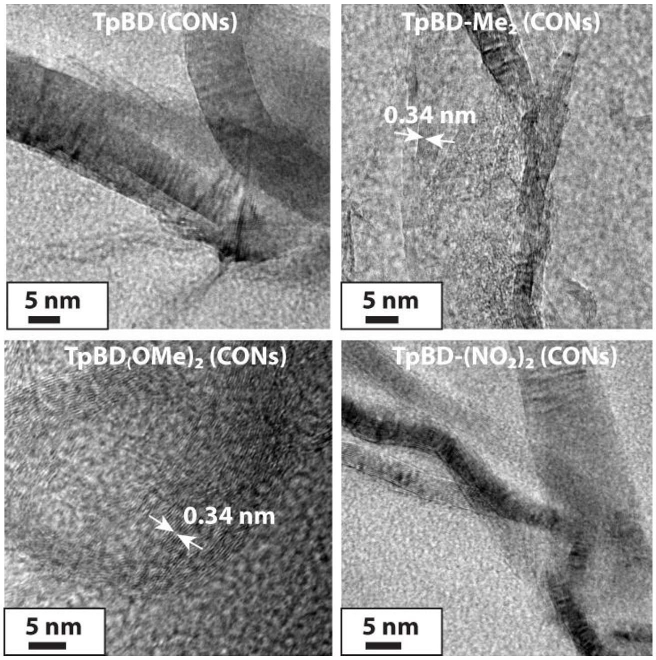

Figure 2.18: *TEM images of COFs belonging to* ***TpBD****-series showing graphite like periodic layers along one direction (fringes).*

The information obtained from AFM imaging is in good agreement with the TEM images. As shown in HR-TEM images some fringes have been observed like graphite-type layered material with a periodic distance of ~0.34 nm along one direction (Figure 2.17 and 2.18). We believe that when subjected to strong mechanical force, the 2D layers of these COFs get easily delaminated producing nanosheet like structures.

This kind of mechanical delamination by grinding has already been known for graphene and other 2D materials but this is the first report of mechanical delamination of as-synthesized COFs to CONs. After the mechanical grinding process, we suspended some CONs material into methanol and subsequently passed green laser light (532 nm) into the solution to check the dispersive nature of the particles. Interestingly, the suspension showed the Tyndall effect (Figure 2.19), which the characteristic phenomenon is typically seen in colloidal solution under a light source, which further confirms the highly dispersive and fine particle nature of these CONs.

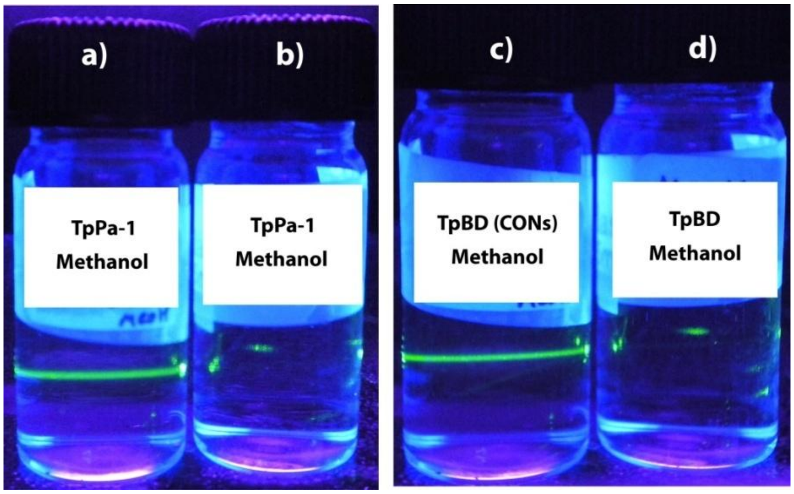

Figure 2.19: *Photographs of a)* ***TpPa-1*** *(CONs), c)* ***TpBD*** *(CONs) showing the Tyndall effect under laser light (532 nm) in methanol (HPLC, Sigma), whereas b)* ***TpPa-1****, d)* ***TpBD*** *does not show Tyndall effect.*

In order to further characterize these CONs, we have used FT-IR which showed exactly similar spectra like as-synthesized COFs and revealed that the compositions, as well as the mode of bonding, are still intact after the mechanical grinding (Figure 2.20 and 2.21). Similarly, to check the crystallinity after grinding, we carried out the PXRD of these CONs and observed that the PXRD profile remained the same as that of the as-synthesized samples (Figure 2.22 and 2.23).

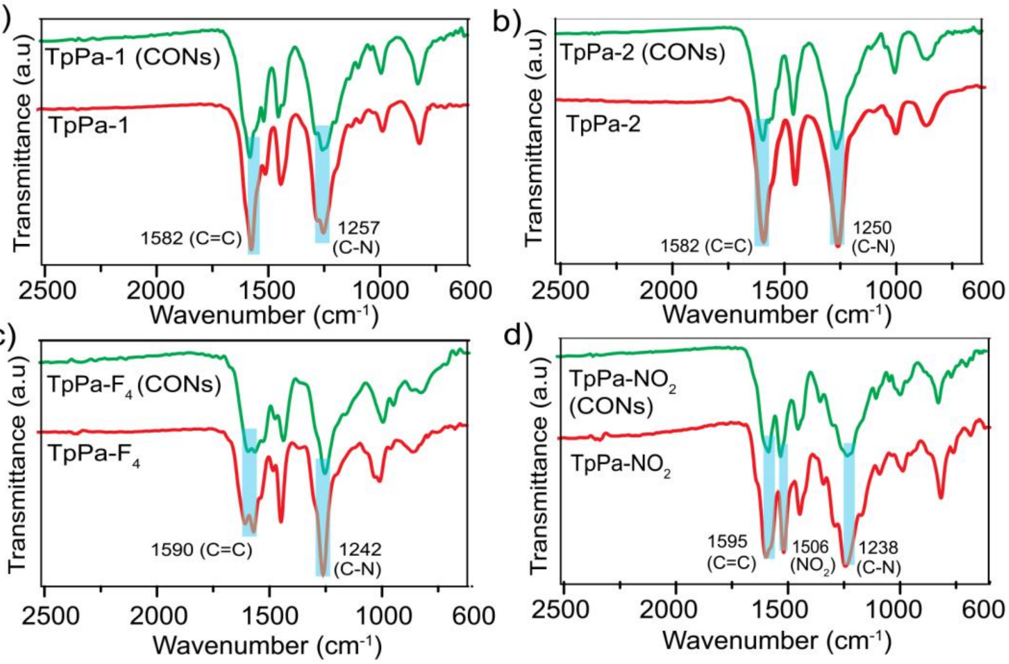

Figure 2.20: *FT-IR spectra of as-synthesized* ***TpPa****-series COFs (red) with corresponding delaminated COFs (CONs) (green).*

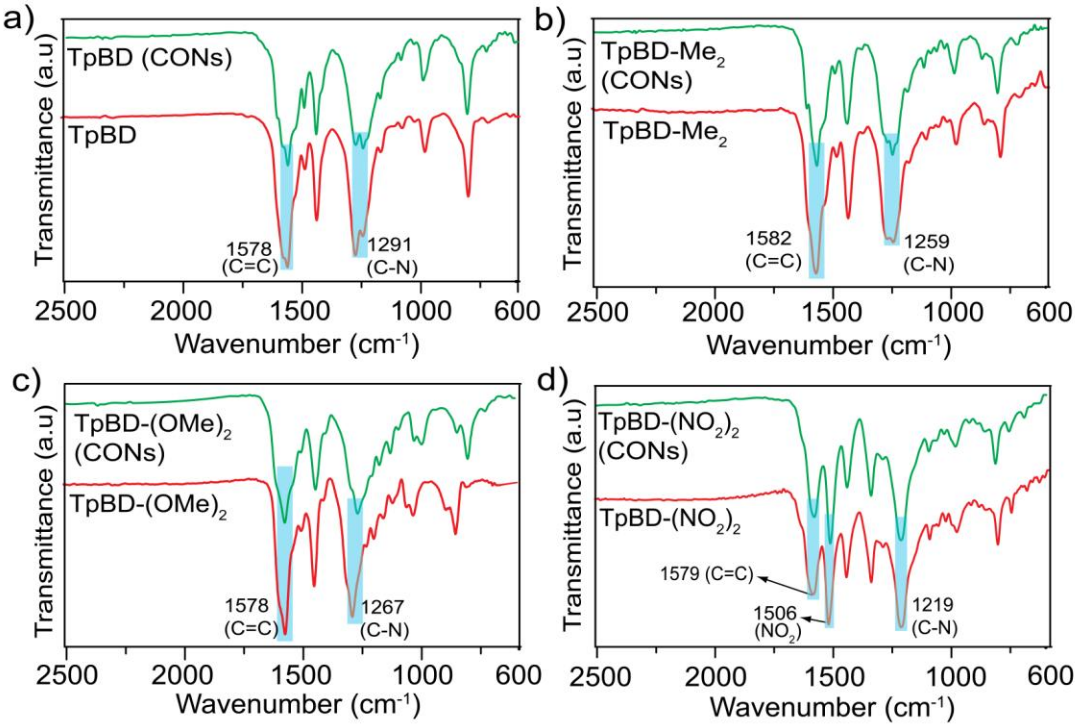

Figure 2.21: *FT-IR spectra of as-synthesized* ***TpBD****-series COFs (red) with corresponding delaminated COFs (CONs) (green).*

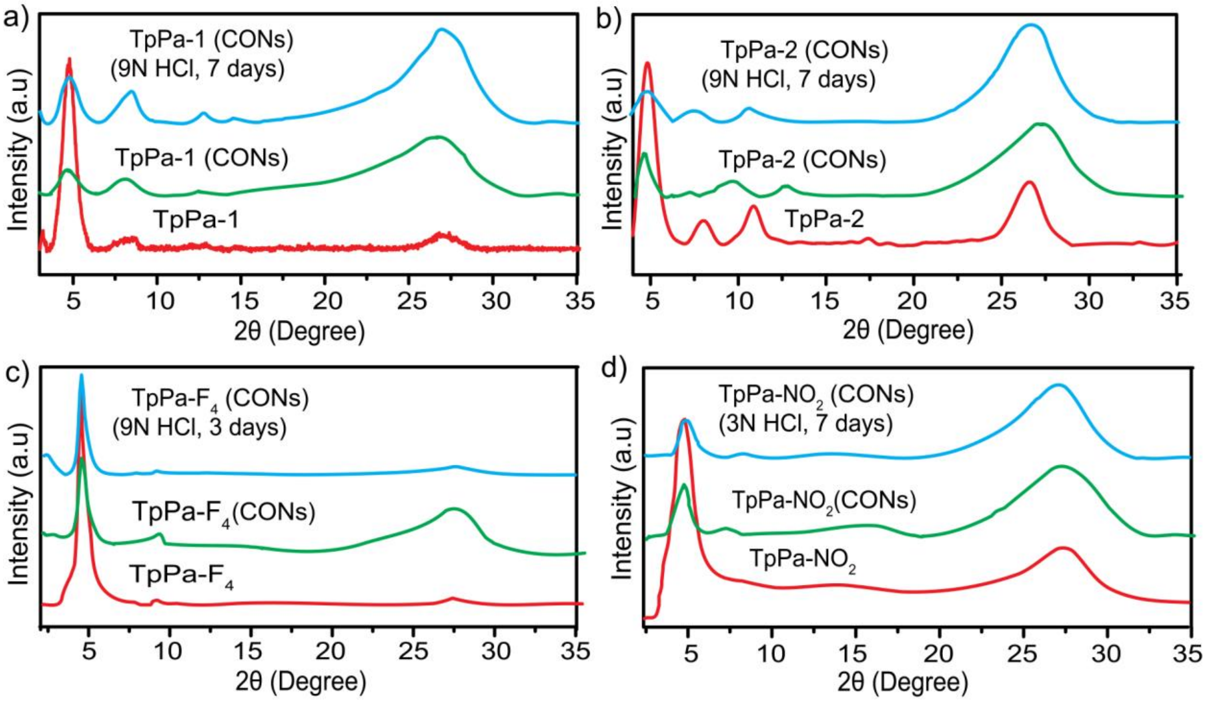

Figure 2.22: *PXRD patterns of as-synthesized* ***TpPa****-series COFs (red), corresponding delaminated COFs (CONs) (green), and acid-treated CONs (cyan).*

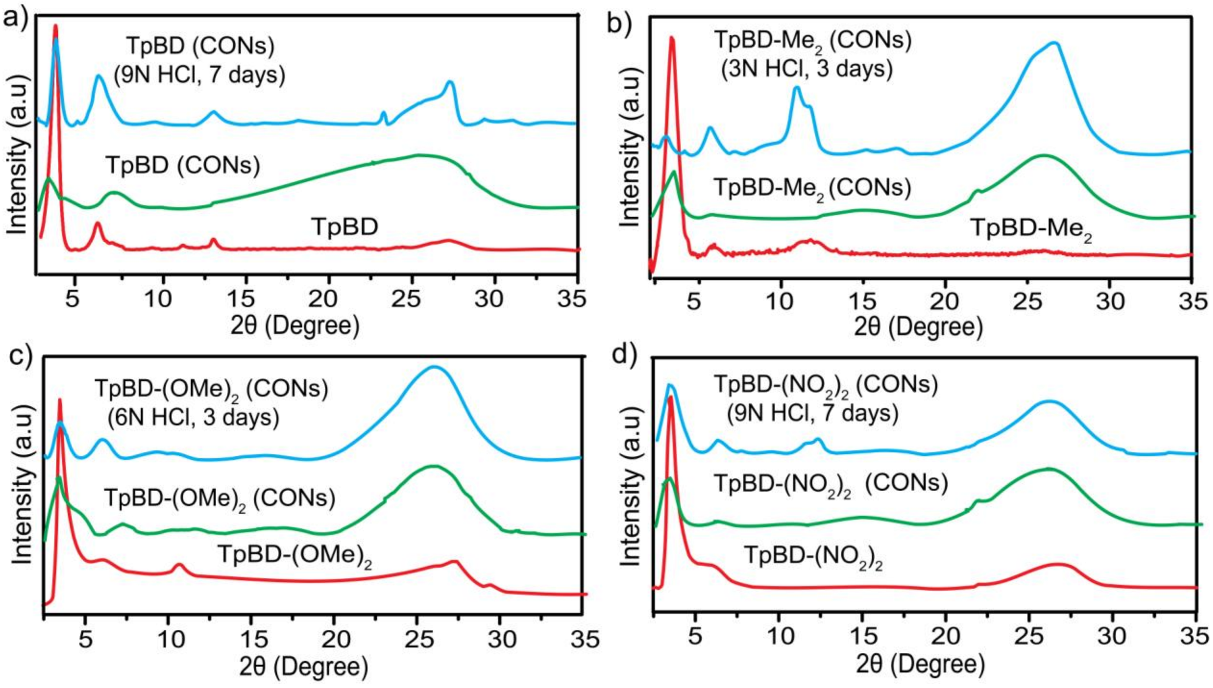

Figure 2.23: *PXRD patterns of as-synthesized* ***TpBD****-series COFs (red), corresponding delaminated COFs (CONs) (green), and acid-treated CONs (cyan).*

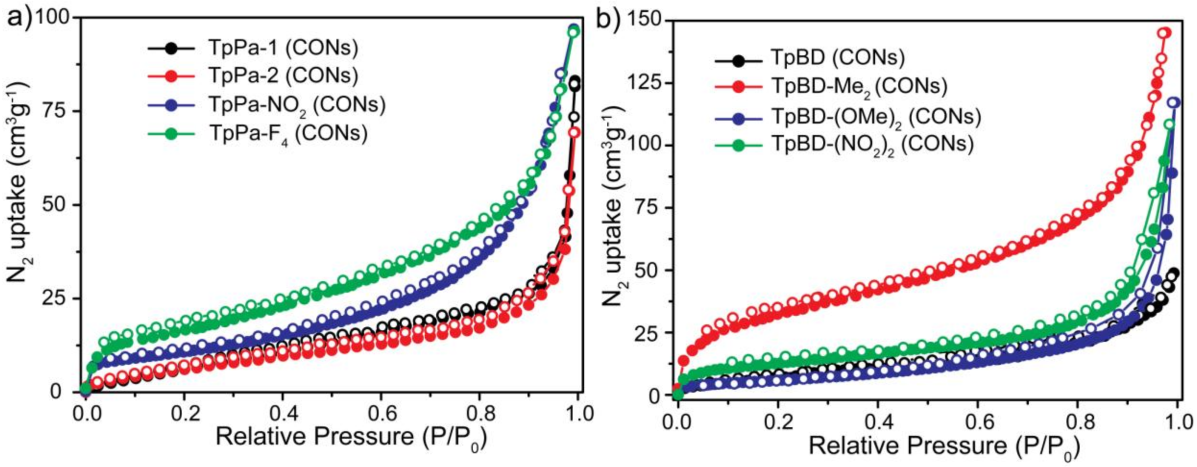

Figure 2.24: *N_2 adsorption of (a) TpPa series CONs [**TpPa-1** (black), **TpPa-2** (red), **TpPa-NO$_2$** (blue), **TpPa-F$_4$** (green)] and (b) TpBD series CONs [**TpBD** (black), **TpBD-Me$_2$** (red), **TpBD-(OMe)$_2$** (blue), **TpBD-(NO$_2$)$_2$** (green)].*

However, a decrease in intensity of the first peak (100 plane) and the broadening of the last peak (001 plane) has been observed, which is the only difference between the PXRD of the COFs and the CONs (Figure 2.22 and Figure 2.23). This could be due to the random displacement of the 2D layers (delaminated) as the distributions of eclipsed pores get affected. As a result, the reflection corresponding to the 100 plane becomes weak. The broader peak at higher 2θ (~27°) is due to the lack of π-π stacking between the COF layers, which is strongly affected by the reduction of the number of stacked layers in these thin CONs. TGA was performed for all CONs to get the information about the thermal stability. Comparison of the TGA curves of CONs and COFs reported in this paper shows that they have almost similar decomposition profiles (Figure 2.9).

N_2 adsorption experiments have also been performed for these CONs to check the effect of surface area upon mechanical grinding. The isotherms obtained are type-I like as-synthesized COFs but the surface area decreases drastically (Figure 2.24). The exact reason for the lower surface area for these CONs is not fully clear to us, but we speculate that due to the mechanical delamination that results in thin layered structures, the long range pore structure gets hindered followed by only fewer depth pores accessible for N_2 sorption.

As far as the chemical stability is concerned, it has been found that these CONs retain their structural integrity throughout the delamination process and also remain stable in aqueous, acidic (3-9N HCl) and basic (3N NaOH) media like the parent COFs, which is confirmed by PXRD and IR analyses (Figure 2.25).

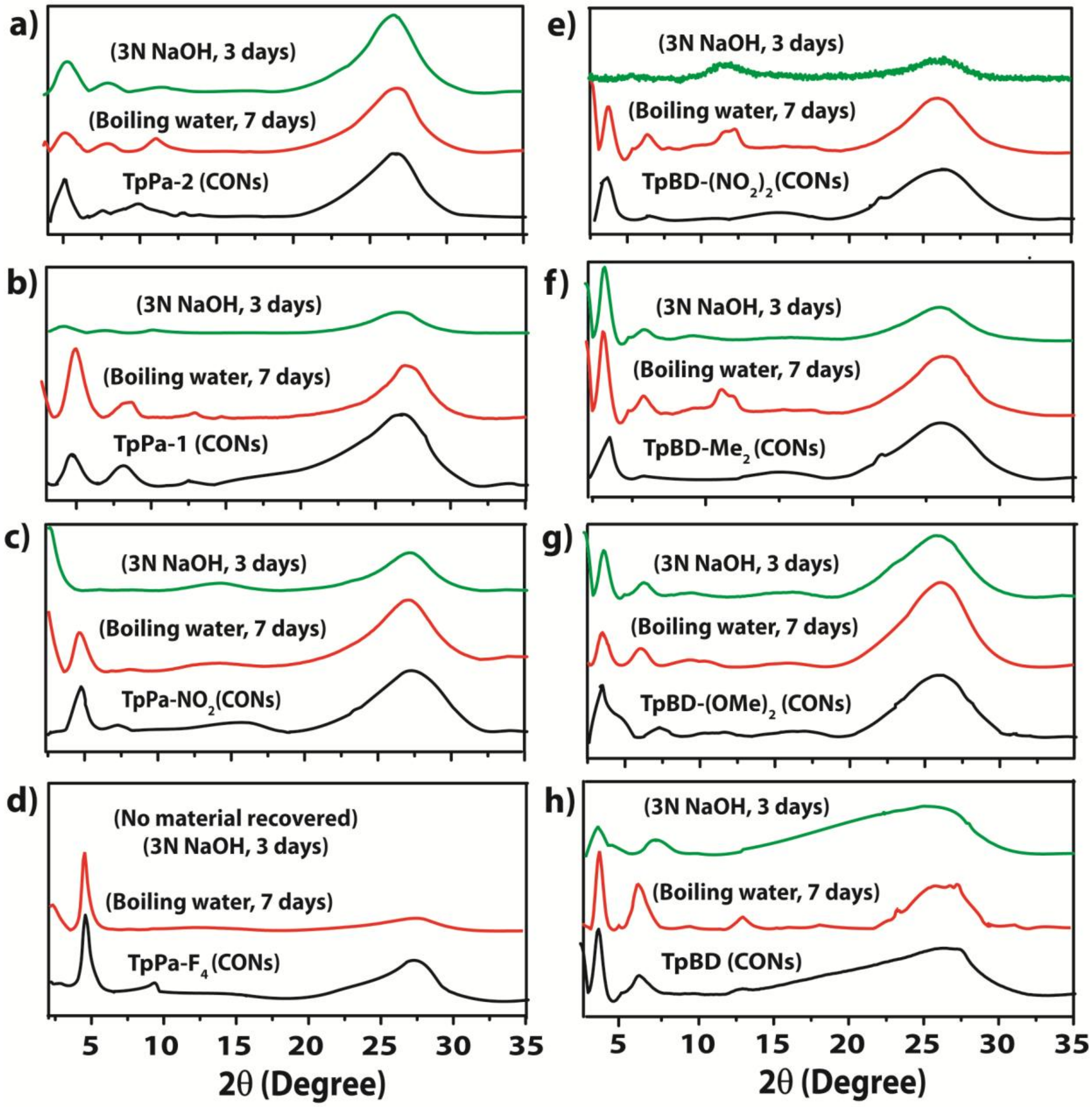

Figure 2.25: *PXRD profiles showing stability and instability of a)* ***TpPa-2*** *(CONs), b)* ***TpPa-1*** *(CONs), c)* ***TpPa-NO$_2$*** *(CONs), d)* ***TpPa-F$_4$*** *(CONs), e)* ***TpBD-(NO$_2$)$_2$*** *(CONs), f)* ***TpBD-Me$_2$*** *(CONs), g)* ***TpBD-(OMe)$_2$*** *(CONs), h)* ***TpBD (CONs)*** *after treatment in boiling water (100 ℃) for 7 days and in NaOH (3N) for 3 days. (Note:* ***TpPa-1*** *(CONs),* ***TpPa-F$_4$*** *(CONs),* ***TpPa-NO$_2$*** *(CONs),* ***TpBD-(NO$_2$)$_2$*** *(CONs) are not stable in base).*

2.2.7 *Chemical stability investigation*

In real life gas storage and separation application, chemical stability of the host framework material is highly important. Natural gases saturated water vapors, humid operating conditions in fuels cells, CO_2 capture from humidified biofuel stream are some of the practical examples where chemical stability plays a detrimental role in determining the performance of adsorbents. The porous framework adsorbent must be chemically stable to water and various acid impurities for their practical implementation in storage application. To investigate the chemical stability of these COFs in water, we have submerged 50 mg of COF materials in 10 mL of deionized water and allowed it to stand for 7 days under boiling condition (100 °C). After the mentioned period, we took the PXRD to confirm the crystallinity and found that all PXRD peak positions and the intensity retained even after 7 days, which indicates the stability of these COFs in boiling water for a period of 7 days or beyond (Figure 2.26). This water stability arises due to the irreversible nature of the enol-to-keto tautomerism, where the equilibrium is driven by the relative base strength of the imine nitrogen (C=N) over the phenolic oxygen (O–H) existing in the tris(N-salicylideneanilines) moiety. Previously, it has been observed that **TpPa-1** and **TpPa-2** were quite stable in acid (9N HCl) up to a period of 7 days. Similarly, other COFs of both the **TpPa** and **TpBD** series are also stable in acid (3-9N HCl), as well as in base. This has been confirmed by the identical peak positions and intensities in the PXRD profile collected after the acid treatment for 3-7 days. It is to be noted that **TpBD** and **TpBD-**$\mathbf{(NO_2)_2}$ is stable up to 7 days in 9N HCl like **TpPa-1** and **TpPa-2**, whereas the rest of the COFs are stable up to 3 days (Figure 2.26). The characteristic IR peaks of as-synthesized COFs do match very well with the acid treated COFs (Figure 2.27). In terms of base stability, **TpPa-2, TpBD, TpBD-**$\mathbf{Me_2}$ and **TpBD-**$\mathbf{(OMe)_2}$ are stable in 3N NaOH for 3 days whereas **TpPa-1, TpPa-**$\mathbf{NO_2}$**, TpPa-**$\mathbf{F_4}$ and **TpBD-**$\mathbf{(NO_2)_2}$ are not stable in the basic medium for even a day (Figure 2.26).

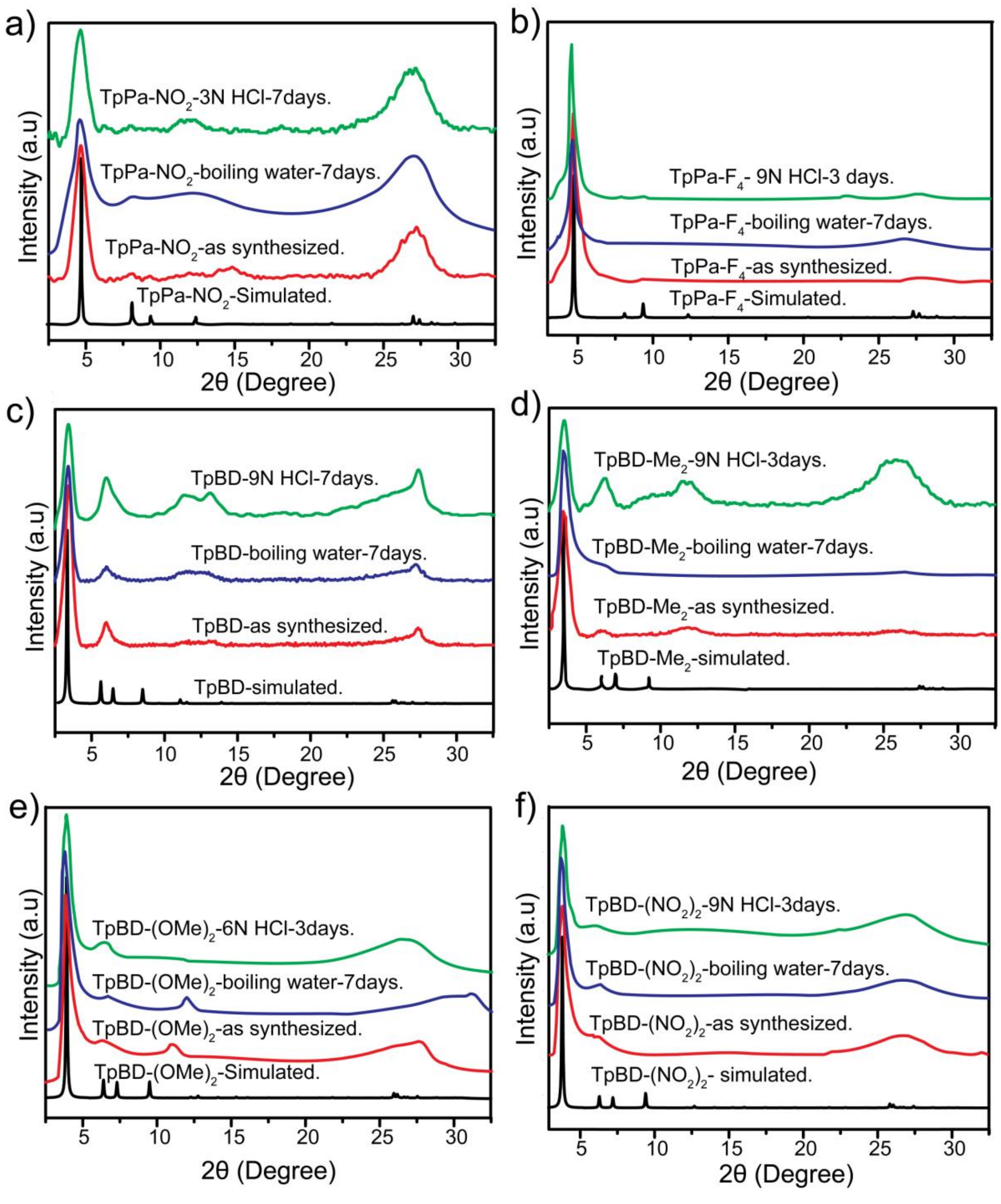

Figure 2.26: *PXRD spectra of a)* ***TpPa-NO_2****, b)* ***TpPa-F_4****, c)* ***TpBD****, d)* ***TpBD-Me_2****, e)* ***TpBD-$(OMe)_2$****, and f)* ***TpBD-$(NO_2)_2$*** *after treatment in boiling water (100 °C) for 7 days, acid (3-9N HCl) and base (3N NaOH) for 3 days. (Note:* ***TpPa-F_4****,* ***TpPa-NO_2****, and* ***TpBD-$(NO_2)_2$*** *are not stable in base (3N NaOH) for 3 days with respect to the crystallinity which has been confirmed by the PXRD analysis but the IR spectra does not show any drastic change in the peak positions or not showing the characteristic peaks correspond to the starting materials).*

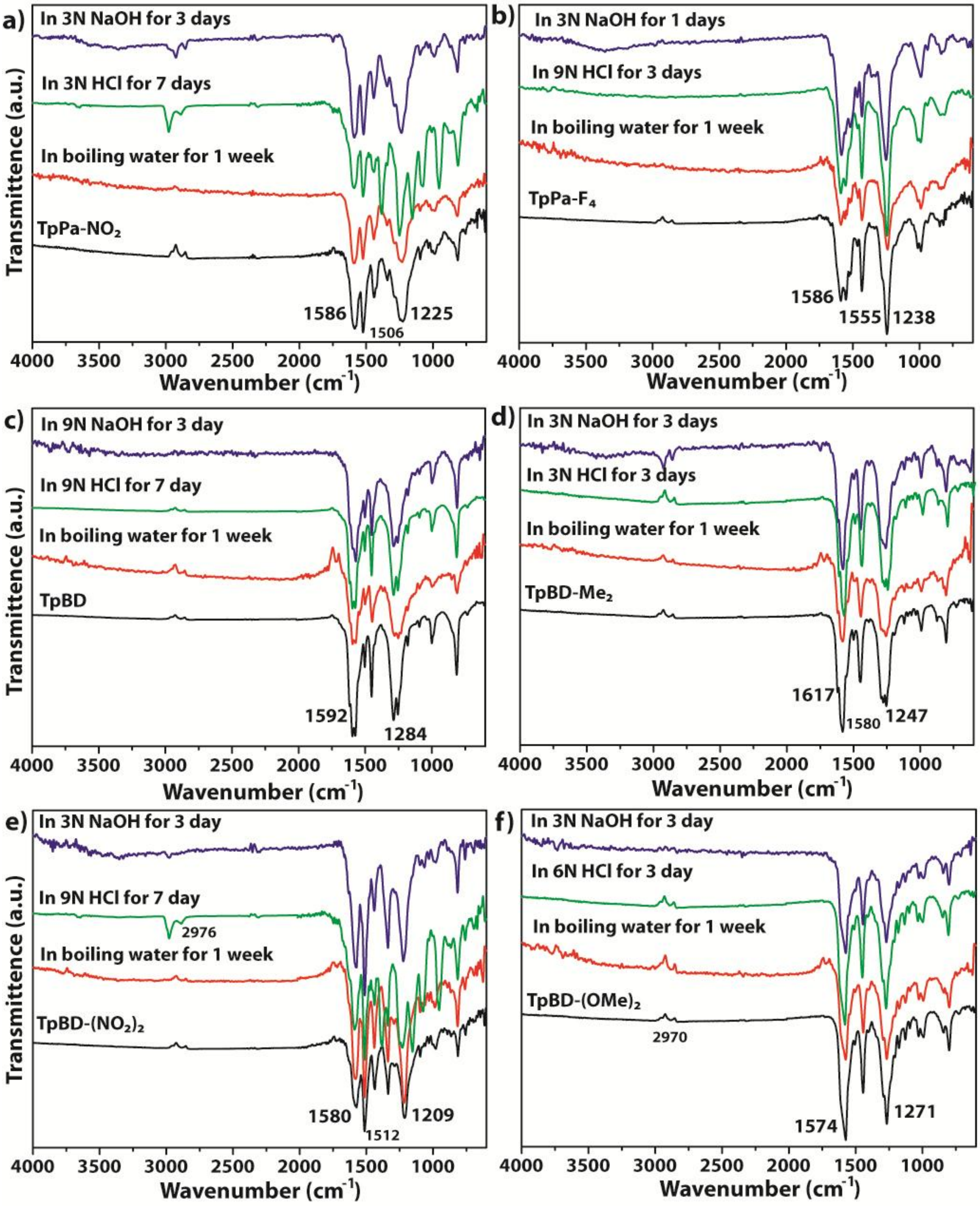

Figure 2.27: *FT-IR spectra showing stability and instability of a)* ***TpPa-NO_2****, b)* ***TpPa-F_4****, c)* ***TpBD****, d)* ***TpBD-Me_2****, e)* ***TpBD-$(NO_2)_2$****, and f)* ***TpBD-$(OMe)_2$*** *after treatment in boiling water (100 ℃) for 7 days, acid (3-9N HCl) and base (3N NaOH) for 3 days.*

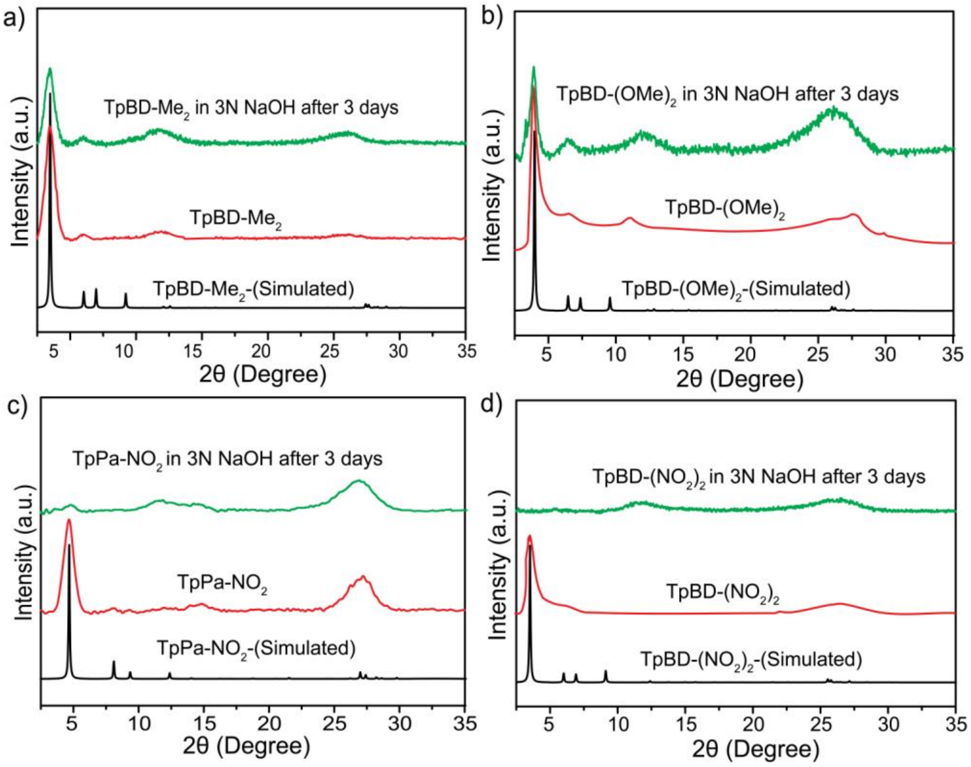

Figure 2.28: *PXRD of a)* ***TpBD-Me$_2$****, b)* ***TpBD-(OMe)$_2$****, c)* ***TpPa-(NO)$_2$*** *and d)* ***TpBD-(NO$_2$)$_2$*** *after treatment with NaOH (3N) for 3 day.*

TpBD-(Me)$_2$ and **TpBD-(OMe)$_2$** showing the base stability (3N NaOH) for 3 days whereas **TpBD-(NO$_2$)$_2$** and **TpPa-(NO)$_2$** are not stable in base as seen from the PXRD profiles (green) the first and intense peak disappears after dipping in base (3N NaOH) for 3 days.

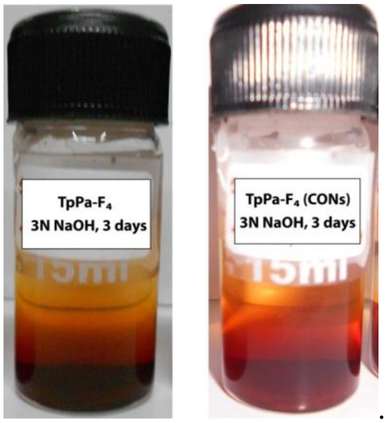

Figure 2.29: *Photographs of* ***TpPa-F$_4$*** *(left) and* ***TpPa-F$_4$*** *(CONs) (right) showing the instability in the basic (3N NaOH) media, which constantly going into the solution and after the end of 3 days almost no solid material left in the vial.*

2.3 Summary

In summary, we have, for the first time, synthesized a library of five chemically stable covalent organic frameworks, namely **TpPa–NO_2**, **TpPa–F_4**, **TpBD–$(NO_2)_2$**, **TpBD–Me_2**, **TpBD–$(OMe)_2$** along with previously reported three (**TpPa–1, TpPa–2** and **TpBD**) using the simple Schiff base reaction. By adopting different functionalized diamines, we could construct these COFs with variable pore apertures ranging from 15 to 24 Å. These COFs are crystalline, porous and exceptionally stable in aqueous, acidic as well as in basic media. The synthesized COFs (all eight) were successfully delaminated by using a simple, safe and environmental-friendly mechanical grinding route, leading to their transformation into thin layered CONs. These CONs were seemed to have graphene like layered morphology (exfoliated layers), unlike parent COFs. We believe that the stability of these COF layers is the main reason for this delamination. Since these individual layers with intrinsic chemical stability are stacked on top of each other with π–π stacking interactions, a mild mechanical force easily delaminates the layers from each other. As mechanical grinding is a scalable and energy efficient method compared to other existing methods like ultrasonication, CVD and layer growth, we believe that this 'top-down' strategy will provide a cost effective and scalable approach for the preparation of novel bulk 2D layered materials in the near future. Also, the observed 2D layered structures of these CONs have the potential to act as a graphene like supportive material for a wide variety of energy or imaging applications.

2.4 Experimental Procedures

2.4.1 *Materials*

Triformylphloroglucinol was prepared from Phloroglucinol using literature procedure [2.19]. All other reagents and solvents were commercially available and used as received.

2.4.2 *Synthesis of 2,4,6-tris((phenylamino)methylene)cyclohexane-1,3,5-trione (Reference compound)*

The reference compound was synthesized by the reaction between 1,3,5-triformylphloroglucinol (0.163 g, 0.8 mmol) and aniline (0.500 g, 5.4 mmol) in 70 mL ethanol under refluxing condition for one day. After this time period, the heating was stopped and the solution was allowed to reach the RT. The product gets precipitated after cooling was then separated by filtration. After this, the powders were thoroughly washed with ethanol and allowed to dry under vacuum (0.210 g, 82% yield).

^{1}H NMR (300 MHz, $CDCl_3$): δ 13.0-13.4 (m, NH), 8.90 (d, HC-N), 8.77 (d, CH), 8.75 (d, CH), 7.44-7.17 (m, Ph) ppm.

IR (powder, cm^{-1}): 1616 (s), 1581, 1553, 1465, 1444, 1340, 1287, 1236, 1041.

2.4.3 *General methods for characterization*

***(a) Powder X-Ray Diffraction (PXRD)*:** The PXRD patterns were collected on a Phillips PANalytical diffractometer on a Cu Kα radiation (λ = 1.5406 Å), with a scan speed of 2° min^{-1}. The tube amperage and voltage were set at 50 mA and 40 kV respectively. The sample plate containing the COF powders was scanned between 2 and 50° 2θ (step size of 0.02°).

***(b) Thermogravimetric Analysis (TGA)*:** TGA was performed on an SDT Q 600 TG-DTA analyzer instrument. Approximately 5 mg of the sample was added to an aluminum crucible and heated from 25 to 800 °C under an N_2 atmosphere (heating rate of 10 °C min^{-1}).

***(d) IR Spectroscopy*:** The Fourier transform (FT) infrared spectra of the MOFs were taken on a *PERKIN ELMER FT-IR SPECTRUM* (Nicolet) spectrometer. KBr samples (2 mg in 20 mg of KBr) were prepared and 10 scans were collected at 4 cm^{-1} resolution for each sample. The spectra were measured over the range of 4000-600 cm^{-1}.

***(f) Gas Adsorption*:** The gas adsorption experiments for the activated COF powders were performed on the Autosorb-1 automatic volumetric instrument (Quantachrome).

COF powder activation procedure: Approximately 50 mg of the COF powders were immersed in dry acetone at room temperature for 48 h. After this time period, the solvent was removed and the COF powders were evacuated under vacuum at room temperature for 24 h. Then the temperature was raised to 150 °C and evacuation continued for 48 h. Finally, the activated samples are treated for gas adsorption (H_2, N_2, and CO_2).

***(g) Water adsorption measurements*:** Low-pressure volumetric water adsorption measurements were performed at 293K, with pressure ranging from 0 to 0.9 [relative pressure (P/P_o)] on a Quantachrome Autosorb-iQ-MP automatic volumetric instrument.

2.4.4 Structure Modeling of COFs

Atomic positions and cell sizes of modeled COF layers were optimized using Self-Consistent Charge Density Functional Tight-Binding (SCC-DFTB) Method. Stacking of layers is affected by the Coulomb repulsion between the partial atomic charges in adjacent layers. Hence, we performed Mulliken population analysis for the charges. The adjacent layers were shifted with respect to each other in different directions in order to avoid Coulomb repulsion from charges alike. Several possibilities were considered, however, the best was taken from a comparison of simulated PXRD pattern with the experimental. Interlayer separation was also determined from the comparison of PXRD patterns. Refinements of PXRD pattern were done using Reflex module of the Material studio.

NOTE: The results of this chapter have already been published in *J. Am. Chem. Soc.***, 2013,** *135,* 17853. with the title: "*Chemically Stable Multilayered Covalent Organic Nanosheets from Covalent Organic Frameworks via Mechanical Delamination*" respectively. These publications were the results of the collaboration among the group of Dr. Rahul Banerjee and his students Suman Chandra, Sharath Kandambeth and Bishnu P. Biswal along with Shrikant M. Kunjir, Minakshi Chaudhary from National Chemical Laboratory, Pune, India; Dr. Thomas Heine and his students Binit Lukose from Jacobs University, Germany; Dr. Ravichandar Babarao from CSIRO, Australia. Apart from computational study major works contributed by Suman Chandra.

CHAPTER 3

Rational Design and Synthesis of Covalent Organic Frameworks for Proton Conduction

Abstract: *In this chapter, we have synthesized two new chemically stable functional crystalline COFs* ***(Tp-Azo*** *and* ***Tp-Stb****) by using the Schiff base reaction between triformylphloroglucinol (****Tp)*** *and 4,4'-azodianiline (****Azo****) or 4,4'-diaminostilbene (****Stb****), respectively. Both COFs show the expected keto-enamine form, and high stability towards boiling water, strong acidic and basic media.* H_3PO_4 *doping in* ***Tp-Azo*** *leads to immobilization of the acid within the porous framework, which facilitates proton conduction in both the hydrous (*$\sigma=9.9\times10^{-4}$ *Scm*$^{-1}$*) and anhydrous state (*$\sigma=6.7\times10^{-5}$ *Scm*$^{-1}$*). This report constitutes the first time emergence of COFs as proton conducting materials.*

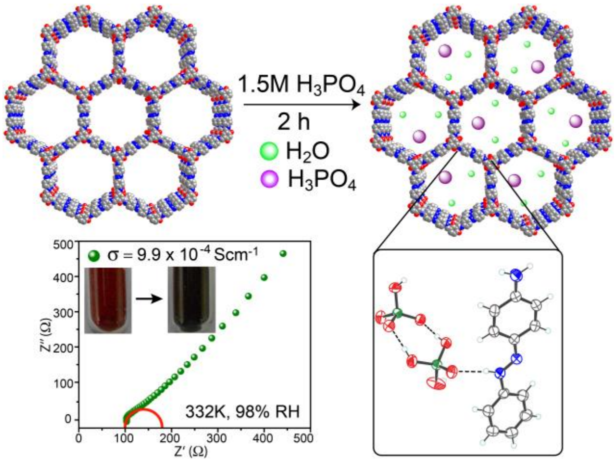

3.1 Introduction

The increasing demands of energy due to the rapid urbanization, population growth, and increasing number of industry along with the depletion of fossil fuel with their huge pollution effect to the environment [3.1] initiate researcher to develop alternative sustainable and renewable energy sources like solar, wind, tidal, geothermal, nuclear, electrochemical etc [3.2]. But most of the naturally available sustainable energy sources are intermittent in nature and therefore we cannot be fully dependent on these sources [3.3]. On the other hand, electrochemical energy is portable and can be used for next generation device fabrication. Electrochemical energy device converted chemical energy into electric energy and vice versa. Fuel cell, Li ion battery, supercapacitor, Zn-air battery, water electrolyzer etc. are the example of some electrochemical devices [3.4]. Among all the electrochemical energy sources, fuel cell considers to be a better substitute to the fossil fuel based energy devices due to its high energy conversion efficiency, environment-friendly, easy and safe operation [3.5]. In general, a fuel cell consists of three components i.e. cathode, anode and an ion conducting solid electrolyte membrane to separate them [3.5e].

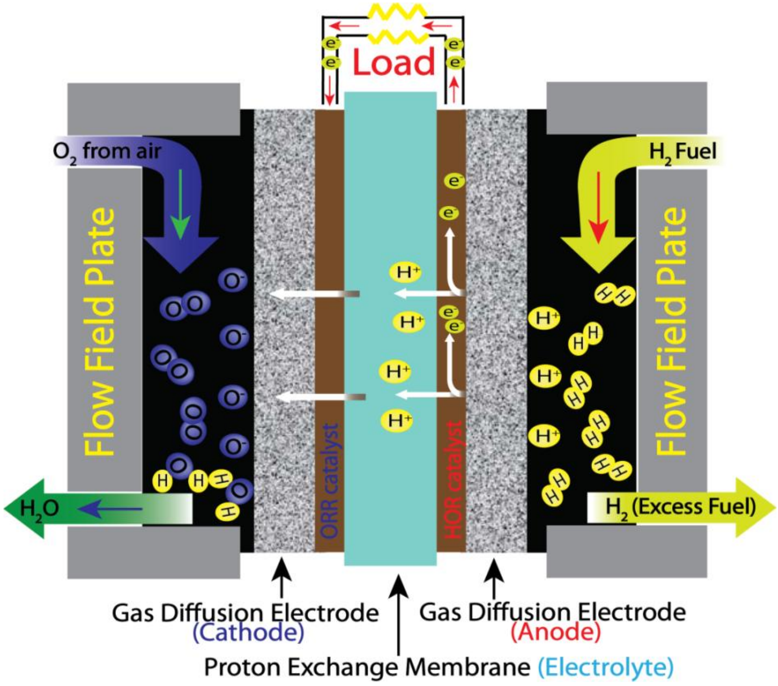

Figure 3.1: *Schematic presentation of the components of PEMFC and its working principle.*

Under the acidic condition, hydrogen gets oxidized to H^+ in anode (Equation 3.1) and transported to the cathode through proton exchange membrane where as oxygen reduction occurs in the cathode (Equation 3.2) and the reduced oxygen reacts with transported H^+ to form neutral water. Furthermore, in alkaline condition similar kind of reaction occurs in anode (Equation 3.4) where as in cathode oxygen get reduced to OH^- (Equation 3.5) and transported to anode through OH^- conduction membrane.

Acidic Condition

$$\textbf{At anode:}\quad 2H_2 \longrightarrow 4H^+ + 4e^- \qquad E^o = 0.00\ V \tag{3.1}$$

$$\textbf{At cathode:}\quad O_2 + 4H^+ + 4e^- \longrightarrow 2H_2O \qquad E^o = -1.23\ V \tag{3.2}$$

$$\textbf{Overall:}\quad H_2 + O_2 \longrightarrow 2H_2O \qquad E^o = 1.23\ V \tag{3.3}$$

Alkaline Condition

$$\textbf{At anode:}\quad H_2 + 2OH^- \longrightarrow 2H_2O + 2e^- \qquad E^o = 0.83\ V \tag{3.4}$$

$$\textbf{At cathode:}\quad ½\, O_2 + 2H_2O + 2e^- \longrightarrow 2OH^- \qquad E^o = 0.40\ V \tag{3.5}$$

$$\textbf{Overall:}\quad H_2 + ½\, O_2 \longrightarrow 2H_2O \qquad E^o = 1.23\ V \tag{3.6}$$

In an H_2 fuel cell, also known as proton exchange membrane fuel cell (PEMFC), hydrogen and oxygen or air were used as fuel along with a proton exchange membrane (PEM) which conducts proton (H^+) from anode to cathode [3.6]. For a good proton exchange membrane, the materials should possess high proton (H^+) conductivity with no electron conductivity and it should be nonporous to prevent the mixing of H_2 and O_2 or air. Besides these basic criteria of the proton exchange membranes, it should also be solid, flexible, thermochemically stable, cheap and compatible to assemble with the other parts of the fuel cell. Depending on the operating temperature in a fuel cell, it divided into two categories: i) Low temperature (LT) fuel cell and ii) High temperature (HT) fuel cell. There are many advantages of high temperature (HT) fuel cell, for example, i) at high temperature the kinetics of the electrode reaction is very fast; ii) the CO poising of the Pt catalyst is minimized at high temperature, which improves the reactivity and durability of the catalyst and iii) there is no need of extra water management system. Nafion, a state of the art membrane consist of sulfonated fluoropolymer, widely used for low temperature (<80 ºC) proton exchange membrane in hydrogen fuel cell [3.7]. But its high cost, low conductivity at high temperature (> 100 ˚C), the requirement of water management system forced the scientist to develop materials which will show good proton conductivity at high temperature (like phosphoric acid doped PBI membrane). On this regard, designing of stable reticular materials (MOF and COF) to control the functionality and pore size for maximizing the proton conductivity is a challenge for researchers. Although many MOFs and their composites have been used for proton conduction [3.8], their high gravimetric weight, low chemical stability and difficult to make membrane motivate scientists to develop stable organic crystalline porous materials to overcome these limitations. In this aspect, covalent organic frameworks have many advantages like tunable pore size and functionalities, high surface area and pore volumes, low density, easy to fabricate membrane [3.9] make scientists believed that this kind of reticular materials can be used for proton conduction. But, their low chemical stability (both acidic and basic medium) hindered its use in proton conduction. Here, for the first time, we solve this problem by synthesizing chemically stable β-keto-enamine azo based (-N=N-) **Tp-Azo** COF, where azo groups act as Lewis basic site to load phosphoric acid in its pore through cation-anion interactions and hydrogen bonds [3.10]. The phosphoric acid loaded Tp-Azo COF (**H_3PO_4@Tp-Azo**) has been tested for proton conduction like phosphoric acid loaded PBI membrane.

3.2 COFs as Polymer Electrolyte Membrane

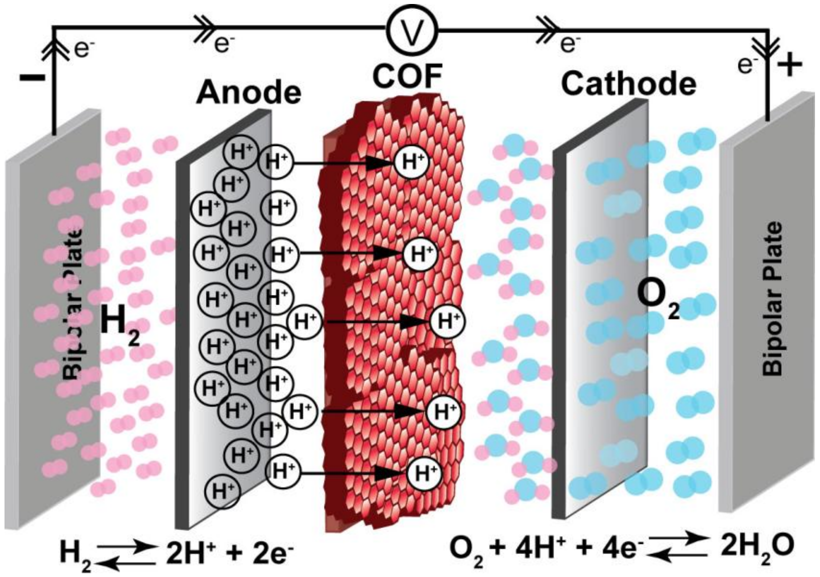

Figure 3.2: *Schematic presentation of COF as proton exchange membrane in PEMFC.*

As discuss earlier, covalent organic frameworks (COFs) are two or three-dimensional crystalline materials made by linking lighter elements (e.g. B, C, N, O) *via* covalent bonds in a periodic manner [3.9]. COFs are synthesized and subsequently crystallized by means of reversible covalent bond formation reactions like boronic acid trimerization, boronate ester formation, and the Schiff base reaction. Structurally, COFs are closely related to metal-organic frameworks (MOFs), where coordination bonds link metal ions and organic struts. Although COFs have shown excellent promise as semiconductive devices [3.11], sensors [3.12], and in gas storage and separation [3.13]; proton conductivity in COFs is still unexplored. In recent years, proton conducting materials have spurred tremendous interest among researchers due to their application in fuel cells, sensors and electronic devices [3.14]. Nafion based proton conducting membranes are considered as the benchmark in this field. Such membranes exhibit high proton conductivity (ca. 10^{-1} Scm^{-1}) at moderate temperature (60-80 °C) under high relative humidity (98% RH) [3.7]. However, the high cost of perfluorinated membranes with less efficiency at fuel cell operating temperatures (ca. 120 ˚C) has always encouraged researchers to search for alternative materials. In this context, MOFs with loaded carrier molecules (e.g. imidazole, triazole, mineral acids) have been envisaged for high temperature proton conduction applications [3.8(c-g)]. However, MOFs suffer poor hydrolytic stability with very low pH tolerance of the occluded guests. As a result, rupture of the coordination bonds and the framework backbone limits its applicability in fuel cell operating conditions. In addition, the high gravimetric weight of MOF, difficulty in forming compact membranes and instability at higher temperatures are major limitations for the future development of proton conducting materials. On the other hand, COFs have the advantages of low density, high thermal stability, pre-required functionality and membrane processability like polymers. These features ensure their sustainability in a harsh fuel cell operating condition and the high degree of internal ordering as in MOFs facilitates loading and transport of proton conducting substrates. Despite these promising features, COFs have never been tested for proton conduction due to their instability [3.15] in ambient humidity conditions.

We have recently been able to overcome this stability problem and developed a general strategy for synthesizing COFs that showcase the stability towards strong acid (9N HCl) and moderately strong base (6N NaOH), even upon isoreticulation and functionalization [3.16]. Moreover, the COF backbone can be suitably functionalized, which can further enhance the interaction with carrier molecules to aid proton conduction pathways. H_3PO_4 loaded PBI based membranes are well documented in the literature for high proton conductivity (ca. 10^{-2} Scm^{-1}) at fuel cell operating temperatures [3.17]. Other than the benzimidazole group, the azo group can also play a vital role in stabilizing H_3PO_4 [3.18]. The crystal structure of the protonated azobenzene unit **[**Ref code: WEVXAX] [3.18a] with the hydrogen bonded $H_2PO_4^-$ anion hints at the potential of azo functionalized COFs to act as proton conducting materials. The extension of the azobenzene monomeric unit in higher dimensions to form a porous COF with a 1D channel may facilitate unidirectional proton transport, while crystallinity and chemical stability may be a boon for providing mechanistic insight. In this regard, we present an azo functionalized COF (**Tp-Azo**) made by the Schiff base reaction between 1,3,5-triformylphloroglucinol (**Tp)** and 4,4'-azodianiline (**Azo**). This COF exhibits excellent structural stability, porosity, and crystallinity even after acid treatment. As mentioned before, we conceived this idea of H_3PO_4 loaded azo functionalized COF (**PA@Tp-Azo**) being a good proton conductor after noticing the crystal structure of H_3PO_4 treated 4-aminoazobenzene, where H_3PO_4 finds an anchoring site at the azo center by protonating it, while the $H_2PO_4^-$ anions are stabilized *via* hydrogen bonds [3.18a]. **PA@Tp-Azo** shows proton conductivity in both humid and anhydrous conditions (9.9×10^{-4} and 6.7×10^{-5} Scm^{-1}, respectively). In order to elucidate the structure-property relationship, we have also synthesized the non-azo counterpart, i.e. stilbene functionalized COF (**Tp-Stb**) which shows less stability, crystallinity, porosity and much less proton conductivity than **Tp-Azo** because of the non-availability of anchoring site.

3.3 Preparative methods and characterization

3.3.1 *Synthesis of COFs*

The synthesis of **Tp-Azo** and **Tp-Stb** were done by reacting **Tp** (63 mg, 0.3 mmol) with **Azo** (96 mg, 0.45 mmol) or **Stb** (128 mg, 0.45 mmol) using (1:1) dimethylacetamide and o-dichlorobenzene as solvent (3 mL) (Figure 3.3). The reactants were first dispersed by ultrasonication for 10 minutes and then degassed through three freeze–pump–thaw cycles. The tubes were then vacuum sealed, and placed in isotherm oven for 3 days at 120 °C. Finally, the material was filtered out and washed with acetone and dried under vacuum at 150 °C for 12 h.

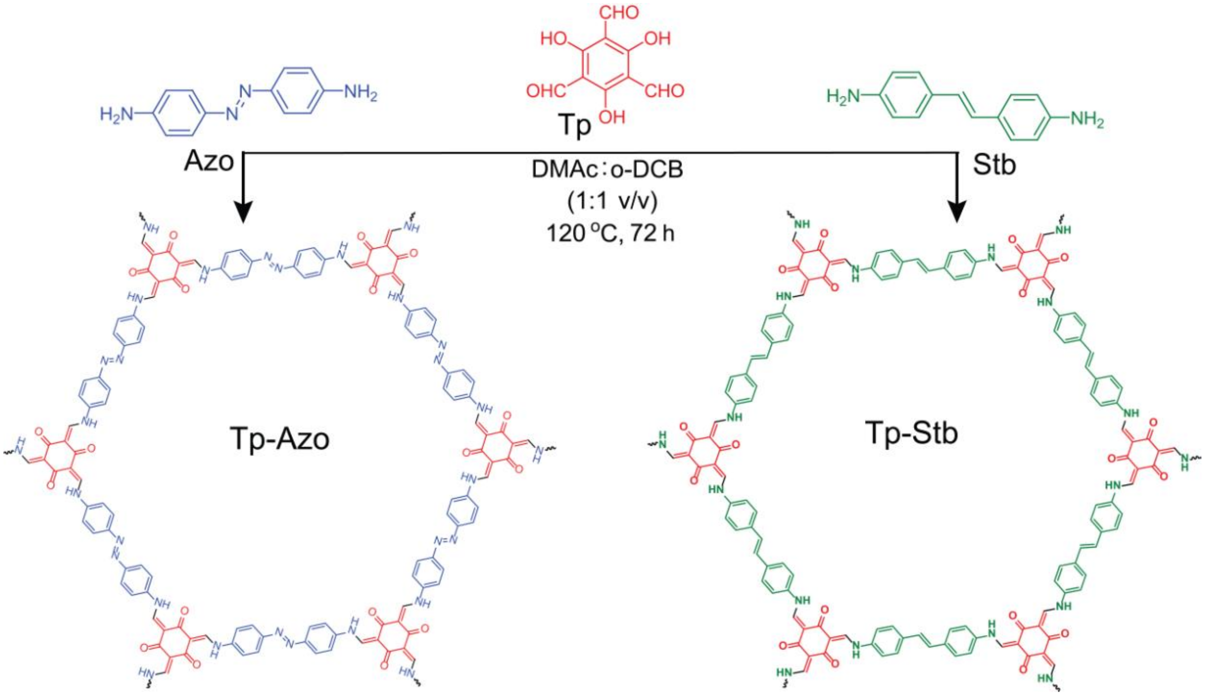

***Figure 3.3**: Synthesis of **Tp-Azo** and **Tp-Stb** via Schiff base condensation reaction.*

3.3.2 *Structural simulation*

The PXRD patterns of **Tp-Azo** indicate an intense peak at 2θ = 3.2°, which corresponds to 100 plane reflections (Figure 3.4a), with minor peaks at 5.5, 6.4, 8.4 and 27° (001 plane). The π-π stacking distance between COF layers was calculated to be 3.3 Å from the *d* spacing between 001 planes. On the other hand, **Tp-Stb** exhibits an intense peak at 2θ = 3.2° followed by a broad peak at 5.5°. In order to elucidate the structure of these COFs and to calculate the unit cell parameters, a possible 2D model was built with an eclipsed structure in the hexagonal space group (*P*6/*m*) and a staggered structure in the *P1* space group, by using the software Crystal 09 [3.19]. Several stacking possibilities were considered for reasons reported in the literature [3.20]. The experimental PXRD patterns are agreeable with the simulated patterns of eclipsed stacking models (Figure 3.4). Hence we propose structures having hexagonal space group (*P*6/*m*) for **Tp-Azo** and **Tp-Stb** by comparing the experimental and simulated PXRD patterns. In order to find out the unit cell parameters, Pawley refinements were done for both the COFs using Reflex module of Material studio [3.21]. The unit cell value was found to be ($a = b = 31.5$ Å, $c = 3.3$ Å) for **Tp-Azo** and ($a = b = 30.500$ Å, $c = 3.49$ Å) for **Tp-Stb**. The intensity ratio of the 1st and 2nd peak in the eclipsed form matches with the PXRD of **Tp-Stb**. The energy calculation of both eclipsed and staggered forms of **Tp-Stb** also suggests an eclipsed stacking model with lower energy. The fractional coordinates of **Tp-Azo** and **Tp-Stb** are given in Table 3.1 and 3.2 respectively.

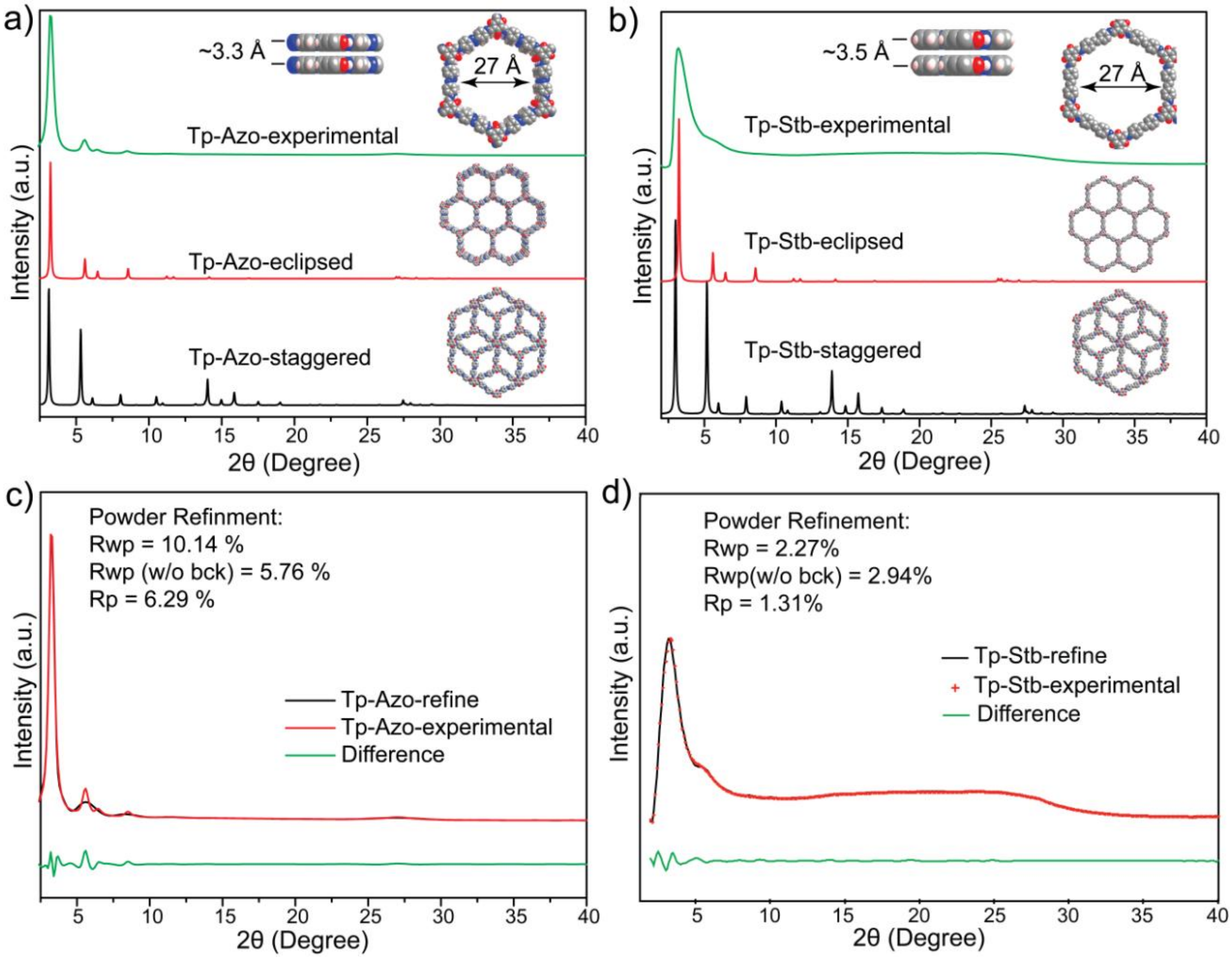

***Figure 3.4**: PXRD spectra of as-synthesized (green) compared with the eclipsed (red) and staggered (black) stacking models for (a) **Tp-Azo** and (b)**Tp-Stb**. Experimental (red) PXRD profiles of (c) **Tp-Azo** and (d) **Tp-Stb** compared with refined (black) with an eclipsed arrangement; difference plot is given in (green).*

Table 3.1: Fractional atomic coordinates for the unit cell of **Tp-Azo.**

	Tp-Azo Hexagonal; P 6/m a = b =31.5 Å, c=3.49 Å, α = 90, β = 90, γ = 120.		
O1	0.29695	0.57697	0
N2	0.38245	0.58505	0
C3	0.31382	0.61757	0
C4	0.39342	0.63145	0
C5	0.41468	0.5699	0
C6	0.46145	0.59947	0

C7	0.49111	0.58277	0
C8	0.47494	0.53664	0
C9	0.42853	0.50701	0
C10	0.39878	0.52354	0
C11	0.36359	0.64675	0
H12	0.42849	0.65656	0
H13	0.47589	0.63531	0
H14	0.34922	0.55946	0
H15	0.36308	0.50007	0
H16	0.52692	0.60571	0
H17	0.41558	0.4712	0
N1	0.50627	0.52081	1

Table 3.2: Fractional atomic coordinates for the unit cell of **Tp-Stb.**

	Tp-Stb Hexagonal; P 6/m; a = b= 30.5; c = 3.4919; α = β =90.0000; γ =120.0000.		
O1	0.29695	0.57697	0
N2	0.38245	0.58505	0
C3	0.31382	0.61757	0
C4	0.39342	0.63145	0
C5	0.41468	0.5699	0
C6	0.46145	0.59947	0
C7	0.49111	0.58277	0
C8	0.47494	0.53664	0
C9	0.42853	0.50701	0
C10	0.39878	0.52354	0
C11	0.36359	0.64675	0
H12	0.42849	0.65656	0
H13	0.47589	0.63531	0
H14	0.34922	0.55946	0
H15	0.36308	0.50007	0
H16	0.52692	0.60571	0
H17	0.41558	0.4712	0
C12	0.50627	0.52081	1

3.3.3 *Chemical characterization*

The FT-IR spectra of **Tp-Azo** and **Tp-Stb** indicate total consumption of starting materials due to the disappearance of the N–H stretching bands (3100-3300 cm^{-1}) of **Azo** or **Stb** and the carbonyl stretching bands (1639 cm^{-1}) of **Tp** (Figure 3.5a).

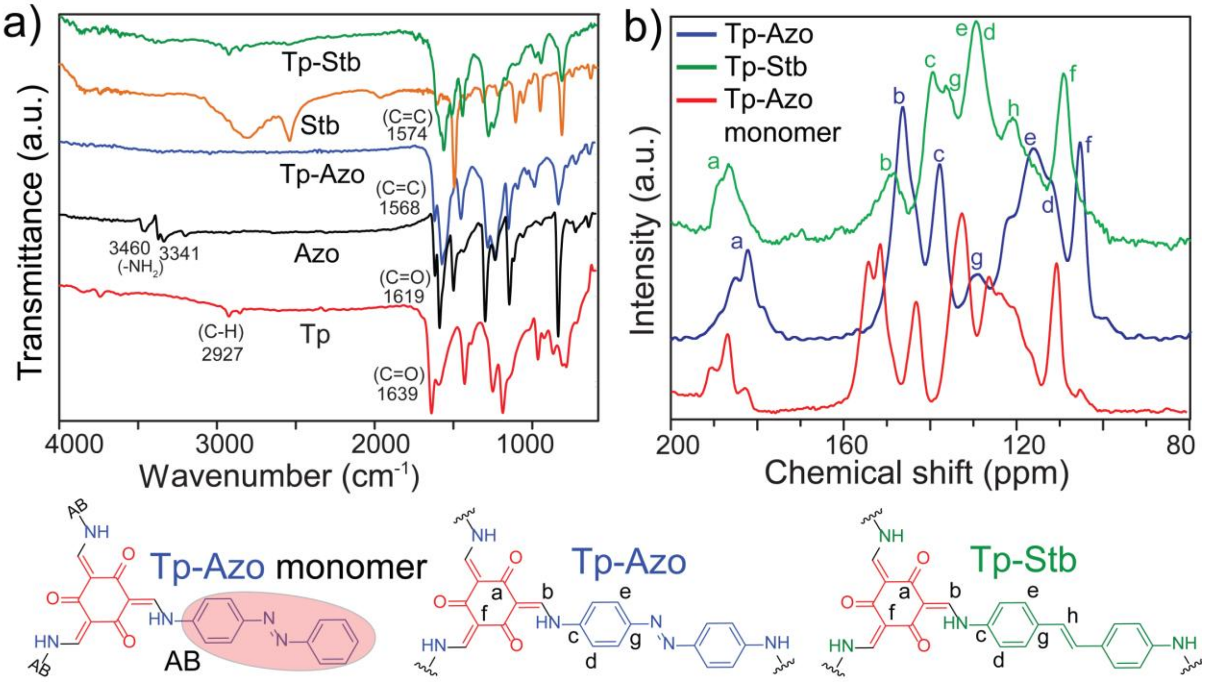

***Figure 3.5**: (a) FT-IR spectra of **Tp-Azo** and **Tp-Stb** compared with starting material **Tp**, **Azo** and **Stb**. (b) ^{13}C NMR comparison of **Tp-Azo** (blue), **Tp-Stb** (green) against the reference compound **Tp-Azo** monomer = 2,4,6-tris(((4-((E)-phenyldiazenyl)phenyl)amino)methylene)cyclohexane-1,3,5-trione (red).*

The strong peak at 1578 cm^{-1} arises due to the C=C stretching in keto-form similar to the FT-IR spectrum of the reference compound 2,4,6-tris((phenyldiazenyl)phenylamino-methylene)cyclohexane-1,3,5-trione. Most of the FT-IR peaks of **Tp-Azo** and **Tp-Stb** match well with that of the reference compound (Figure 3.5a). The C=O peaks (1619 cm^{-1}) of **Tp-Azo** and **Tp-Stb** get merged with the C=C stretching band (1582 cm^{-1}). The isolation of **Tp-Azo** and **Tp-Stb** as keto form was confirmed by ^{13}C CP-MAS solid state NMR. Both the COFs show carbonyl (C=O) carbon signals at δ=181 and 186 ppm for **Tp-Azo** and **Tp-Stb** respectively. In the starting material, the trialdehyde carbonyl (C=O) carbon resonates at a downfield position around δ=192 ppm. The absence of peak at δ=192 ppm in the ^{13}C CP-NMR spectrum also indicates the total consumption of the starting materials (Figure 3.5b). To investigate the protonation of the azo bond by phosphoric acid in **PA@Tp-Azo,** we have done ^{31}P CP-NMR, which shows two distinct peaks at δ -1.31 ppm and δ -14.3 ppm. The ^{31}P resonance peak at δ -1.31 ppm is attributed to the undissociated H_3PO_4 and the shoulder at δ -14.3 ppm corresponds to the $H_2PO_4^-$ anion, which indicates the protonation of the azo bond. However, in **PA@Tp-Stb**, only a single intense peak at δ -0.88 ppm, corresponding to undissociated H_3PO_4, has been observed and the peak at δ -14.3 ppm was absent. This explains the absence of the $H_2PO_4^-$ anion due to the lack of protonation sites in **Tp-Stb** (Figure 3.6a).

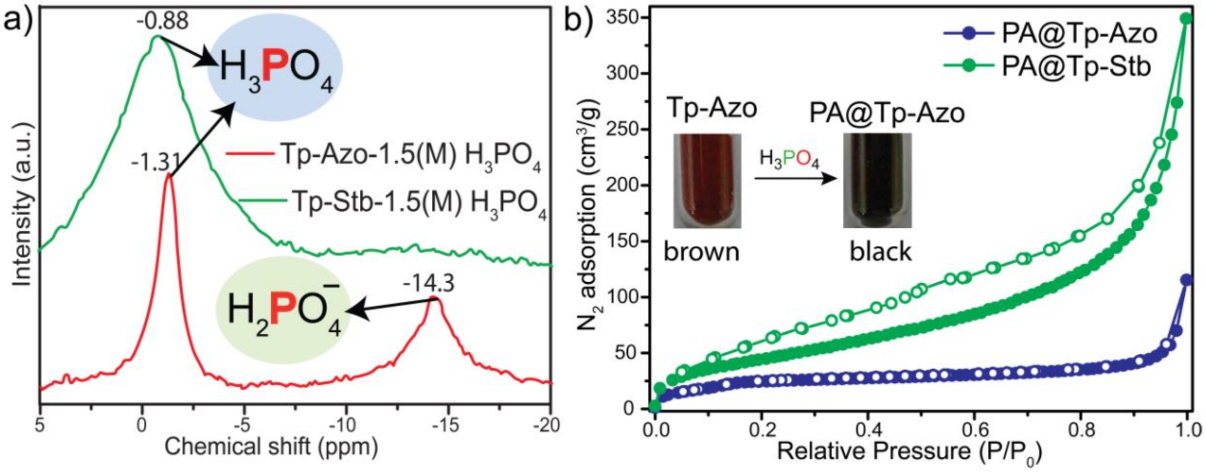

Figure 3.6: *(a) Comparison of solid state CP-MAS ^{31}P NMR spectra of phosphoric acid loaded **Tp-Azo** (**PA@Tp-Azo**) with phosphoric acid loaded Tp-Stb (**PA@Tp-Stb**). (b) N_2 adsorption isotherms of phosphoric acid loaded **Tp-Azo** (**PA@Tp-Azo**) (blue) and phosphoric acid loaded **Tp-Stb** (**PA@Tp-Stb**) (green).[Inset showing the colour change due to the protonation of azo-bond in **Tp-Azo** COF by phosphoric acid].*

SEM and TEM images showed that **Tp-Azo** and **Tp-Stb** crystallize with a flower like morphology with the aggregation of a large number of petals with an average length of 40-50 nm (Figure 3.7).

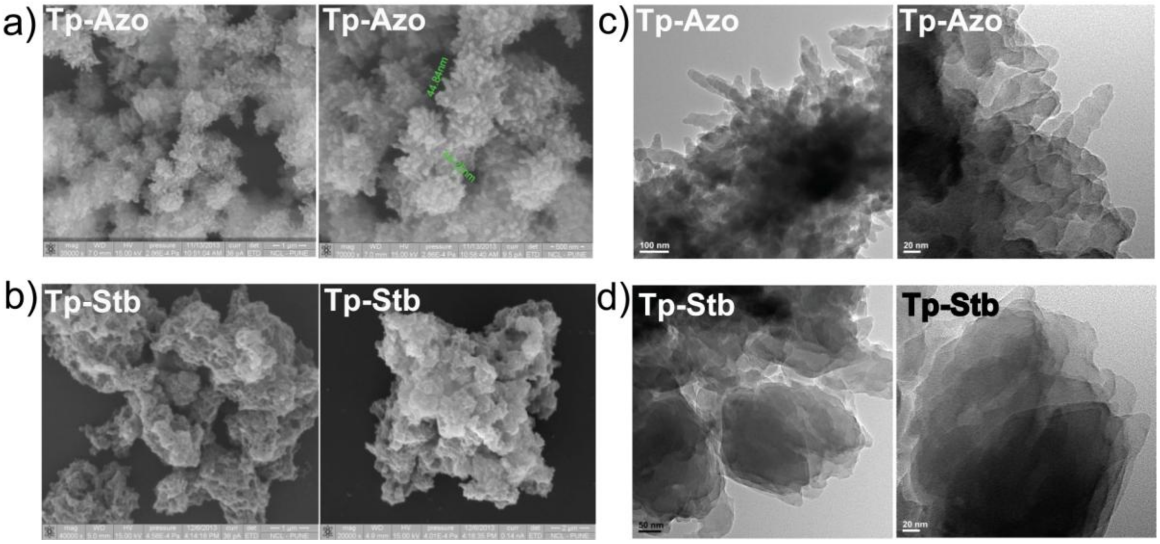

Figure 3.7: *SEM images of (a) **Tp-Azo** and (b) **Tp-Stb** respectively. TEM images of (c) **Tp-Azo** and (d) **Tp-Stb** respectively.*

Thermogravimetric analysis (TGA) of the activated **Tp-Azo** and **Tp-Stb** show thermal stability up to 350 °C, with a gradual weight loss of 50% after 360 °C due to the decomposition of the framework (Figure 3.8).

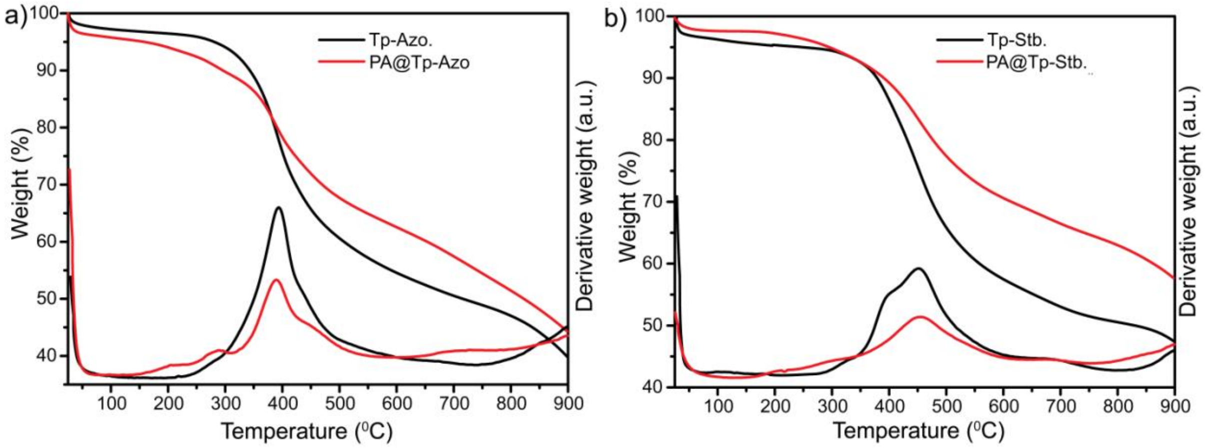

***Figure 3.8**: TGA data of activated COF (a) **Tp-Azo** (black) compared with **PA@Tp-Azo** (red) and (b) **Tp-Stb** (black) compared with **PA@Tp-Stb** (red) under N_2 atmosphere.[Inset showing the derivative plot].*

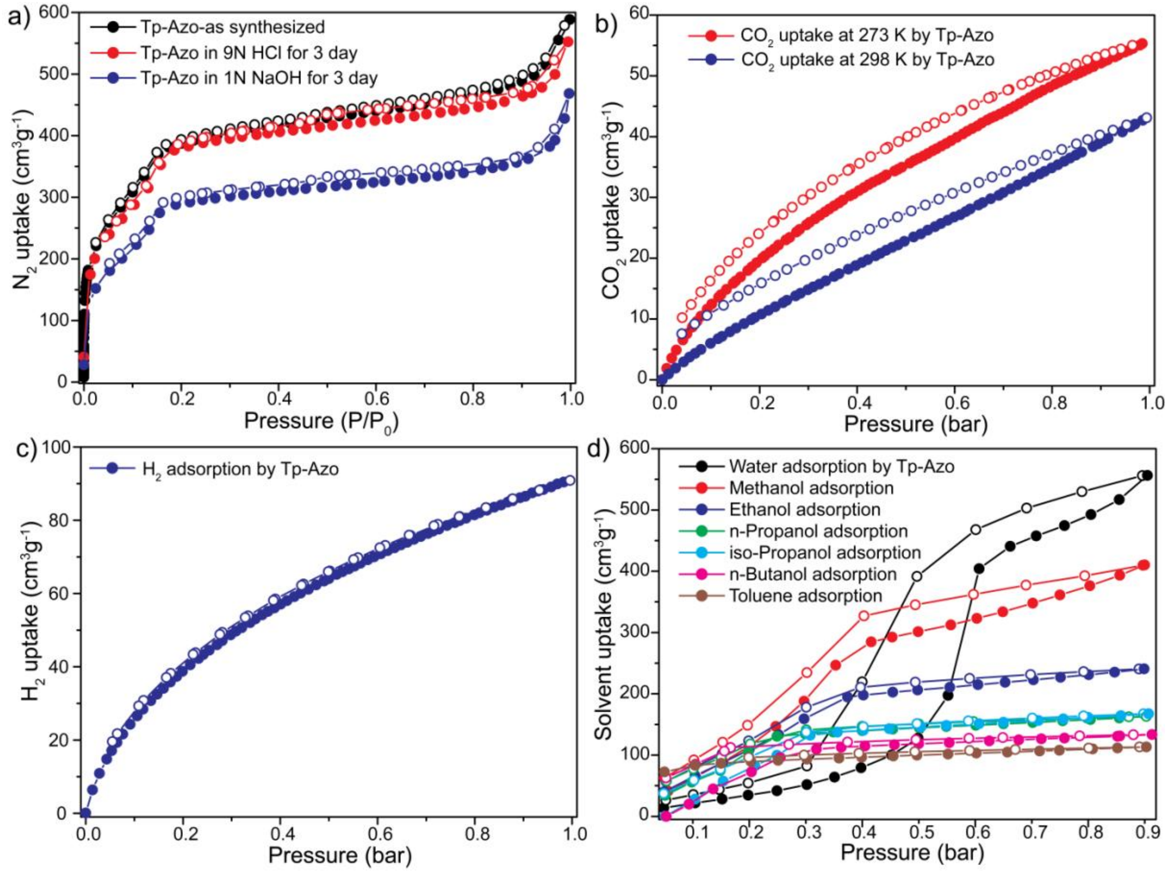

***Figure 3.9**: (a) N_2 adsorption of as-synthesized **Tp-Azo** (black), after 9(N) HCl treatment (red) and after 1(N) NaOH treatment. (b) CO_2 adsorption of **Tp-Azo** at 273 K (red) and 298 K (blue), (c) H_2 adsorption of **Tp-Azo**. (d) Vapor adsorption isotherm of **Tp-Azo**, water (black), methanol (red), ethanol (blue), n-propanol (green), iso-propanol (cyan), n-butanol (pink) and toluene (brown). The filled symbol corresponds to adsorption and empty symbols represent desorption isotherms.*

3.3.4 *Gas adsorption studies*

The permanent porosity of **Tp-Azo** and **Tp-Stb** were evaluated by the N_2 adsorption isotherm at 77 K, which showed a reversible type IV adsorption isotherm. The surface areas of the activated COFs, calculated using the BET model, were found to be 1328 and 422 m²/g for **Tp-Azo** and **Tp-Stb**, respectively (Figure 3.9). The lower surface area of **Tp-Stb** may be due to the poor crystallinity and not so uniform channels resulting from the lower solubility of **Stb** precursors in organic solvents. The pore size distribution of **Tp-Azo** and **Tp-Stb** shows a narrow distribution in the range 1.6–2.5 nm (Figure 3.10).

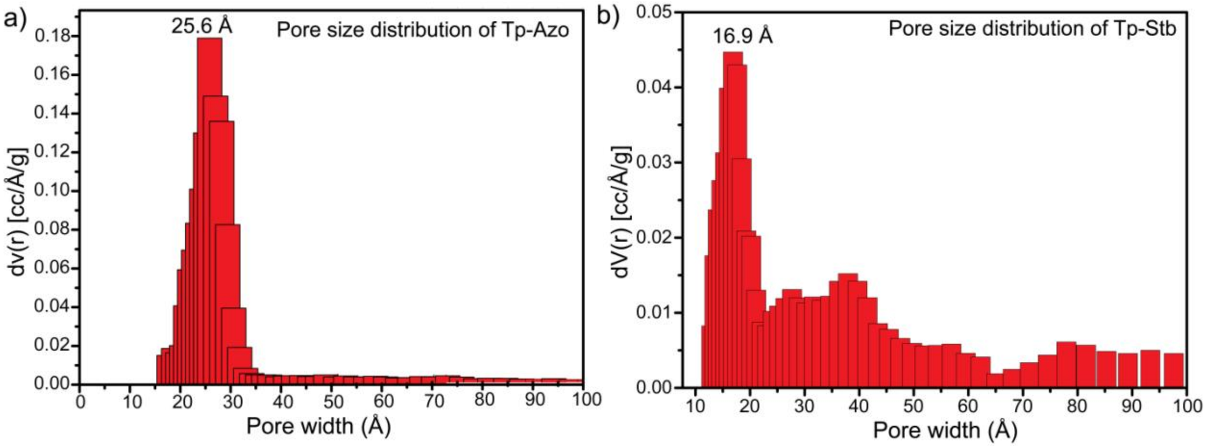

***Figure 3.10:** NLDFT Pore size distribution of (a) **Tp-Azo** and (b) **Tp-Stb**.*

3.3.5 *Chemical stability investigation*

The stability of **Tp-Azo** and **Tp-Stb** were assayed by immersing 50 mg of COFs in either 20 ml boiling water or standing in 20 ml strong mineral acids (9 N HCl/1.5 M H_3PO_4) and bases (3-6 N NaOH). Interestingly, both **Tp-Azo** and **Tp-Stb** remain stable, crystalline and porous while directly submerged in boiling water for several days (7 days), as verified by PXRD, FT-IR spectra and N_2 adsorption isotherm studies (Figure 3.11). They also exhibit strong acid (9 N HCl) stability with near retention of molecular crystallinity (Figure 3.11). However, base treated (3-6 N NaOH) COFs show moderate base stability with partial

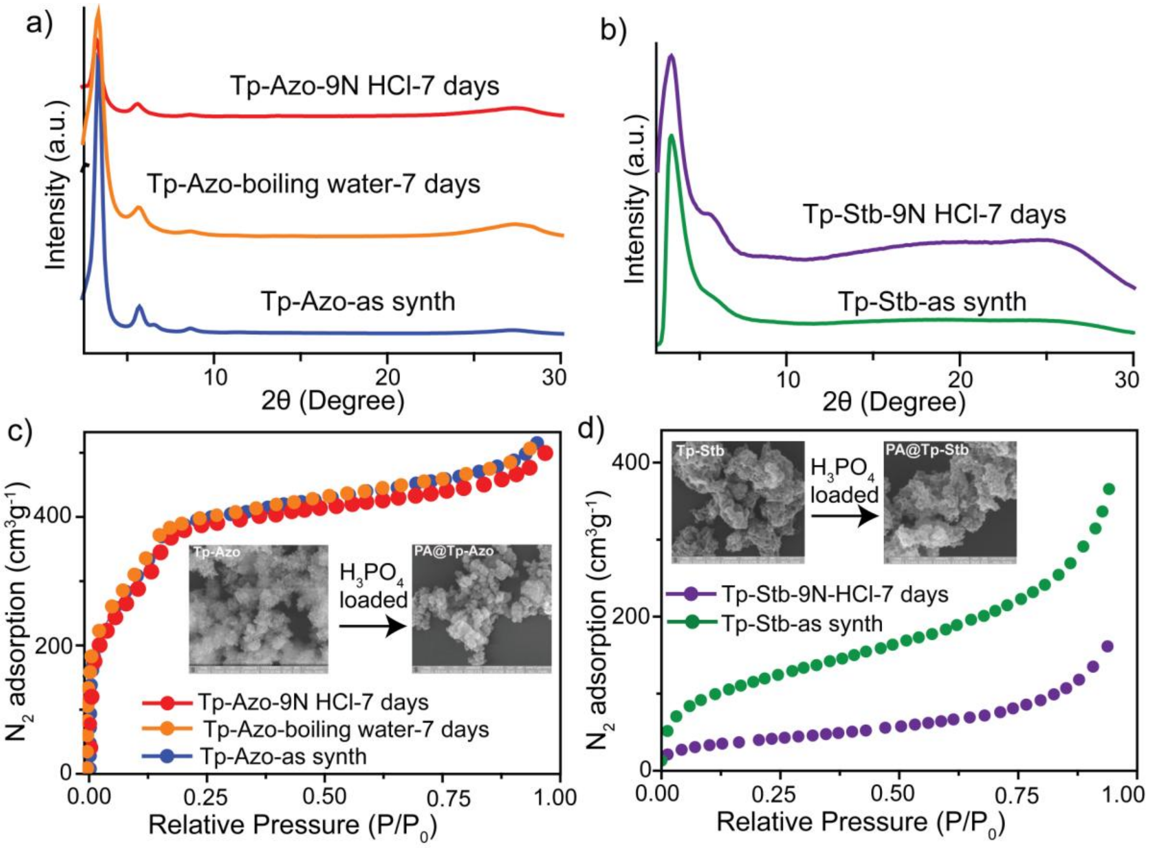

Figure 3.11: *(a) PXRD patterns of HCl (red), boiling water (orange) treated and as-synthesized* ***Tp-Azo*** *(blue). (b) PXRD patterns of HCl treated (blue) and as-synthesized* ***Tp-Stb*** *(green). (c) N_2 adsorption isotherms of* ***Tp-Azo*** *(blue), boiling water (orange) and acid treated* ***Tp-Azo*** *(red). (d) N_2 adsorption isotherms of as-synthesized* ***Tp-Stb*** *(green) and 9 N HCl treated* ***Tp-Stb*** *(Blue). [Inset showing the changes in the morphology after phosphoric acid loading in COFs].*

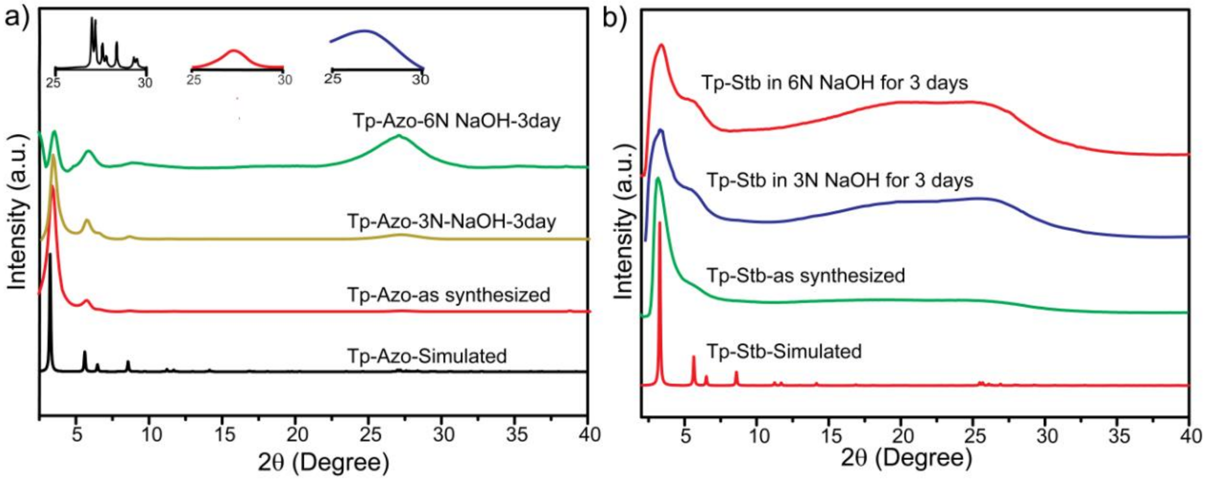

Figure 3.12: *PXRD comparison of as synthesized and base treated (a)* ***Tp-Azo*** *and (b)* ***Tp-Stb*** *samples respectively.*

retention of crystallinity (Figure 3.12). The N_2 adsorption isotherm of the 9 N HCl treated **Tp-Azo** indicates the retention of its intrinsic porosity, while **Tp-Stb** shows a decrease in porosity after the acid treatment (Figure 3.9a and 3.11c,d). However, 1.5 M H_3PO_4 treatments show significant loss of porosity in both cases, (Figure 3.6b) which is indicative of H_3PO_4 loading.

3.3.6 *Proton conductivity studies*

The protonation of the -N=N- functionality in 4-aminoazobenzene [3.18a] by H_3PO_4 and the well established phenomena of colour change of methyl orange in acidic medium [3.18b] suggested to us that azo-groups are susceptible for the protonation and can stabilize the counter anions like phosphate or dihydrogen phosphate.

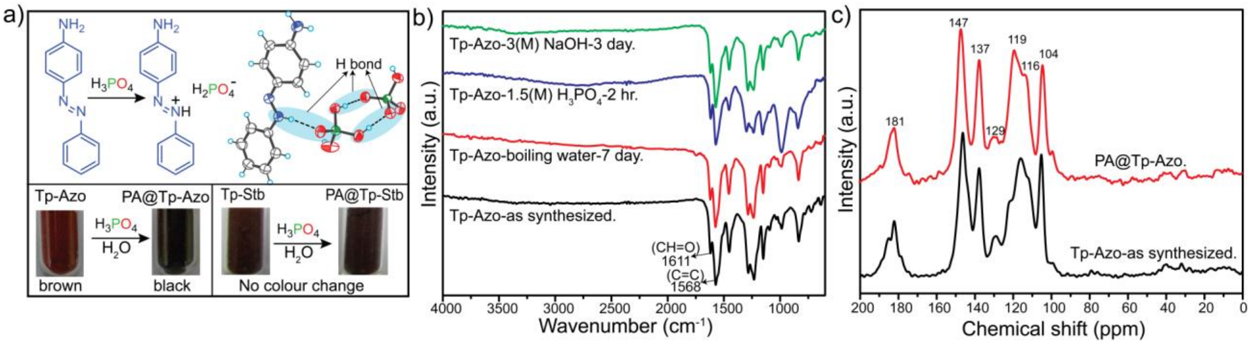

Figure 3.13: *(a) Protonation of the 4-Aminoazobenene and the crystal structure of 4-[(E)-phenyl-diazenyl]anilinium dihydrogen phosphate.[Inset showing the colour change due to the protonation of azo bond in* ***Tp-Azo*** *COF unlike* ***Tp-Stb*** *COF]. (b) IR comparison of as synthesized, water, acid and base treated* ***Tp-Azo*** *samples.(c) Comparison of solid state CP-MAS ^{13}C NMR spectra of as synthesized and phosphoric acid loaded* ***Tp-Azo*** *samples.*

Moreover, H_3PO_4 exhibits high proton conductivity (10^{-1} Scm^{-1}) due to low volatility (>158 °C) and high proton mobility resulted from the extended hydrogen bonding utilizing three ionizable O–H bonds. So we decided to apply this concept in covalent organic frameworks for the synthesis of azo based proton conducting COFs. H_3PO_4 loading in **Tp-Azo** and **Tp-Stb** was achieved by simply immersing the evacuated COF materials in 1.5 M H_3PO_4 for 2 h. Further washing with a copious amount of water (× 2) followed by activating overnight at 353K under dynamic vacuum lead to H_3PO_4 loaded **PA@Tp-Azo** and **PA@Tp-Stb** (Figure 3.14a). It is noteworthy that the H_3PO_4 loaded COFs exhibit identical IR spectra and ^{13}C NMR spectra along with moderate crystallinity and porosity compared to the parent

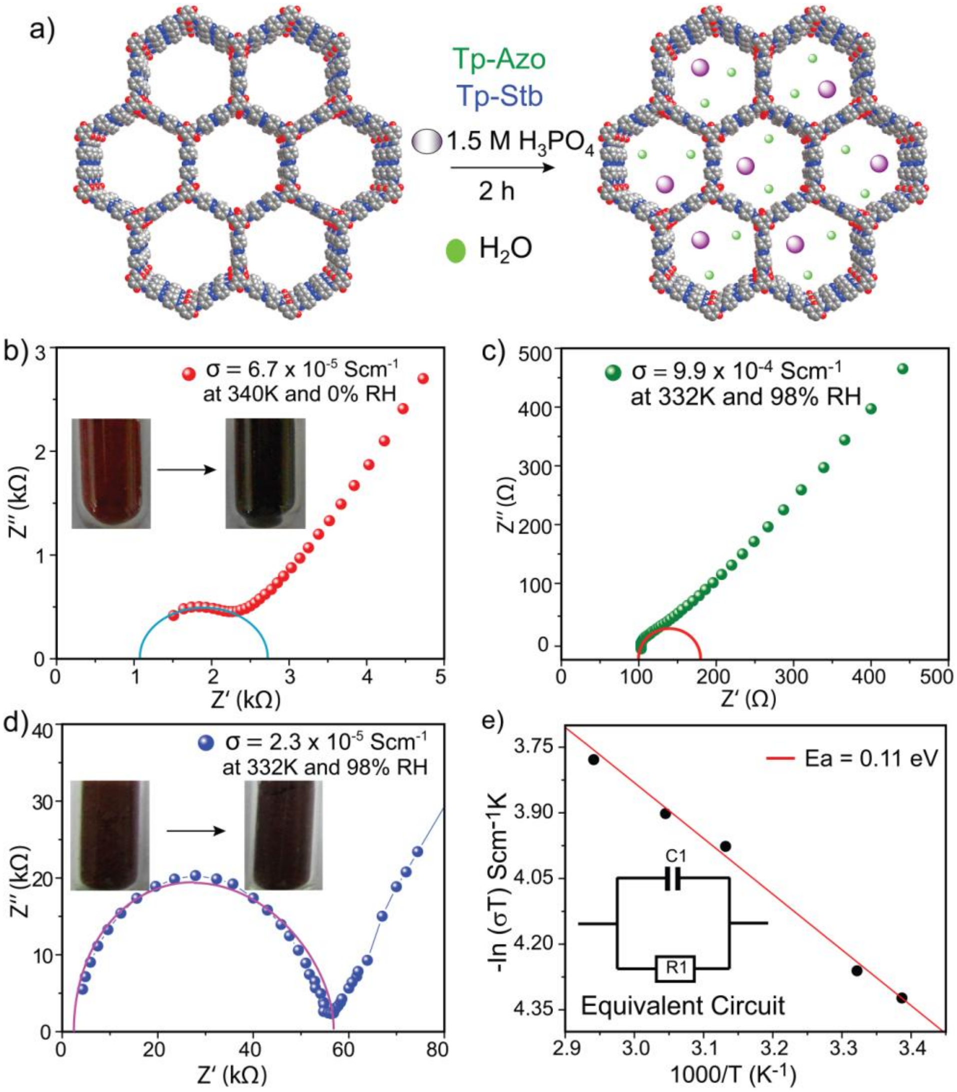

Figure 3.14: *(a) Schematic representation of H_3PO_4 doping in COFs. The proton conductivity of **PA@Tp-Azo** in (b) anhydrous condition (c) hydrous condition. (d) The proton conductivity of **PA@Tp-Stb** in hydrous condition. (e) Arrhenius plot for **PA@Tp-Azo** in hydrous condition. Inset showing the equivalent circuit model representation for the proton conduction in COFs.*

COFs (Figure 3.13). **Tp-Azo** possesses a higher acid loading (5.4 wt%) as compared to **Tp-Stb** (2.8 wt%), which is evident from the TGA analysis. The proton conductivities of **Tp-Azo, Tp-Stb, PA@Tp-Azo,** and **PA@Tp-Stb** were measured in both hydrous and anhydrous conditions. The conductivities were determined from the semicircles in the Nyquist plots (Figure 3.14). Interestingly, both **Tp-Azo** and **Tp-Stb** exhibit almost zero conductivity, which signifies that the COF backbones are acting as a support. The proton conductivity of **PA@Tp-Azo** and **PA@Tp-Stb** were measured from 295K to 415 K.

Conductivity values gradually increase upon heating, which reaches a maximum at a temperature ca. 332-340 K and then decreases gradually upon increasing the temperature. The proton conductivity of **PA@Tp-Azo** was measured as 6.7 × 10^{-5} S cm^{-1} at 340K under anhydrous conditions. This value was highly humidity-dependent and increased upon humidification. Finally, **PA@Tp-Azo** exhibited a proton conductivity of 9.9 × 10^{-4} S cm^{-1} at 332K under 98% relative humidity (RH) (Figure 3.15).

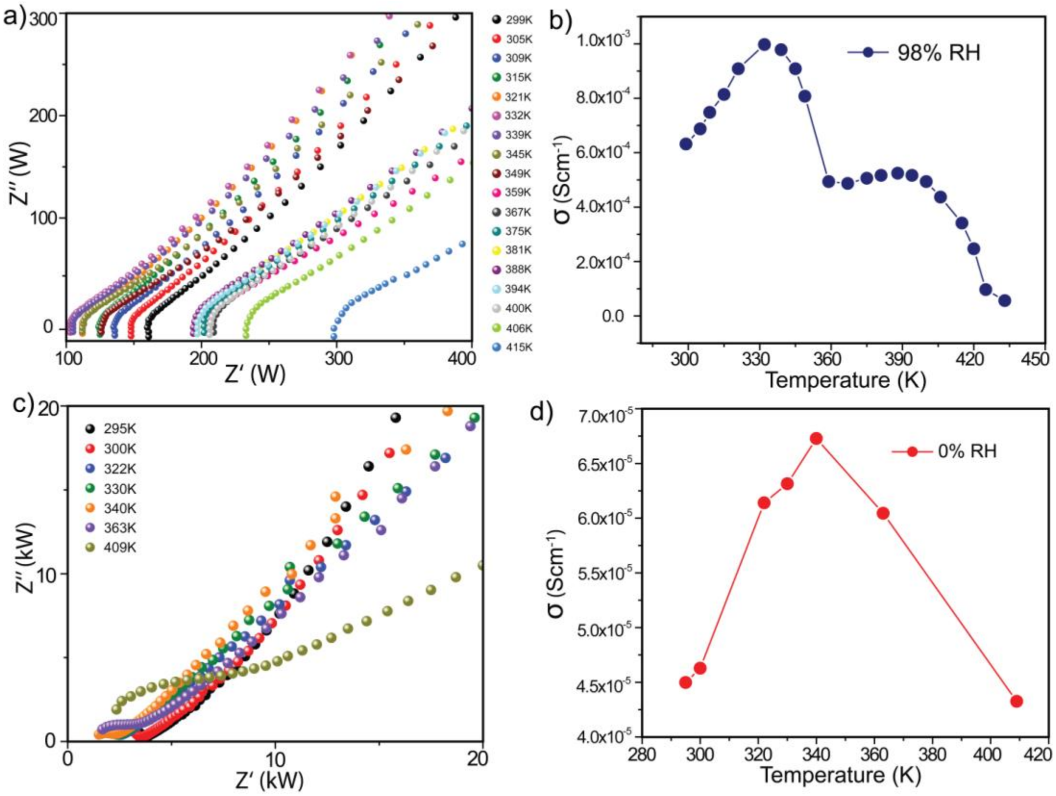

Figure 3.15: *(a) and (c) are the Nyquist plots for* ***PA@Tp-Azo*** *at different temperatures in hydrous and anhydrous condition respectively. (b) and (d) are the variation of proton conductivity as a function of temperature in hydrous and anhydrous condition respectively.*

The proton conductivity of **PA@Tp-Azo** is lower than its MOF counterparts i.e. ferrous oxalate dihydrate (1.3 x 10^{-3} S cm $^{-1}$ at 298K, 98% RH) and 1,2,4-triazole loaded β-PCMOF2 (5 × 10^{-4} S cm^{-1} at 423K, 20% RH) (Figure 3.17). Surprisingly, **PA@Tp-Stb** shows almost zero proton conductivity in anhydrous conditions, while exhibiting a poor proton conductivity value of 2.3 × 10^{-5} S cm^{-1} at 332 K under 98% RH. Notably, **PA@Tp-Azo** exhibited an activation energy value of 0.11 eV (Figure 3.14e), which is much lower than Nafion (0.22 eV) and its MOF counterparts operating under humid conditions.

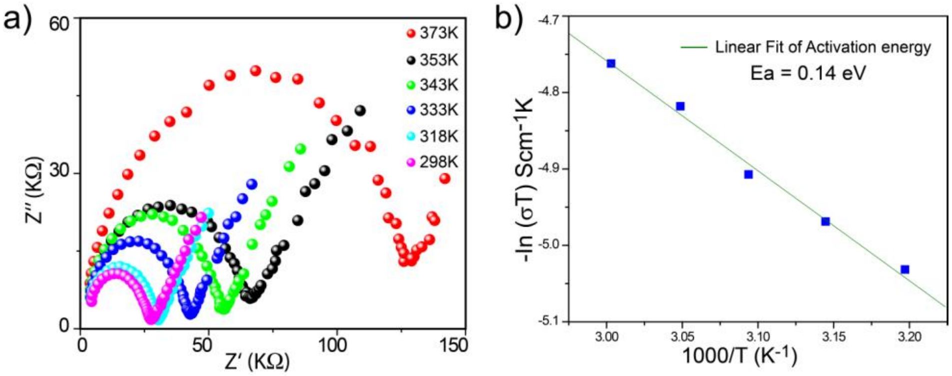

Figure 3.16: *(a) Selected Nyquist plots for **PA@Tp-Stb** in hydrous condition at different temperatures. (b) Activation energy fitting for **PA@Tp-Stb**.*

Clearly, **PA@Tp-Azo** and **PA@Tp-Stb** show distinct proton conductivity behavior under similar conditions, although they are treated with the same amount of H_3PO_4. Nevertheless, **Tp-Azo** exhibits a distinct color change (red to black) upon H_3PO_4 treatment, while the color of **Tp-Stb** remains almost unchanged (gray).

The (Figure 3.17) shed light on the comparison between prototypical MOFs and the new COFs as proton conducting materials. Clearly, the state of the art polymer membranes has two order higher proton conductivity than these COFs, while MOFs have one order higher to comparable conductivity. The conductivity values in MOFs are highly dependent on the amount and nature of the dopants used for enhancing conductivities. We presume similar control over conductivity along with the boon of polymeric materials in COFs with

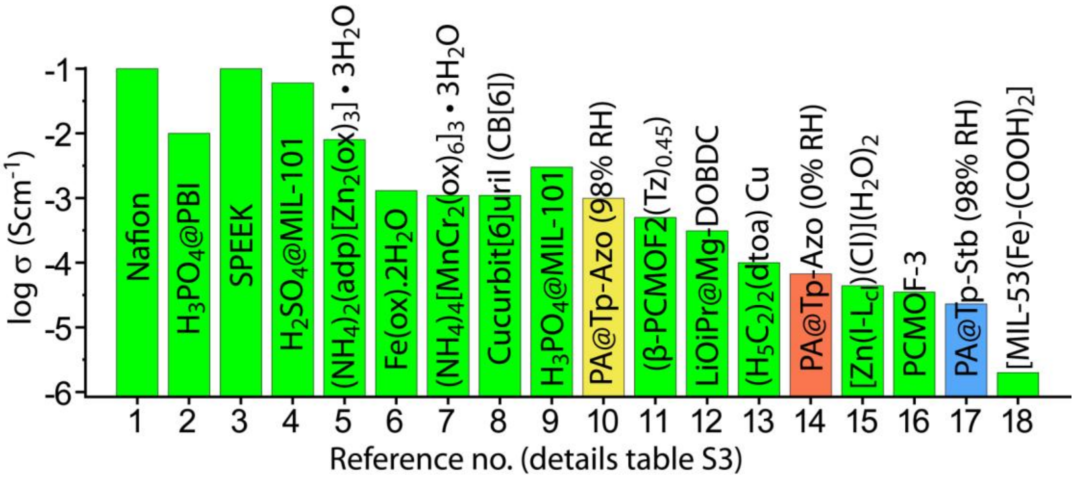

Figure 3.17: *Comparison of proton conductivity of **Tp-Azo** and **Tp-Stb** compared with standard proton conducting materials.*

higher dimensionality, porosity, and stability to facilitate higher loading of guest conductors in future.

The UV-Vis spectra of H_3PO_4 treated **Tp-Azo** monomer are red shifted from 380 nm to 496 nm due to the protonation of the azo bond (Figure 3.18). However, the -NH- and the –C=C- group remain unaffected after acid treatment, which can be proved from the intact UV-Vis spectra of 2,4,6-tris(([1,1'-biphenyl]-4-ylamino)methylene)cyclohexane-1,3,5-trione (monomer of **TpBD**) and stilbene.

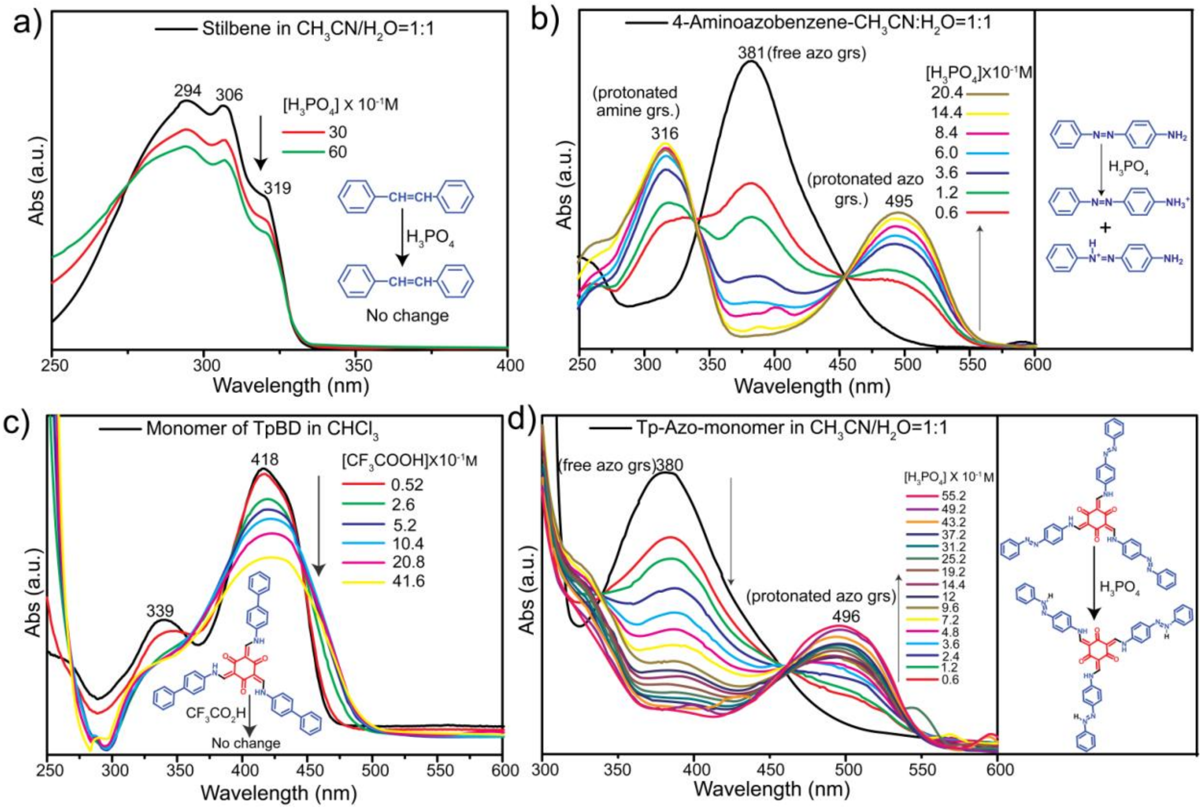

Figure 3.18: *Changes in the absorption spectra with increasing concentration of H_3PO_4 for (a)* ***Stilbene****, (b)* ***4-Aminoazobenzene*** *and (d)****Tp-Azo monomer*** *(ca. 2.5x10 $^{-5}$ M in CH_3CN-H_2O). (c) Changes in the absorption spectra of* ***TpBD monomer*** *(ca. 2.5x10 $^{-5}$ M in $CHCl_3$) with increasing concentration of CF_3CO_2H.*

These observations hint at the interaction between the proton responsive azo group and H_3PO_4, which is the governing factor for the high proton conductivity value of **PA@Tp-Azo** in both humid and anhydrous conditions, a mechanism absent in **PA@Tp-Stb**. We anticipate that the loaded H_3PO_4 along with adsorbed water molecules get hydrogen bonded with the protonated azo groups stacked along crystallographic *an* axis, which conduct the proton through the framework (Figure 3.19).

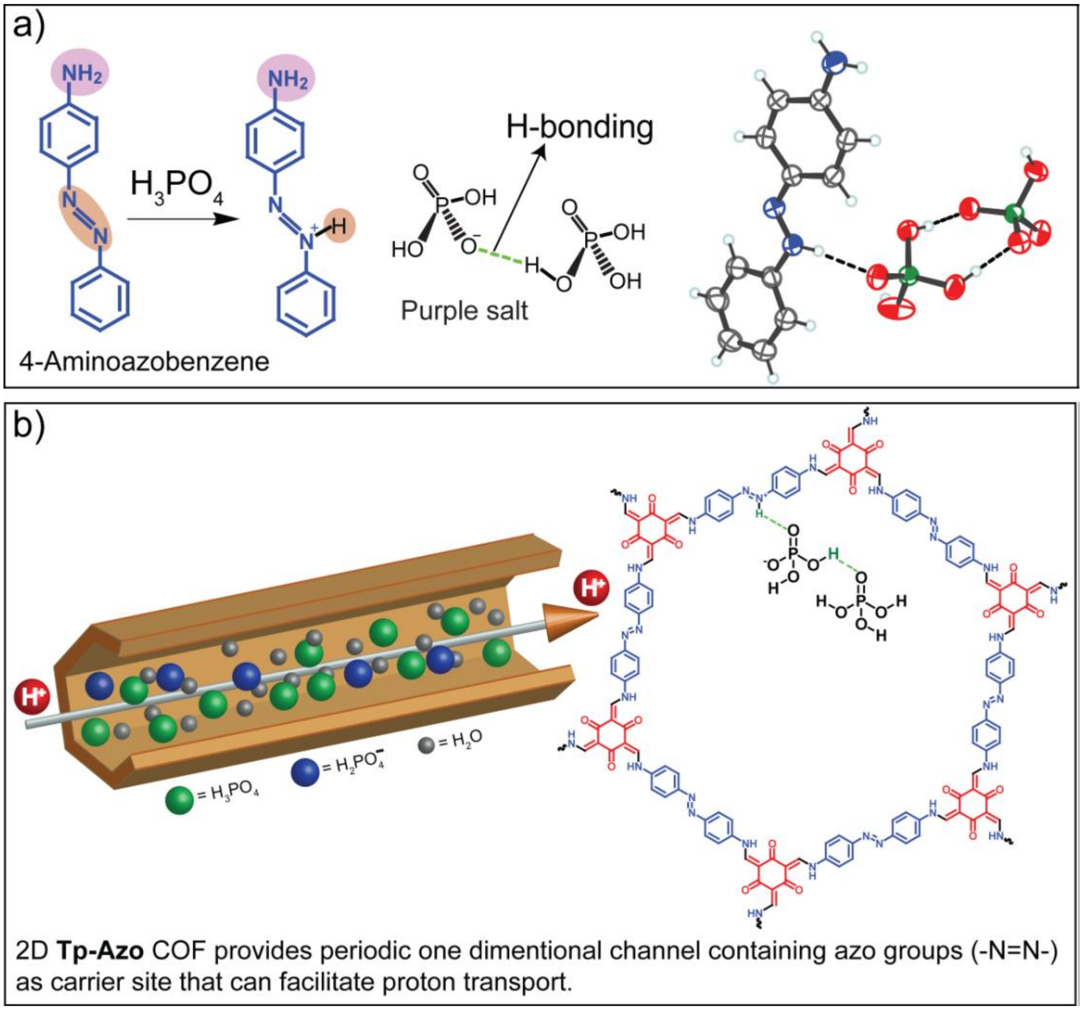

Figure 3.19: *(a) Crystal structure of 4-[(E)-phenyl diazenyl]anilinium dihydrogen phosphate and (b) Graphical representation of proton conduction along the 1D channels.*

3.4 Summary

In this chapter, we have for the first time reported azo and alkene functionalized COFs (**Tp-Azo** and **Tp-Stb**) as proton conducting materials. Exceptional chemical stability, low density, and high thermal stability make them advantageous over their MOF counterparts. We have demonstrated a simple impregnation strategy to load mineral acid *viz.* H_3PO_4 inside the framework. Interestingly, after the acid treated samples are washed, the COFs retain their crystallinity, porosity, and stability, which makes them attractive for proton conduction applications. While the parent COFs exhibit negligible conductivity, **PA@Tp-Azo** shows decent proton conductivity values under both hydrous and anhydrous conditions. **PA@Tp-Stb**, on the other hand, exhibits poor proton conductivity and, that too, only under hydrous conditions. Thus, minute changes in functionality lead to a drastic change in proton conducting ability, which establishes the crucial role of the proton responsive azo group in facilitating proton conduction pathways. Although 2D COFs lack long range ordering in bulk solid and generate a grain boundary (like MOFs) which may decrease proton conductivity, 3D COFs [3.22] with the azo group (-N=N-) acting as phosphoric acid anchoring site could prove advantageous in the long run. In addition, the membrane compatibility of COFs may serve as a boon towards the preparation of COF-polymer composites, an ongoing effort in our laboratory. We believe that our findings will encourage further work in COF based functional proton conducting materials in near future.

3.5 Experimental Procedures

3.5.1 *Materials*

1,3,5-triformylphloroglucinol was prepared from phloroglucinol using literature procedure [3.23]. All other reagents and solvents were commercially available and used as received from Sigma Aldrich.

3.5.2 *Synthesis of Tp-Azo COF*

The Synthesis of **Tp-Azo** COF was carried out by utilizing a mixture of 1,3,5-triformylphloroglucinol (**Tp**) (0.3 mmol) and 4,4′-azodianiline (**Azo**) (0.45 mmol) in presence of 6 M acetic acid (0.5 mL) using dimethylacetamide and o-dichlorobenzene (1:1) as a solvent combination (3 mL). This mixture was sonicated for 10 minutes in order to get a homogeneous dispersion. The tube was then flash frozen at 77 K (liquid N_2 bath) and degassed by three freeze-pump-thaw cycles. The tube was sealed off and then heated at 120 °C for 3 days. A dark red coloured precipitate was collected by centrifugation or filtration and washed with dimethylacetamide thrice. The powder collected was then solvent exchanged with acetone 5-6 times and dried at 180 °C under vacuum for 12 hours to get corresponding COFs in ~75 % isolated yield. **FT-IR** (powder, υmax cm^{-1}): 1619 (w), 1568 (s), 1450 (m),1284 (w), 1240 (s), 1147 (s), 987 (w), 839 (m). **Elemental Analysis;** Anal. Calcld. For $C_9ON_2H_6$: C, 68.35; H, 3.79; N, 17.72; found: C, 48.12; H, 5.27; N, 11.12.

3.5.3 *Synthesis of Tp-Stb COF*

The synthesis of **Tp-Stb** COF was carried out by utilizing the same protocol with a mixture of triformylphloroglucinol (**Tp**) (0.3 mmol) and 4,4′-diaminostilbene dihydrochloride (**Stb**) (0.45 mmol) in presence of 6 M acetic acid (0.5 mL) using dimethylacetamide and o-dichlorobenzene (1:1) as solvent combination (3 mL). This mixture was sonicated for 10 minutes in order to get a homogeneous dispersion. The tube was then flash frozen at 77 K (liquid N_2 bath) and degassed by three freeze-pump-thaw cycles. The tube was sealed off and then heated at 120 °C for 3 days. A dark red coloured precipitate was collected by centrifugation or filtration and washed with dimethylacetamide thrice. The powder collected was then solvent exchanged with acetone 5-6 times and dried at 180 °C under vacuum for 12 hours to get corresponding COFs in ~75 % isolated yield. **FT-IR** (powder, υmax cm^{-1}): 1574 (s), 1518 (w), 1450 (s), 1255 (m), 991 (w), 958 (w), 824 (m). **Elemental Analysis;** Anal. Calcld. For $C_{10}H_6ON$: C, 76.92; H, 3.84; N, 8.97; found: C, 69.84; H, 4.50; N, 7.89.

3.5.4 *General methods for characterization*

All reagents were commercially available and used as received. Microscopy images of these hollow fibers were taken in Zeiss SteREO Discovery V20.

a) ***Wide-angle X-Ray Diffraction (WAXD)*****:** The wide-angle X-Ray Diffraction (WAXD) analysis of MOFs and the composite membranes were carried on a Rigaku SmartLab X-ray diffractometer in reflection mode using CuKα radiation ($\lambda = 1.54$ Å). The 2θ range from 5° to 40° was scanned with a scan rate of 3° min^{-1}. The instrument was previously calibrated using a silicon standard.

b) ***FT-IR spectroscopy*****:** The Fourier transform infrared spectra (FT-IR) were taken on a Bruker Optics ALPHA-E spectrometer with a universal Zn-Se ATR (attenuated total reflection) accessory in the 600-4000 cm^{-1} region or using a Diamond ATR (Golden Gate). The spectra were measured over the range of 4000-400 cm^{-1}.

c) ***Scanning Electron Microscopy*****:** Scanning Electron Microscopy (SEM) was performed on an FEI Quanta 200 3D ESEM (dual beam) instrument with a field emitter as an electron source and in FEI Nova Nano SEM 650 Scanning Electron Microscope. SEM images of membrane cross section were taken after freeze cut off membranes in LN_2. Samples for SEM were gold sputtered before analyses.

3.5.5 *Structure modeling and optimization*

Atomic positions and cell sizes of modeled COF layers were optimized using Self-Consistent Charge Density Functional Tight-Binding (SCC-DFTB) Method. Stacking of layers is affected by the Coulomb repulsion between the partial atomic charges in adjacent layers. Hence, we performed Mulliken population analysis for the charges. The adjacent layers were shifted with respect to each other in different directions in order to avoid Coulomb repulsion from charges alike. Several possibilities were considered, however, the best was taken from a comparison of simulated PXRD pattern with the experimental. Interlayer separation was also determined from the comparison of PXRD patterns.

NOTE: The results of this chapter have already been published in *J. Am. Chem. Soc.**2014**, 136, 6570−6573* with the title: "*Phosphoric Acid Loaded Azo (−N=N−) Based Covalent Organic Framework for Proton Conduction.*" These publications were the results of the collaboration between the group of Dr. Rahul Banerjee and his students Suman Chandra, Tanay Kundu, Sharath Kandambeth, Yogesh Marathe, Shrikant M. Kunjir from National Chemical Laboratory, Pune, India and Dr. Ravichandar BabaRao from Commonwealth Scientific and Industrial Research Organization (CSIRO), Australia. Apart from computational study major works contributed by Suman Chandra.

CHAPTER 4

Covalent Organic Frameworks as Intrinsic and Extrinsic Proton Conducting Materials

Abstract: *In this chapter, we have synthesized a sulfonic acid based covalent organic framework (**TpPa-SO_3H**) which exhibits intrinsic proton conductivity under anhydrous condition. The sulfonic acid groups are aligned on the 2D layers at periodic intervals and promote the proton hopping inside the hexagonal one-dimensional channel. The intrinsic proton conductivity of **TpPa-SO_3H** was measured as 1.7 × 10^{-5} Scm^{-1} at 120 ℃ under anhydrous condition. To enhance the proton conductivity, we have synthesized a hybrid COF **TpPa-(SO_3H-Py)** by a ligand-based solid solution approach that contains sulfonic acid as the acidic site, as well as pyridine as the basic site in order to immobilize acidic proton carrier molecules. Impregnation of phytic acid molecules inside the framework increases the anhydrous proton conductivity up to 5 × 10^{-4} Scm^{-1} at 120 °C. Such an approach highlights the advantage and first-time use of hybrid COF for interplaying intrinsic to extrinsic proton conductivity.*

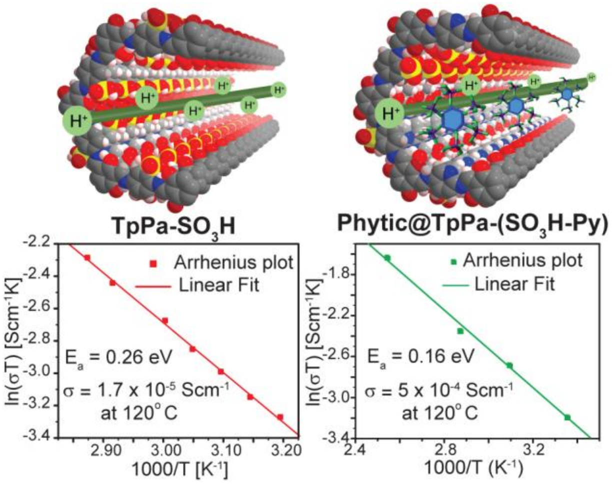

4.1 Introduction

Design and development of anhydrous proton conducting materials for high temperature (> 100 °C) polymer electrolyte membrane fuel cells (HT-PEMFCs) is a challenge for researchers [4.1]. The use of higher temperature in the PEMFCs is advantageous because it creates faster kinetics and less CO poisoning at the Pt electrode. In addition, the energy and water management becomes considerably easier as the process does not require an additional humidifier [4.2]. At present, the industrial standard Nafion [4.3], a perfluorinated sulfonated polymer, shows highest proton conductivity (10^{-1} S cm^{-1}) at 60 °C. However, high cost, difficult synthetic strategy, and very low conductivity at higher temperatures (>100 °C) restrict its usage in the HT-PEMFCs. In this context, researchers have explored a few relatively inexpensive and easy to synthesize polymers like phosphoric acid (H_3PO_4) doped polybenzimidazole [H_3PO_4@PBI] [4.4] and sulfonated polyethylether ketone (SPEEK) [4.5] with good proton-conductivity values under anhydrous conditions and higher temperatures (> 100 °C). More recently, crystalline porous materials [4.6-4.12] such as metal-organic frameworks (MOFs)/porous coordination polymers (PCPs) and their composites [4.13-4.23] have been used as proton conducting materials. Although inherent proton conducting materials based on PBI [4.24], $CsHSO_4$ [4.25], poly(vinyl phosphoric acid) (PVPA) [4.26] are known, inherent proton conducting MOFs/PCPs [4.27-4.30] are quite limited. Moreover, the possibility of fuel crossover across the porous MOF membranes and their instability in a harsh fuel cell operating conditions might hinder their potential applicability in PEMFCs [4.10]. In addition, metal ion coordination to the sulfonic/phosphonic acids mostly decreases the number of free protons, which results in low proton concentration and conductivity of the sulfonated/phosphonated linker bearing MOFs [4.10]. Such shortcomings have been addressed by acid doping (e.g. H_3PO_4, H_2SO_4, TfOH) inside the MOF pores [4.15, 4.23], but the toxicity of the constituting transition metals and long term sustainability of this acid loaded MOF raises further concerns about their real-time applicability.

Covalent organic frameworks (COFs) are the metal-free counterpart of the MOFs, constructed by spacers linked through different covalent bonds [4.31, 4.32]. However, unlike MOFs, these materials have been used primarily for gas storage, catalysis and photoconductivity [4.33-4.35]. Recently, the emergence of chemically stable COFs [4.36] has paved the way for electrochemical applications such as charge storage [4.37] and proton conductivity [4.21]. However, the proton conductivity reported so far has been achieved by the immobilization of the mineral acid H_3PO_4 within the COF backbone, thereby reducing the number of available protons for transportation [4.21]. As a result, the values are low and these COFs lack high-temperature operational behavior. This has led us to design COFs to circumvent these shortcomings by adopting two distinct approaches namely, i) by decorating the COF backbone with suitably functionalized acidic units (such as sulfonic [4.12] /phosphonic groups) that can conduct protons intrinsically without the aid of any other external carriers, and ii) by immobilizing guest molecules with very low pKa to ensure high proton concentration and facile proton conduction inside the COFs even at high temperature and anhydrous conditions. Herein, for the first time, we report the combination of both these aspects within a single regime to realize both intrinsic and extrinsic proton conduction phenomena in the COFs. We have synthesized sulfonic acid functionalized COF (**TpPa-SO_3H**) that can act as an intrinsic proton conductor. The free –SO_3H groups stack within the COF backbone to provide a continuous array of proton conducting sites. To implement the second possibility, we have also synthesized pyridine functionalized COF by incorporating a pyridinic site within the COF structure (**TpPa-Py**) and a hybrid COF containing both pyridinic and sulfonic acid groups [**TpPa-(SO_3H-Py)**] by the ligand-based solid solution approach (Figure 4.1) [4.38, 4.39]. This was further followed by the impregnation of the phytic acid [*myo*-Inositol hexakis-(dihydrogen phosphate)] in **TpPa-Py** and **TpPa-(SO_3H-Py)** to give phytic**@TpPa-Py** and phytic**@TpPa-(SO_3H-Py)** respectively. The phytic**@TpPa-(SO_3H-Py)** can conduct proton (intrinsically) through the sulfonic groups in combination with neighboring pyridinic units and also transport protons (extrinsically) *via* the immobilized phytic acid at the pyridinic sites. As a proof of the concept, phytic**@TpPa-(SO_3H-Py)** shows the higher anhydrous proton conductivity (5×10^{-4} Scm^{-1} at 120 °C) than phytic**@TpPa-Py** and phytic**@TpPa-SO_3H**.

4.2 Preparative methods and characterization

4.2.1 *Synthesis of COFs*

Synthesis of **TpPa-SO_3H** was accomplished by reacting 1,3,5–triformylphloroglucinol (**Tp**, 0.3 mmol) and 2,5-diaminobenzenesulfonic acid (**Pa-SO_3H**, 0.45 mmol), 3 mL (4:1, v/v) solvent mixture of mesitylene and 1,4-dioxane with 0.6 mL of 6(M) acetic acid (Figure 4.1). After sonication for 10 min reaction mixture was flash frozen at 77 K and degassed by three freeze-pump-thaw cycles. The reaction tube was sealed off and heated at 120 °C for 3 days. After filtration, a red coloured precipitate was collected and washed with 1,4-dioxane for several times followed by solvent exchanged with acetone 5-6 times and dried at 120 °C under vacuum for 12 h to get corresponding COFs in ~70% isolated yield.

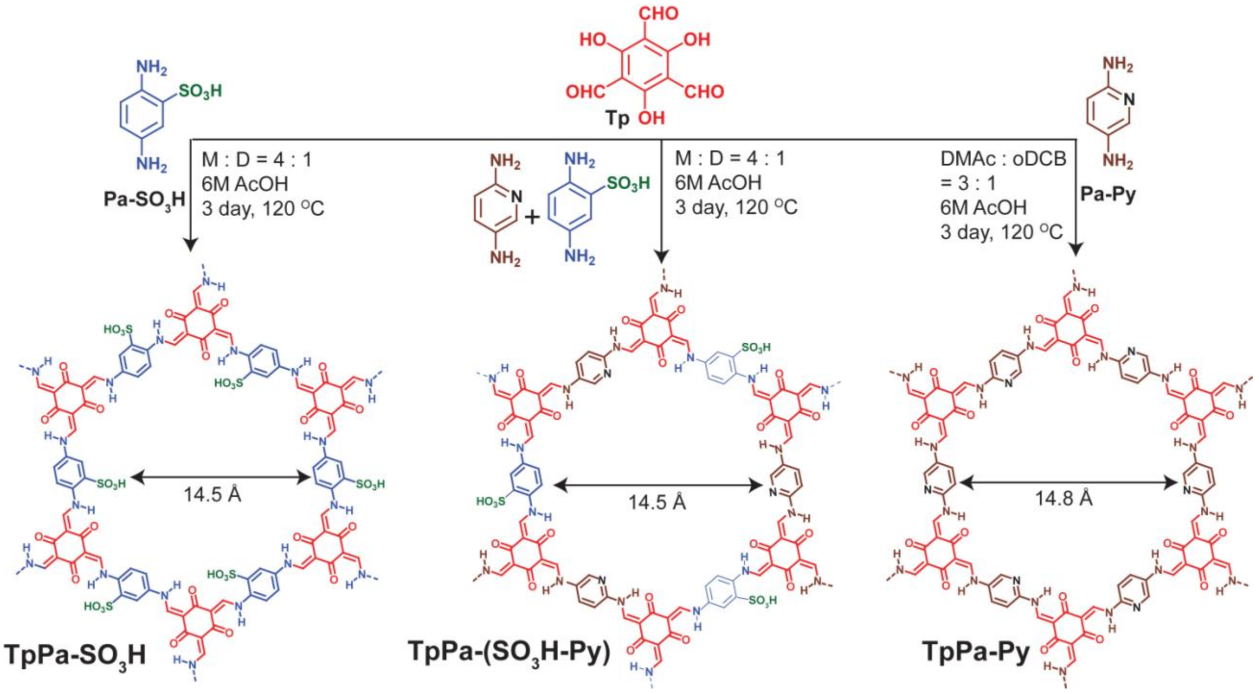

***Figure 4.1**: Schematic representation of the synthesis of **TpPa-SO$_3$H**, **TpPa-(SO$_3$H-Py)** and **TpPa-Py** via Schiff base condensation reaction.*

4.2.2 Phytic acid loading inside COFs (Phytic@COFs)

Activated COFs (150 mg) were added to 10 mL phytic acid (50% aqueous solution) and suspensions were stirred for 60 min at room temperature. Then the suspension was filtered and washed with a copious amount of water to remove the surface absorbed acid followed by drying under vacuum at 80-90 ºC for 6 h.

4.2.3 *Structural simulation and characterization*

The Powder XRD analysis of the three COFs revealed diffraction peaks at 2θ of 4.8°, 8.3°, 26.8-27.2°, which have been assigned for the (100), (110) and (001) planes, respectively (Figure 4.2). The broadening of the PXRD peaks results from a combination of small particle size and small crystalline domain zone as observed from SEM and TEM images (Figure 4.14). The pi-pi stacking distances between 001 planes are ca. 3.3 Å for **TpPa-SO$_3$H, -Py,** and **-(SO$_3$H-Py)**. Possible 2D models were built and optimized employing the Self-Consistent Charge Density Functional Tight Binding (SCC-DFTB) method with London dispersion corrections with four different stacking modes including eclipsed (AA), slip-AA-x, slip-AA-y and staggered (AB). All possible relative positions of the -SO_3H and –Py functional groups were optimized and the lowest energy configurations were used to simulate the PXRD patterns. The simulated PXRD patterns of the slip-AA eclipsed stacking model match well with the experimental PXRD patterns of all the COFs. The simulated PXRD patterns obtained from eclipsed (AA), slip-AA-x and slip-AA-y stacking mode were quite similar except (001) plane (Figure 4.3). In order to determine the unit cell parameters, Pawley refinements of the observed PXRD patterns were performed for all the COFs (Figure 4.2).

Structures of **TpPa-SO_3H** and **TpPa-Py** were modeled using Self-Consistent Charge Density Functional Tight-Binding (SCC-DFTB) method including Lennard-Jones dispersion as implemented in DFTB+ version 1.2. Parameters for all atoms were taken from the mio-0-1 set. Lattice dimensions and atomic positions were optimized simultaneously. From the optimized monolayers, the bulk structure was simulated using a bilayer model and investigating AA, AB and slipped-AA structures [4.2, 4.3]. In the bilayer model, there may be disorder in the stacking of the –Py and –SO_3H functional groups, all possible permutations were optmised and the lowest energy structure was kept. Interlayer separation was initialized at 3.5Å, except in the AA

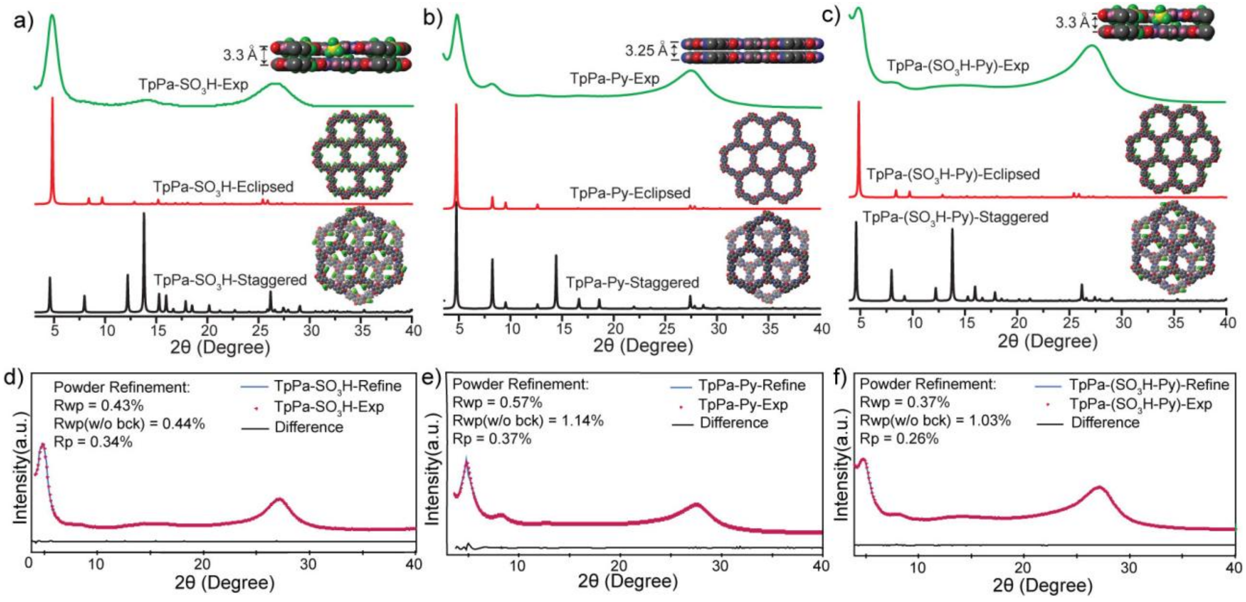

***Figure 4.2**: PXRD spectra of as-synthesized (green) compared with the eclipsed (red) and staggered (black) stacking models for (a) **TpPa-SO_3H**, (b) **TpPa-Py** and (c)**TpPa-(SO_3H-Py)**. Experimental (pink) PXRD profiles of (d) **TpPa-SO_3H**, (e) **TpPa-Py** and (f) **TpPa-(SO_3H-Py)** compared with Pawley refined (blue) of an eclipsed offset arrangement COF based on P1 symmetry; difference plot is given in (black).*

stacking of **TpPa-SO_3H**, which was initialized at 5Å to account for the bulky functional groups. The fractional coordinates of **TpPa-SO_3H**, **TpPa-Py,** and **TpPa-(SO_3H-Py)** are given in Table 4.6, 4.7 and 4.8 respectively. The experimental PXRD patterns are agreeable with the simulated patterns of eclipsed offset stacking models (slip-AA-x/y) (Figure 4.3). Hence we propose structures having triclinic space group (*P* 1) for both **TpPa-SO_3H** and **TpPa-Py** by comparing the experimental and simulated PXRD patterns. Refinements of PXRD pattern were done using Reflex module of Material Studio 6.0 [4.4].

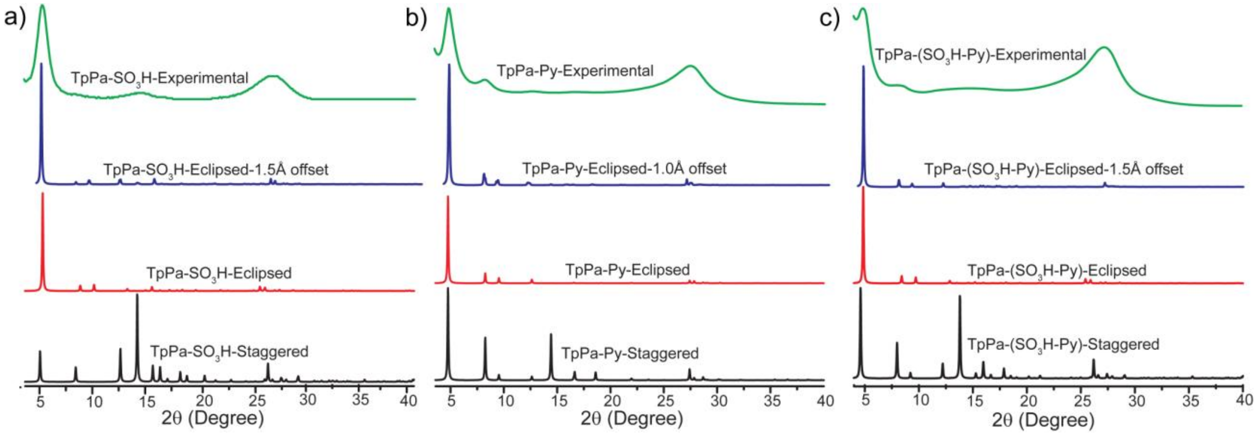

***Figure 4.3**: PXRD comparison of the experimental (green), simulated offset with (1.0-1.5Å) parallel layer displacement (blue), simulated perfectly eclipsed (AA) (red) and simulated perfectly staggered (AB) (black) for (a) **TpPa-SO_3H**, (b) **TpPa-Py** and (c)**TpPa-(SO_3H-Py)**.*

Table 4.1: The total DFTB energies, Lennard-Jones contributions (LJ), and the crystal stacking energies per monolayer as well as the corresponding HOMO-LUMO energy gap for **TpPa-SO_3H.**

Stacking	Slipped distance along a and/or b direction	*c* [Å]	Total DFTB Energy [a.u.]	LJ energy [a.u.]	Per unit Crystal Stacking energy [kcal.mol^{-1}]	HOMO-LUMO gap [eV]
monolayer	---	---	-142.189055	0.4629	---	2.021
AA	---	4.90	-284.603159	0.7269	-70.61	1.953
slipAA-x	1.5 Å in a	3.43	-284.600204	0.7256	-69.68	1.922
slipAA-y	1.5 Å in b	3.41	-284.602439	0.7290	-70.38	1.879
AB	---	3.39	-284.596298	0.7504	-68.46	1.972

Table 4.2: The total DFTB energies, Lennard-Jones contributions (LJ), and the crystal stacking energies per monolayer as well as the corresponding HOMO-LUMO energy gap for **TpPa-Py.**

Stacking	Slipped distance along a and/or b direction	*c* [Å]	Total DFTB Energy [a.u.]	LJ energy [a.u.]	Per unit Crystal Stacking energy [kcal.mol^{-1}]	HOMO-LUMO gap [eV]
monolayer	---	---	-105.643914	0.3794	---	2.057
AA	---	3.48	-211.435512	0.5912	-46.34	1.778
slipAA-x	1.0 Å in a	3.35	-211.455577	0.5893	-52.63	1.976
slipAA-y	1.0 Å in b	3.33	-211.456513	0.5887	-52.93	1.976
AB	---	3.28	-211.392325	0.6585	-32.79	1.979

Table 4.3: The total DFTB energies, Lennard-Jones contributions (LJ), and the crystal stacking energies per monolayer as well as the corresponding HOMO-LUMO energy gap for **TpPa-(SO$_3$H-Py).**

Stacking	Slipped distance along a and/or b direction	*c* [Å]	Total DFTB Energy [a.u.]	LJ energy [a.u.]	Per unit crystal stacking energy [kcal.mol^{-1}]	HOMO-LUMO gap [eV]
monolayer	---	---	-130.005261	0.4351	---	2.031
AA	---	4.95	-260.220380	0.6793	-65.84	1.919
slipAA-x	1.5 Å in a	3.41	-260.214902	0.6698	-64.13	1.872
slipAA-y	1.5 Å in b	3.37	-260.222460	0.6746	-66.50	1.841
AB	---	3.43	-260.219834	0.6829	-65.67	1.816

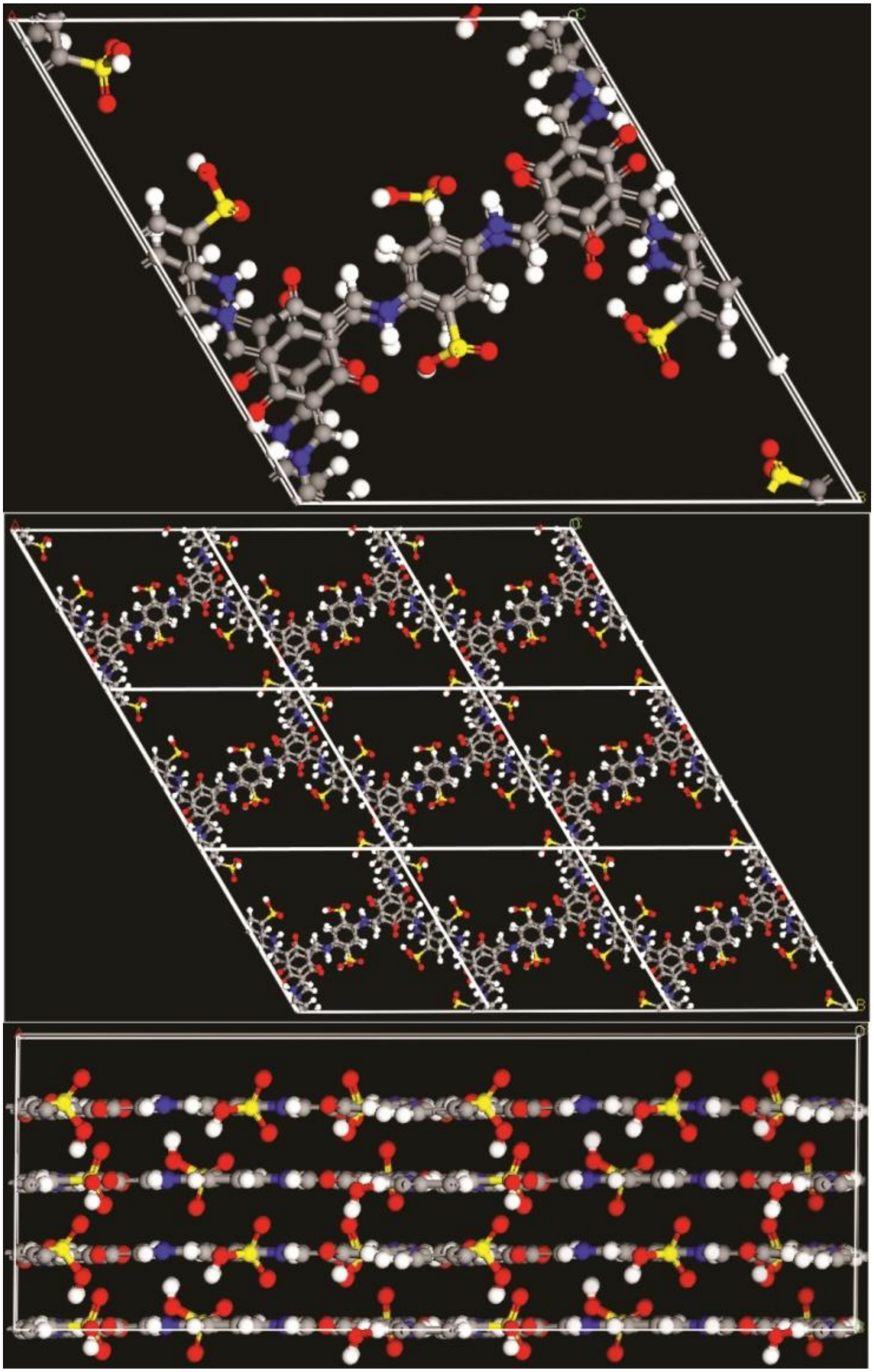

Figure 4.4: *Simulation of the unit cell content calculated in an eclipsed-AA-1.5 Å off set arrangement* ***TpPa-SO$_3$H***: *top view onto the ab-plane and view perpendicular to the c-axis.*

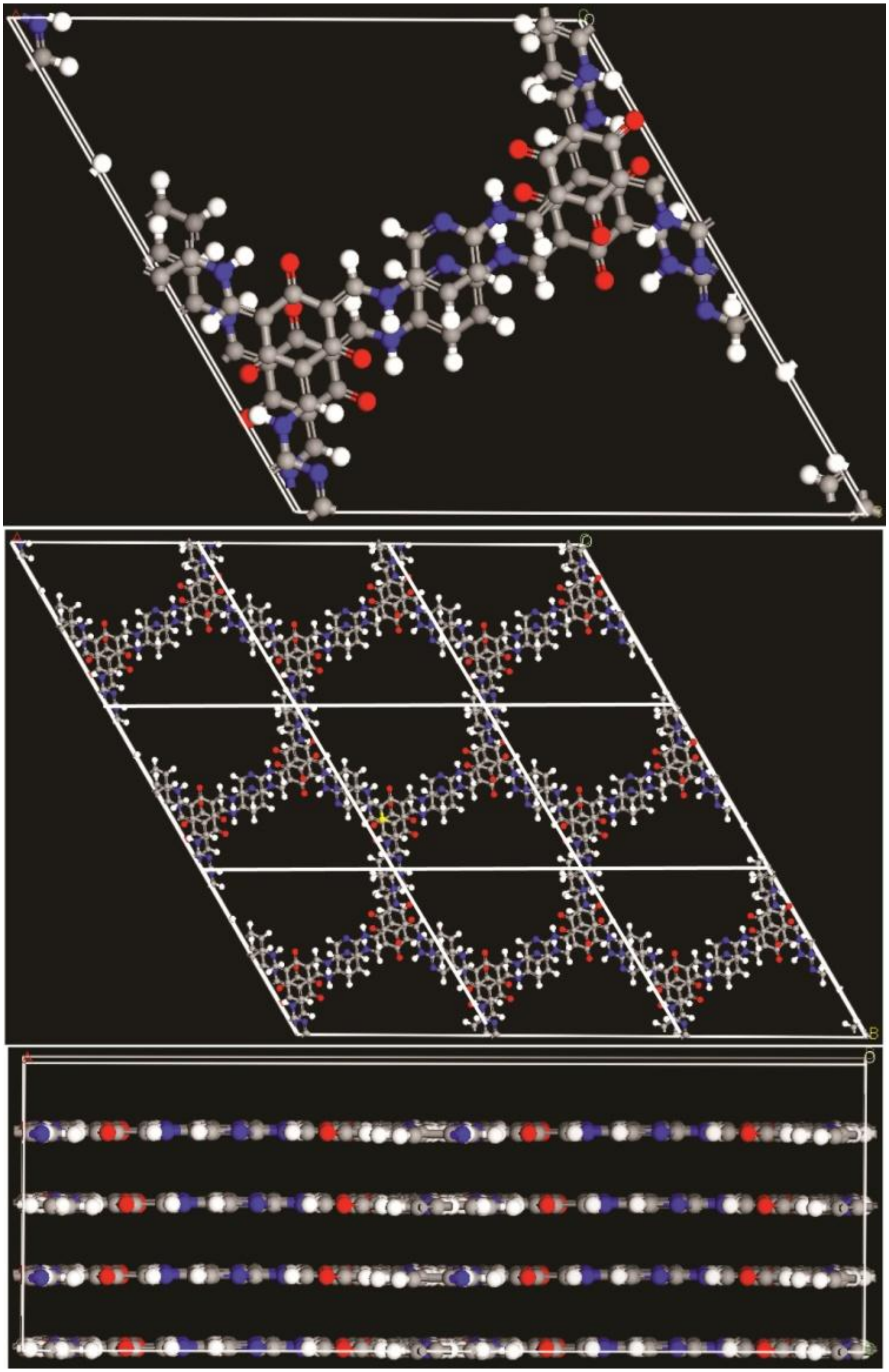

Figure 4.5*: Simulation of the unit cell content calculated in an eclipsed-AA-1.0 Å off set arrangement of* ***TpPa-Py****: top view onto the ab-plane and view perpendicular to the c-axis.*

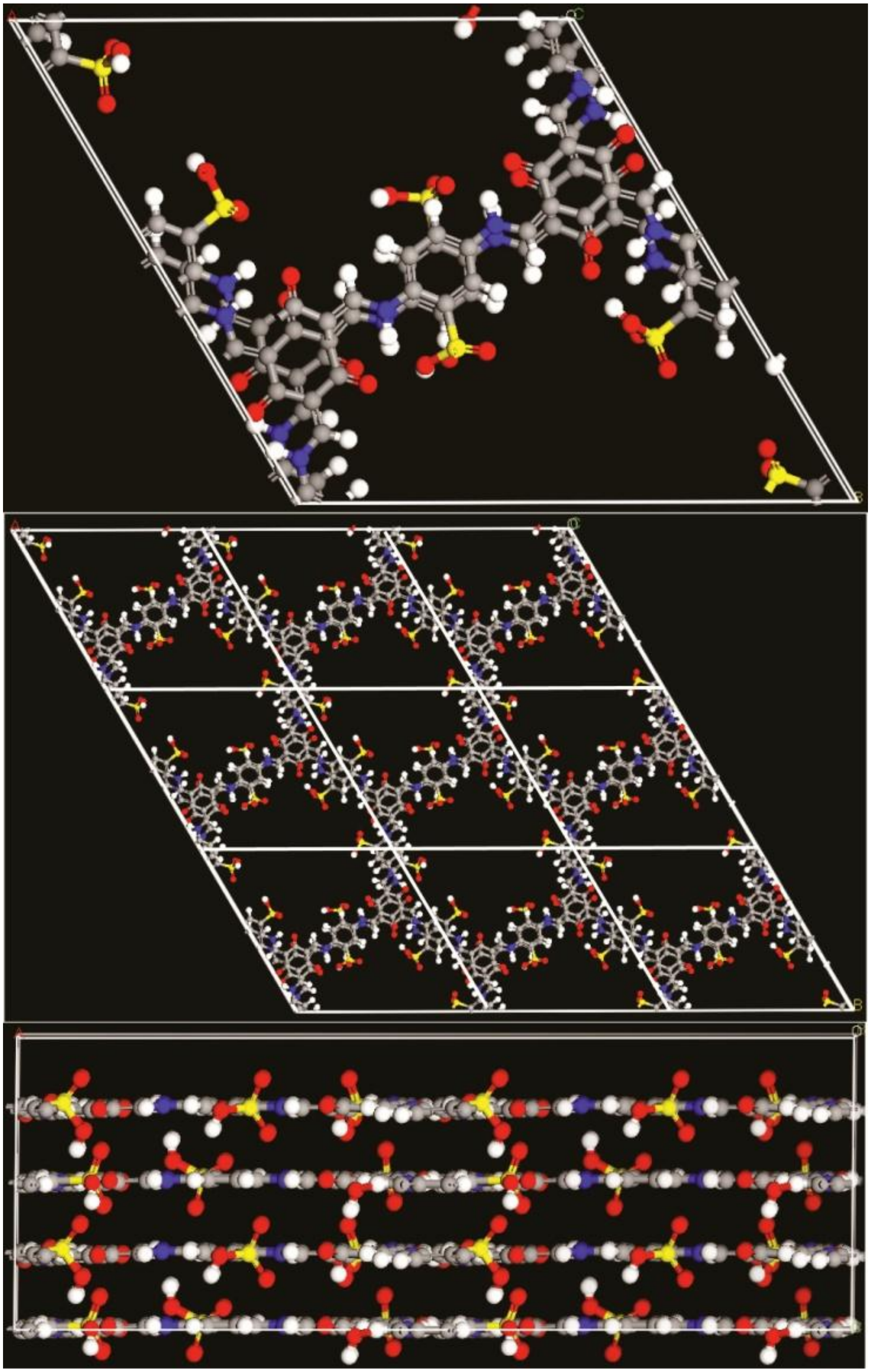

Figure 4.6*: Simulation of the unit cell content calculated in an eclipsed-AA-1.5 Å off set arrangement of* ***TpPa-(SO_3H-Py)****: top view onto the ab-plane and view perpendicular to the c-axis.*

4.2.4 *Chemical characterization*

The FT-IR spectra of **TpPa-SO$_3$H, TpPa-Py,** and **TpPa-(SO$_3$H-Py**) indicated complete consumption of the reactants (Figure 4.7) by absence of the characteristic N−H stretching band (3335−3425 cm^{-1}) of the free diamine and aldehydic -CH=O (1650 cm^{-1}) of the free **Tp**. Moreover, the absence of C=N stretching peaks (1620 cm^{-1}) and the occurrence of a new C=C peak at 1576 cm^{-1} indicates the presence of the keto tautomer rather than the expected enol tautomer [4.36]. The aromatic C=C peak appeared at 1438 cm^{-1} and the newly formed C−N bonds of the keto tautomer in the COF were observed at 1231 cm^{-1}. The peak at 1005 cm^{-1} for **TpPa-SO$_3$H** and -(**SO$_3$H-Py**) indicated the S-OH stretching mode of the -SO$_3$H unit (Figure 4.7a and 4.8a).

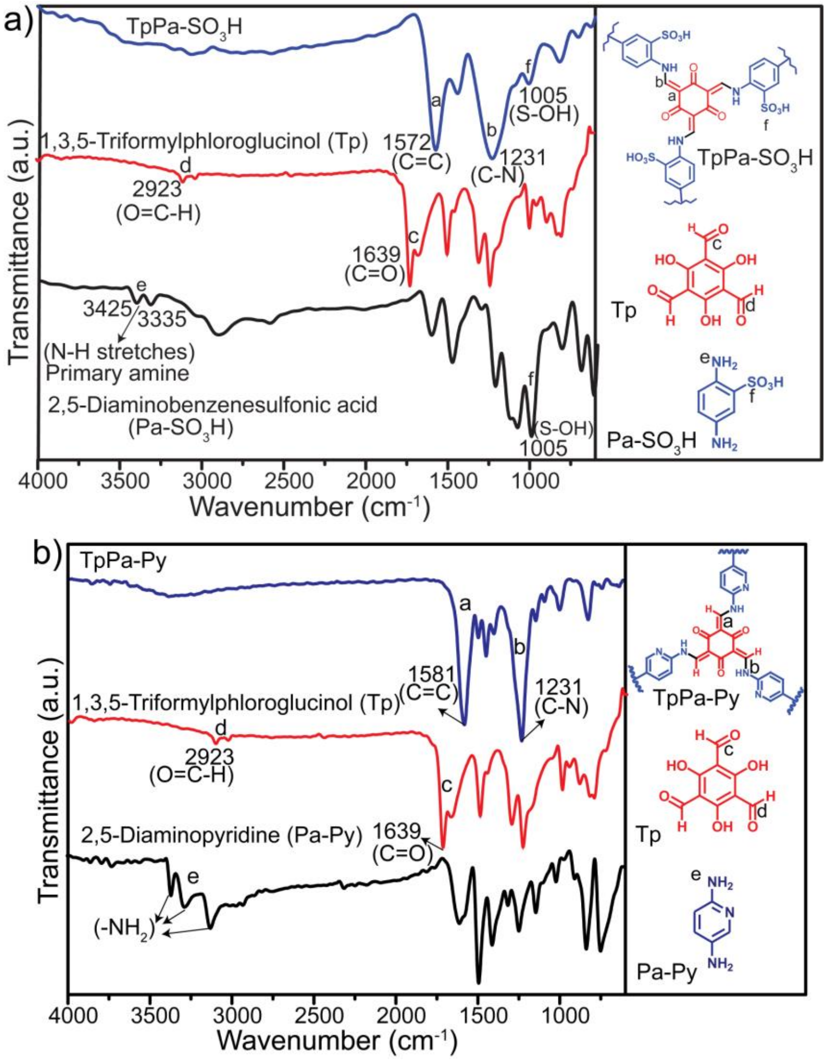

*Figure 4.7: FT-IR spectra of (a) **TpPa-SO$_3$H** (Blue) and (b) **TpPa-Py** (Blue) compared with starting material **Tp** (Red), (**Pa-SO$_3$H**) (Black) and (**Pa-Py**) (Black).*

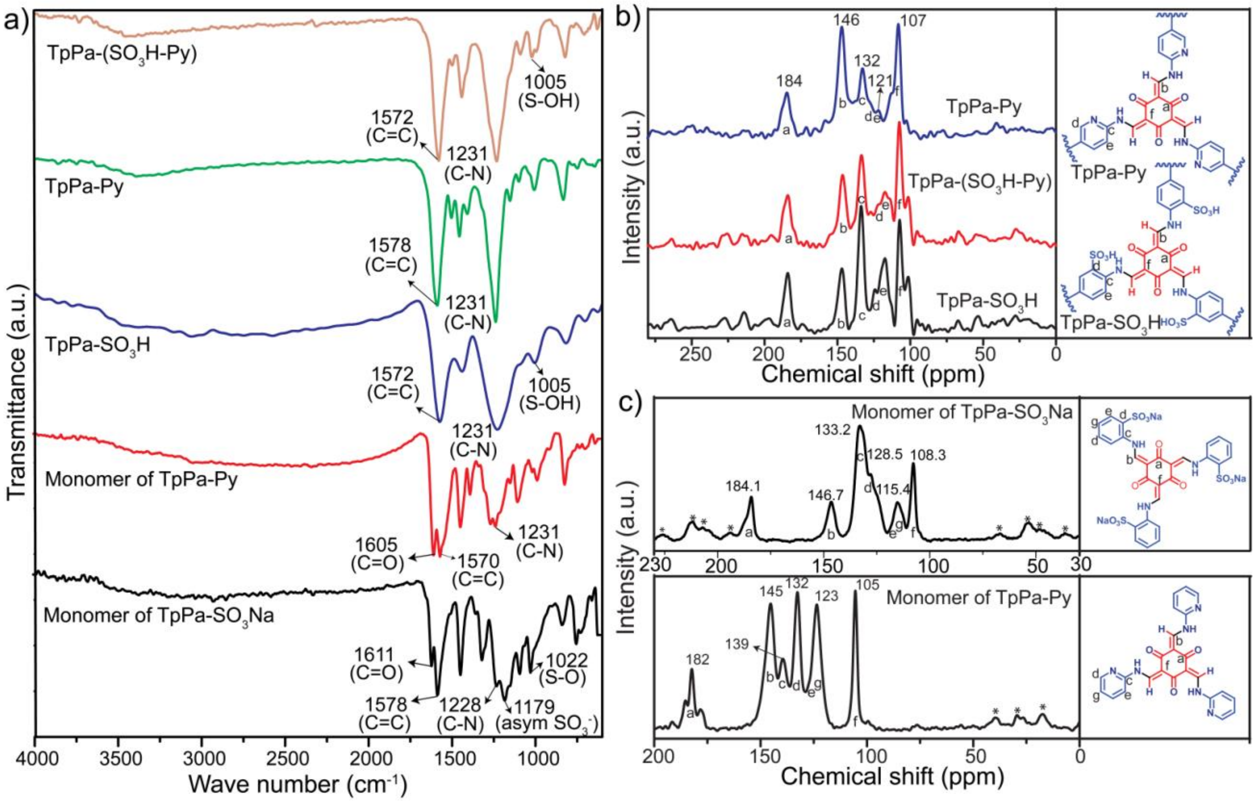

Figure 4.8: (a) FT-IR spectra of ***TpPa-SO₃H*** *and* ***TpPa-Py*** *compared with their reference (monomer) compounds. (b) Solid state ^{13}C CP-MAS spectrum comparison of* ***TpPa-SO₃H*** *(black)****, TpPa-(SO₃H-Py)*** *(red) and* ***TpPa-Py*** *(blue). (c) Solid state ^{13}C CP-MAS spectrum of the reference compound* ***TpPa-SO₃Na monomer*** *= Trisodium salt of 2,4,6-tris[(2-sulfophenylamino)methylene]cyclohexane-1,3,5-trione and* ***TpPa-Py monomer*** *= (2,4,6-tris[(3-pyridylamino)methylene]cyclohexane-1,3,5-trione). (*) represent the spinning side band.*

The Cross-Polarization Magic Angle Spinning (CP-MAS) ^{13}C solid state NMR spectroscopy indicated the existence of the keto tautomer rather than the enol by the presence of the peak at ~184 ppm due to the keto (-C=O) group [4.36] (Figure 4.8b). In addition, ^{13}C solid-state NMR spectra for these COFs matched well with the reference compound, which signifies a similar structural environment in all the COFs (Figure 4.8b and 4.8c). The slightly broad peak at 75 ppm for phytic acid doped COFs [phytic**@TpPa-SO₃H,** phytic **@TpPa-Py** and phytic **@TpPa-(SO₃H-Py)**] appeared due to the presence of the phytate anions irrespective of their degree of ionization (Figure 4.9a).The down field shift of the peaks for phytic acid loaded COFs as compared to the pure phytic acid in ^{31}P CP- MAS indicates the H-bonding between the phytic acid molecules with the COF framework (Figure 4.9b).

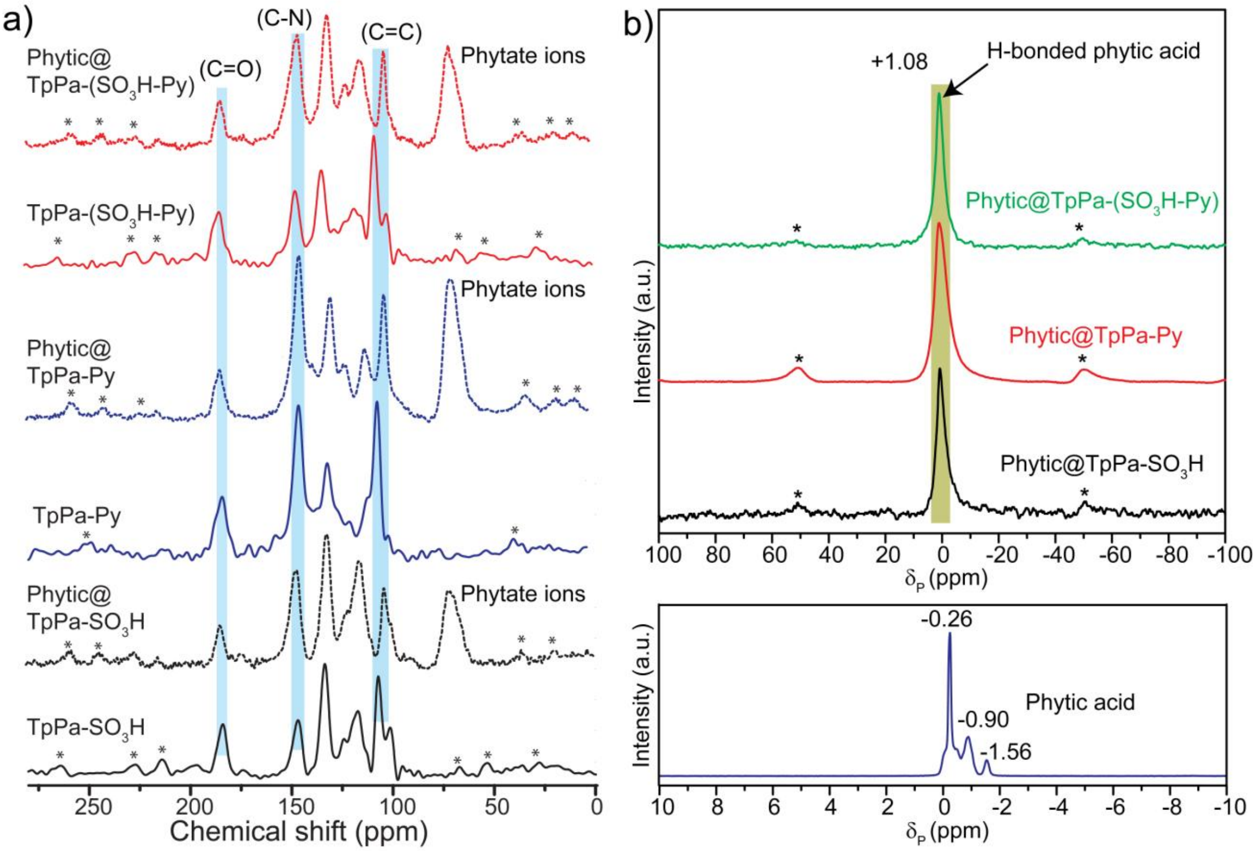

***Figure 4.9**: (a) Solid state ^{13}C CP-MAS spectrum comparison of **TpPa-SO$_3$H** (solid black line)**, TpPa-Py** (solid blue line) and **TpPa-(SO$_3$H-Py)** (solid red line) with their phytic acid loaded COFs (dotted line). (b) Solid state ^{31}P CP-MAS spectra comparison between phytic acid loaded **TpPa-SO$_3$H** (black)**, TpPa-Py** (red) and **TpPa-(SO$_3$H-Py)** (green) with pure phytic acid (blue). (*) represent the spinning side band.*

We have performed XPS analysis of the three COFs [**TpPa-SO$_3$H, TpPa-Py**, and **TpPa-(SO$_3$H-Py)**] in order to get further insight into the compositions and interaction. The binding energy of N1s of **TpPa-SO$_3$H** shows two types of nitrogens, one at 400.2 eV for the free secondary amine (–NH) and another at 402.3 eV for the protonated secondary amine (–NH$_2^+$). Similarly, the XPS study of **TpPa-Py** shows two different types of nitrogens; one at 398.5 eV for the pyridinic (-C$_5$H$_3$N) nitrogen and the next one at 400.2 eV that alludes to the free secondary amine (–NH). To ensure that the hybrid COF [**TpPa-(SO$_3$H-Py)**] contains both pyridinic and sulfonic acid functionality within the COF backbone, we have compared the XPS data of all three COFs. The N1s peak at 401.1 eV and S2p peak at 167.0 eV in **TpPa- (SO$_3$H-Py)** originate from the pyridinium (-C$_5$H$_3$NH$^+$) and sulfonate (SO$_3^-$) ions respectively which form due to the protonation of the pyridinic N by the -SO$_3$H group. Notably, the N1s peak of pyridinium ion (-C$_5$H$_3$NH$^+$) is absent in the case of **TpPa-Py** and **-SO$_3$H** (Figure 4.10).

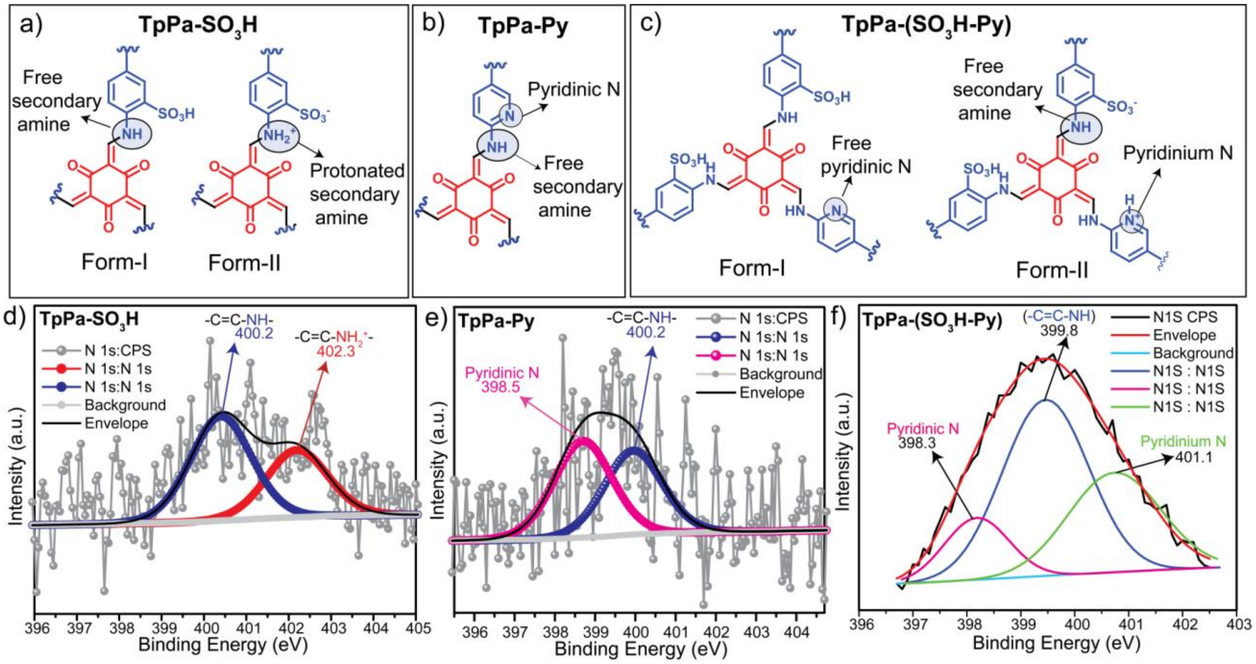

Figure 4.10: *(a), (b), (c) are the probable chemical structures of* ***TpPa-SO$_3$H****,* ***TpPa-Py****,* ***TpPa-(SO$_3$H-Py)*** *and (d), (e), (f) are the corresponding binding energy of N1s respectively.*

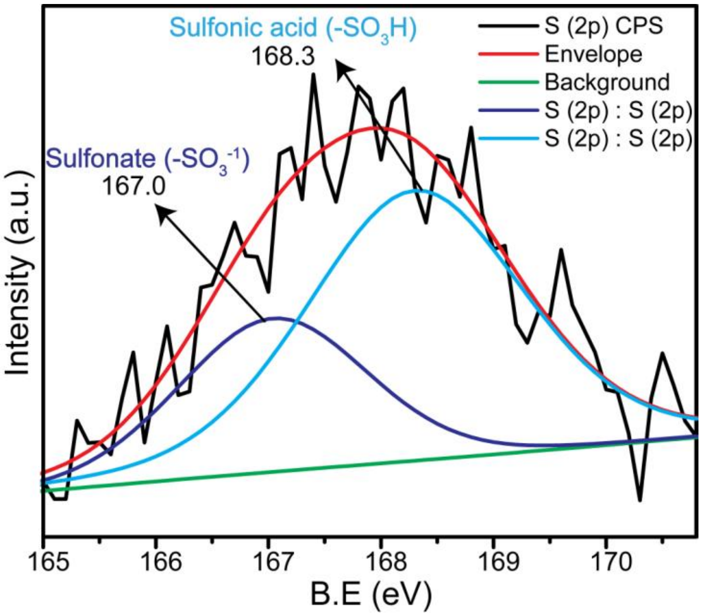

Figure 4.11: *Binding energy of S2p for hybrid COF* ***TpPa-(SO$_3$H-Py)****.*

The weight percentage ratio of N/S for hybrid COF **TpPa-(SO$_3$H-Py)**, as obtained from the elemental analysis, matches well with the simulated structure where the sulfonic acid unit (**Pa-SO$_3$H**) and pyridinic unit (**Pa-Py**) are distributed in 1:1 ratio. To further confirm that the hybrid COF **TpPa-(SO$_3$H-Py)** is not a physical mixture of **TpPa-SO$_3$H** and **TpPa-Py**, we have compared the values with an equimolar (1:1) physical mixture of the individual COFs where the ratio of sulfonic group unit and the pyridinic unit is 1:1 (Figure 4.12).

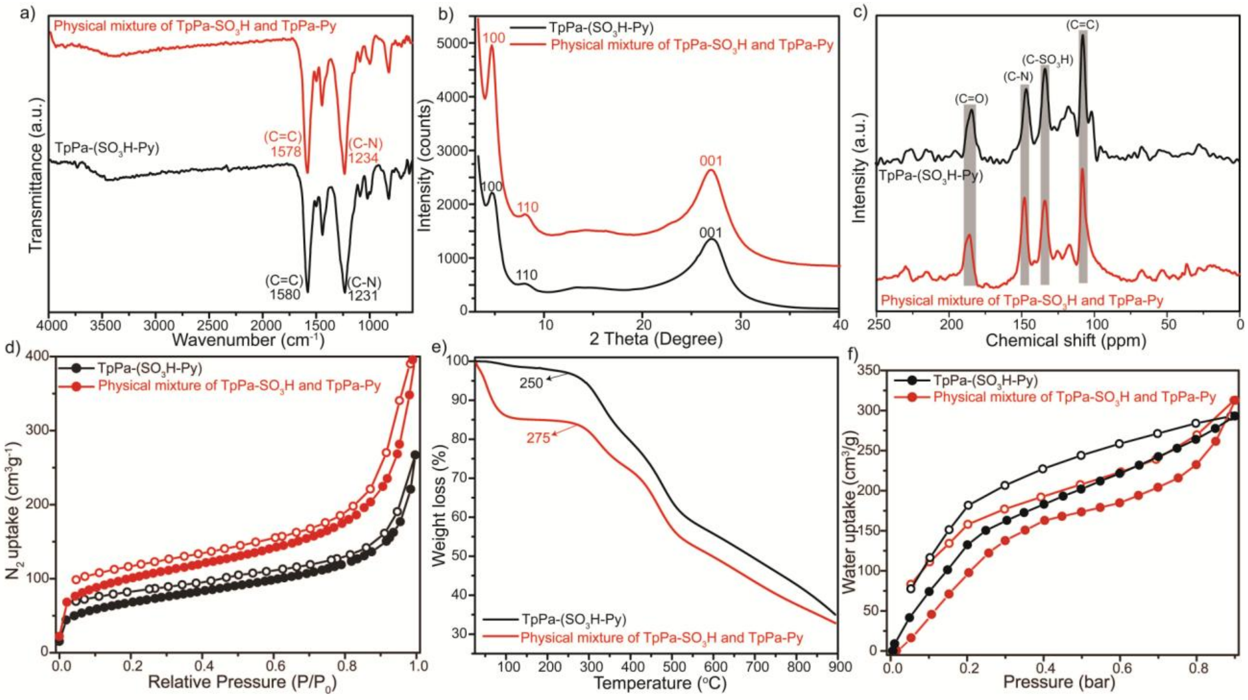

Figure 4.12: *(a) IR, (b) PXRD, (c) ^{13}C-SSNMR, (d) N_2 adsorption isotherms, (e) TGA and (f) Water adsorption comparison between hybrid COF* ***TpPa-(SO_3H-Py)*** *(Black) and physical mixture of* ***TpPa-SO_3H*** *and* ***TpPa-Py*** *(Red).*

(a) Physical mixture of TpPa-SO$_3$H and TpPa-Py

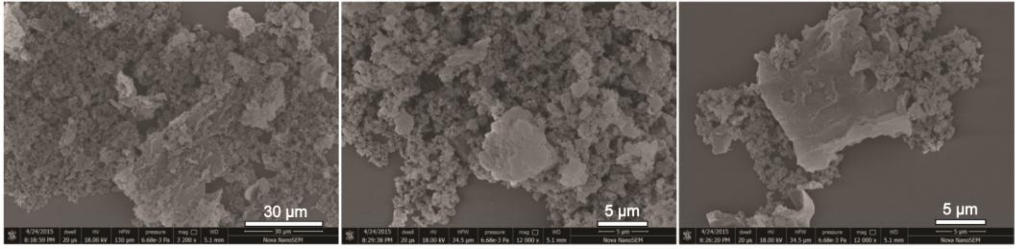

(b) TpPa-(SO$_3$H-Py)

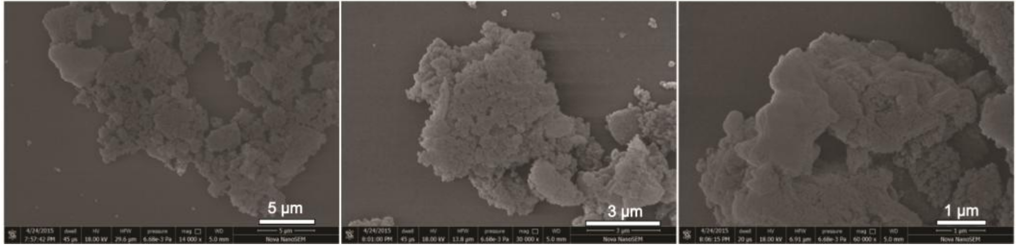

Figure 4.13: *Difference between the SEM images of (a) Physical mixture of* ***TpPa-SO_3H*** *and* ***TpPa-Py****, (b)* ***TpPa-(SO_3H-Py)****.*

The morphological homogeneity observed in the SEM images of hybrid COF **TpPa-(SO_3H-Py)** clearly omits the possibility of formation of a mixture of **TpPa-SO_3H** and **TpPa-Py** (Figure 4.13**).** All the three COFs [**TpPa-SO_3H, -Py** and **-(SO_3H-Py)**] have a fibrous type of morphology that were analyzed from their FESEM and TEM images (Figure 4.14). The EDX- mapping of all three phytic acid loaded COFs revealed a uniform distribution of phytic acid (Figure 4.17).

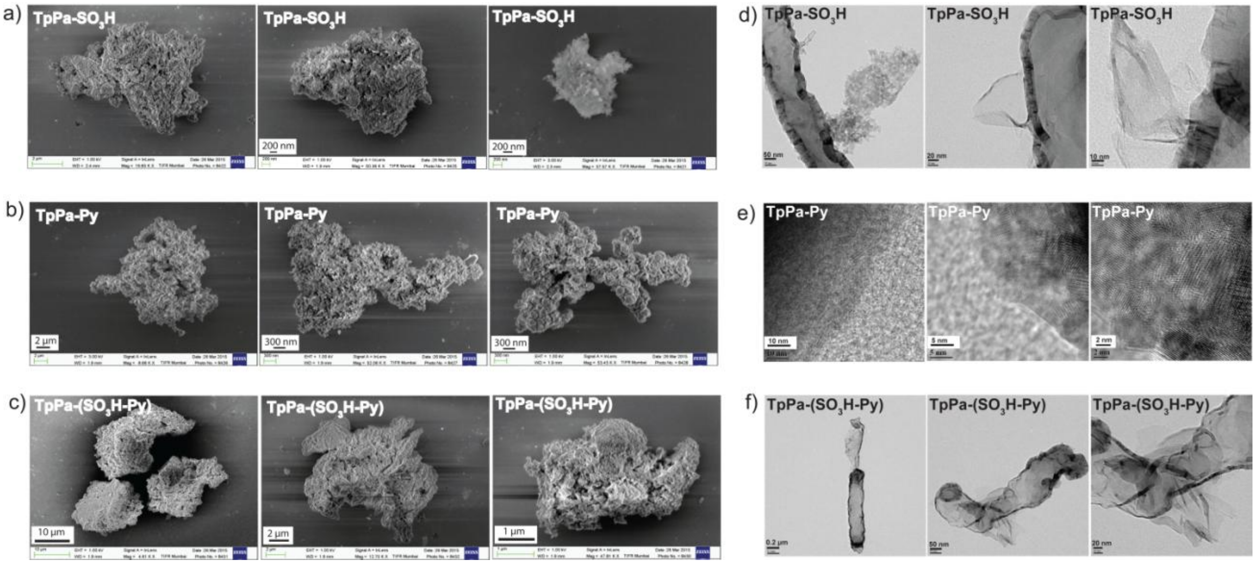

Figure 4.14: *(a)-(c) SEM images and (d)-(f) TEM images of* ***TpPa-SO_3H****,* ***TpPa-Py*** *and* ***TpPa-(SO_3H-Py)*** *respectively.*

The TGA of the activated COF samples shows no weight loss till 250 °C (Figure 4.15a). However, the as-synthesized **TpPa-SO_3H** and **-(SO_3H-Py)** exhibit three stage weight loss 50-120 °C, 220-380 °C and above 380 °C. The initial weight loss is due to the removal of occluded solvent molecules, second stage weight loss is account for the disintegration of sulfonic acid groups and the third one due to the decomposition of COF backbones (Figure 4.15a). Above 200 °C both the crystallinity and porosity decreases suggesting framework decomposition. The thermal stability of the pristine COFs have also been tested by IR and PXRD (Figure 4.15b and 4.15c). In the case of phytic acid loaded samples the gradual weight loss above 130 °C can be attributed to the self-condensation of the phosphonic acid groups (Figure 4.16). The phytic acid doped COFs were also stable at 150 ºC, which confirm from their IR spectrum (Figure 4.15d).

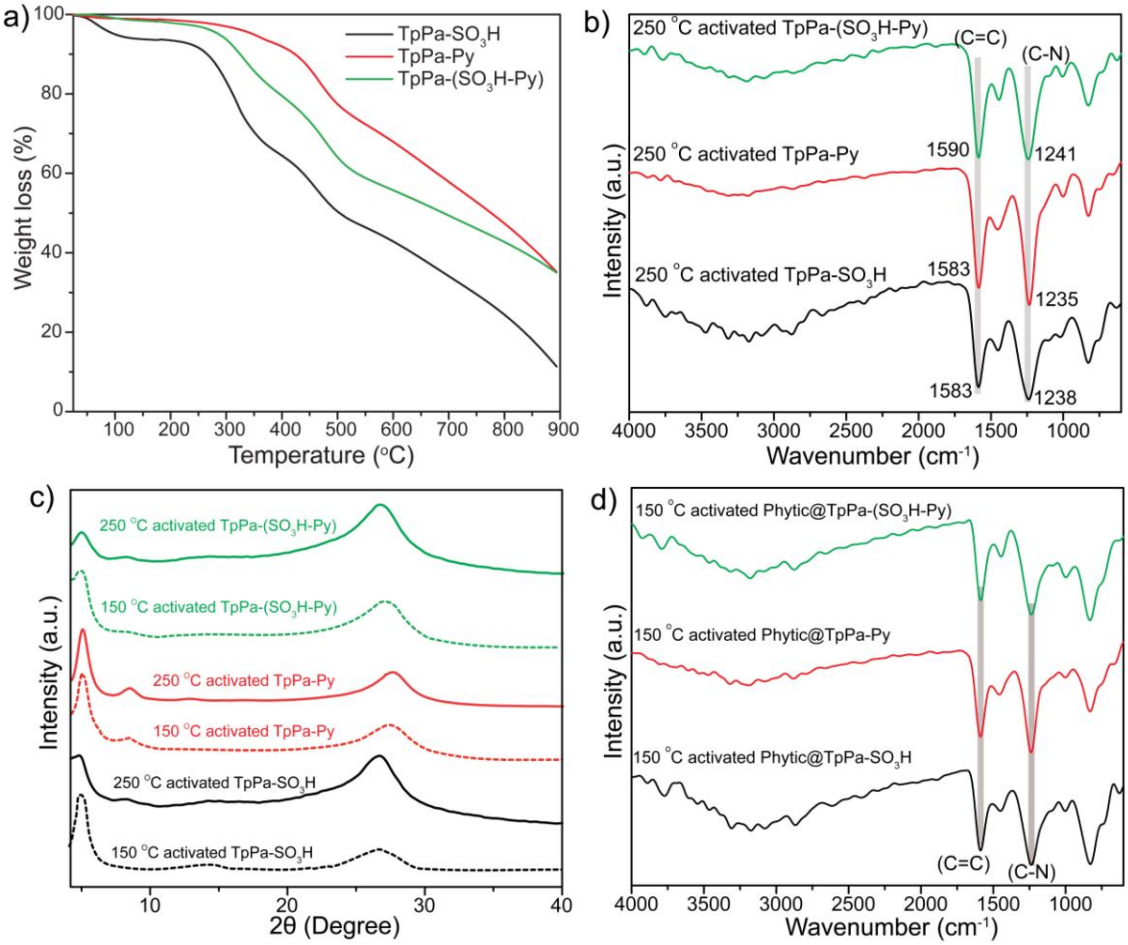

Figure 4.15: *(a)TGA of* ***TpPa-SO$_3$H*** *(black)****,*** ***TpPa-Py*** *(red) and* ***TpPa-(SO$_3$H-Py)*** *(green) under N$_2$ atmosphere after. (b) FT-IR spectra of 250 ℃ activated* ***TpPa-SO$_3$H*** *(black)****,*** ***TpPa-Py*** *(red) and* ***TpPa-(SO$_3$H-Py)*** *(green). (c) PXRD comparison between 250 ℃ activated (solid line) and 150 ℃ activated (dash line)* ***TpPa-SO$_3$H*** *(black)****,*** ***TpPa-Py*** *(red) and* ***TpPa-(SO$_3$H-Py)*** *(green). (d) FT-IR spectra of 150 ℃ activated phytic acid loaded COFs; Phytic@* ***TpPa-SO$_3$H*** *(black)****,*** *Phytic@****TpPa-Py*** *(red) and Phytic@* ***TpPa-(SO$_3$H-Py)*** *(green).*

The amount of the phytic acid in the COFs will surely affect the measurement results. For this purpose, in our conductivity experiments, we have considered the COFs with the optimum loading of phytic acid to ensure the reproducibility of the results. The optimum loading was achieved by impregnating with 1:1 aqueous phytic acid solution and washing with a copious amount of water to remove surface adhered phytic acid that might otherwise hinder reproducibility. It was observed from TGA that the optimum loadings of phytic acid are 3.18, 5.62 and 4.11 wt% for **TpPa-SO$_3$H**, **TpPa-Py** and **TpPa-(SO$_3$H-Py)** respectively (Figure 4.16). The loading of phytic acid and the proton conductivity is not linear suggests that in addition to the amount of loaded phytic acid, the number of –SO_3H groups present in the framework plays a vital role in the proton conductivity.

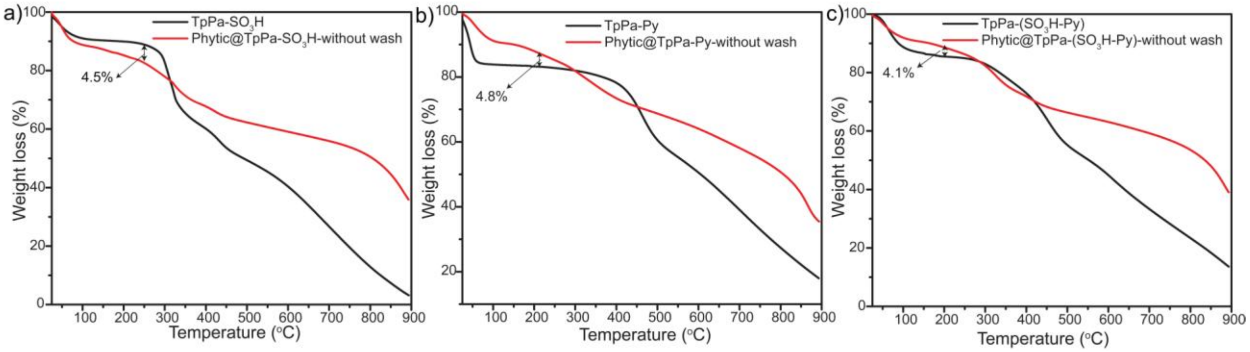

Figure 4.16: *TGA data of activated (a)* ***TpPa-SO$_3$H*** *(black) compared with Phytic@* ***TpPa-SO$_3$H*** *(red); (b)* ***TpPa-Py*** *(black) compared with Phytic@****TpPa-Py*** *(red) and (c)* ***TpPa-(SO$_3$H-Py)*** *compared with Phytic@* ***TpPa-(SO$_3$H-Py)*** *(red) under N_2 atmosphere.*

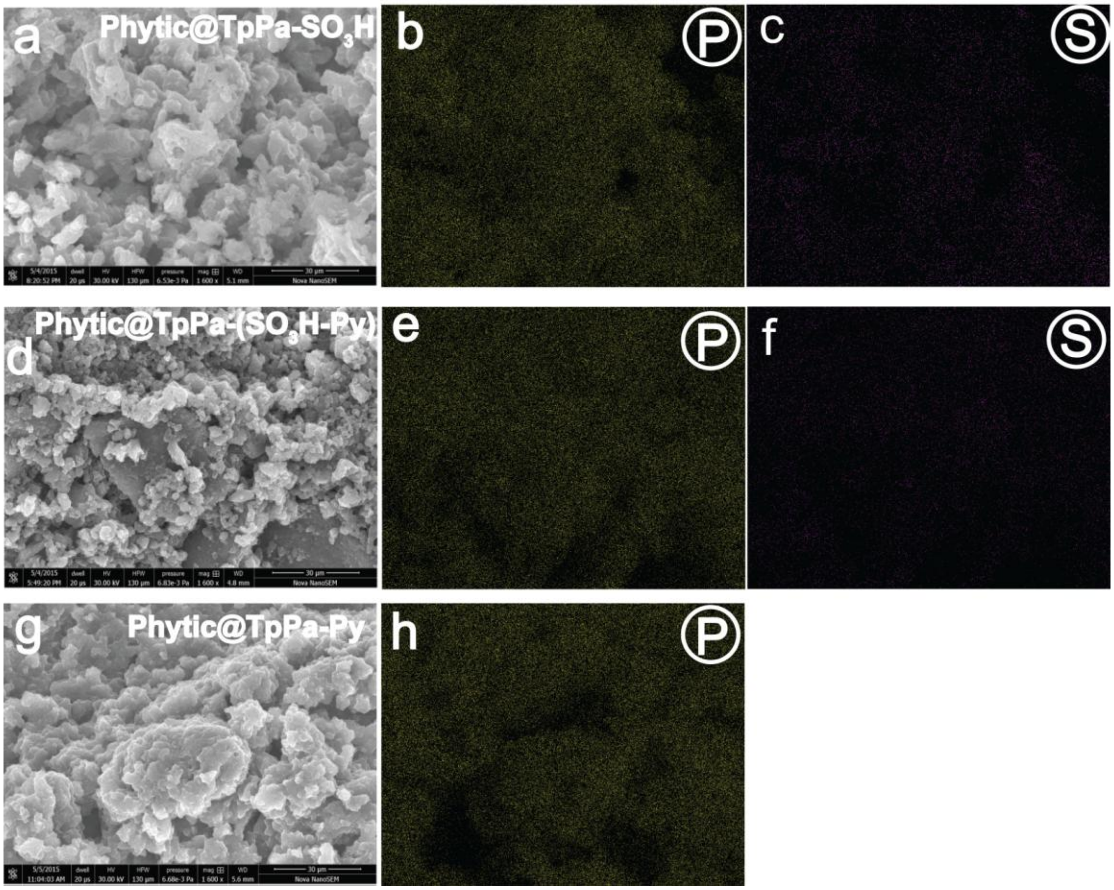

Figure 4.17: *Elemental distribution of phytic@****COFs*** *probed by EDS-mapping: (a) FETEM image, (b) distribution of phosphorus, (c) distribution of sulfur for phytic@****TpPa-SO$_3$H****; (d) FETEM image, (e) distribution of phosphorus, (f) distribution of sulfur for phytic@****TpPa-(SO$_3$H-Py)****; (g) FETEM image and (h) distribution of phosphorus for phytic@****TpPa-Py****.*

4.2.5 *Gas and water vapour adsorption studies*

The BET surface areas for **TpPa-SO_3H, TpPa-(SO_3H-Py)** and **TpPa-Py** are 215, 235 and 370 m^2g^{-1} respectively (Figure 4.18). The low surface area of the sulfonic acid based COFs [**TpPa-SO_3H** and **TpPa–(SO_3H-Py)**] results due to the steric bulkiness of the functional –SO_3H groups [4.12] which can be explained by calculated the the Nitrogen Accessible Surface Areas (NASA) of the lowest energy geometry of **TpPa-SO_3H**, **TpPa-Py** and **TpPa-(SO_3H-Py)** by using the geometric method as performed by Snurr et. al. [4.40] and implemented in the Pore Blazer program [4.41]. Using this method, the surface area varies little (Table 4.4) but the key thing is that the pore limiting diameter of **TpPa-SO_3H** is only 7.6 Å compared to 14 Å for **TpPa-Py** and 11 Å for hybrid **TpPa-(SO_3H-Py)**. So these pores are significantly obstructed by the bulky SO_3H groups. The total DFTB pore volume for **TpPa-SO_3H, -(SO_3H-Py)** and **–Py** are 0.431, 0.273 and 0.281 cm^3g^{-1} respectively.

Table 4.4: Calculated Nitrogen Accessible Surface Areas (NASA) and pore size of the lowest energy geometry of **TpPa-SO_3H**, **TpPa-Py**, and **TpPa-(SO_3H-Py)**.

	TpPa-SO_3H	**TpPa-Py**	**TpPa-(SO_3H-Py)**
Accessible surface area in $Å^2$	349.08	325.65	310.83
Accessible surface area per volume in m^2cm^{-3}	1264.77	1109.49	1067.66
Accessible surface area per mass in m^2g^{-1}	1199.58	1534.34	1235.33
Pore limiting diameter in Å	7.63	14.14	11.44
Maximum pore diameter in Å	11.15	14.43	12.01

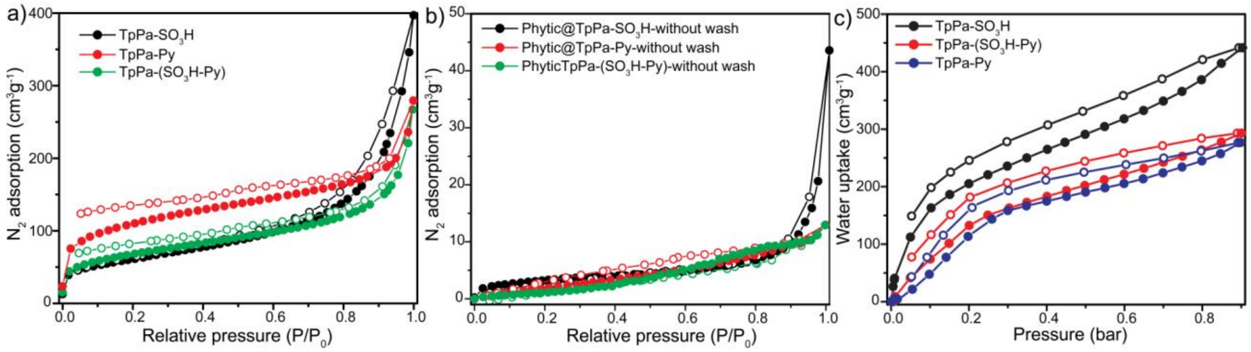

***Figure 4.18**: N_2 adsorption isotherms of (a) COFs; **TpPa-SO_3H** (black), **TpPa-Py** (red), **TpPa-(SO_3H-Py)** (green) and (b) phytic acid loaded COFs; Phytic@**TpPa-SO_3H** (black), Phytic@**TpPa-Py** (red) and Phytic@**TpPa-(SO_3H-Py)** (green). (c) Water adsorption of **TpPa-SO_3H** (black), **TpPa-Py** (red) and **TpPa-(SO_3H-Py)** (blue) collected up to P/P_o=0.9 (STP) at 293 K.[filled symbols for adsorption and empty symbols for desorption.]*

Pore size distributions of **TpPa-SO$_3$H** and **TpPa-(SO$_3$H-Py)** suggests a pore diameter of ~14.5 Å and for **TpPa-Py** it is ~14.8 Å (Figure 4.19), a value also obtained from the modeled structure. The irregular pore size distribution is expected to arise from few inter-particle voids as well as lack of sufficient long range ordering (as evident from the XRD) of these 2D COFs, especially sulfonic acid based one.

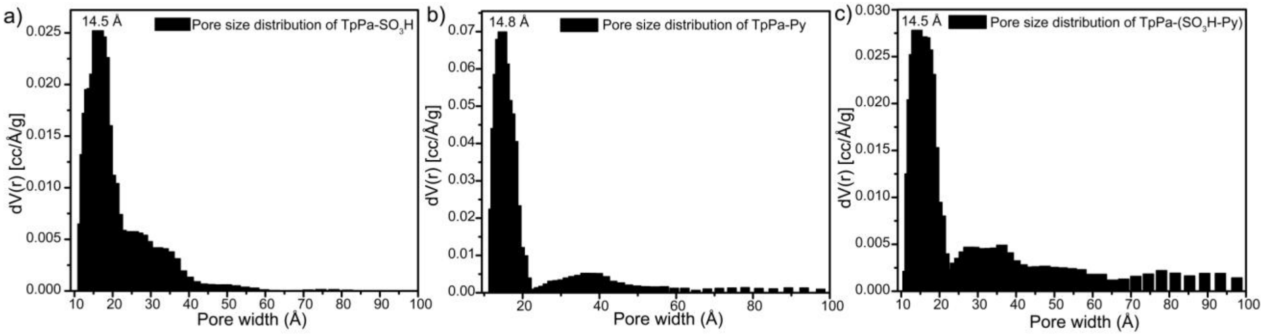

Figure 4.19: *NLDFT Pore size distribution of (a)* ***TpPa-SO$_3$H ,*** *(b)* ***TpPa-Py*** *and (c)* ***TpPa-(SO$_3$H-Py)****.*

4.2.6 *Chemical stability investigation*

It is to be noted that the impregnation of phytic acid molecules inside the COFs and the pelletization of the COF powders did not rupture their framework architecture, confirmed by checking the bulk crystallinity (Figure 4.20 and 4.21c), IR (Figure 4.21a), ^{13}C NMR (Figure 4.21b) and SEM (Figure 4.21d) of these COF samples. However, the absence of low angle peaks in PXRD for phytic acid loaded COFs is due to the X-ray absorption and/or scattering by impregnated phytic acid (Figure 4.20).

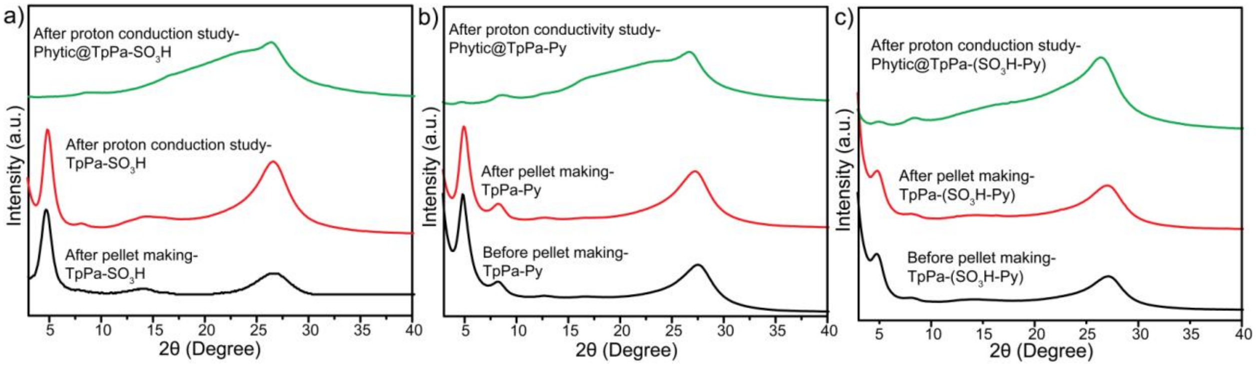

Figure 4.20: *PXRD comparison of as synthesized COFs (black) with before proton conductivity studies (red) and after proton conductivity studies (green) for (a)* ***Tp-SO$_3$H****; (b)* ***TpPa-Py*** *and (c)* ***TpPa-(SO$_3$H-Py)*** *respectively.*

Notably, the crystallinity of all three pristine COFs were largely restored upon prolonged water treatment of the phytic acid loaded COFs (phytic@COFs) (Figure 4.21c).

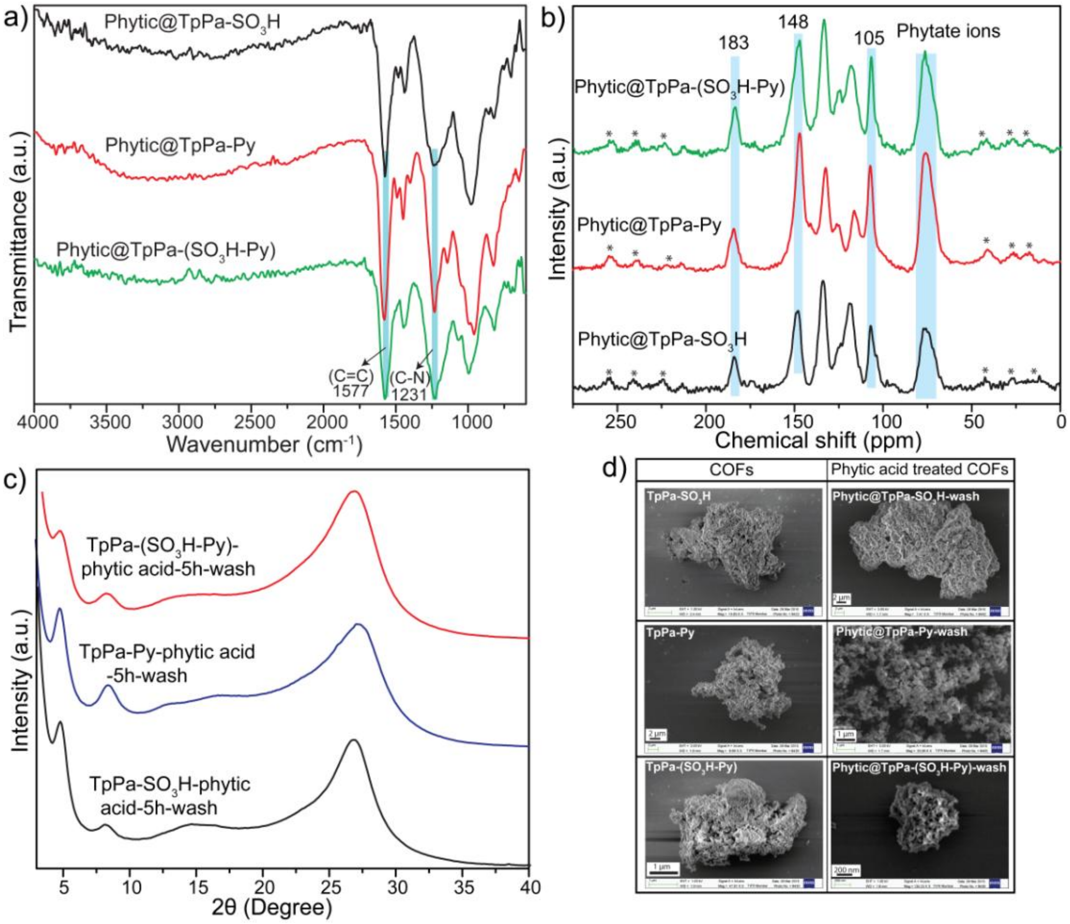

Figure 4.21: *(a) FT-IR spectra of Phytic@**TpPa-SO$_3$H** (black)**,** Phytic@**TpPa-Py** (red) and Phytic@**TpPa-(SO$_3$H-Py)** (green). (b) Solid state ^{13}C CP-MAS spectrum of Phytic@**TpPa-SO$_3$H** (black)**,** Phytic@**TpPa-Py** (red) and Phytic@**TpPa-(SO$_3$H-Py)** (green). (c) PXRD comparison phytic acid treated **TpPa-SO$_3$H** (black)**, TpPa-Py** (blue) and **TpPa-(SO$_3$H-Py)** (red). (d) Comparison of SEM of COFs with phytic acid treated COFs.*

4.2.7 *Proton conductivity studies*

All the proton conductivities were measured in the anhydrous medium in a temperature range between 25-130 °C. The **TpPa-SO$_3$H** exhibits a conductivity of 1.2 × 10^{-5} Scm^{-1} at 25 °C under the anhydrous condition, as evident from the Nyquist plots. The conductivity reaches a maximum of 1.7 × 10^{-5} Scm^{-1} at 120 °C (Figure 4.22c). The proton conduction is aided by the sulfonic acid units within the linker backbone, which acts as a proton source and the polar groups (S=O, NH, C=O) situated in very close proximity act as a proton transporter within the COF backbone. However, the **TpPa-Py** and **TpPa-(SO$_3$H-Py)** didn't exhibit proton conductivity under similar conditions. The absence of protogenic groups in **TpPa-Py** and immobilization of the proton by the pyridinic nitrogen in **TpPa-(SO_3H-Py)** are presumed to be the main reasons for their non-conductiveness. Notably, this observation also establishes the necessary structure to property relationship of the COFs for proton conduction.

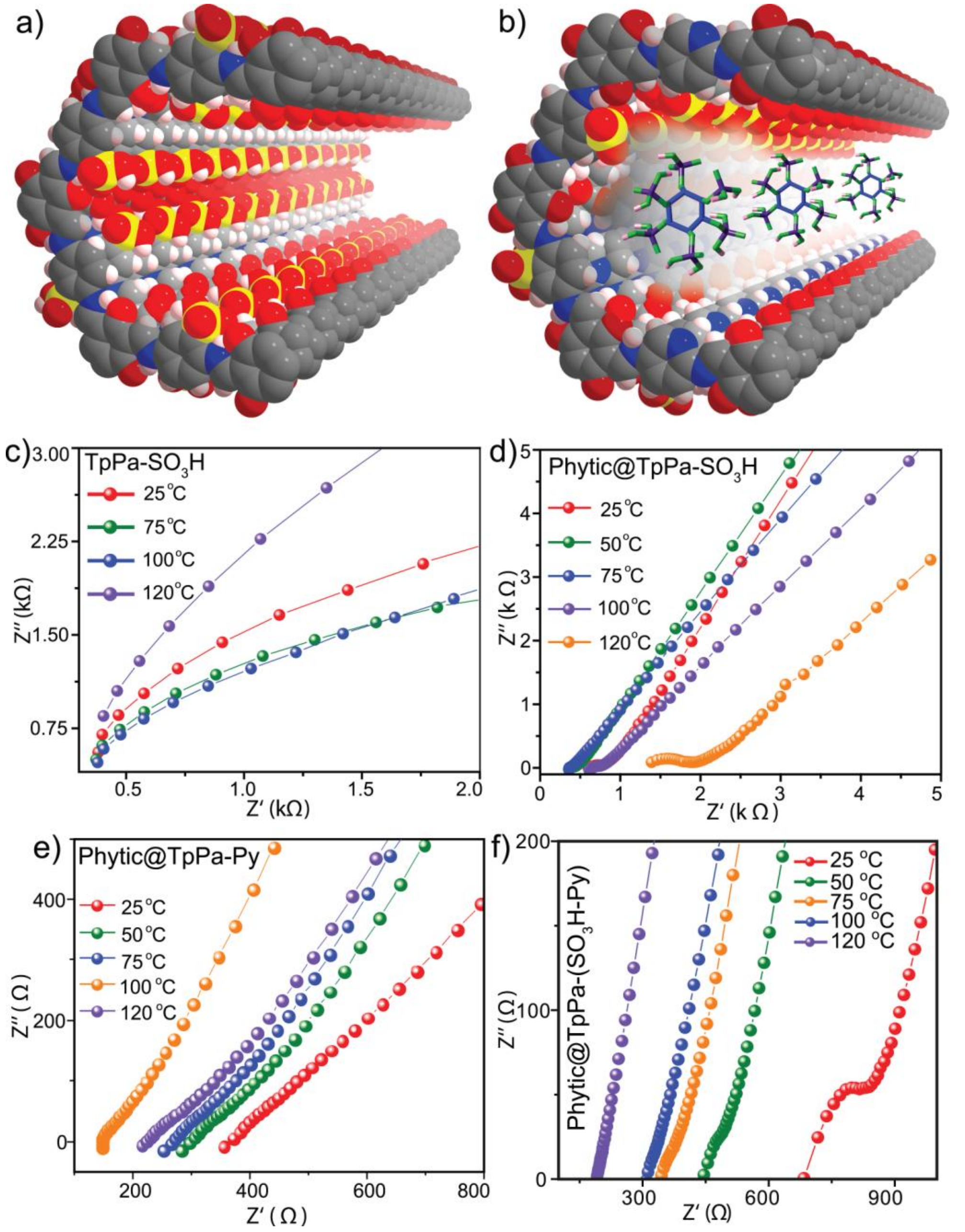

Figure 4.22: *(a) and (b) are the graphical representations of proton conduction pathways inside the hexagonal nanochannels of **TpPa-SO3H** and phytic acid loaded **TpPa-(SO3H-Py)**respectively. Nyquist plots for (c) **TpPa-SO_3H**, (d) phytic**@TpPa-SO_3H**, (e) phytic@**TpPa-Py** and (f) phytic@**TpPa-(SO_3H-Py)** respectively in anhydrous condition at different temperatures.*

The proton conductivity (σ = Σ n.q.μ) in solid state materials can be improved by tuning three independent functions, i.e. the density of mobile protons (n), charge (q) and the mobility (μ) of the protons. Notably, in previous accounts, the conductivity was achieved by impregnating H_3PO_4 molecules inside COF pores [4.21]. Herein, we have decided to enhance the proton conductivity by introducing phytic acid as the proton source and carrier inside the porous architecture of the COFs.

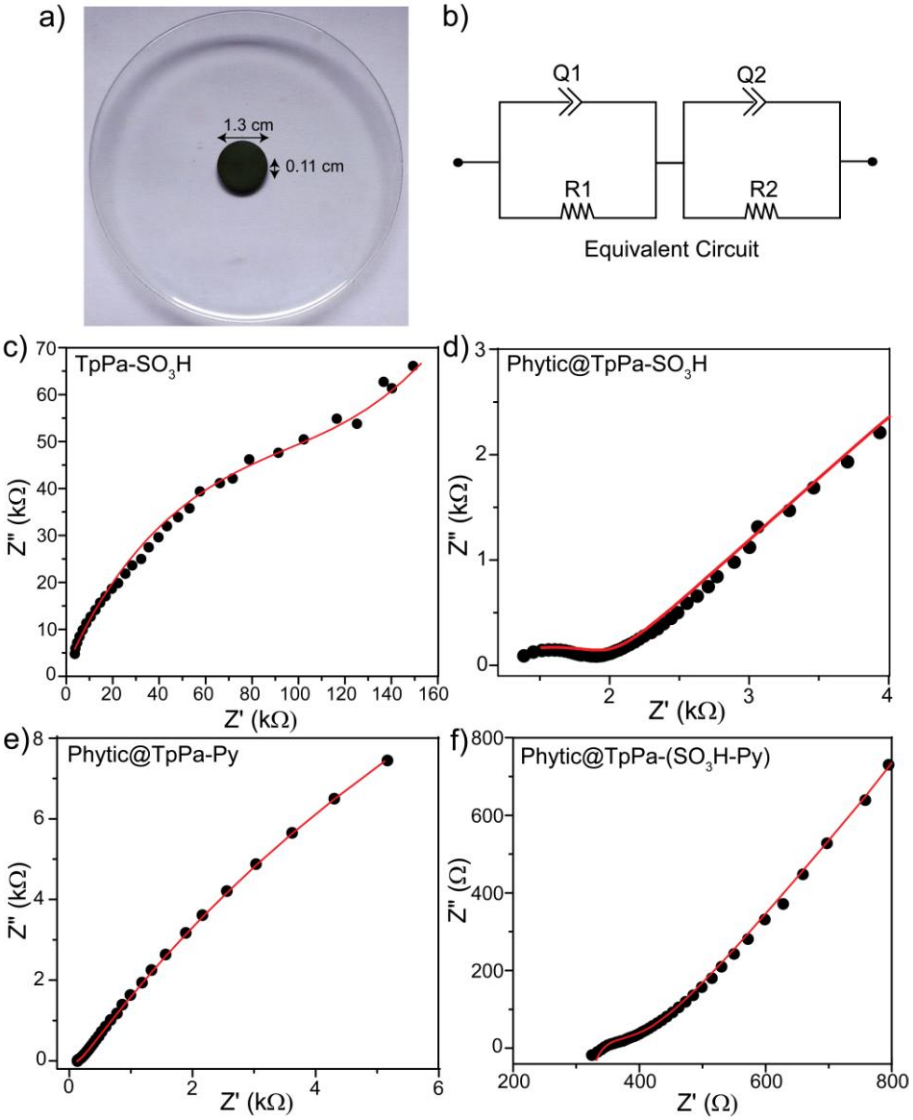

Figure 4.23: *(a) Digital image of the pallet of **TpPa-SO_3H** used for proton conductivity measurements with dimension.(b) (R_1/Q_1)(R_2/Q_2) as an equivalent circuit for the proton conduction in COFs wherein R_1, R_2 represent resistors and Q_1, Q_2 represent imperfect capacitors in the circuit. Black dots (●) are experimental data and the red line (▬) are the simulated data from the (R_1/Q_1)(R_2/Q_2) as equivalent circuits on Nyquist plots for (c) **TpPa-SO_3H**, (d) phytic**@TpPa-SO_3H**, (e) phytic@**TpPa-Py** and (f) phytic@**TpPa-(SO_3H-Py)** respectively.*

We have chosen phytic acid over H_3PO_4 as i) the low volatility of phytic acid over H_3PO_4 increases the higher temperature operational possibilities, and ii) the dimension of phytic acid (ca. 11 Å) is comparable with the COF pores (ca. 14.5 Å) that may prevent the leaching problem. The phytic acid loaded **TpPa-SO$_3$H** (phytic**@TpPa-SO$_3$H**) shows only slightly improved proton conductivity of 7.5×10^{-5} Scm^{-1} at 120 °C (Figure 4.22d). On the other hand, in the case of phytic**@TpPa-Py**, the conductivity was 3.0×10^{-4} Scm^{-1} at 120 °C that was comparatively higher due to the immobilization of the phytic acid by the basic pyridinic nitrogen (Figure 4.22e). The phytic**@TpPa-(SO$_3$H-Py)** exhibits highest proton conductivity of 5×10^{-4} Scm^{-1} at 120 °C due to the operation of both the phenomena a) the intrinsic conductivity due to the – SO_3H group and b) the extrinsic conductivity *via* the immobilization of the phytic acid by the pyridinic nitrogen (Figure 4.22f). The aforementioned phenomena establish the logic behind the preparation of the hybrid COF for proton conduction, where properties of both the linkers could be leveraged to achieve higher proton conductivity. The temperature dependent proton conductivity values were utilized to calculate the activation energy of the systems. For example, phytic**@TpPa-Py** exhibits an activation energy of 0.10 Ev while phytic**@TpPa-(SO$_3$H-Py)** has an activation energy of 0.16 Ev (Figure 4.24).

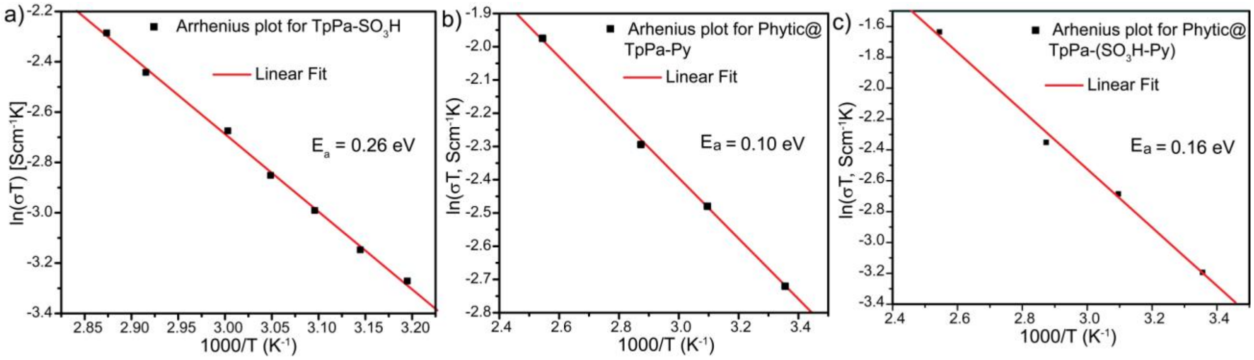

Figure 4.24: *(a), (b) and (c) are the activation energy plot for phytic@**TpPa-SO$_3$H,** phytic@**TpPa-Py** and phytic@**TpPa-(SO$_3$H-Py)** respectively.*

To check the reproducibility of proton conductivity we have performed the proton conductivity of COF pellets at variable conditions and using different pellet widths to ensure the reproducibility of measurements. The proton conductivity of three different pellets made from three different batches of **TpPa-SO$_3$H** having an almost same width (0.92-0.94mm) yielded a value of $1.7(\pm1) \times 10^{-5}$ Scm^{-1} at 120 °C for at least 24h and has been reproduced for 3 different runs (Figure 4.25a). Such reproducibility has also been demonstrated for Phytic@**TpPa-(SO_3H-Py)** under similar condition. Moreover, to assay the role of pellet width on proton conductivity we have made two different batches of pellets, one having a width of 1.35 mm and another having 0.75 mm (as thinner pellets are more desirable in fuel cell systems). Interestingly, both the pellets exhibit same proton conductivity of 5(±2) x 10^{-4} Scm^{-1} at 120 °C (Figure 4.25b).

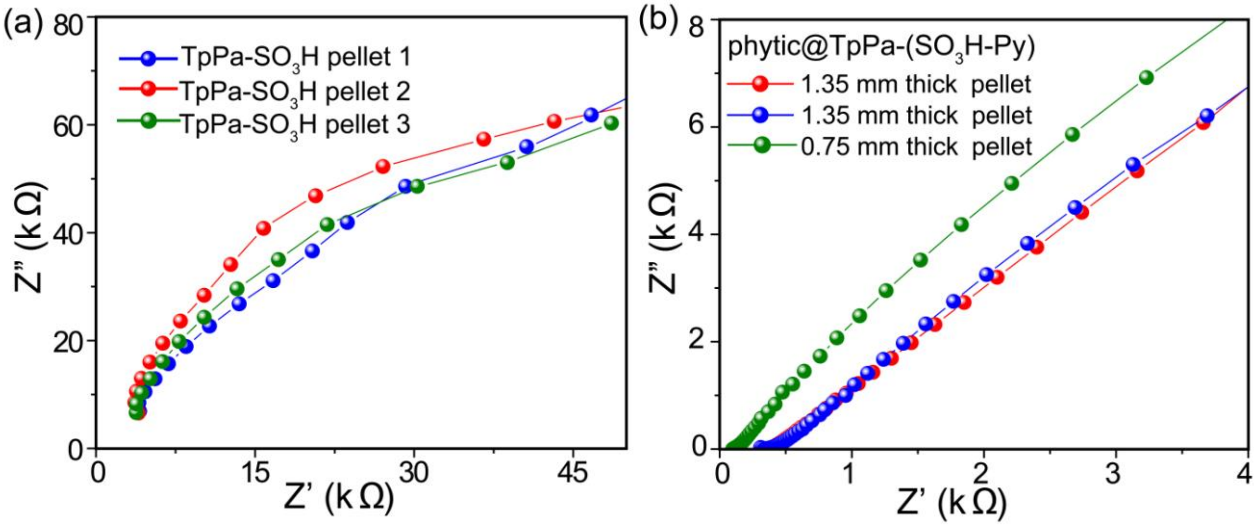

Figure 4.25: (a) proton conductivity of three different pellets of ***TpPa-SO_3H*** *(prepared using samples from three different batches) having the same width (0.92-0.94mm) of the pellets.(b) the proton conductivity of phytic acid loaded* ***TpPa-(SO_3H-Py)*** *with different pellet widths; 0.75 mm (green) and 1.35 mm (red and blue).*

It is noteworthy that the values are lower than Nafion, but are comparable to the previously reported **PA@Tp-Azo** COF, and most of the state of the art MOFs (Table 4.5).

Table 4.5: Comparison of proton conductivity of phytic acid loaded COFs with state of the art MOFs and COFs.

	Compound Name	**Conductivity ($Scm-^1$)**	**Ea (Ev)**	**Conditions**	***References***
1	Im@{Al(μ_2-OH)(1,4-ndc)}$_n$	2.2×10^{-5}	0.6	120 °C, Anhydrous	*Nat. Mater. 2009, 8, 831.*
2	Im@{Al(μ_2-OH)(1,4-bdc)}$_n$	1.0×10^{-7}	0.9	120 °C, Anhydrous	*Nat. Mater. 2009, 8, 831.*
3	β-PCMOF-2(Tz)$_{0.45}$	5.0×10^{-4}	0.34	150 °C, Anhydrous	*Nat. Chem. 2009, 1, 705.*
4	Mg_2(dobdc) · 0.35LiO^{i}Pr · 0.25LiBF$_4$ · EC · DEC	3.1×10^{-4}	0.14	27 °C, Anhydrous	*J. Am. Chem. Soc. 2011, 133, 14522.*
5	His@[Al(OH)(ndc)]$_n$	1.7×10^{-3}	0.25	150 °C,	*Angew. Chem. Int. Ed.*

				Anhydrous	*2011, 50, 11706.*
6	$[Zn(HPO_4)(H_2PO_4)_2]$ $(ImH_2)_2$	2.5×10^{-4}	0.47	130 °C, Anhydrous	*J. Am. Chem. Soc. 2012, 134, 7612.*
7	$[Zn(H_2PO_4)_2(TzH)_2]_n$	1.2×10^{-4}	0.6	150 °C, Anhydrous	*J. Am. Chem. Soc.2012, 134, 12780.*
8	H_2SO_4@MIL-101	1.0×10^{-2}	0.42	150 °C, 0.13% RH	*J. Am. Chem. Soc.2012, 134, 15640.*
9	H_3PO_4@MIL-101	3.0×10^{-3}	0.25	150 °C, 0.13% RH	*J. Am. Chem. Soc 2012, 134, 15640.*
10	$[Zn_2(2,5\text{-DOTP})]_n$-His	4.3×10^{-9}		146 °C, N_2 atmosphere	*Dalton Trans. 2012, 41, 13261.*
11	In-IA-2D-2	2.7×10^{-5}	0.48	77 °C, Anhydrous	*Chem. Commun.2013,49, 6197.*
12	$[Zn_3(H_2PO_4)_6](Hbim)$	1.3×10^{-3}	0.5	120 °C, Anhydrous	*J. Am. Chem. Soc. 2013, 135, 11345.*
13	$(NH_4)_2(adp)[Zn_2(ox)_3]$	10^{-12}		25°C, Anhydrous	*J. Am. Chem. Soc.*, 2014 , *136*, 7701.
14	PA@Tp-Azo	6.7×10^{-5}	0.11	67 °C, Anhydrous	*J. Am. Chem. Soc.* *2014, 136, 6570.*
15	$[ImH_2][Cu(H_2PO_4)_{1.5}(HPO_4)_{0.5} \cdot Cl_{0.5}]$	2.0×10^{-2}	1.1	130 °C, Anhydrous	*Chem. Commun.* *2014, 50, 10241.*
16	$\{[(Me_2NH_2)_3(SO_4)]_2[Zn_2(ox)_3]\}_n$	1.0×10^{-4}	0.13	150 °C, N_2 atmosphere	*Angew. Chem. Int. Ed. 2014, 53, 2638.*
17	Im@Td-PPI 2	3.49×10^{-4}	0.30	90 °C, Anhydrous	*J. Am. Chem. Soc. 2015, 137, 913.*
18	TfOH@MIL-101	$8 \text{ x } 10^{-2}$	0.18	60 °C, 15% RH	*ACS Appl. Mater.* *Interfaces 2014, 6, 5161.*
19	phytic@TpPa-(SO_3H-Py)	5×10^{-4}	0.16	120 °C, Anhydrous	This work
20	phytic@TpPa-SO_3H	7.5×10^{-5}		120 °C, Anhydrous	This work
21	phytic@TpPa-Py	3.0×10^{-4}	0.10	120 °C, Anhydrous	This work
22	TpPa-SO_3H	1.7×10^{-5}		120 °C, Anhydrous	This work

4.3 Summary

In this chapter, we have synthesized a sulfonic acid (-SO_3H) functionalized COF **TpPa-SO_3H** for intrinsic anhydrous proton conduction at 120 °C. Further enhancement of conductivity was achieved by synthesizing a hybrid COF **TpPa-(SO_3H-Py)** and subsequent phytic acid loading. The combined effect of intrinsic and extrinsic proton conductivity in COFs has also been demonstrated for the first time to show anhydrous proton conductivity of 5×10^{-4} Scm^{-1} at 120 °C. We believe that such structure-conductivity relationships in COFs will provide a roadmap towards COF based anhydrous proton conductors in the near future.

4.4 Experimental Procedures

4.4.1 *Materials*

1,3,5-triformylphloroglucinol was prepared from phloroglucinol using literature procedure [4.42]. All other reagents and solvents were commercially available and used as received from Sigma Aldrich and TCI chemicals.

4.4.2 *Synthesis of reference compound for TpPa-SO_3H*

To prevent the solubility problem we have first synthesized the sodium salt of the 2-aminobenzenesulfonic acid by taking (1:2) eq ratio of 2-aminobenzenesulfonic acid and sodium hydroxide and solubilized it in the methanol-water medium. Then, the reference compound was synthesized by the reaction between 1,3,5-triformylphloroglucinol (0.210 g, 1 mmol) and sodium 2-aminobenzenesulfonate (0.624 g, 3.2 mmol) in 30 Ml water-methanol mixture (v/v = 5 Ml : 25 Ml) under refluxing condition for 72h. After this time the solution was cooled to room temperature and the precipitate was collected by filtration, washed with ethanol and dried under vacuum to give 0.130 g (0.192 mmol, 64%) of the sodium salt of reference compound i.e. 2,4,6-tris[(2-sulfophenylamino)methylene]cyclohexane-1,3,5-trione as yellow solid.

IR (powder, cm-1): 1611 (m), 1576 (s), 1438 (s), 1310 (s), 1228 (m), 1168 (m), 1081 (m), 1016 (m), 829 (s).

4.4.3 *Synthesis of reference compound for TpPa-Py*

The reference compound i.e. 2,4,6-tris[(3-pyridylamino)methylene]cyclohexane-1,3,5-trione) was synthesized by the reaction between 1,3,5-triformylphloroglucinol (0.210 g, 1 mmol) and 3-aminopyridine (0.302 g, 3.2 mmol) in 20 Ml ethanol under refluxing condition for three day. After this time the solution was cooled to room temperature and the precipitate was collected by filtration, washed with ethanol and dried under vacuum to give 0.90 g (0.205 mmol, 68.4%) of a yellow solid.

IR (powder, cm^{-1}): 1605 (m), 1570 (s), 1438 (s), 1382 (s), 1260 (w), 1231 (m), 1142 (m), 1096 (s), 980 (s).

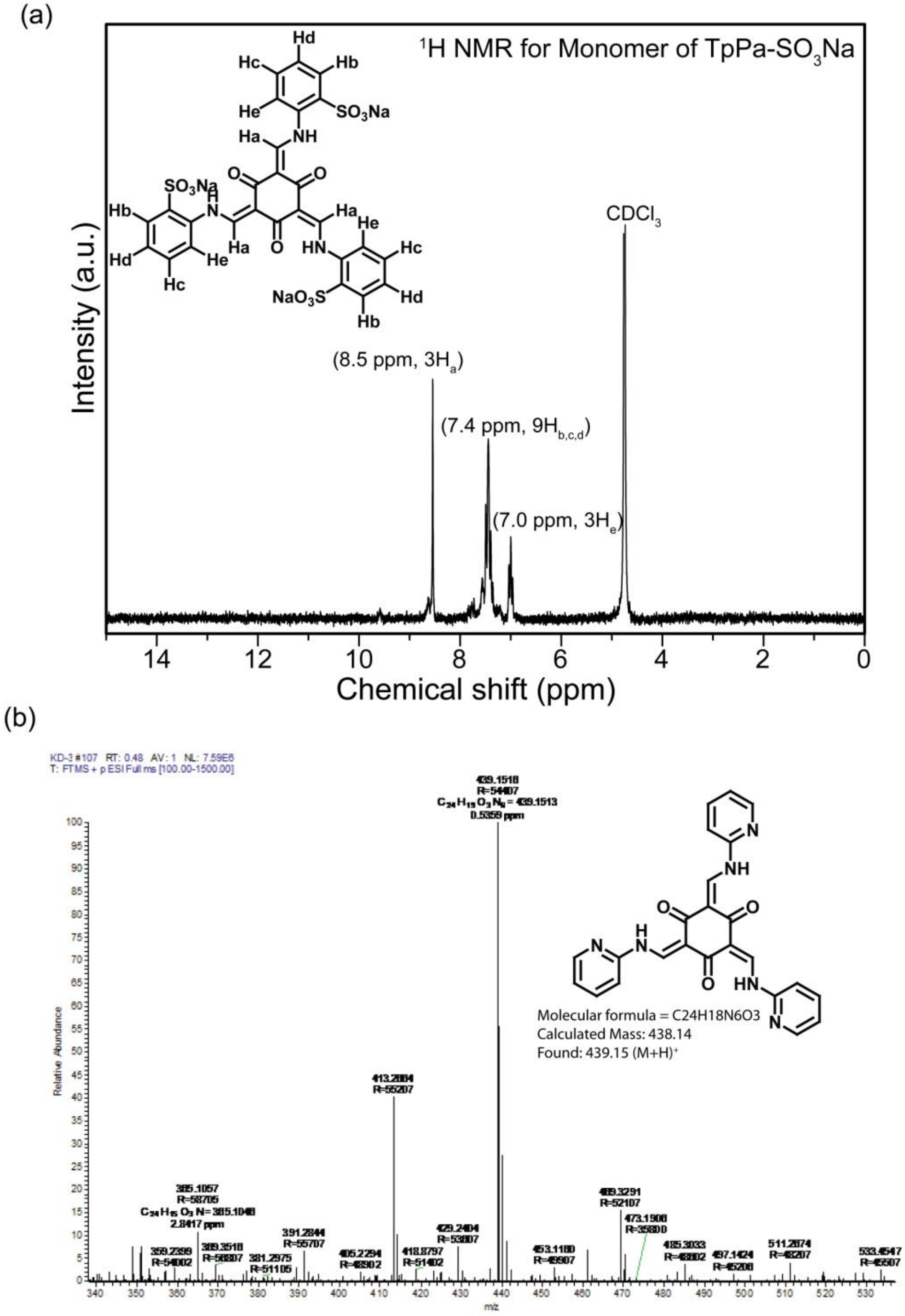

Figure 4.26: *(a) Liquid state ^{1}H-NMR for trisodium salt of 2,4,6-tris[(2-sulfophenylamino)methylene]cyclohexane-1,3,5-trionend) i.e* ***TpPa-SO$_3$Na monomer*** *and (b) HR-MS of 2,4,6-tris[(3-pyridylamino)methylene]cyclohexane-1,3,5-trione i.e* ***TpPa-Py monomer****.*

4.4.4 *Synthesis of TpPa-SO_3H, TpPa-Py and hybrid COF TpPa-(SO_3H-Py)*

In the typical synthesis, a pyrex tube (o.d. × i.d. = 10 × 8 mm^2 and length 18 cm) is charged with 1,3,5-triformylphloroglucinol (**Tp**) (0.3 mmol), 2,5-diaminobenzenesulfonic acid (Pa-SO_3H, 0.45 mmol), 3 Ml (4:1) solvent mixture of mesitylene and 1,4-dioxane with 0.6 Ml of 6(M) acetic acid. This mixture was sonicated for 10 min. In order to get a homogeneous dispersion. The tube was then flash frozen at 77 K (liquid N_2 bath) and degassed by three freeze-pump-thaw cycles. The tube was sealed off and then heated at 120 °C for 72h. A red coloured precipitate was collected by filtration and washed with 1,4-dioxane thrice. The powder collected was then solvent exchanged with acetone 5-6 times and dried at 120 °C under vacuum for 12 h to get corresponding COFs in ~70% isolated yield.

The same synthesis procedure is followed for the synthesis of **TpPa-Py** except for this COF we have taken 2,5-diaminopyridine (Pa-Py, 0.45 mmol) and 3 ml (3:1) solvent mixture of dimethylacetamide and o-dichlorobenzene with 0.6 ml of 6(M) acetic acid. The yield of this COF is ~68%.

In the case of hybrid COF **TpPa-(SO_3H-Py)**, we have taken 2,5-diaminobenzenesulfonic acid (**Pa-SO_3H**, 0.225 mmol) and 2,5-diaminopyridine (**Pa-Py**, 0.225 mmol). The same synthetic procedure and same solvent mixture [mesitylene, 1,4-dioxane and 6M acetic acid in (4:1:1) ratio] as like **TpPa-SO_3H** was followed to give ~60% isolated yield.

FT-IR (**TpPa-SO_3H**, powder, cm^{-1}): 1608 (w), 1572 (s), 1438 (m), 1231 (s), 1084 (w), 1005 (m), 814 (m).

FT-IR (**TpPa-Py**, powder, cm^{-1}): 1608 (w), 1581 (s), 1501 (m), 1451 (m), 1400 (m) 1231 (s), 1145 (w), 1091 (w), 827 (m).

FT-IR {**TpPa-(SO_3H-Py)**, powder, cm^{-1}}: 1608 (w), 1572 (s), 1500 (w), 1442 (m), 1234 (s), 1092 (w), 1026 (w), 1003 (w), 822 (m).

4.4.5 *Phytic acid loading inside COFs*

Activated COFs (150 mg) were added to 10 mL phytic acid (50% aqueous solution) and suspension were stirred for 60 min at room temperature. Then the suspension was filtered and washed with a copious amount of water to remove the surface absorbed acid followed by drying under vacuum at 80 ºC for 5 h. Yield: ca. 190 mg for **phytic@TpPa-SO_3H**; 220 mg for **phytic@TpPa-Py** and 198 mg for **phytic@TpPa-(SO_3H-Py)**.

4.4.6 *General methods for characterization*

All reagents were commercially available and used as received. Microscopy images of these hollow fibers were taken in Zeiss SteREO Discovery V20.

a) ***Wide-angle X-Ray Diffraction (WAXD)*****:** The wide-angle X-Ray Diffraction (WAXD) analysis of MOFs and the composite membranes were carried on a Rigaku SmartLab X-ray diffractometer in reflection mode using CuKα radiation (λ = 1.54 Å). The 2θ range from 5° to 40° was scanned with a scan rate of 3° min^{-1}. The instrument was previously calibrated using a silicon standard.

b) ***FT-IR spectroscopy*****:** The Fourier transform infrared spectra (FT-IR) were taken on a Bruker Optics ALPHA-E spectrometer with a universal Zn-Se ATR (attenuated total reflection) accessory in the 600-4000 cm^{-1} region or using a Diamond ATR (Golden Gate). The spectra were measured over the range of 4000-400 cm^{-1}.

c) ***Scanning Electron Microscopy*****:** Scanning Electron Microscopy (SEM) was performed on an FEI Quanta 200 3D ESEM (dual beam) instrument with a field emitter as an electron source and in FEI Nova Nano SEM 650 Scanning Electron Microscope. SEM images of membrane cross section were taken after freeze cut off membranes in LN_2. Samples for SEM were gold sputtered before analyses.

d) Proton Conductivity Studies of COFs: Proton Conductivities of the COFs were measured using Solartron 1287 Electrochemical Interface with 1255B frequency response analyzer via the quasi-four-probe method. ca.180mg of activated samples were pressed in a pellet maker to obtain uniform pellets of 0.110-0.180 cm thickness, which was subject to the anhydrous chamber and subsequently measured the conductivities at different conditions. Proton conductivity was measured by the following equation; $\sigma = L/(R.A)$ where σ = proton conductivity, L = thickness of the pellet, R = resistance of the pellet and A = area of the pellet. For high-temperature proton conductivity measurements, the pellets were inserted within an anhydrous chamber with flushing of dry N_2.The chamber was encircled with a controlled heating coil jacket attached with an automated temperature controller. The heat flow within the chamber was controlled by a dimmerstat and monitored by an infrared temperature sensor accordingly, having a sensing accuracy of ±0.5 °C.

e) Fractional coordinates of the unit cell of COFs:

Table 4.6: Fractional atomic coordinates for the unit cell of **TpPa-SO$_3$H**.

	TpPa-SO$_3$H **Triclinic; P 1** **a = 22.8345 Å; b = 22.9434 Å; c = 6.8744 Å** **α = 89.8514, β = 89.7964, γ = 120.5433.**		
Atom list	x	y	z
C1	0.98279	0.92925	0.0095
C2	0.05503	0.97458	0.00825
C3	0.08084	0.04513	0.00496
C4	0.03711	0.07238	0.0031
C5	0.96568	0.02714	0.00449
C6	0.93926	0.95715	0.00849
H1	0.13655	0.07961	0.00182
H2	0.9306	0.04722	0.00313
H3	0.88342	0.92403	0.0104
H4	0.98762	0.83785	0.01264
H5	0.02451	0.15804	0.99712
N1	0.06081	0.14214	0.99801
N2	0.95546	0.85875	0.01047
C7	0.12646	0.19405	0.9922
H6	0.16812	0.18221	0.99266
C8	0.88815	0.81122	0.00781
H7	0.84996	0.82775	0.00482
C9	0.8637	0.7416	0.00753
C10	0.90961	0.71324	0.01014
C11	0.78871	0.69738	0.00219
C12	0.87845	0.63823	0.00461
C13	0.75953	0.62297	0.9944
C14	0.80359	0.59215	0.99475
C15	0.14354	0.26192	0.98661
C16	0.09077	0.2818	0.98518
C17	0.21758	0.31335	0.98249
C18	0.11334	0.35508	0.98558
C19	0.23785	0.38608	0.98425
C20	0.18658	0.40774	0.98779

O1	0.97276	0.75079	0.01578
O2	0.26049	0.29468	0.97844
O3	0.20588	0.46984	0.99174
O4	0.02844	0.23808	0.98327
O5	0.75157	0.72321	0.00385
O6	0.77763	0.52929	0.98662
C21	0.30622	0.43777	0.98344
H8	0.3181	0.49126	0.98548
C22	0.92352	0.61378	0.00552
H9	0.9788	0.65139	0.01222
C23	0.68946	0.57863	0.98582
H10	0.67115	0.52354	0.97927
C24	0.06251	0.37237	0.98353
H11	0.00841	0.33119	0.98161
H12	0.34201	0.3724	0.97929
H13	0.84919	0.51519	0.99311
C25	0.94517	0.51847	0.99439
C26	0.91664	0.44641	0.9885
C27	0.01729	0.56102	0.99485
C28	0.96053	0.41969	0.98279
C29	0.06005	0.53384	0.99049
H14	0.041	0.61666	0.99873
C30	0.03214	0.46249	0.98505
H15	0.93836	0.3642	0.97576
H16	0.11578	0.56812	0.99156
C31	0.42822	0.47122	0.97793
C32	0.47221	0.44413	0.97768
C33	0.45734	0.54257	0.97367
C34	0.54254	0.48699	0.97864
H17	0.45075	0.3888	0.97885
C35	0.52868	0.58694	0.97195
H18	0.42382	0.56446	0.97045
C36	0.57242	0.55873	0.97864
H19	0.57467	0.46361	0.98165
N3	0.35801	0.42471	0.98018
N4	0.90276	0.54655	0.99812
H20	0.66611	0.65352	0.9915

N5	0.64345	0.60012	0.9849
H21	0.13021	0.47375	0.98548
N6	0.07741	0.43785	0.98329
S1	0.55614	0.67867	0.97247
O7	0.57333	0.70295	0.17359
O8	0.50477	0.68604	0.86287
O9	0.62908	0.71473	0.85618
H22	0.63223	0.72229	0.71554
S2	0.11605	0.94359	0.99049
O10	0.12115	0.93074	0.78383
O11	0.09933	0.89166	0.14156
O12	0.18825	0.01269	0.04338
H23	0.20044	0.02233	0.18066
S3	0.82363	0.38783	0.98132
O13	0.80042	0.39125	0.78502
O14	0.79294	0.39905	0.15666
O15	0.81846	0.31346	0.99578
H24	0.81908	0.29579	0.12503
C37	0.97307	0.97721	0.50687
C38	0.92968	0.00451	0.49166
C39	0.95529	0.07517	0.48475
C40	0.02744	0.12074	0.49565
C41	0.07063	0.09257	0.51121
C42	0.04446	0.02265	0.51564
H25	0.12631	0.12594	0.52147
H26	0.0795	0.00271	0.52807
H27	0.98517	0.89126	0.52243
H28	0.02306	0.21213	0.49152
N7	0.0554	0.19129	0.49132
N8	0.94909	0.90744	0.51247
C43	0.12279	0.23876	0.48615
H29	0.16098	0.22224	0.48117
C44	0.88334	0.8558	0.50489
H30	0.84213	0.86814	0.49512
C45	0.86576	0.78773	0.50765
C46	0.91871	0.76794	0.51789
C47	0.7921	0.73619	0.49917

C48	0.89684	0.69488	0.51132
C49	0.7723	0.6636	0.4944
C50	0.82392	0.64211	0.50079
C51	0.14693	0.30838	0.48568
C52	0.10044	0.33588	0.48977
C53	0.22186	0.35388	0.47899
C54	0.13056	0.41067	0.48653
C55	0.25006	0.42837	0.48687
C56	0.20502	0.45774	0.49417
O16	0.98046	0.81156	0.53245
O17	0.25972	0.32905	0.46825
O18	0.22999	0.52097	0.50831
O19	0.03725	0.29811	0.4949
O20	0.74844	0.75429	0.49785
O21	0.80464	0.58014	0.49661
C57	0.32027	0.47359	0.48862
H31	0.33845	0.52864	0.49644
C58	0.94829	0.67833	0.51367
H32	0.00224	0.71975	0.51952
C59	0.70433	0.61159	0.48539
H33	0.69268	0.55818	0.48765
C60	0.08379	0.43311	0.48251
H34	0.02869	0.39461	0.4864
H35	0.34353	0.39906	0.47551
H36	0.88083	0.57713	0.50369
C61	0.97832	0.58771	0.50387
C62	0.05018	0.62921	0.50966
C63	0.94858	0.51622	0.49184
C64	0.09251	0.60074	0.50003
C65	0.9898	0.4873	0.48294
H37	0.89267	0.48334	0.48843
C66	0.06184	0.52872	0.48415
H38	0.96524	0.43166	0.47199
C67	0.43763	0.49364	0.48168
C68	0.46841	0.56539	0.48367
C69	0.48041	0.46433	0.47942
C70	0.53893	0.60698	0.48299

H39	0.43726	0.58979	0.48767
C71	0.55188	0.50741	0.47511
C72	0.58202	0.57886	0.47641
H40	0.56119	0.66244	0.48459
N9	0.36647	0.45251	0.48181
N10	0.93361	0.61299	0.50874
H41	0.66906	0.67688	0.46568
N11	0.65242	0.62454	0.47332
H42	0.15642	0.53144	0.46072
N12	0.10341	0.49977	0.47238
S4	0.88948	0.0987	0.44837
O22	0.84772	0.05875	0.28372
O23	0.91997	0.17279	0.45114
O24	0.84128	0.06449	0.64338
H43	0.8554	0.08907	0.76645
H44	0.87411	0.96993	0.48259
H45	0.58476	0.48481	0.46927
H46	0.07377	0.68476	0.52194
S5	0.44393	0.37111	0.48379
O25	0.41595	0.34394	0.29139
O26	0.40155	0.34371	0.6609
O27	0.51288	0.36556	0.50218
H47	0.53256	0.36936	0.63094
S6	0.18602	0.66049	0.49066
O28	0.19746	0.72565	0.56178
O29	0.20955	0.65366	0.29542
O30	0.21526	0.63103	0.65894
H48	0.22924	0.59766	0.62569

Table 4.7: Fractional atomic coordinates for the unit cell of **TpPa-Py.**

	TpPa-Py **Triclinic; *P* 1;** ***a* = 22.6913 Å; *b* = 22.8236 Å; *c* = 6.6694 Å;** **α = 89.4875; β = 91.1500; γ = 121.1059.**		
Atom list	x	y	z
C1	0.96333	0.89674	0.9975
C2	0.03556	0.94005	0.99969

C3	0.06309	0.01083	0.9984
C4	0.01804	0.03696	0.99473
C5	0.94642	0.98945	0.99275
H1	0.06941	0.9183	0.00263
H2	0.11908	0.04507	0.00045
H3	0.90968	0.00825	0.98972
H4	0.96654	0.80469	0.99946
H5	0.0025	0.12147	0.99214
N1	0.04001	0.10698	0.99307
N2	0.93448	0.82585	0.99864
C6	0.10528	0.16022	0.99264
H6	0.14781	0.14938	0.99306
C7	0.86636	0.7798	0.99807
H7	0.83093	0.80009	0.9975
C8	0.84072	0.70933	0.99803
C9	0.88691	0.68098	0.99846
C10	0.7653	0.66387	0.99716
C11	0.85641	0.60578	0.997
C12	0.73659	0.58886	0.99459
C13	0.78136	0.55867	0.99478
C14	0.12154	0.22844	0.99156
C15	0.06803	0.24758	0.99185
C16	0.19554	0.28087	0.99068
C17	0.08981	0.32116	0.99215
C18	0.21529	0.35391	0.99016
C19	0.16317	0.37489	0.991
O1	0.95079	0.71869	0.00016
O2	0.239	0.26242	0.9903
O3	0.1817	0.43714	0.9908
O4	0.00569	0.20286	0.99219
O5	0.72711	0.68896	0.99844
O6	0.75608	0.49517	0.99316
C20	0.28382	0.40629	0.98914
H8	0.29583	0.46017	0.98892
C21	0.90242	0.58209	0.99796
H9	0.95794	0.62021	0.99935
C22	0.66604	0.54331	0.99147

H10	0.64723	0.4877	0.98905
C23	0.03828	0.33764	0.99426
H11	0.98417	0.2957	0.99557
H12	0.32093	0.34132	0.98833
H13	0.82861	0.48184	0.99704
C24	0.92423	0.48579	0.99861
C25	0.8928	0.41359	0.00345
C26	0.99697	0.52489	0.99429
C27	0.93333	0.38344	0.00301
H14	0.83655	0.3813	0.00765
H15	0.02465	0.5816	0.99026
C28	0.00555	0.42662	0.99725
H16	0.90892	0.32734	0.00712
C29	0.40642	0.44068	0.98777
C30	0.43598	0.51287	0.98894
C31	0.51363	0.4499	0.98684
C32	0.50729	0.55377	0.98958
H17	0.4043	0.53706	0.98976
C33	0.54788	0.52254	0.98899
H18	0.54268	0.42256	0.9856
H19	0.53175	0.61001	0.991
N3	0.33611	0.39366	0.98822
N4	0.88223	0.51465	0.99779
H20	0.64119	0.61772	0.99352
N5	0.61946	0.5641	0.99101
H21	0.10454	0.44058	0.99263
N6	0.05194	0.40322	0.99481
N7	0.44547	0.41103	0.98636
N8	0.92023	0.92172	0.99418
N9	0.03558	0.49575	0.9936
C34	0.00147	0.98631	0.49626
C35	0.07376	0.02951	0.49871
C36	0.10156	0.10023	0.49692
C37	0.05661	0.12655	0.49259
C38	0.98496	0.07925	0.49017
H22	0.10747	0.00758	0.50235
H23	0.15755	0.13428	0.49921

H24	0.9484	0.09826	0.48631
H25	0.00603	0.89523	0.50115
H26	0.04239	0.21204	0.49021
N10	0.07921	0.19662	0.49105
N11	0.97319	0.91548	0.49827
C39	0.14496	0.24876	0.49093
H27	0.18679	0.23693	0.49089
C40	0.90538	0.86807	0.49686
H28	0.86882	0.88696	0.49427
C41	0.88153	0.79798	0.49829
C42	0.92911	0.77115	0.50065
C43	0.80616	0.75117	0.49667
C44	0.90016	0.69625	0.49926
C45	0.77935	0.67649	0.49647
C46	0.8255	0.64817	0.49759
C47	0.1626	0.31736	0.49073
C48	0.11028	0.33796	0.49149
C49	0.23672	0.36856	0.48992
C50	0.13347	0.41186	0.49232
C51	0.25821	0.44209	0.49014
C52	0.20719	0.46487	0.49155
O7	0.99282	0.81054	0.50359
O8	0.27965	0.3493	0.48906
O9	0.22664	0.52713	0.49202
O10	0.04751	0.29458	0.49142
O11	0.76727	0.77525	0.4955
O12	0.80089	0.58459	0.49692
C53	0.32715	0.49284	0.48935
H29	0.34083	0.54721	0.48984
C54	0.94679	0.67317	0.49903
H30	0.00218	0.71144	0.49998
C55	0.70919	0.62915	0.49416
H31	0.69186	0.57382	0.49413
C56	0.08246	0.42901	0.49355
H32	0.02818	0.38722	0.49416
H33	0.36237	0.42591	0.48777
H34	0.87298	0.57287	0.49838

C57	0.96836	0.57671	0.49633
C58	0.93691	0.50448	0.50104
C59	0.04101	0.61583	0.48999
C60	0.97752	0.47442	0.49996
H35	0.88064	0.47215	0.50635
H36	0.06849	0.67252	0.48529
C61	0.04977	0.51776	0.49428
H37	0.95307	0.4183	0.50479
C62	0.44908	0.52481	0.48808
C63	0.47873	0.597	0.48819
C64	0.5562	0.53377	0.48867
C65	0.54991	0.63772	0.48907
H38	0.44714	0.62124	0.48764
C66	0.59046	0.60643	0.48979
H39	0.58525	0.50638	0.48833
H40	0.57457	0.69396	0.4893
N12	0.37857	0.47853	0.48806
N13	0.92663	0.60584	0.49788
H41	0.68281	0.70214	0.49164
N14	0.66175	0.64857	0.49169
H42	0.14885	0.53182	0.49196
N15	0.09631	0.49458	0.49348
N16	0.48791	0.4949	0.48792
N17	0.9585	0.01137	0.492
N18	0.0797	0.58682	0.48931

Table 4.8: Fractional atomic coordinates for the unit cell of **TpPa-(SO$_3$H-Py).**

	TpPa-(SO$_3$H-Py) **Triclinic: *P* 1;** ***a* = 22.7020 Å; *b* = 22.6423 Å; *c* = 6.6170 Å;** **α = 85.4098; β = 95.4433; γ = 120.6010.**		
Atom list	x	y	z
C1	0.9628	0.94431	0.9856
C2	0.05953	0.05322	0.98975
C3	0.01915	0.08452	0.99282
C4	0.94722	0.04171	0.99372
C5	0.91849	0.97106	0.98983

H1	0.11613	0.08432	0.99018
H2	0.91435	0.06421	0.99766
H3	0.86261	0.93781	0.99131
H4	0.97473	0.85805	0.97987
H5	0.01085	0.1729	0.99566
N1	0.04566	0.15515	0.99569
N2	0.93891	0.87419	0.9807
C6	0.11175	0.2055	0.99592
H6	0.15222	0.19203	0.99608
C7	0.87215	0.82398	0.97613
H7	0.83275	0.83891	0.9755
C8	0.84974	0.75457	0.97301
C9	0.89766	0.72864	0.97505
C10	0.77466	0.70798	0.97074
C11	0.86865	0.65352	0.97749
C12	0.74798	0.63341	0.98217
C13	0.79416	0.60532	0.98475
C14	0.13071	0.27451	0.99603
C15	0.07969	0.29645	0.99347
C16	0.20469	0.32444	0.99623
C17	0.10481	0.37088	0.99376
C18	0.22755	0.39814	0.99658
C19	0.17837	0.42172	0.99955
O1	0.96088	0.76883	0.97476
O2	0.2462	0.30347	0.99597
O3	0.1993	0.48508	0.00877
O4	0.01672	0.25455	0.99057
O5	0.73602	0.73228	0.96149
O6	0.76967	0.54185	0.99479
C20	0.29693	0.44822	0.99515
H8	0.31201	0.50296	0.99242
C21	0.91499	0.63065	0.97441
H9	0.97004	0.66958	0.9708
C22	0.67858	0.58639	0.99638
H10	0.66164	0.53107	0.00807
C23	0.05523	0.39009	0.98859
H11	0.00073	0.34919	0.98633

H12	0.32734	0.37856	0.98922
H13	0.8416	0.53025	0.97449
C24	0.93769	0.53564	0.97317
C25	0.90923	0.46309	0.96958
C26	0.00992	0.57922	0.97649
C27	0.95389	0.43719	0.97389
C28	0.05326	0.55259	0.97893
H14	0.03314	0.6352	0.97744
C29	0.02559	0.48079	0.97929
H15	0.93194	0.38133	0.97252
H16	0.10909	0.58748	0.98215
C30	0.4167	0.47632	0.0002
C31	0.45912	0.44899	0.97422
C32	0.44701	0.54673	0.03613
C33	0.52983	0.49185	0.97577
H17	0.43625	0.39383	0.95046
C34	0.51834	0.59053	0.04117
H18	0.41453	0.56798	0.06336
C35	0.56072	0.56304	0.00627
H19	0.56134	0.46927	0.95136
N3	0.34593	0.4316	0.99452
N4	0.8951	0.5633	0.9742
H20	0.6532	0.65982	0.99437
N5	0.63152	0.60605	0.00048
H21	0.12374	0.49224	0.98541
N6	0.07104	0.45617	0.98454
S1	0.55113	0.67901	0.11277
O7	0.60226	0.69433	0.28218
O8	0.49197	0.68757	0.12919
O9	0.59426	0.72431	0.91743
H22	0.56943	0.72779	0.79331
S2	0.81679	0.39776	0.9639
O10	0.80914	0.3355	0.88681
O11	0.77685	0.42799	0.86678
O12	0.80457	0.38193	0.20453
H23	0.80639	0.41666	0.29111
C36	0.01065	0.88683	0.48234

C37	0.08204	0.93484	0.48202
C38	0.06516	0.02712	0.49025
C39	0.99318	0.98343	0.49008
C40	0.96573	0.91268	0.48649
H24	0.95924	0.00472	0.49341
H25	0.90985	0.87839	0.48657
H26	0.02589	0.80241	0.47591
H27	0.06244	0.11938	0.49599
N7	0.09422	0.09827	0.49405
N8	0.98871	0.81688	0.47815
C41	0.16231	0.1444	0.49506
H28	0.19693	0.12348	0.49305
C42	0.92369	0.76381	0.47958
H29	0.88155	0.77479	0.48238
C43	0.90676	0.69534	0.4782
C44	0.95934	0.67549	0.47687
C45	0.83319	0.64343	0.48228
C46	0.93636	0.60133	0.4738
C47	0.81237	0.57013	0.48236
C48	0.86305	0.54881	0.46992
C49	0.18915	0.21502	0.4981
C50	0.14426	0.2445	0.49887
C51	0.26466	0.25956	0.49846
C52	0.17599	0.31999	0.49933
C53	0.29476	0.33499	0.49783
C54	0.25106	0.36593	0.50043
O13	0.0217	0.71908	0.47864
O14	0.30151	0.23339	0.49931
O15	0.27757	0.42954	0.50268
O16	0.08045	0.20697	0.49881
O17	0.78999	0.66208	0.48537
O18	0.84367	0.48598	0.45589
C55	0.36514	0.37981	0.49484
H30	0.3864	0.436	0.49337
C56	0.9875	0.58425	0.4759
H31	0.04155	0.62627	0.47757
C57	0.74362	0.51838	0.48903

H32	0.7307	0.4643	0.4889
C58	0.13113	0.34495	0.49732
H33	0.07572	0.3068	0.49391
H34	0.38847	0.30411	0.49696
H35	0.92153	0.48171	0.48011
C59	0.02007	0.49501	0.48176
C60	0.09169	0.53874	0.47918
C61	0.99305	0.42325	0.48694
C62	0.03672	0.39685	0.4921
H36	0.93734	0.38799	0.4877
C63	0.10888	0.44049	0.49192
H37	0.0136	0.3408	0.49773
C64	0.48159	0.39986	0.49574
C65	0.52365	0.37003	0.5091
C66	0.59446	0.41274	0.51099
H38	0.50083	0.31395	0.51893
C67	0.57601	0.50976	0.48777
C68	0.62216	0.48462	0.49858
H39	0.62751	0.39004	0.52311
N9	0.41055	0.35775	0.49431
N10	0.97383	0.51875	0.47831
H40	0.70888	0.58468	0.49395
N11	0.69252	0.53195	0.49586
H41	0.20517	0.44519	0.50388
N12	0.15168	0.4125	0.49896
H42	0.11867	0.91633	0.47822
H43	0.59596	0.56584	0.47919
H44	0.11326	0.59464	0.47238
N13	0.10812	0.00252	0.48613
N14	0.50801	0.46854	0.48618
N15	0.03163	0.98518	0.98652
C69	0.13663	0.51309	0.4829
S3	0.22916	0.5804	0.48122
O19	0.25997	0.58596	0.68761
O20	0.23084	0.64022	0.37188
O21	0.26199	0.54764	0.3539
H45	0.24765	0.53628	0.20883

NOTE: The results of this chapter have already been published in *Chem. Mater.**2016**, 28, 1489−1494*. with the title: "*Interplaying Intrinsic and Extrinsic Proton Conductivities in Covalent Organic Frameworks.*" These publications were the results of the collaboration between the group of Dr. Rahul Banerjee and his students Suman Chandra, Tanay Kundu, and Koushik Dey from National Chemical Laboratory, Pune, India and the group of Dr. Thomas Heine and his post doctorate student Matthew Addicoat from Jacobs University, Germany. Apart from computational study major works contributed by Suman Chandra.

CHAPTER 5

Redox Active Covalent Organic Frameworks as Pseudocapacitor and the Role of Hydrogen Bonding in Capacitance

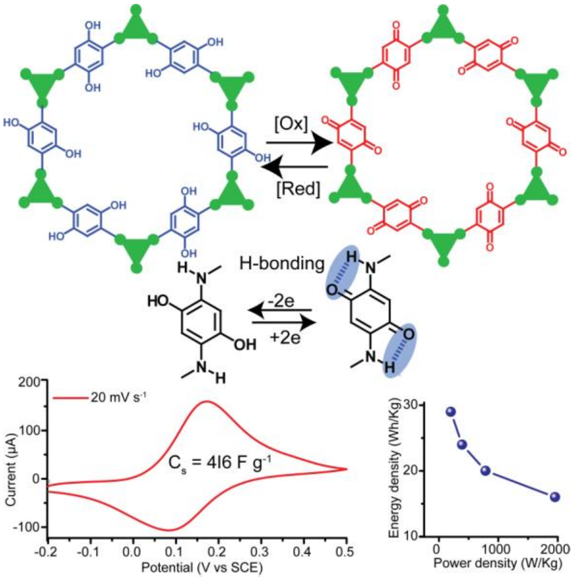

Abstract: *Two-dimensional redox-active covalent organic frameworks (COFs) are ideal materials for energy storage applications due to their high surface area, extended π conjugated structure, tunable pore size, and adjustable functionalities. In this chapter, we report the synthesis and supercapacitor application of two redox active COFs [***TpPa-(OH)*$_2$ *and* ***TpBD-(OH)*$_2$*] along with the role of their redox active functional groups for the enrichment of specific capacitance. Of these COFs,* ***TpPa-(OH)*$_2$ *exhibited a highest specific capacitance of 416 F* g^{-1} *at 0.5 A* g^{-1} *current density in three electrode configuration while highest specific capacitance was 214 F* g^{-1} *at 0.2 A* g^{-1} *current density in two electrode configuration. Superior specific capacitance was due to the emergence of excellent pseudocapacitance by virtue of precise molecular level control over redox functionalities present in the COF backbone. This COF also demonstrated 66% capacitance retention after 10,000 cycles along with 43% accessibility of the redox-active hydroquinone (*H_2Q*) moieties in three electrode configuration while capacitance retention was 88% after 10,000 cycles in two electrode configuration. The exceptionally high specific capacitance of* ***TpPa-(OH)*$_2$ *was due to the reversible proton-coupled electron transfer (*$2H^+/2e^-$*) of hydroquinone/benzoquinone (*H_2Q/Q*) moieties wherein* H_2Q *and Q had comparable chemical stability during redox cycling originated from H-bonding which was supported by calculated structures.*

5.1 Introduction

Global energy consumption has been increasing due to the over growing human population and the rapid development of global economy. Fast growing market of portable electronic devices and the development of hybrid electric vehicles accelerating the energy consumption [5.1-5.3]. The consumption of global energy in current consumption rate will soon become inevitable in future. It has been reported that the global energy demands will roughly double in mid-century and triple by 2100 [5.4]. Therefore, there has been an urgent need of rapid development not only clean, sustainable and renewable energies (solar, tide, winds) but also cheap, advanced, environmentally friendly energy conversion and storage devices to fulfill the needs of modern society [5.2,5.5]. Among various energy conversion and storage devices, lithium ion batteries (LIBs) [5.6] and supercapacitors [5.7, 5.8] are the widely used. Although LIBs exhibited high energy density, their low power density hinders its use in energy storage systems where fast and high power delivery is needed [5.5, 5.9]. As a result, a considerable responsibility has been given to the supercapacitor [5.10].

5.1.1 Supercapacitor

Supercapacitors, also known as electrochemical capacitors (ECs), have found great attention due to its high power density, high rate of charging/discharging, long cycle life (>100 000 cycle), easy to handle and low maintenance cost [5.7,5.8]. As observed from the Ragone plot (Figure 5.1), supercapacitor bridges the power gap between the battery and electrolytic capacitor. The supercapacitors can be divided into two categories based on their charge storage mechanism; i) electrical double layer capacitor (EDLC) and ii) pseudocapacitor. In electrical double layer capacitor, charges are storage by adsorption of ions on the surface of the material, whereas in pseudocapacitor, faradic reactions are happening on the surface or near to the surface. To take the advantage of both high energy density of the battery and high power density supercapacitor, scientists are made hybrid or asymmetric supercapacitor where one electrode acts as a supercapacitor and other one acts as a battery. The activated carbons, carbide–derived carbons, carbon fabrics, carbon nanotubes, nanoonions, and nanohorns have been tested for EDLC applications [5.13]. Among these carbon materials, the activated carbons are the most widely used electrode materials because of their high surface area, better stability, and low cost. Similar to the carbon electrode materials, the conducting polymers (polyaniline, polypyrrole, PEDOT) and metal oxides (Co_3O_4, MnO_2, RuO_2 etc.) are being continuously investigated to get high capacitance; however, the ECs derived by using these materials have very low cycling stability [5.13-5.17]. Moreover, to get higher energy density, the operating potential window is also being tuned by using the organic electrolytes and ionic liquid [5.18, 5.19]. To improve the energy density of supercapacitor researchers focus on the development of new materials with the high accessible surface area, high electric conductivity, optimized pore size, high density of redox active units and high electrochemical stability [5.20-5.25].

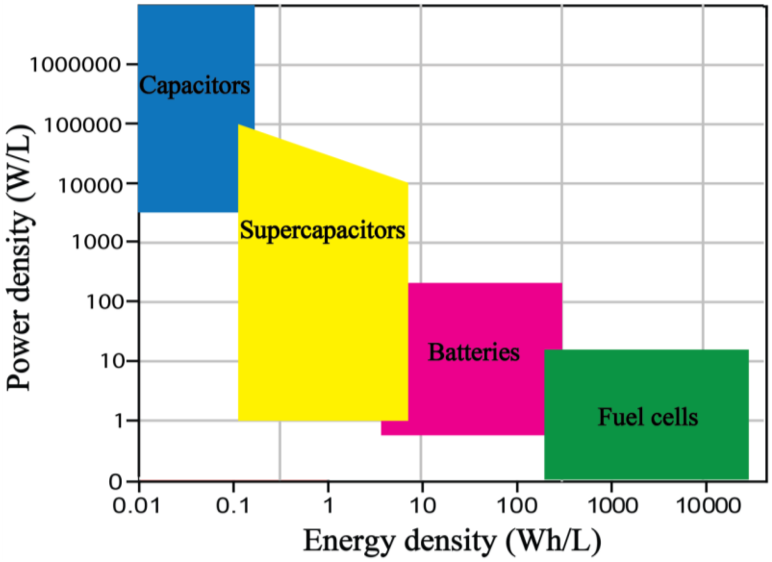

Figure 5.1: *Ragone plot for the electrochemical energy devices with rough guidelines of the power density and energy density.*

5.1.2 Two dimensional nanomaterials as capacitive energy storage

2D nanomaterials having at least one dimension in nanometer scale, are promising materials for supercapacitor because of their high surface area. 2D nanomaterials like Graphene [5.26], transition metal oxide [5.27-5.29], transition metal dichalcogenides [5.28, 5.30], transition metal carbides and nitrides (MXenes) [5.31-5.35] have recently been used as capacitive energy storage materials.

Inorganic 2D nanomaterials have reactive basal planes and edges that can provide pseudocapacitance. They can be modified by chemical functionalization and doping to provide additional reactive sites. This is the case also for reduced graphene oxide (rGO) that holds oxygen-containing chemical functionalities. 2D nanomaterials have the ability to intercalate ions and thus can provide intercalation pseudocapacitance. Moreover, 2D nanomaterials can store energy in the 2D channels between nanosheets by a fast ion adsorption mechanism enabled by the pre-intercalation of water molecules and a rapid expansion and contraction of the multilayered and flexible 2D nanomaterials [5.36]. Unlike rigid porous 3D materials, such as hard carbons undergoing slow diffusion processes, the nature of 2D nano-materials favors a fast ionic transport through 2D channels that are free to expand and contract. Due to their sub-nanometer thickness, 2D nanomaterials have a high packing density that leads to a high volumetric capacitance, which is important for manufacturing thin-film supercapacitors. The flexibility of 2D nanomaterials, good mechanical properties, and high packing densities make them suitable for the development of thin, flexible and all-solid state supercapacitors and micro supercapacitors [5.29, 5.37].

5.1.3 Advantages of Covalent Organic Frameworks as electrode materials

There are several advantages of covalent organic frameworks as electrode materials, such as

(a) Porous structure: Porous structure of COFs will improve the permeability of the electrolytes and mobility of the ions.

(b) Rigidity: High rigidity and robustness of the framework will help to maintain the electrochemical stability during the electrochemical reaction on the electrode surface.

(c) Control Pore size: The control pore size will improve the capacity of the materials. As we know that sub nanometer pore is more effective towards the improvement of capacitance than micro/meso pore.

(d) The Precise introduction of redox active units with proper design strategies via reticular chemistry: It will enable us to design high energy density electrode materials by incorporating a large number of redox active moieties within a given structure.

(e) High crystallinity: It will help to characterize these materials easily and give us the opportunity to study the mechanism during the electrochemical process.

(f) High surface area: It will help to maximize the interaction between the electrolytes and electrodes which improve the double layer capacitance of the materials.

(g) Band gap tuning: By proper design strategies it is possible to made semiconducting COFs and their band gap can be tuned.

(h) Insolubility: As COFs are two and three-dimensional organic crystalline polymers, it completely insoluble in any solvents. So the loss of capacitance due to the leaching of the active materials (COFs) will be completely prevented.

(i) Eco-friendly: As COFs are metal free organic crystalline polymer and composed by only light atom like C, H, N, O, S etc, it will completely harmless to the environment.

5.2 Hydroquinone based COF as 2D capacitive energy storage nanomaterials

As discussed earlier, covalent organic frameworks (COFs) are lightweight, porous, crystalline, high surface area materials comprising of strong covalent bonds between light atoms such as B, C, H, N, O etc [5.38, 5.39]. Employing reticular chemistry, COF backbone can be functionalized with pre-requisite groups and tuned pore size. Although COFs have been used in applications like gas storage, gas separation, catalysis, and optoelectronics, their use as energy storage materials (like carbon,[5.40] graphene,[5.41] porous polymers[5.42]) is limited due to their low electrochemical stability. In this regard, recently we have demonstrated the construction of chemically stable β-ketoenamine-linked two-dimensional COFs by using a combined reversible and irreversible bond formation route [5.43]. Since then, applications such as catalysis [5.44], proton conduction [5.45] and also in a few cases supercapacitor [5.46-5.50] have been envisaged with these chemically stable β-ketoenamine-linked COFs.

Literature reports suggest that the physisorption of hydroquinone on activated charcoal can also provide electrochemical reversibility in hydroquinone (H_2Q)/benzoquinone (Q) because of a proton shuttling mechanism between H_2Q and oxide sites of activated charcoal due to intermolecular H-bonding [5.51]. But the chemical instability of the oxidized benzoquinone species also jeopardizes its application in the field of capacitors [5.52]. Furthermore, some conducting polymers [5.53-5.56], and graphene based materials [5.57] had been successfully functionalized with hydroquinone (H_2Q) to enhance the pseudocapacitance. However, the precise control over redox functionalization, porosity, structural diversity, and stability has been found to be inadequate for most of the carbon based materials, conducting polymer along with COFs.

Excited by the fascinating H_2Q/Q electrochemistry, we hypothesized that this chemistry could be incorporated in the COF backbone wherein intramolecular H-bonding can provide much superior electrochemical stability for the H_2Q/Q system and simultaneously redox functionalization can be incorporated in a controllable manner which can significantly improve pseudocapacitance (redox contribution). Hence, we synthesized a H_2Q based COF, namely **TpPa-(OH)$_2$**, by the Schiff base condensation between 1,3,5-triformylpholoroglucinol (**Tp**) and 2,5-dihydroxy-1,4-phenyldiamine [**Pa-(OH)$_2$**] via the solvothermal method. In order to confirm the role of the H_2Q functionality in the pseudocapacitance, we have also synthesized the phenolic and methoxy functionalized COFs [**TpBD-(OH)$_2$**, **TpPa-(OMe)$_2$** and **TpBD-(OMe)$_2$**] along with their non-functionalized counterparts [**TpPa-1** and **TpBD**] (Figure 5.2).

5.3 Preparative methods and characterization

5.3.1 *Synthesis of COFs*

Synthesis of **TpPa-(OH)$_2$** was accomplished by reacting 1,3,5-triformylphloroglucinol(**Tp**) (0.3 mmol), 2,5-diaminohydroquinone dihydrochloride [**Pa-(OH)$_2$.2HCl**, 0.45 mmol], 3 mL (1:1) solvent mixture of mesitylene and 1,4-dioxane with 0.5 mL of 6(M) acetic acid. This mixture was sonicated for 10 min. in order to get a homogeneous dispersion. After flash froze in liquid N_2, the reaction tube was degassed by freeze-pump-thaw cycles thrice. Finally, the reaction tube was vacuum sealed and heated at 120 °C for 3 days. A black coloured precipitate was collected by filtration and washed with dimethylacetamide followed by water and finally acetone for several times. Then, the powder was dried at 120 °C under vacuum for 12 h to get corresponding COFs in ~75% isolated yield.

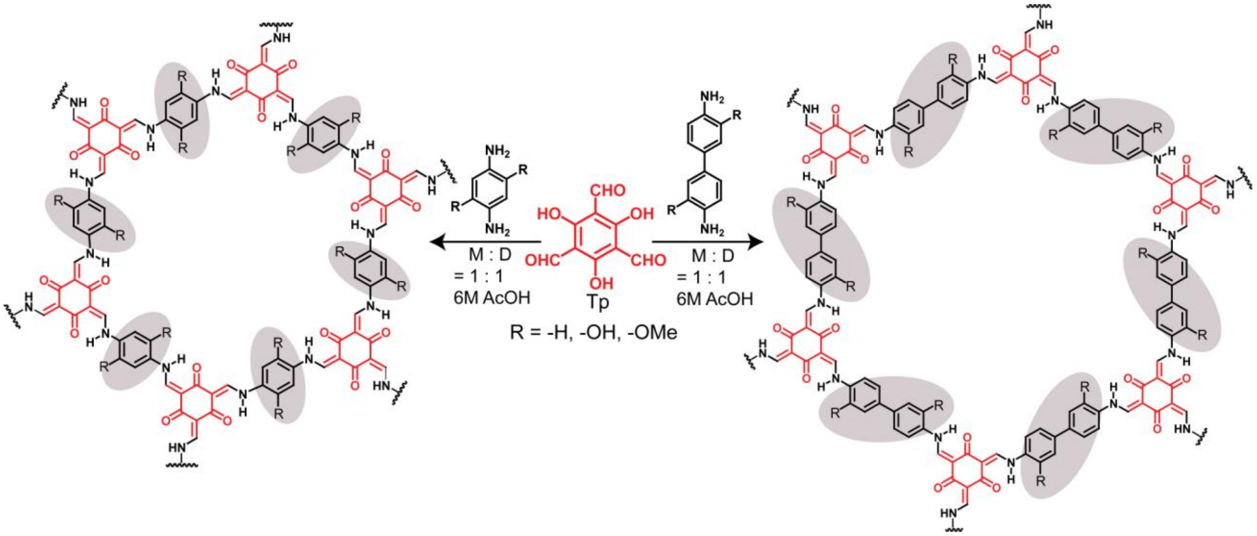

Figure 5.2*. Schematic representation of the synthesis of* ***TpPa-R$_2$*** *[****TpPa-1****,* ***TpPa-(OH)$_2$*** *and* ***TpPa-(OMe)$_2$****] and* ***TpBD-R$_2$*** *[****TpBD****,* ***TpBD-(OH)$_2$*** *and* ***TpBD-(OMe)$_2$****] where* ***R*** *=* ***H****,* ***OH*** *and* ***OMe****.*

The similar synthesis procedure along with the same amount of solvent mixtures and catalyst [mesitylene, 1,4-dioxane and 6M acetic acid in (1.5mL: 1.5mL: 0.5mL) ratio] is followed for the synthesis of **TpBD-(OH)$_2$** and **TpPa-(OMe)$_2$** except for these COFs we have taken 3,3′-dihydroxybenzidine [**BD-(OH)$_2$**, 0.45 mmol] and 2,5-dimethoxy-p-phenylenediamine [**Pa-(OMe)$_2$**, 0.45 mmol] respectively as amine counterpart.

5.3.2 *Structural simulation and characterization*

The PXRD profiles of **TpPa-(OH)$_2$**, **TpPa-(OMe)$_2$** and **TpPa-1** exhibit peaks at 2θ ~ 4.9°, ~ 8.1° and ~ (26.5°-27.5°). On the other hand, **TpBD-(OH)$_2$**, **TpBD-(OMe)$_2$** and **TpBD** show 2θ peaks at ~ 3.4°, ~ 6.3° and ~ 26°. The low angle [2θ ~ (3.4°-4.9°)] peaks were assigned to (100) reflection planes that exhibited the highest intensity, indicating high crystallinity and periodicity of these COFs. On the other hand, the high angle broad peaks [2θ ~ (26°-27.5°)] correspond to the π-π stacking between COF layers and could be assigned to the (001) reflection planes. In order to further determine the exact structure of these COFs, a 2D model of the COF was made using the Self-consistent charge density functional tight-binding (SCC-DFTB) method.

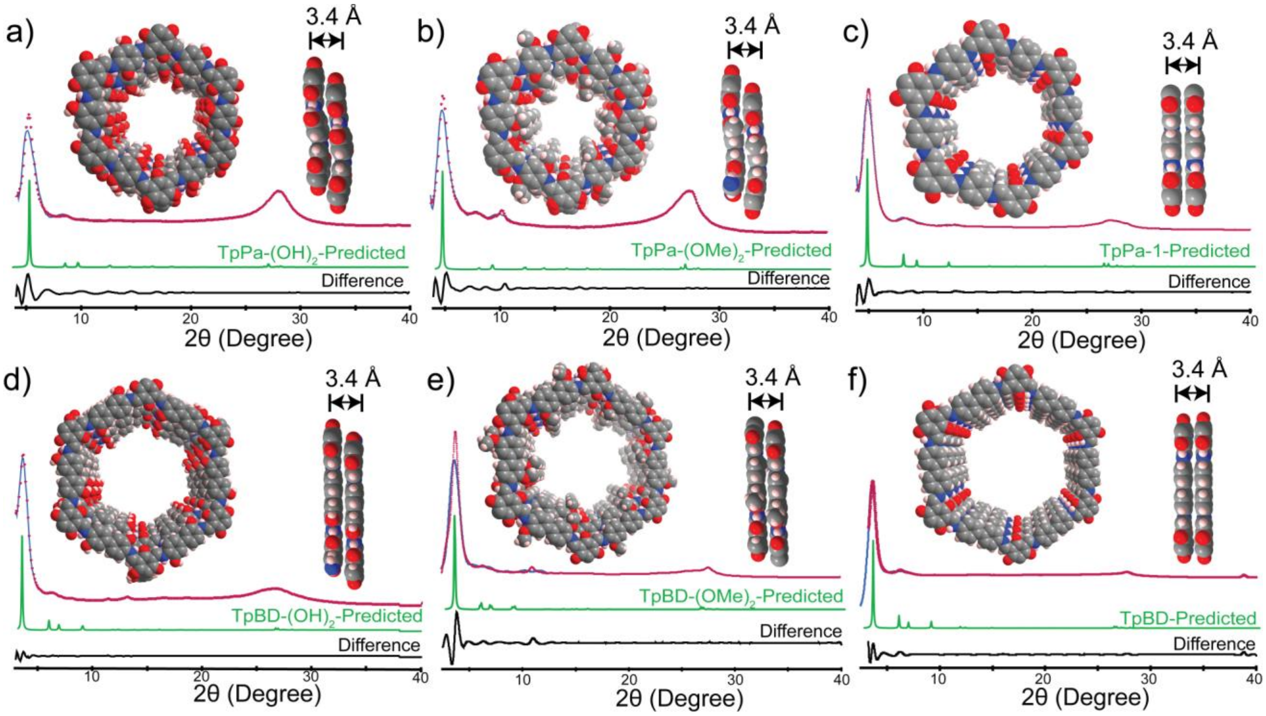

***Figure 5.3**. Comparison of the observed (blue), predicted (green) and refine (red) PXRD patterns with their difference (black) for (a) **TpPa-(OH)$_2$**, (b) **TpPa-(OMe)$_2$**, (c) **TpPa-1**, (d)**TpBD-(OH)$_2$**, (e) **TpBD-(OMe)$_2$** and (f)**TpBD**. Inset figures show the pore structure and π-π stacking distance for each of the COFs.*

These COFs crystallize in 2D serrated hexagonal network structures (slight slipping along the ab plane to stabilize the entire framework). The experimental PXRD profiles agree well with the simulated PXRD profiles of the serrated (slip-AA) stacking mode [especially the (001) peaks] (Figure 5.3 and 5.4) except **TpPa-1** and **TpBD,** which crystallize in a hexagonal space group (P6/m), as reported earlier [5.43]. The H$_2$Q based **TpPa-(OH)$_2$** COF crystallizes in the P1 space group with unit cell parameters a = 22.4 Å; b = 22.3 Å; c = 6.7 Å and α = 90.7; β = 90.3; γ = 119.3 along with an Rp = 3.4% and Rwp = 5.7%.

Structures of **TpPa-(OH)$_2$, TpBD-(OH)$_2$, TpPa-(OMe)$_2$ and TpBD-(OMe)$_2$** were modeled using Self-Consistent Charge Density Functional Tight-Binding (SCC-DFTB) method including Lennard-Jones dispersion as implemented in DFTB+ version 1.2. Parameters for all atoms were taken from the mio-0-1 set. Lattice dimensions and atomic positions were optimized simultaneously. From the optimized monolayers, the bulk structure was simulated using a bilayer model and investigating AA, AB, and slipped-AA structures. In the bilayer model, there may be disorder in the stacking of the **–OH** and **–OMe** functional groups, all possible permutations were optimised and the lowest energy structure was kept. The fractional coordinates of **TpPa-(OH)$_2$, TpBD-(OH)$_2$**, **TpPa-(OMe)$_2$** and **TpBD-(OMe)$_2$** are given in Table 5.11, Table 5.12, Table 5.13 and Table 5.14 respectively.

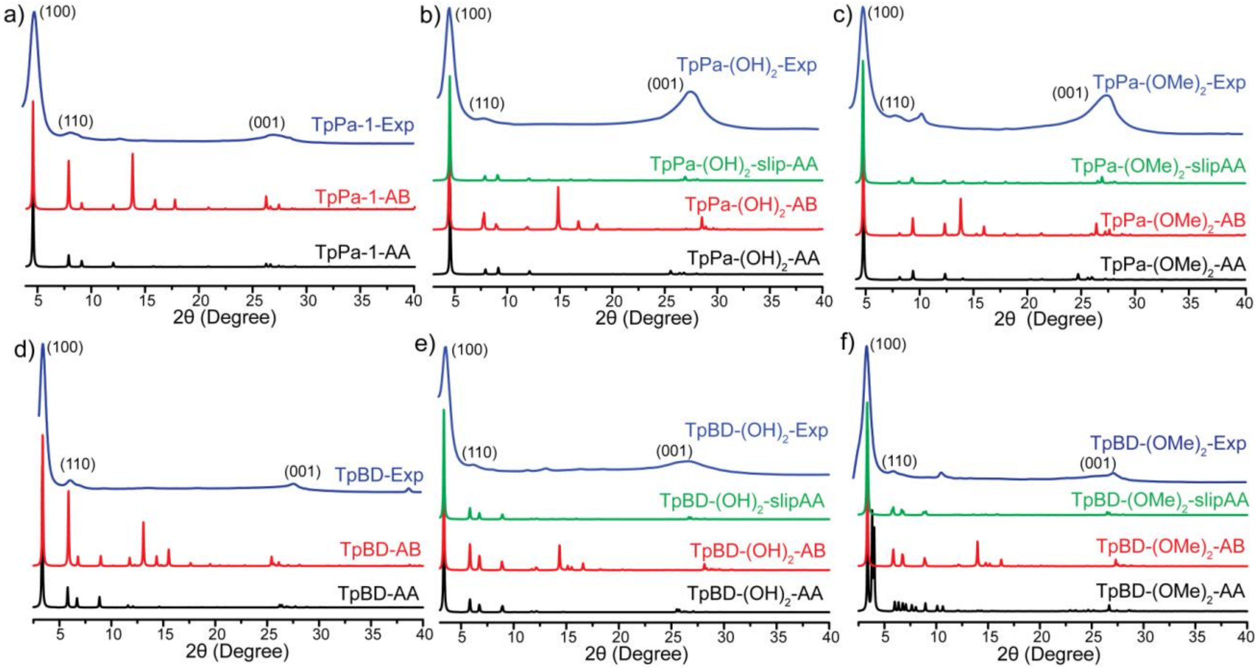

Figure 5.4*: Comparison of the experimental PXRD (Blue) with their simulated PXRD patterns for (a)* ***TpPa-1****; (b)* ***TpPa-(OH)$_2$****; (c)* ***TpPa-(OMe)$_2$****; (d)* ***TpBD****; (e)* ***TpBD-(OH)$_2$*** *and (f)* ***TpBD-(OMe)$_2$****. [parallel layer displacement (slip-AA) (Green) (see Table 5.1-5.4 for magnitude of slip), perfectly staggered fashion (AB) (Red) and perfectly eclipsed fashion (AA) (Black)].*

The experimental PXRD patterns are agreeable with the simulated patterns of eclipsed offset stacking models (slip-AA-x/y) (Figure 5.4). Hence we propose structures having triclinic space group (*P* 1) for all four COFs by comparing the experimental and simulated PXRD patterns. Refinements of PXRD pattern were done using Reflex module of Material studio 6.0.

Table 5.1: The total DFTB energies, Lennard-Jones contributions (LJ), and the crystal stacking energies per monolayer as well as the corresponding HOMO-LUMO energy gap for **TpPa-(OH)$_2$**.

Stacking	Slip distance [Å]	c [Å]	Total DFTB Energy [a.u.]	LJ energy [a.u.]	Per unit crystal stacking energy [kcal.mol^{-1}]	HOMO-LUMO gap [eV]
monolayer			-124.751610	0.4240		1.833
AA		3.53	-249.673605	0.6524	-53.46	1.673
slipAA-x	2.2	3.37	-249.695398	0.6563	-60.30	1.722
slipAA-y	2.4	3.34	-249.697614	0.6586	-60.99	1.723
AB		3.13	-249.6166892	0.7506	-35.60	1.720

Table 5.2. The total DFTB energies, Lennard-Jones contributions (LJ), and the crystal stacking energies per monolayer as well as the corresponding HOMO-LUMO energy gap for **TpPa-(OMe)$_2$**.

Stacking	Slip distance [Å]	c [Å]	Total DFTB Energy [a.u.]	LJ energy [a.u.]	Per unit crystal stacking energy [kcal.mol^{-1}]	HOMO-LUMO gap [eV]
monolayer			-139.400643	0.4926		1.869
AA		4.11	-279.042068	0.7568	-75.55	1.718
slipAA-x	2.5	3.43	-279.031677	0.7539	-72.29	1.830
slipAA-y	2.5	3.37	-279.034539	0.7589	-73.18	1.791
AB		3.40	-278.9731087	0.8266	-53.91	1.770

Table 5.3: The total DFTB energies, Lennard-Jones contributions (LJ), and the crystal stacking energies per monolayer as well as the corresponding HOMO-LUMO energy gap for **TpBD-(OH)$_2$**.

Stacking	Slip distance [Å]	c [Å]	Total DFTB Energy [a.u.]	LJ energy [a.u.]	Per unit crystal stacking energy [kcal.mol^{-1}]	HOMO-LUMO gap [eV]
monolayer			-160.104445	0.6000		1.964
AA		3.49	-320.436787	0.9345	-71.50	1.665
slipAA-x	1.6	3.36	-320.461150	0.9308	-79.15	1.891
slipAA-y	1.9	3.34	-320.463621	0.9345	-79.92	1.811

AB	3.17	-320.3375779	1.0729	-40.38	1.875

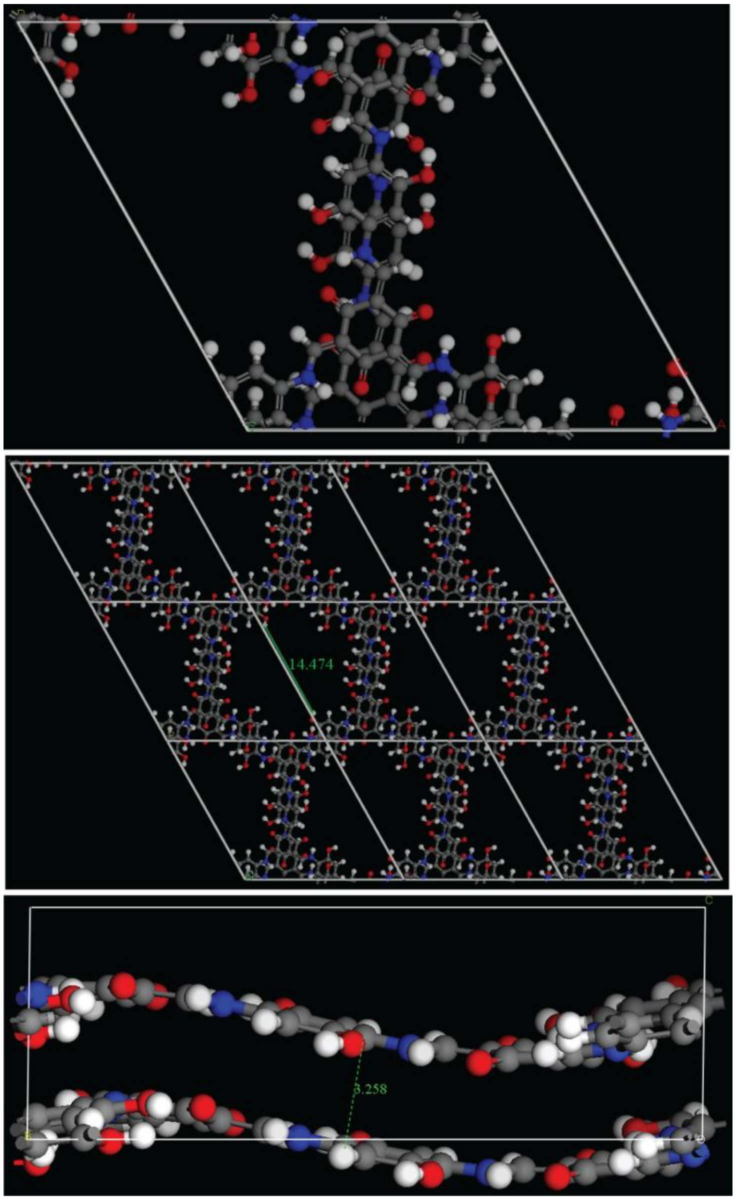

Figure 5.5: *Simulation of the **TpPa-(OH)$_2$** unit cell content calculated in a slip-AA arrangement (2.3Å along the y-axis): top view onto the ab-plane and view perpendicular to the c-axis.*

Table 5.4: The total DFTB energies, Lennard-Jones contributions (LJ), and the crystal stacking energies per monolayer as well as the corresponding HOMO-LUMO energy gap for **TpBD-(OMe)$_2$**.

Stacking	Slip distance [Å]	*c* [Å]	Total DFTB Energy [a.u.]	LJ energy [a.u.]	Per unit crystal stacking energy [kcal.mol^{-1}]	HOMO-LUMO gap [eV]

monolayer			-174.772527	0.6695		1.958
AA		4.03	-349.834459	1.0388	-90.80	1.799
slipAA-x	2.2	3.38	-349.832518	1.0404	-90.19	1.784
slipAA-y	2.3	3.34	-349.834945	1.0424	-90.95	1.797
AB		3.26	-349.6981584	1.1861	-48.04	1.856

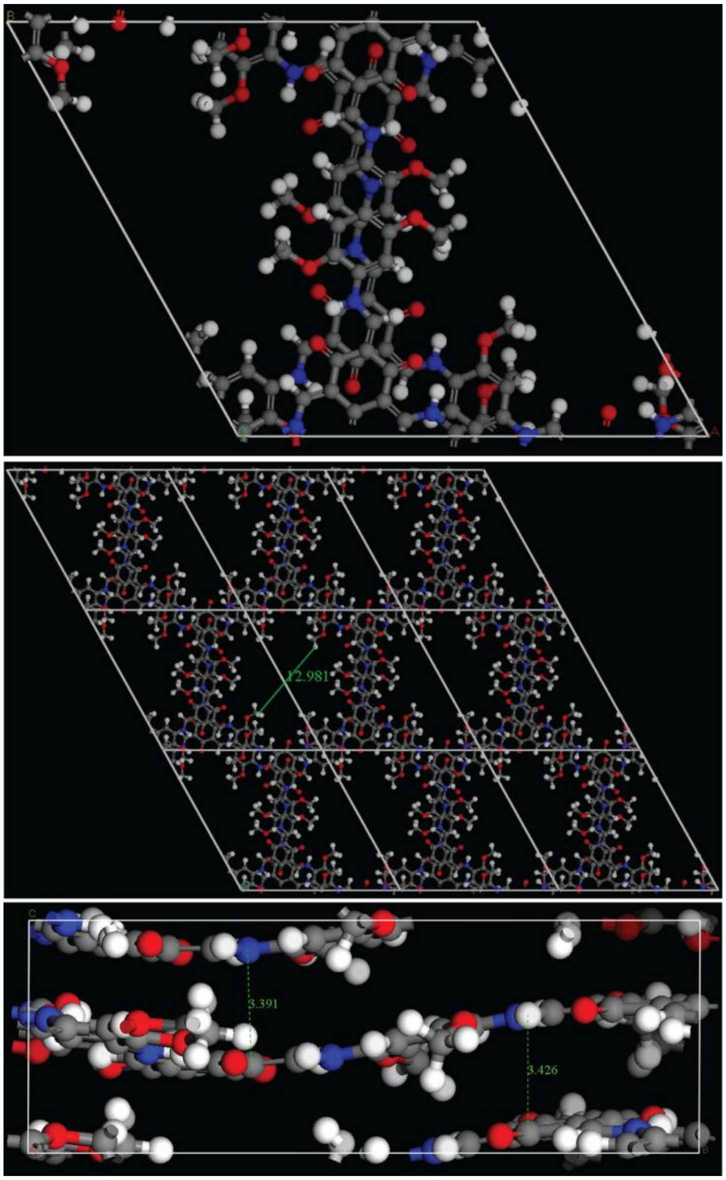

Figure 5.6*: Simulation of the* **TpPa-(OMe)$_2$** *unit cell content calculated in a slip-AA arrangement (1.9Å along the y-axis): top view onto the ab-plane and view perpendicular to the c-axis.*

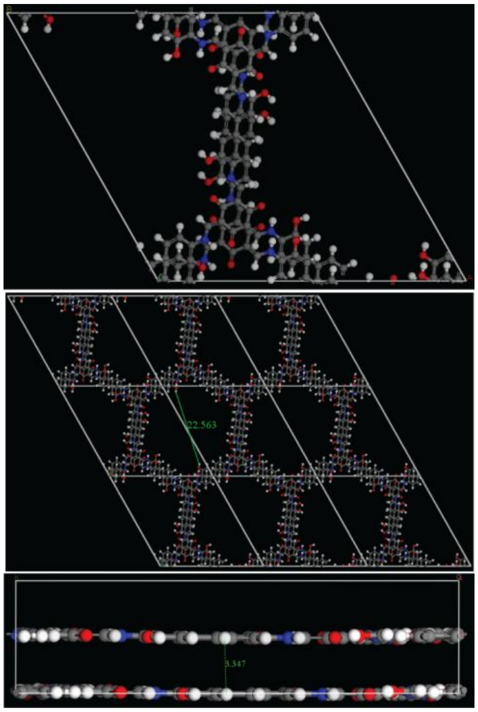

Figure 5.7: *Simulation of the **TpBD-(OH)$_2$** unit cell content calculated in a slip-AA arrangement (2.5Å along the y-axis) arrangement: top view onto the ab-plane and view perpendicular to the c-axis.*

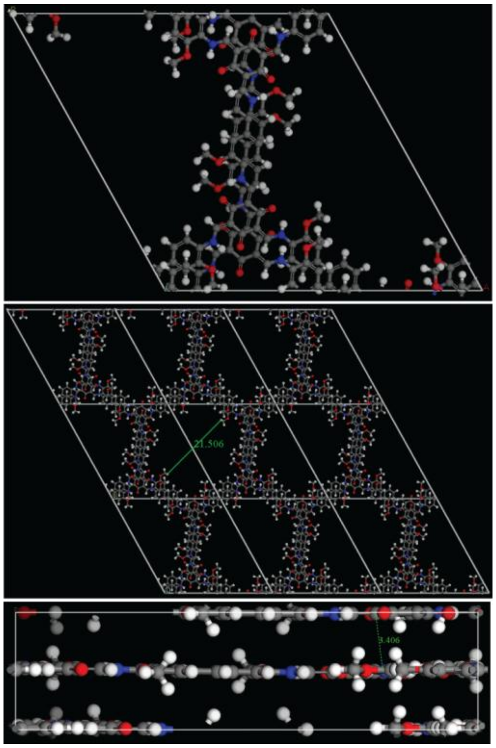

Figure 5.8: *Simulation of the **TpBD-(OMe)$_2$** unit cell content calculated in a slip-AA arrangement (2.3Å along the y-axis): top view onto the ab-plane and view perpendicular to the c-axis.*

5.3.3 Calculation of single point energy of hydrated bilayer of oxidized (Q) and reduced (H_2Q) form of TpPa-(OH)$_2$

Discrete models of the Q and H_2Q forms of **TpPa-(OH)$_2$** were constructed. Each model included a Tp center and three Pa-(OH)$_2$ linkers, which were cut at the amine nitrogen and capped with methyl groups. Bilayer models were created by adding a second model 3.35Å above the first (interlayer separation) and slipped by 2.5Å in order to replicate the geometry of the periodic **TpPa-(OH)$_2$** structure. Each model was solvated in a cylinder 13.5Å high with 15Å radius, resulting in a total of 107 water molecules.

Solvated bilayer models were then optimized, without constraint, using DFTB+ version 1.2, mio-0-1 parameters and Lennard-Jones dispersion. Using the fully optimised structures, the stabilisation energy was calculated as E(stabilisation) = E(hydrated bilayer) - [E(bilayer) + E(water)], where E(bilayer) and E(water) are single point energies of the bilayer model and water shell, calculated from the optimised hydrated bilayer model.

The calculated stabilization energy for Q and H_2Q form of **TpPa-(OH)$_2$** were 1288 and 1312 kJ mol^{-1} respectively.

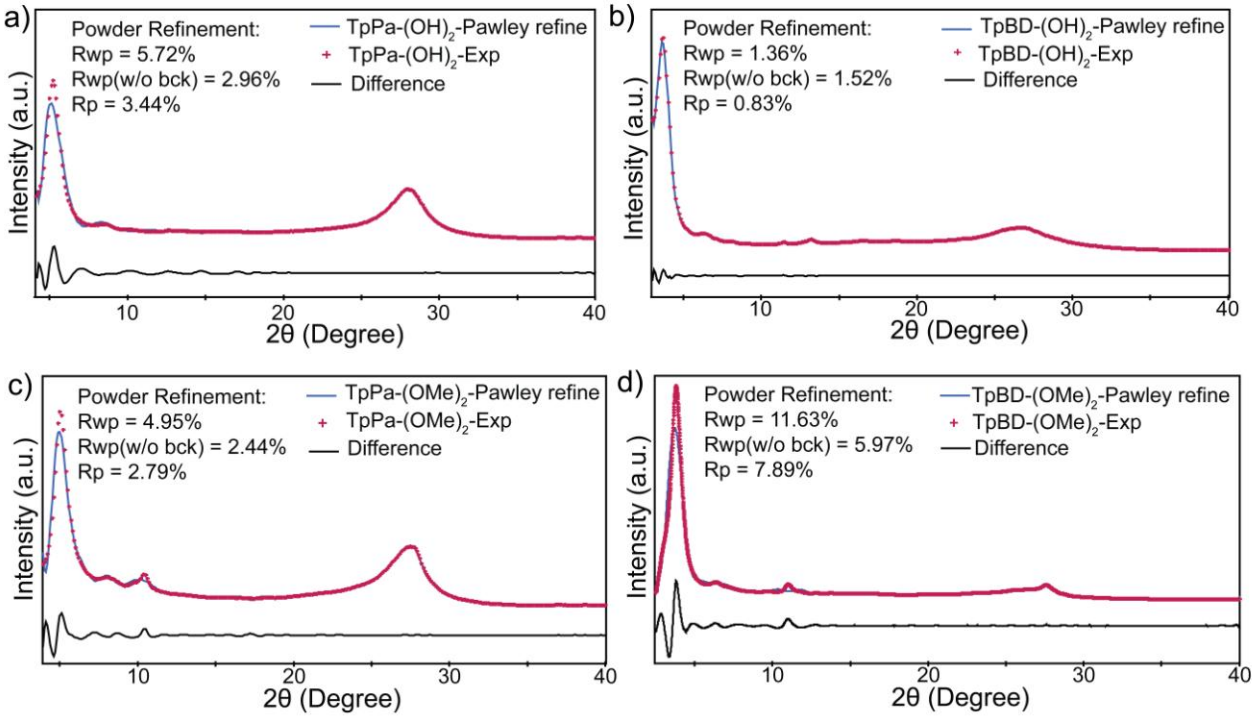

***Figure 5.9**: Experimental (pink) PXRD profiles of (a) **TpPa-(OH)$_2$**, (b) **TpBD-(OH)$_2$**, (c) **TpPa-(OMe)$_2$** and (d) **TpBD-(OMe)$_2$** compared with Pawley refined (blue) of an eclipsed offset arrangement COF based on P1 symmetry; difference plot is given in (black).*

5.3.4 *Chemical characterization*

The FT-IR spectra of these COFs show strong stretching bands at ~1572 and ~1252 cm^{-1} for the (C=C) and (C-N) bonds respectively, confirming the existence of the keto tautomer [5.43]. All the FT-IR peaks of **TpPa-(OH)$_2$** and **TpBD-(OH)$_2$** COF match with the reference compound (Figure 5.10 and 5.11a). In the cross-polarization magic angle spinning (CP-MAS) carbon-13 solid-state nuclear magnetic resonance spectroscopy, the absence of the characteristic aldehyde carbon (HC=O) at ~192 ppm and the presence of exocyclic keto carbon (C=O) at ~184 ppm again indicate the formation of a stable keto tautomer instead of the enol tautomer. The signals at ~148 ppm and ~105 correspond to the sp^{3}C attached with sp^{3}N (C-N) and the exocyclic sp^2 C attached with sp^{2}C (C=C) respectively, in the keto tautomer structure. The extra peak at ~55 ppm arises due to the methoxy carbon (C–O) in the case of methoxy substituted **TpPa-(OMe)$_2$** and **TpBD-(OMe)$_2$** COF (Figure 5.11b).

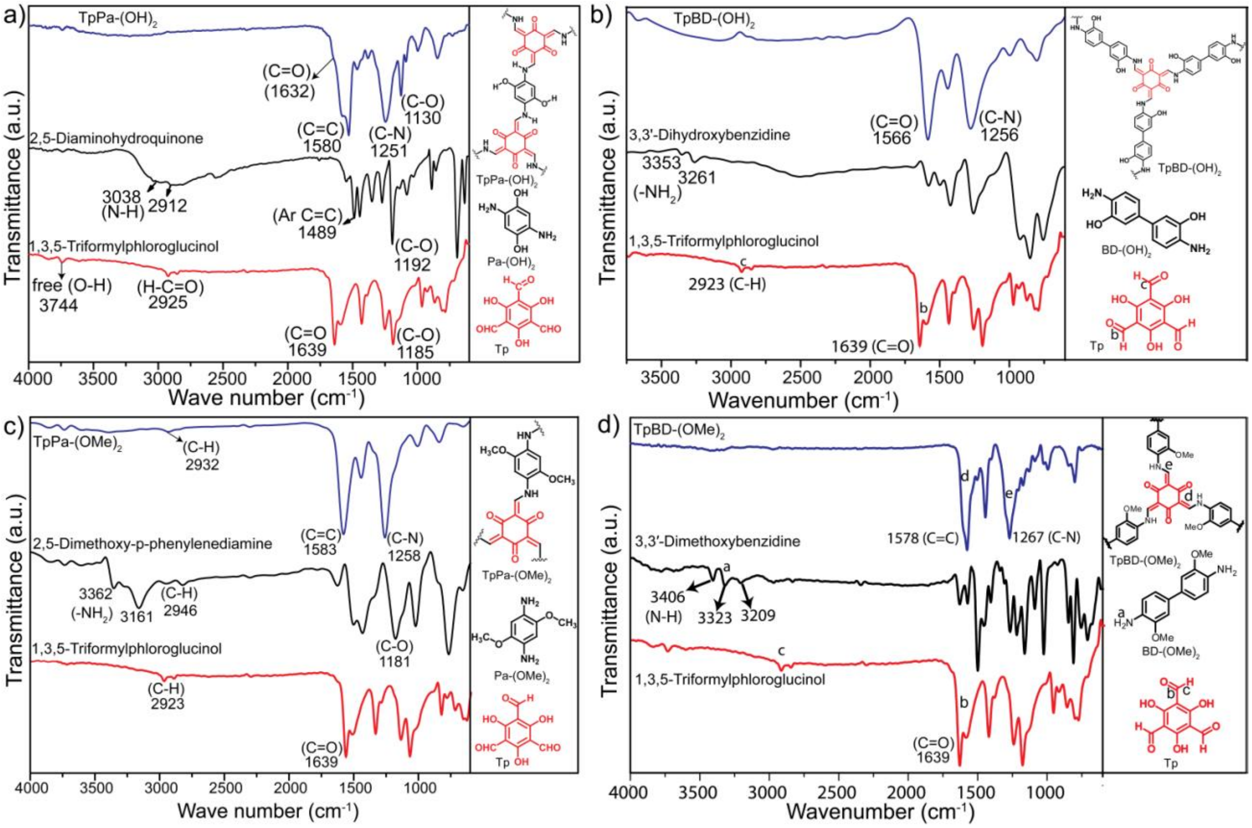

Figure 5.10: *FT-IR spectra of (a)* ***TpPa-(OH)$_2$****, (b)* ***TpBD-(OH)$_2$****, (c)* ***TpPa-(OMe)$_2$*** *and (d)* ***TpBD-(OMe)$_2$*** *compared with starting material* ***Tp*** *(Red),* ***Pa-(OH)$_2$*** *(Black),* ***Pa-(OMe)$_2$****, (Black)* ***BD-(OH)$_2$****, (Black) and* ***BD-(OMe)$_2$****, (Black).*

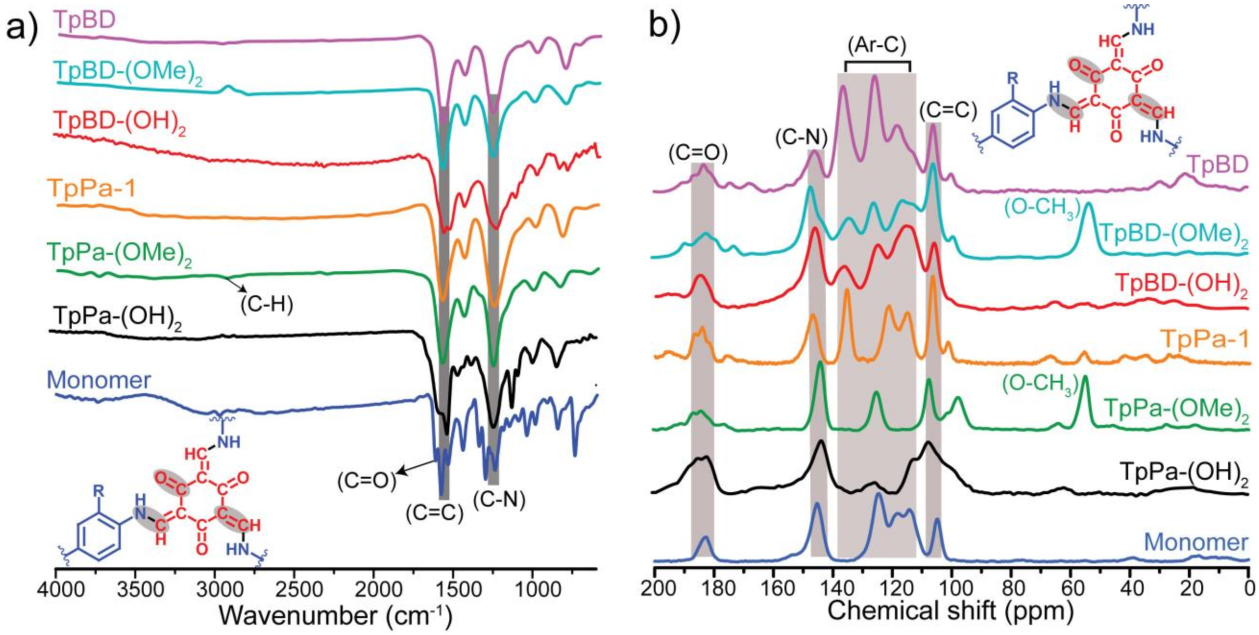

***Figure 5.11**: (a) FT-IR comparison spectra among reference compound (Blue) [Monomer of **TpPa-(OH)$_2$** and **TpBD-(OH)$_2$**] and **TpPa-(OH)$_2$** (Black), **TpPa-(OMe)$_2$** (Green), **TpPa-1** (Brown), **TpBD-(OH)$_2$** (Red), **TpBD-(OMe)$_2$** (Cyan) and **TpBD** (Magenta). (b) Solid state ^{13}C CP-MAS spectrum comparison of reference compound [i.e Monomer of **TpPa-(OH)$_2$** and **TpBD-(OH)$_2$**] (Blue), **TpPa-(OH)$_2$** (Black), **TpPa-(OMe)$_2$** (Green), **TpPa-1** (Brown), **TpBD-(OH)$_2$** (Red), **TpBD-(OMe)$_2$** (Cyan) and **TpBD** (Magenta).*

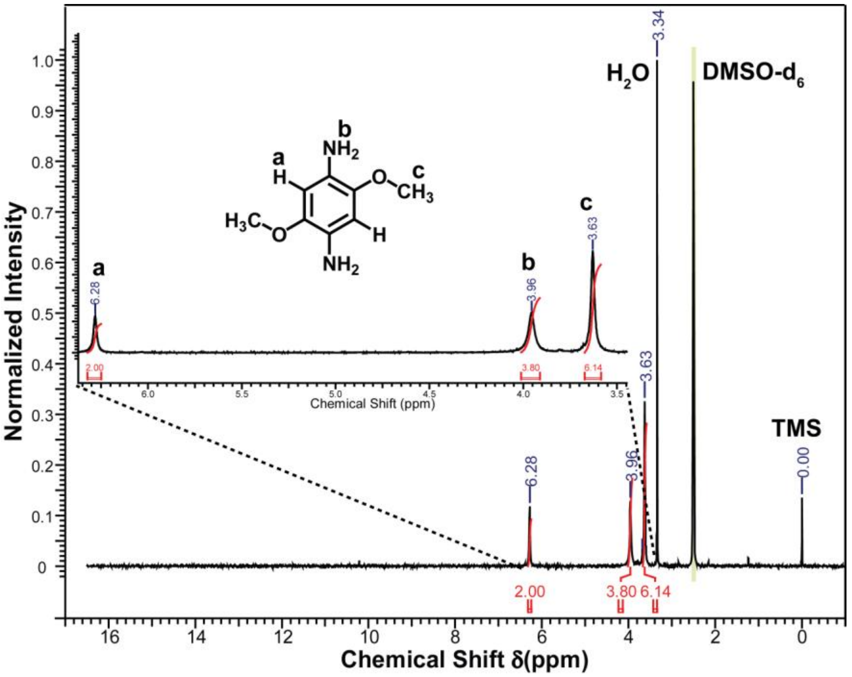

***Figure 5.12**: Liquid state ^{1}H-NMR for 2,5-Dimethoxy-p-phenlenediamine [**Pa-(OMe)$_2$**]. Inset showing the zoom portion.*

Both field emission scanning electron microscope (FE-SEM) and transmission electron microscopy (TEM) revealed a uniform plate-like morphology with ~(100-300) nm size for **TpPa-(OH)$_2$** and **TpBD-(OH)$_2$**. However, **TpPa-(OMe)$_2$** and **TpBD-(OMe)$_2$** showed ~(100-300) nm sized flake like morphology (Figure 5.13).

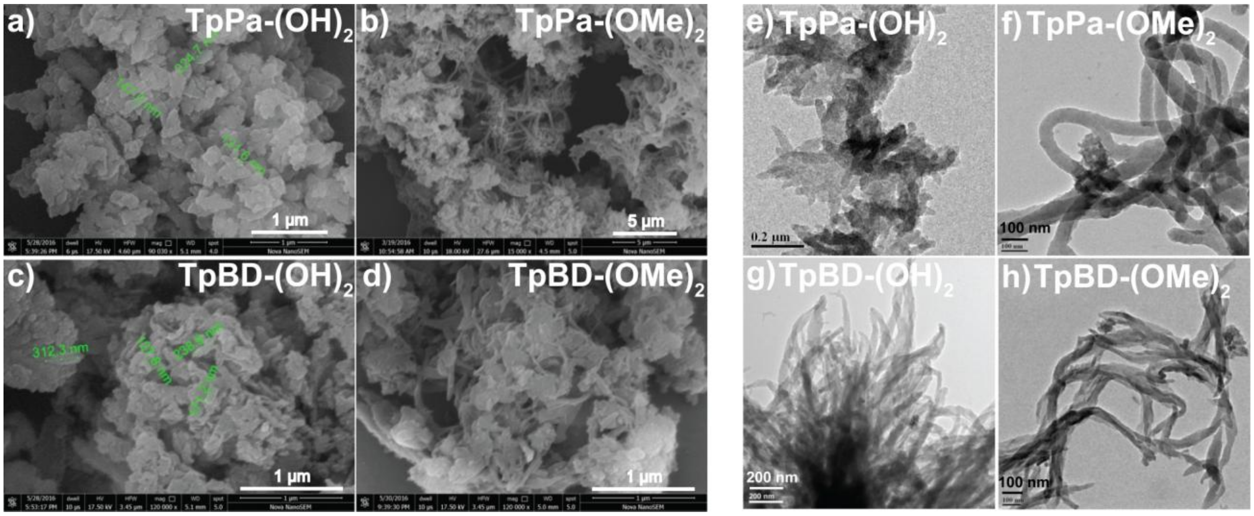

Figure 5.13: *(a)-(d) SEM images and (e)-(h) TEM images of* ***TpPa-(OH)$_2$****,* ***TpPa-(OMe)$_2$****,* ***TpBD-(OH)$_2$****, and* ***TpBD-(OMe)$_2$*** *respectively.*

The TGA showed that both hydroxyl based COFs [**TpPa-(OH)$_2$** and **TpBD-(OH)$_2$**] are stable up to 250 °C (Figure 5.14).

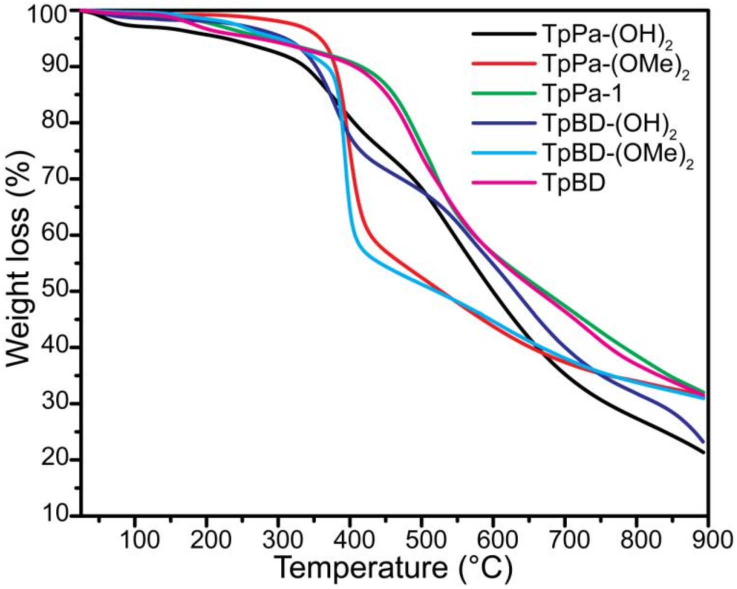

Figure 5.14: *TGA of* ***TpPa-(OH)$_2$*** *(Black),* ***TpPa-(OMe)$_2$*** *(Red),* ***TpPa-1*** *(Green),* ***TpBD-(OH)$_2$*** *(Blue),* ***TpBD-(OMe)$_2$*** *(Cyan) and* ***TpBD*** *(Magenta) under N_2 atmosphere after pre-activation of all three COFs.*

5.3.5 *Gas adsorption studies*

Both **TpPa-(OH)$_2$** and **TpBD-(OH)$_2$** exhibit characteristics of type-I adsorption isotherms (Figure 5.15). The Brunauer−Emmett−Teller (BET) surface area of **TpPa-(OH)$_2$** and **TpBD-(OH)$_2$** are 369 and 197 $m^2 g^{-1}$ with pore volume 0.417 and 0.241 $cm^3 g^{-1}$ respectably. The observed moderate surface areas for these two COFs may be due to the lack of sufficient long range ordering in their 2D layer structure because of their serrated stacking mode. The pore width calculated from the N_2 adsorption isotherm closely matches with the pore width generated from the serrated (slip-AA) stacking mode rather than the eclipsed (AA) stacking mode.

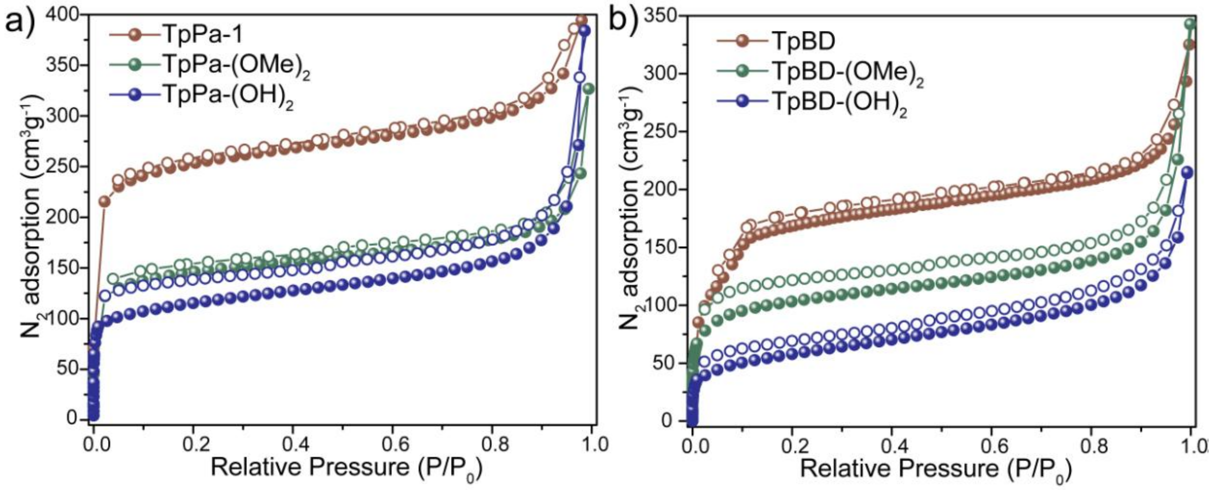

***Figure 5.15**: Comparison of N_2 adsorption isotherms at 77 K for (a) TpPa series [**TpPa-(OH)$_2$** (blue), **TpPa-(OMe)$_2$** (green) and **TpPa-1** (brown)] and (b) TpBD series [**TpBD-(OH)$_2$** (blue), **TpBD-(OMe)$_2$** (green) and **TpBD** (brown)]. [filled symbols for adsorption and empty symbols for desorption.]*

Again, both **TpPa-(OH)$_2$** and **TpBD-(OH)$_2$** have a pore size in the range of ~(10-18) Å calculated by non-local density functional theory (NLDFT) model, indicating the formation of micropores (Figure 5.16).

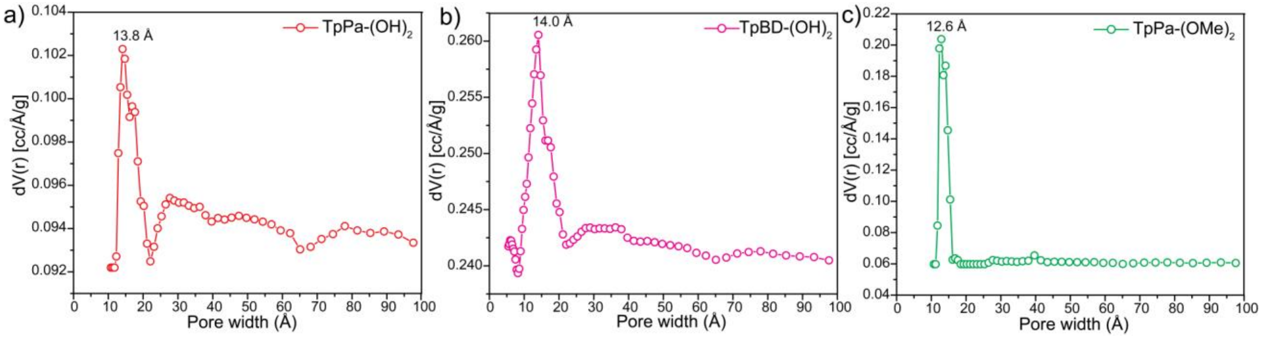

***Figure 5.16**: NLDFT Pore size distribution of (a) **TpPa-(OH)$_2$**, (b) **TpBD-(OH)$_2$** and (c) **TpPa-(OMe)$_2$** calculated by using DFT method.*

5.3.6 Electro*chemical stability investigation*

As reported earlier [5.43] keto-enamine COFs are chemically stable, so here we have checked only the electrochemical stability of the prepared COFs. We have examined the changes of morphologies for bulk COF **TpPa-(OH)$_2$**, COF with binder PVDF and carbon black before and after the electrochemical studies. The morphological changes observed from SEM for bulk COF and COF with binder and carbon was due to the mixing all of them together in NMP solvent via mechanical grinding (Figure 5.17a and 5.17b). There was negligible change in the morphology of COF based electroactive material before and after of electrochemical studies confirms the electrochemical stability (Figure 5.17b and 5.17c).

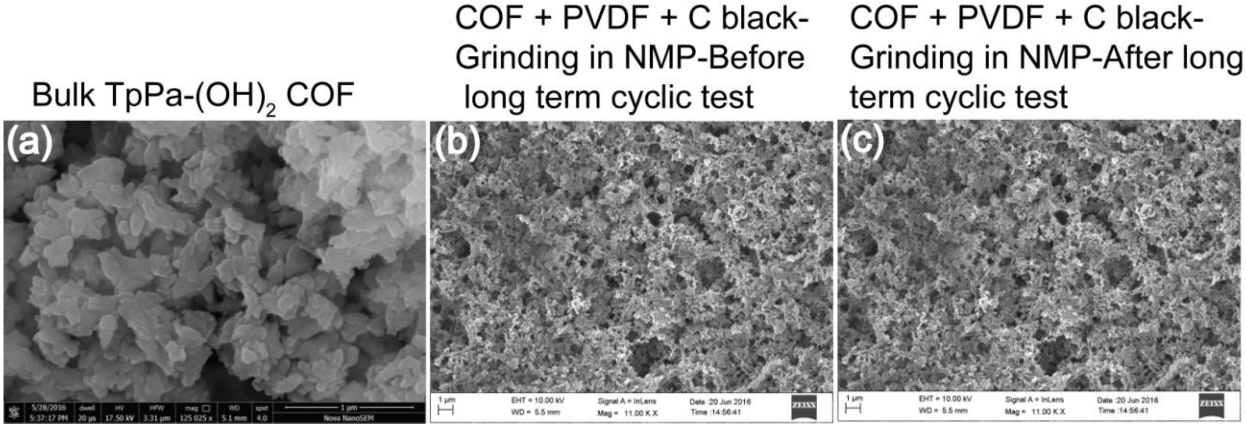

Figure 5.17: *SEM images of* ***TpPa-(OH)$_2$*** *; (a) Bulk COF after synthesis and activation, (b) After mixing with carbon black and PVDF follow by grinding in NMP and (c) After long term cyclic test.*

5.3.7 *Capacitance studies*

Capacitor performances of these COFs were evaluated in 1 M phosphate buffer (pH 7.2) using three electrode configuration. Cyclic voltammograms (CVs) of **TpPa-(OH)$_2$** reveal that the specific capacitance is predominantly pseudocapacitive (capacitance due to redox transitions of H_2Q/Q) in nature. The highest specific capacitance of 396 F g^{-1} has been obtained at a scan rate of 2 mV s^{-1} (Figure 5.18a and Table 5.5). The separation between cathodic and anodic peaks (ΔE_p) is only 72 mV at a faster scan rate of 20 mV s^{-1} (Table 5.6), which is indicative of fast electron transfer kinetics between COF and the electrode interface. Similar capacitance values were obtained from galvanostatic charge/discharge experiments while the maximum specific capacitance obtained was 416 F g^{-1} at 0.5 A g^{-1} current density (Figure 5.18b and Table 5.5). To the best of our knowledge, this is the highest specific capacitance obtained for COF based materials and higher than most of the carbon-based materials reported in the literature (Table 5.10).

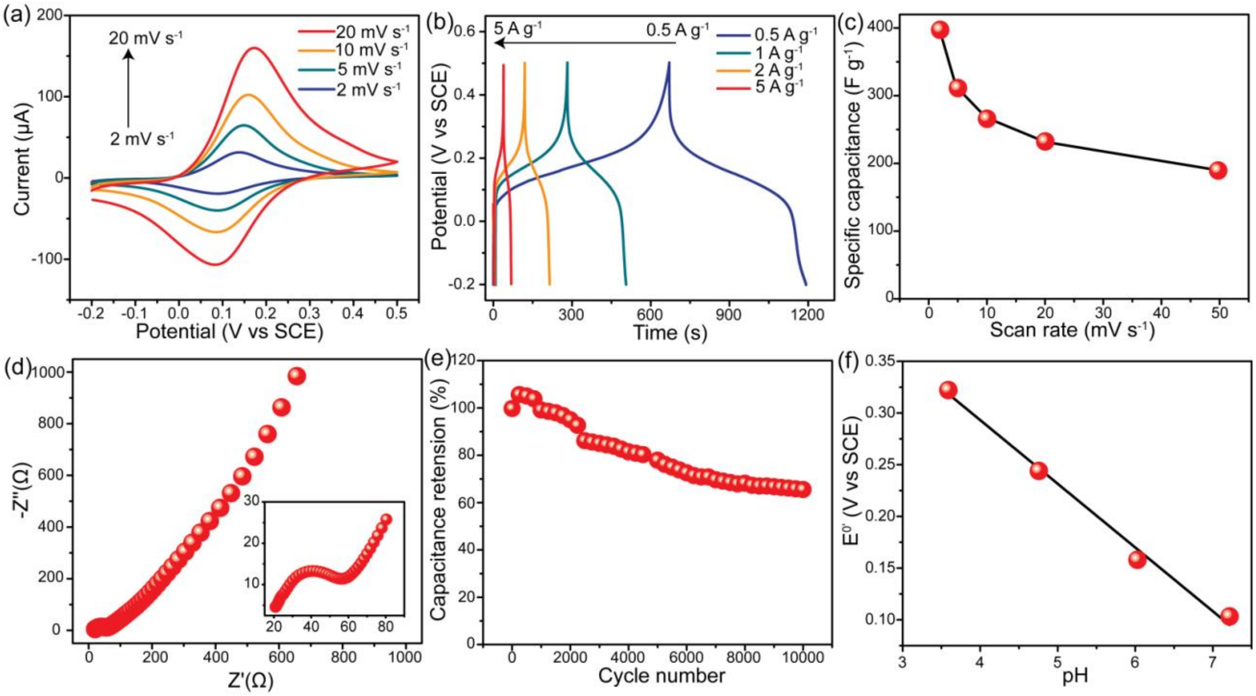

Figure 5.18. *Electrochemical performance of* ***TpPa-(OH)$_2$****. (a) CVs at different scan rates (2, 5, 10 and 20 mV s^{-1}). (b) Galvanostatic charge/discharge experiments at different current densities (0.5, 1, 2 and 5 A g^{-1}). (c) Specific capacitance dependence on scan rates of voltammetry. (d) The Nyquist plot of EIS results collected at 0.12 V vs SCE (inset: high-frequency region). (e) Long-term cyclic stability performance at a current density of 5 A g^{-1}of galvanostatic charge/discharge experiment. (f) Pourbaix diagram (E^{0}′vs pH).*

Table 5.5: Specific capacitance (F g^{-1}) of **TpPa-(OH)$_2$**, **TpPa-(OMe)$_2$** and **TpPa-1** at different scan rates (mV s^{-1}) of cyclic voltammograms and current densities (A g^{-1}) of galvanostatic charge/discharge experiment.

Scan Rate	**TpPa-(OH)$_2$**	**TpPa-(OMe)$_2$**	**TpPa-1**	**Current density**	**TpPa-(OH)$_2$**	**TpPa-(OMe)$_2$**	**TpPa-1**
2	396±1	13±1	6±1	0.5	416±12	10±1	4±1
5	309±11	7±1	3±1	1	344±11	4±1	3±1
10	264±12	5±1	2±1	2	288±13	3±1	2±1
20	230±11	4±1	2±1	5	214±19	2±1	1±1

Table 5.6: Anodic and cathodic peak separation (ΔE_p) at different scan rates of voltammetry for **TpPa-(OH)$_2$**.

Scan rate (mV s^{-1})	**Δ*E*p (mV)**
2	47

5	49
10	59
20	72

However, 58% specific capacitance retention was obtained at a high scan rate of voltammetry (20 mV s^{-1}) (Figure 5.18c). The drop of specific capacitance at high scan rate during the CV presumably was due to restriction for ion insertion during rapid potential scanning [5.58].

Electrochemical impedance spectroscopy experiment (EIS) was performed at the formal potential of H_2Q/Qredox transition. The Nyquist plot of **TpPa-(OH)$_2$** revealed the slightly inclined rise of impedance along the imaginary axis in the low-frequency region, which is indicative of a good mass transport inside the material (Figure 5.18d). EIS result was fitted using an equivalent circuit model to assess the resistance for charge/electron transfer due to the H_2Q/Q transition at the electrode/electrolyte interface (R_{ct}) and a value of 37.5 Ω was obtained (Figure 5.19 and Table 5.7). Detailed justification for the equivalent circuit, fitted result for EIS, and equivalent circuit parameters values have been provided below.

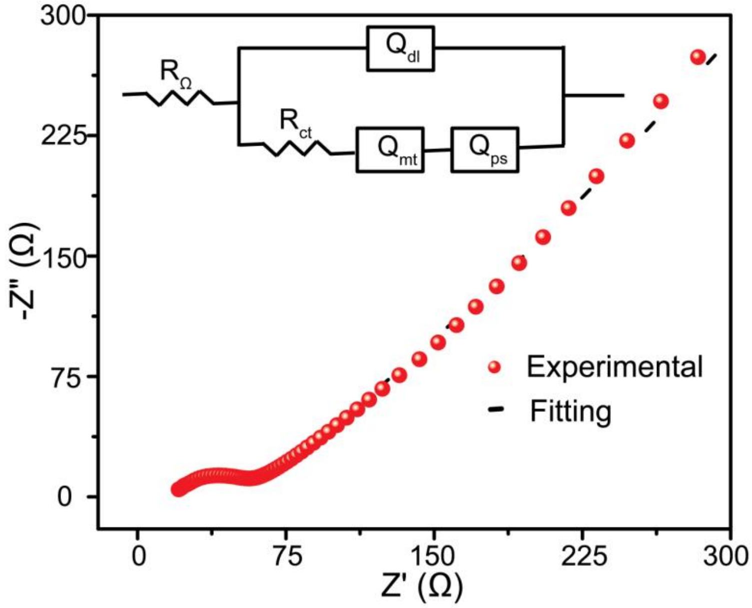

Figure 5.19: *Nyquist plot of* ***TpPa-(OH)$_2$*** *collected at the formal potential (black empty circles) of H_2Q moiety. The solid black line represents best fitted EIS result (χ^2 <0.05) utilizing the equivalent circuit shown in the inset.*

Justification for equivalent circuit and related results: In this equivalent circuit, R_{Ω}, R_{ct}, Q_{dl}, Q_{mt}, and Q_{ps} represent electrolyte solution resistance, resistance associated with charge/electron transfer reaction due to proton-coupled electron transfer reaction of H_2Q moiety at the electrode/electrolyte interface, charging capacity at the electrode/electrolyte interface, electrolyte ion diffusion inside the nanomaterial in the low frequency region and pseudocapacitive charging in the low frequency region respectively. The semicircle in the high-frequency region represents R_{ct} and the value was found to be 37.5 Ω. Q_{dl}, Q_{mt} and Q_{ps} are constant phase elements where n represents exponent term (Table 5.7) and the value of n ranges from 0 to 1. n=0 represents an ideal resistor while n=1 represents an ideal capacitor. In general, a capacitor element (C_{dl}) is used for EIS fitting, however, Q_{dl} has been used here which provided better fitting. The obtained n value for Q_{dl} was less than 1 (Table 5.7) presumably due to electrode roughness. Q_{dl} was much less than Q_{ps} indicating pseudocapacitive charging was the dominant process for charge storage [5.40, 5.41].

Table 5.7: Values of equivalent circuit parameters calculated from EIS results for **TpPa-(OH)₂**.

		Q_{dl}		Q_{mt}		Q_{ps}	
R_{Ω} (Ω)	**R_{ct} (Ω)**	**Y_{dl} (F)**	**n**	**Y_{mt} (F)**	**n**	**Y_{ps} (F)**	**n**
18.5	37.5	1.8×10^{-5}	0.72	0.0028	0.48	0.015	0.98

In the long term cyclic test, 66% specific capacitance retention was obtained after 10,000 cycles at a current density of 5 A g^{-1} (Figure 5.18e). Initially, CVs were collected for **TpPa(OH)₂** in different pH solutions (pH 3.6-7.2) and the electrochemistry revealed a reversible redox peak, presumably due to the presence of the H_2Q functionality in the COF (Figure 5.18f) wherein the formal potential ($E^{0\prime}$) was pH dependent. The $E^{0\prime}$ values were shifted towards the cathodic direction with increasing pH and the slope of the Pourbaix diagram [5.59] ($E^{0\prime}$ vs pH) was found to be 61 mV/pH (Figure 5.18f), suggesting a $2H^+/2e^-$ proton-coupled electron transfer (PCET) [5.60] reaction for the H_2Q/Q redox transition.

The coulometric charge calculation of CV revealed that at least 43% H_2Q functionalities responded during an electrochemical experiment. The high redox accessibility presumably was due to crystalline nature of the material which exposed edges of the interlayer gaps for facile ion insertion [5.61].

Determination of hydroquinone accessed:

1. TpPa-(OH)₂ COF mass on electrode= 142.9 μg/cm^2

H_2Q comprises 44 % of this mass.

$142.9\ \mu g\ cm^{-2}$ *(0.44) = $62.9\ \mu g/cm^2$ of **H_2Q** on surface

2. Convertion of mass to moles

$62.9 \times 10^{-6}\ g/cm^2$ (mol/140 g) = $4.49 \times 10^{-7}\ mol/cm^2$ **H_2Q** present on electrode surface

3. Each hydroquinone involved in a 2 e^- transfer process.

Determination of the number of moles of e^-

$$4.49\text{x}10^{-7}\ \frac{mol}{cm^2}\ \mathbf{H_2Q}\left(\frac{2mol-e^-}{molH_2Q}\right) = 8.98\text{x}10^{-7}\ \text{mol/cm}^2\ \text{e}^-$$

4. Determination of the maximum charge possible to pass

$$8.98\text{x}10^{-7}\ \frac{mol}{cm^2}\left(\frac{96485C}{mol-e^-}\right) = 86.6\ \text{mC/cm}^2$$

5. Charge obtained from the integration of the oxidation wave

Example: At 2 mV s^{-1}: 37.1 mC/cm^2 of charge is passed

6. Dividing the integrated charge by the theoretical and multiplying by 100

$$\frac{37.1\mu C / cm^2}{86.6\mu C / cm^2} x100 = 43\%\ \text{of}\ \mathbf{H_2Q}\ \text{responded during electrochemistry}$$

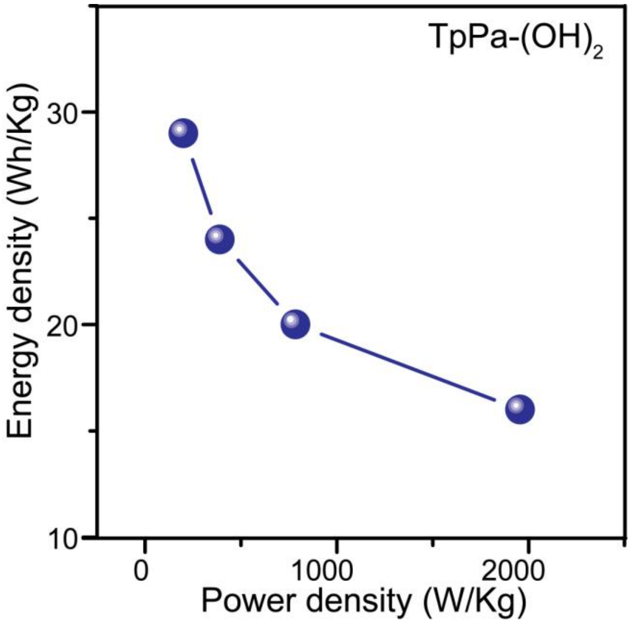

Figure 5.20: *Ragone plot for* ***TpPa-(OH)$_2$****.*

The Ragone plot revealed that the **TpPa-(OH)$_2$** showed the maximum energy and power density of 29 Wh kg^{-1} and 1956 W kg^{-1} respectively (Figure 5.20).

In order to further verify that the obtained specific capacitances are predominantly due to H$_2$Q functionalities, experiments were performed for COFs that are devoid of H$_2$Q [**TpPa-1** and **TpPa-(OMe)$_2$**]. The highest specific capacitances for **TpPa-1** and **TpPa-(OMe)$_2$** were 6 and13 F g^{-1} at a 2 mV s^{-1} scan rate of voltammetry and CVs were devoid of redox peaks as well (Table 5.5 and Figure 5.21a).

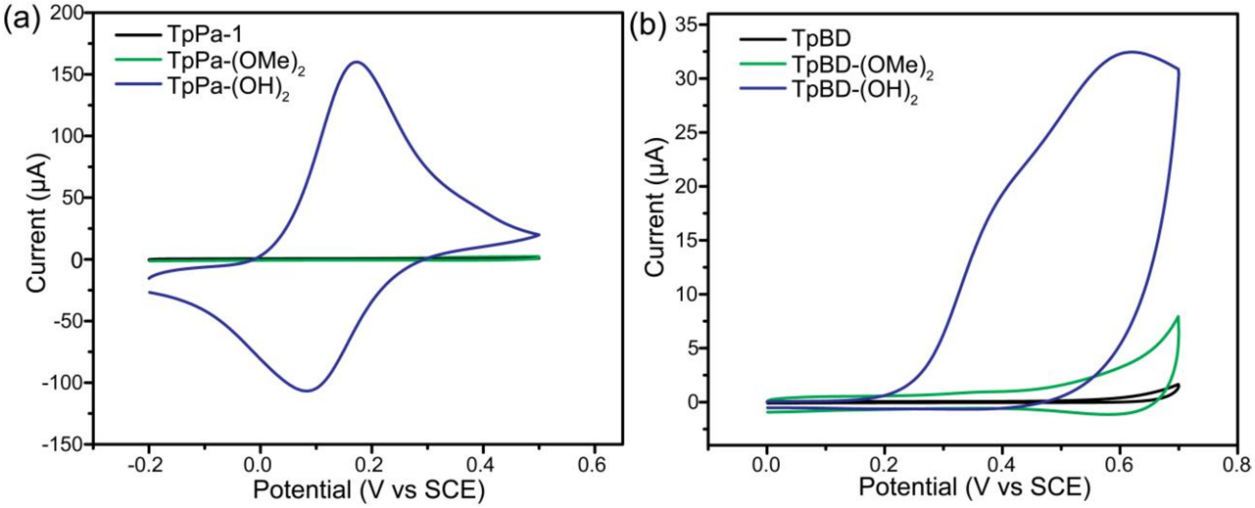

Figure 5.21: *(a) CVs of* ***TpPa(OH)$_2$*** *(blue),* ***TpPa-(OMe)$_2$*** *(green) and* ***TpPa-1*** *(black) at 20 mV s^{-1}. (b) CVs of* ***TpBD-(OH)$_2$**** *(blue),* ***TpBD-(OMe)$_2$*** *(green) and* ***TpBD*** *(black) at 20 mV s^{-1}.*

* **[**The peak appeared at ~0.55 V vs SCE for **TpBD-(OH)$_2$** was due to stepwise proton transfer followed by electron transfer reaction (PT-ET) of phenolic functional groups to produce phenoxy radical following literature precedence [5.62] in which proton abstraction was assisted by HPO$_4^{2-}$. We speculate that the weak redox peak appeared at ~0.35 V vs SCE for **TpBD-(OH)$_2$** was due to concerted electron-proton transfer (EPT) reaction of phenolic functional groups to generate phenoxy radical in which proton transfer was assisted by HPO$_4^{2-}$ [5.63]. This redox peak becomes more prominent at slower scan rates indicating kinetic sluggishness.**]**

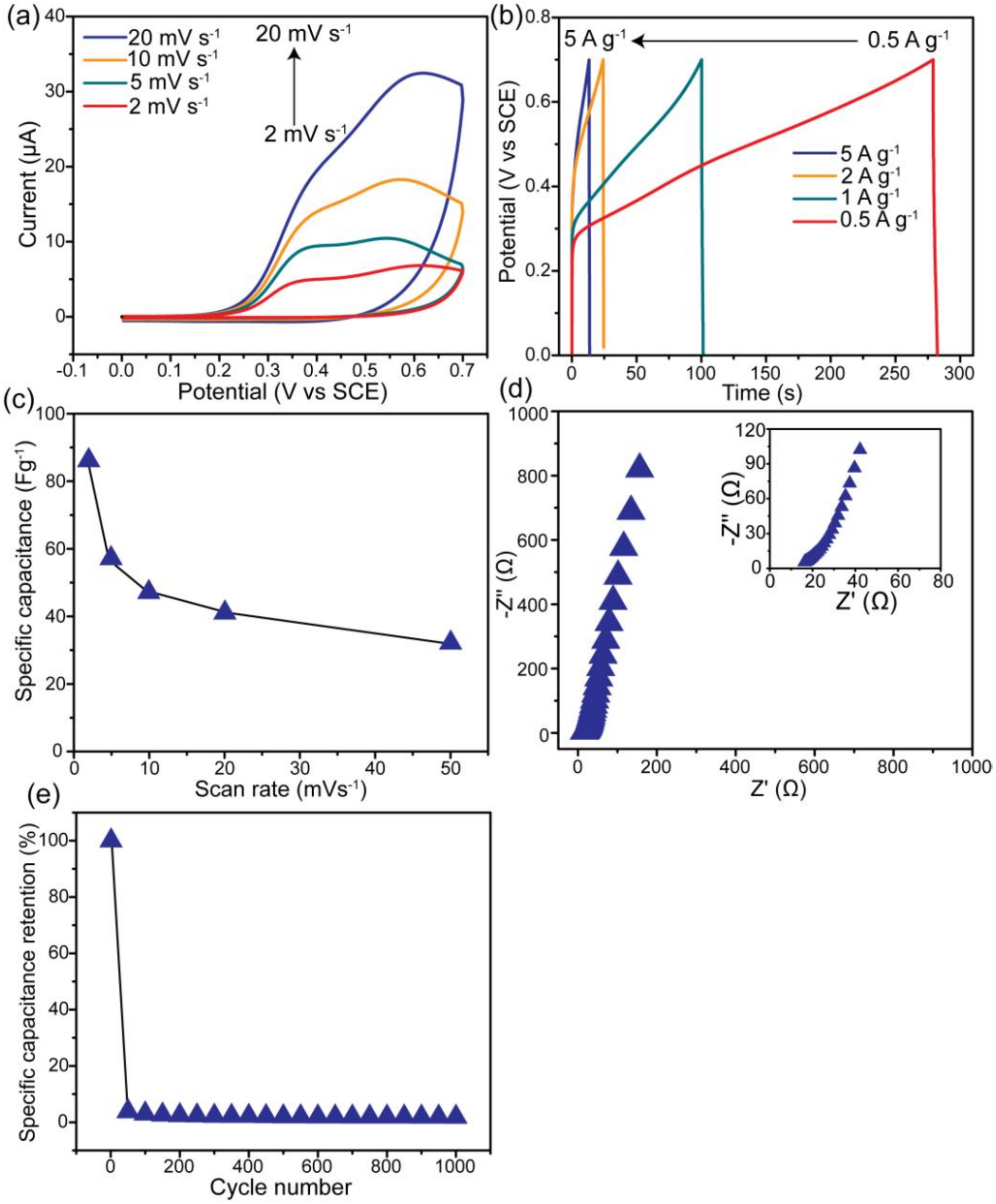

Figure 5.22: *Electrochemical performance of* **TpBD-(OH)$_2$**. *(a) Cyclic voltammograms at different scan rates (2, 5, 10 and 20 mV s^{-1}). (b) Galvanostatic charge/discharge at different current densities (0.5, 1, 2 and 5 A g^{-1}). (c) Specific capacitance dependence on scan rates of voltammetry. (d) Nyquist plot of EIS results collected at 0 V vs. SCE (inset: high-frequency region) and (e) Long term cyclic stability performance at a scan rate of 20 mV s^{-1} in CV.*

The supercapacitor studies for **TpBD-(OH)$_2$** revealed a highest specific capacitance of 86 F g^{-1} at 2 mV s^{-1} scan rate (Figure 5.22 and Table 5.8). Irreversible redox transition due to the phenol/phenoxy radical was responsible for modest specific capacitances. However, the phenoxy radical quickly decomposes and hence, in the long term cyclic test, only 2% capacitance retention was observed (Figure 5.22e) [5.64]. In order to verify that the redox transition is due to phenol functionalities, experiments were performed for **TpBD** and **TpBD-(OMe)$_2$**. For both the COFs, redox peaks were not observed and the highest specific capacitances were only 29 and 16 Fg^{-1} at the 2 mV s^{-1} scan rate for **TpBD** and **TpBD-(OMe)$_2$** respectively (Figure 5.22b and Table 5.8).

Table 5.8: Specific capacitance (F g^{-1}) of **TpBD-(OH)$_2$**, **TpBD-(OMe)$_2$** and **TpBD** at different scan rates (mV s^{-1}) of cyclic voltammograms and current densities (A g^{-1}) of galvanostatic charge/discharge experiment.

Scan Rate	**TpBD-(OH)$_2$**	**TpBD-(OMe)$_2$**	**TpBD**	**Current density**	**TpBD-(OH)$_2$**	**TpBD-(OMe)$_2$**	**TpBD**
2	86±9	29±1	16±3	0.5	90±10	26±1	27±3
5	57±2	10±1	6±1	1	67±5	4±1	20±5
10	47±4	7±1	3±1	2	48±3	3±1	9±2
20	41±1	5±1	2±1	5	44±5	2±1	3±1

Recent investigations on the redox interconversion mechanism of H_2Q/Q in a buffer solution [5.65] suggests that during the oxidation, pre-association occurs between H_2Q and the base present in the buffer solution, followed by an occurrence of the concerted electron-proton transfer (EPT) reaction in which the proton of H_2Q was transferred to the base and an electron was transferred to the electrode to form $HQ^{\cdot}$. In the final step, $HQ^{\cdot}$ was seen to rapidly lose a proton and transfer the second electron to the electrode. A similar mechanism operates during the reduction process to regenerate H_2Q, in which pre-association occurs between the acid present in the buffer and the benzoquinone moiety (Figure 5.23).

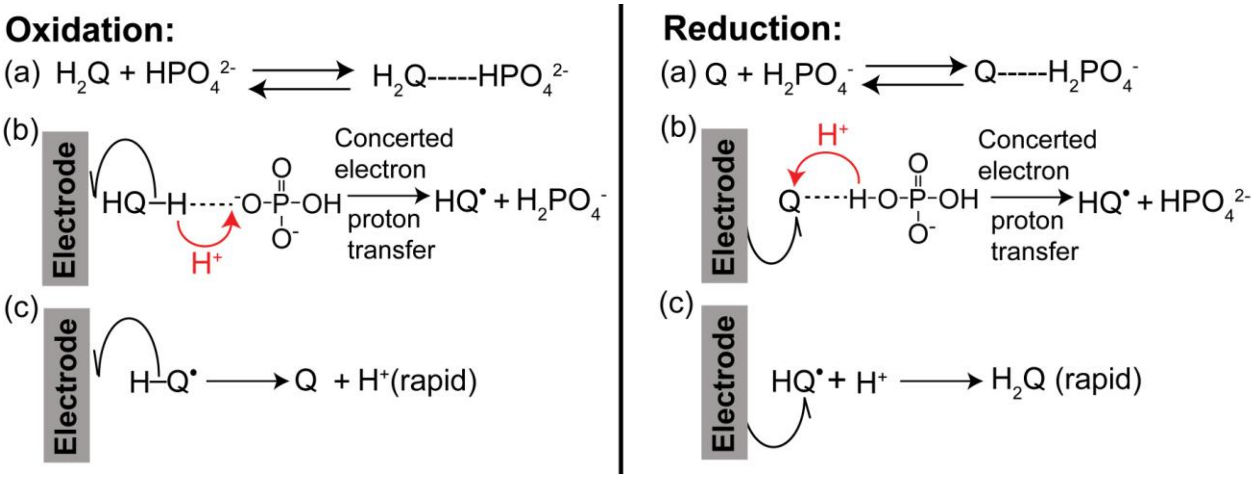

***Figure 5.23**. Probable redox reaction happening on the electrode surface of **TpPa(OH)$_2$**.*

However, benzoquinone usually decomposes rapidly, resulting in a rapid drop in specific capacitance within a few cycles [5.52]. Interestingly, in this study, an electrochemical reversibility was observed, which was confirmed by a long-term cyclic test. In order to explain the chemical reversibility, we propose that the carbonyl oxygen (C=O) of the benzoquinone functionality is involved in H-bonding with the neighboring amine functionality present in the COF, which inhibits the decomposition of Q (Figure 5.24), a mechanism which has precedence in recent literature [5.66-5.71]. The comparable stability of the Q form (oxidized form) and the H_2Q form (reduced form) in water is also supported by calculated stabilization energies of both Q and H_2Q forms of **TpPa-(OH)$_2$** fragments cut from the optimized bilayer structures, which were 1288 and 1312 kJ mol^{-1} respectively.

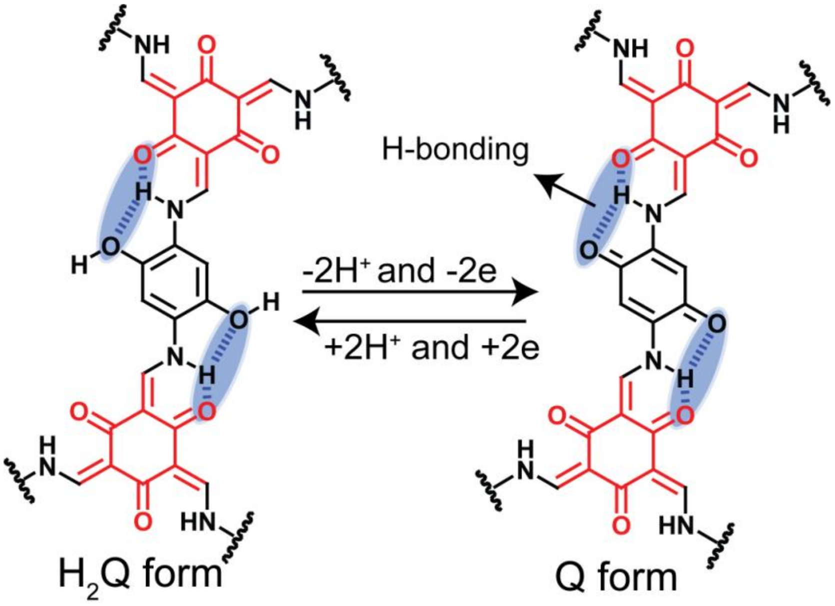

***Figure 5.24**. The proposed H-bonding stabilized both the hydroquinone (H_2Q) and benzoquinone (Q).*

It is interesting to note that all COFs [except **TpBD-(OH)$_2$**] had surface area higher than **TpPa-(OH)$_2$**. However, their specific capacitance values were insignificant compared to **TpPa-(OH)$_2$**. This observation suggests that the pseudo-capacitance is a large contributor to the total capacitance. The low surface area, the high molecular weight of **BD-(OH)$_2$** units and lower stability of the oxidized form might be the reasons for the low specific capacitance of **TpBD-(OH)$_2$**. The comparatively high stability of both the Q and H_2Q forms due to the H-bonding [5.72-5.75] in **TpPa-(OH)$_2$** COF is a possible reason for the high reversibility of the hydroquinone-quinone redox interconversion, which may also be due to the improved electron transfer kinetics. Moreover, the high specific capacitance of **TpPa-(OH)$_2$** arises due to the low molecular weight of the **Pa-(OH)$_2$** units. The high surface area, excellent chemical reversibility, and low molar mass make **TpPa-(OH)$_2$** an exceptional pseudocapacitor.

5.3.7.1 Evaluation of supercapacitor performance using symmetric two electrode cell

TpPa-(OH)$_2$ was tested as a supercapacitor nanomaterial for real-time applications using Swagelok-cells type two electrode system. Cyclic voltammograms and galvanostatic charge/discharge experiments were performed in a 0.7 V potential window as used for three electrode system (Figure 5.25 and Table 5.9). Highest specific capacitances were 211 and 214 F g^{-1} at 2 mV s^{-1} of CV and 0.2 A g^{-1} galvanostatic charge/discharge experiments (Figure 5.25a and 5.25b). These values are 48% lower compared to the results obtained from three electrode system. The drop in specific capacitance in two electrode system in comparison to three electrode system was slightly at higher end which presumably was due to the low conductivity of COF [5.76]. Research directed towards improving the conductivity of COF based material is currently underway in our laboratory. Nonetheless, the maximum specific capacitance values obtained here are significantly higher compared to the recent reports on COF based supercapacitor in two electrode system [5.42-5.50]. Moreover, 35% capacitance retention was obtained by increasing the scan rate of CV by 10 times (Figure 5.25c). In the long term cyclic test, 88% capacitance retention was observed after 10,000 cycles at a current density of 0.8 A g^{-1} (Figure 5.25d).

Table 5.9: Specific capacitance (F g^{-1}) from cyclic voltammetry at different scan rates and galvanostatic charge/discharge at different current densities for **TpPa-(OH)$_2$** using symmetric two electrode cell.

Scan rate (mV s^{-1})	**Specific capacitance (F g^{-1})**	**Current density (A g^{-1})**	**Specific capacitance (F g^{-1})**
2	211±3	**0.2**	214±1
5	139±2	**0.3**	165±7
8	113±2	**0.5**	120±2
10	96±5	**0.8**	92±1
20	73±2	**1**	74±1

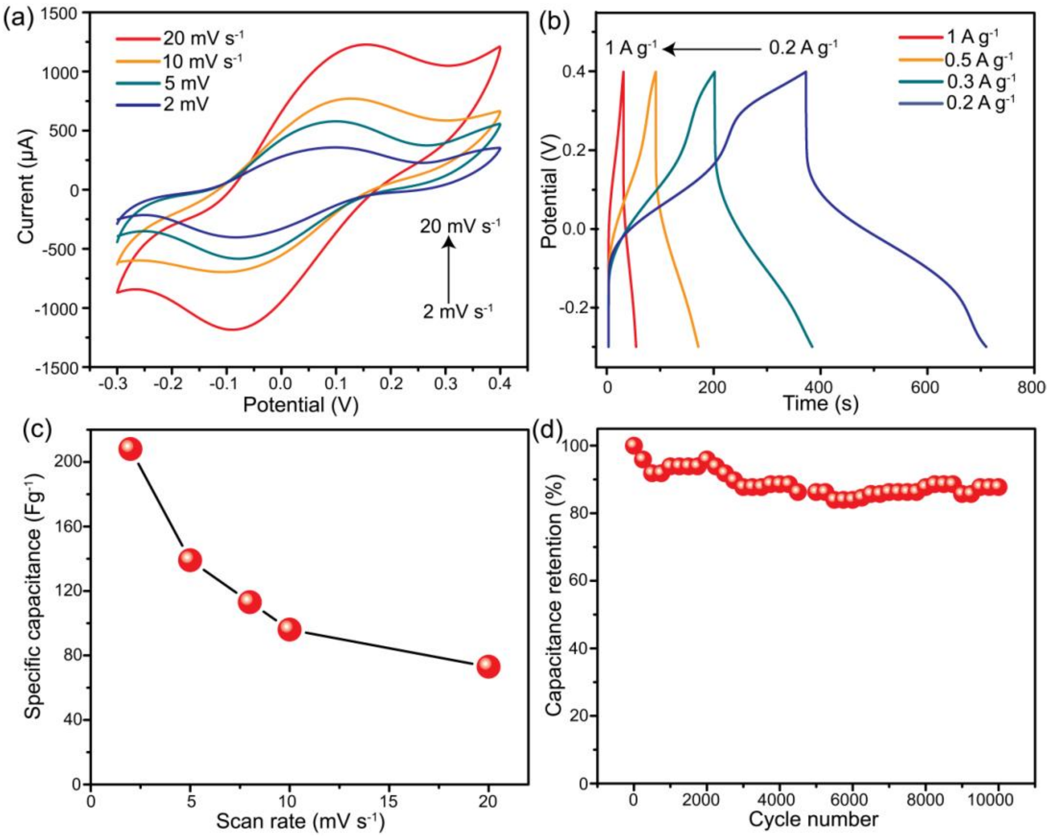

***Figure 5.25**: Electrochemical performance of **TpPa-(OH)$_2$** in two electrode system. (a) CVs at different scan rates (2, 5, 10 and 20 mV s^{-1}). (b) Galvanostatic charge/discharge experiments at different current densities (0.2, 0.3, 0.5 and 1 A g^{-1}). (c) Specific capacitance dependence on scan rates of voltammetry. (d) Long term cyclic stability performance at a current density of 0.8 A g^{-1} of galvanostatic charge/discharge experiment.*

Table 5.10: Comparison of specific capacitances obtained for different COFs and carbon based materials.

Active material	Electrolyte	Specific capacitance (F g^{-1})	Reference
TpPa-(OH)$_2$	1 M Phosphate buffer (pH = 7.2)	**416 at 0.5 A g^{-1}**	This work
DAAQ-TFP COF	1 M H_2SO_4	48±10 at 10 mV s^{-1}	*J. Am. Chem. Soc.* **2013**, *135*, 16821−16824.
[TEMPO]100%-NiP-COF [TEMPO]50%-NiP-COF	0.1 M $(C_4H_9)_4NClO_4$ in CH_3CN	(i) 167 at 0.1 A g^{-1} (ii) 124 0.1 A g^{-1}	*Angew. Chem. Int. Ed.* **2015**, *54*, 6814 –6818
Reduced graphene oxide	1 M H_2SO_4	348 at 0.2 A g^{-1}	*Carbon* **2011**, *49*, 573-580.
Functionalized carbon	6 M KOH	318 at 0.5 A g^{-1}	*Energy Environ. Sci.* **2013**, 6, 2497

Interconnected microporous carbon	1 M H_2SO_4	258 at 0.5 A g^{-1}	*Energy Environ. Sci.* **2014**, *7*, 728-735.
Nitrogen-Doped Porous Graphitic Carbon	6 M KOH	293 at 1 A g^{-1}	*Chem. Eur. J.* **2014**, *20*, 564-574.
Porous N-doped carbon spheres	6 M KOH	398 at 0.2 A g^{-1}	*J. Mater. Chem. A*, **2014**, *2*, 3317-3324.
Graphene/Polyaniline Nanofiber Composite	2 M H_2SO_4	480 at 0.1 A g^{-1}	*Chem. Mater.* **2010**, *22*, 1392-1401.
Hydroquinone physisorbed on Activated Charcoal	1 M H_2SO_4	207 at 5 mV s^{-1}	*J.Phys.Chem.C,* **2015**, *119*, 11382−11390.
Nitrogen doped carbon nanotube	1 M H_2SO_4	215 at 0.2 A g^{-1}	*ACS Appl.Mater.Interfaces,* **2015**, *7*, 20083–20089.
Nitrogen Enriched Porous Carbon Sphere	1 M H_2SO_4	388 at 1 A g^{-1}	*Chem. Mater.* **2014**, *26*, 2820-2828.
Leaves derived carbon	1 M H_2SO_4 1 M $LiPF_6$ in EC–DEC	400 at 0.5 A g^{-1} 88 at 2 A g^{-1}	*Energy Environ. Sci.* **2013**, 6, 1249-1259.
Three-dimensional (3D) honeycomb-like porous carbon	6 M KOH	342 at 0.2 A g^{-1}	*Nanoscale,* **2014**, *6*, 13831-13837.
Hierarchical cashmere-derived micro-/mesoporous carbon	1 M H_2SO_4 1 M KOH	460 at 0.5 A g^{-1} 363 at 0.5 A g^{-1}	*Green Chem.* **2015**, *17*, 2373-2382.
Hair-derived carbon	6 M KOH	340 at 2 A g^{-1}	*Energy Environ. Sci.* **2014**, *7*, 379.
ZIF-derived porous carbon	6 M KOH	228 at 0.1 A g^{-1}	*J. Mater. Chem. A*, **2014**, 2, 12873-12880.
2D quasi-ordered nitrogen-enriched porous carbon nanohybrids	6 M KOH	426 at 1 A g^{-1}	*Nanoscale,* **2016**, *8*, 10166-10176.
Porous nitrogen–doped hollow carbon spheres	6 M KOH	213 at 0.5 A g^{-1}	*J. Mater. Chem. A*, **2014**, *2*, 5352-5357.
1D activated carbon nanotube	1 M H_2SO_4	319 at 1 A g^{-1}	*J. Mater. Chem. A*, **2014**, *2*, 5236-5243.

5.4 Summary

In this chapter, we have explored the possibility of precise integration of redox-active hydroquinone moieties (H_2Q) into a stable microporous 2D covalent organic framework for pseudocapacitor applications. In addition, molecular level control of the specific capacitance was achieved by tuning the functionality in the COF backbone. The remarkable high specific capacitance (416 F g^{-1} at 0.5 A g^{-1} current density) of **TpPa-(OH)$_2$** was due to the reversible proton-coupled electron transfer ($2H^+/2e^-$) redox chemistry of hydroquinone/benzoquinone (H_2Q/Q) along with high accessibility (43%) of redox active hydroquinone units due to crystalline nature of the COF. These findings are notable which will help to design more energy efficient pseudocapacitor and other electrochemical devices in the near future.

5.5 Experimental Procedures

5.5.1 *Materials*

1,3,5-triformylphloroglucinol was prepared from Phloroglucinol using literature procedure. All other reagents and solvents were commercially available and used as received.

5.5.2 *Synthesis of* 2,4,6-tris-((2-hydroxyphenylamino)methylene)cyclohexane-1,3,5-trione *(Reference compound)*

The reference compound was synthesized by the reaction between 1,3,5-triformylphloroglucinol (0.210 g, 1 mmol) and 2-aminophenol (0.349 g, 3.2 mmol) in 20 mL ethanol under refluxing condition for three days. After this time the solution was cooled to room temperature and the precipitate was collected by filtration, washed with ethanol and dried under vacuum to give 0.32 g (0.662 mmol, 66%) of a yellow solid. IR (powder, cm^{-1}): 2969 (w), 1610 (m), 1583 (s), 1533(m), 1441 (s), 1299 (m), 1246 (m), 1142 (m), 1046 (s), 977 (w), 852(m).

5.5.3 *Synthesis of TpPa-(OH)$_2$, TpPa-(OMe)$_2$ and TpBD-(OH)$_2$*

In the typical synthesis, a pyrex tube (o.d. × i.d. = 10 × 8 mm^2 and length 18 cm) is charged with 1,3,5-triformylphloroglucinol (**Tp**) (0.3 mmol), 2,5-diaminohydroquinone dihydrochloride [**Pa-(OH)$_2$.2HCl**, 0.45 mmol], 3 mL (1:1) solvent mixture of mesitylene and 1,4-dioxane with 0.5 mL of 6(M) acetic acid. This mixture was sonicated for 10 min. in order to get a homogeneous dispersion. The tube was then flash frozen at 77 K (liquid N_2 bath) and degassed by three freeze-pump-thaw cycles. The tube was sealed off and then heated at 120 °C for 72h. A black coloured precipitate was collected by filtration and washed with DMAc followed by water and finally acetone for several times.Then the powder was dried at 120 °C under vacuum for 12 h to get corresponding COFs in ~75% isolated yield.

The similar synthesis procedure along with the same amount of solvent mixtures and catalyst [mesitylene, 1,4-dioxane and 6M acetic acid in (1.5mL: 1.5mL: 0.5mL) ratio] is followed for the synthesis of **TpBD-(OH)$_2$** and **TpPa-(OMe)$_2$** except for these COFs we have taken 3,3′-dihydroxybenzidine [**BD-(OH)$_2$**, 0.45 mmol] and 2,5-dimethoxy-p-phenylenediamine [**Pa-(OMe)$_2$**, 0.45 mmol] respectively as amine counterpart.

FT-IR [**TpPa-(OH)$_2$**, powder, cm^{-1}]: 3744 (w), 1633 (w), 1580 (s), 1465 (m), 1251 (s), 1130 (s), 853 (m).

FT-IR [**TpBD-(OH)2**, powder, cm^{-1}]: 1610 (w), 1580 (s), 1446 (m), 1280 (s), 1186 (w), 1091 (w), 866 (m).

FT-IR [**TpPa-(OMe)$_2$**, powder, cm^{-1}]: 2932 (w), 1583 (s), 1442 (m), 1258 (s), 1026 (w), 1003 (w), 836 (m).

Elementary analysis:

TpPa-(OH)$_2$, Anal. Calcd. C, 59.09; H, 3.14; N, 11.49. Found C, 50.83; H, 4.01; N 8.67.

TpBD-(OH)2, Anal. Calcd. C, 67.50; H, 3.75; N, 8.75. Found C, 59.73; H, 4.20; N 6.82.

TpPa-(OMe)$_2$, Anal. Calcd. C, 61.76; H, 4.41; N, 10.29. Found C, 54.88; H, 4.76; N 8.03.

TpBD-(OMe)$_2$, Anal. Calcd. C, 68.96; H, 4.59; N, 8.04. Found C, 63.13; H, 4.40; N 6.48

The difference in the C (wt %) and N (wt %) between the observed and calculated elemental micro analysis is might be due to the formation of noncombustible carbon nitride byproducts and hygroscopic nature of these COFs.

Other three COFs [**TpPa-1**, **TpBD,** and **TpBD-(OMe)$_2$**] have been synthesized by previously reported procedure [5.43].

5.5.4 Electrode Fabrication

For electrochemical measurements, glassy carbon electrode was coated with active materials (COFs). First, glassy carbon electrode was polished to a mirror finish by using 0.05 micron alumina powder, thoroughly cleaned in water by sonication for 15 min and dried in air. Thereafter, in 500 µl NMP, COF (5 mg; 75%), PVDF binder (1 mg; 15%), and carbon black (0.66 mg; 10%) were added. The solution was stirred for 20 h to make the solution homogeneous. In the next step, 1 µl of the solution was drop cast on the glassy carbon electrode. Finally, the electrode was dried in a hot air oven for 20 min. The total mass loading on an electrode was 0.2 mg/cm^2.

5.5.5 Electrochemical Measurements

All electrochemical experiments were carried using CH Instruments, Austin, TX potentiostat (Model CHI 620E). Three electrode cell was used in which SCE, Pt wire, and COF coated glassy carbon electrode was used as a reference, counter, and working electrode respectively. 1 M phosphate buffer (pH 7.2) was used as an electrolyte solution. Cyclic voltammetry (CV) experiments were carried out at different scan rates (2, 5, 10 and 20 mV s^{-1}) in a potential window of 0.7 V. All the CVs were collected at an uncompensated cell resistance of 0.2 Ω using *iR* compensation tool of CH potentiostat, however, long term cyclic stability experiments were carried out without *iR* compensation correction. Galvanostatic charge/discharge experiments were carried out at different current densities (0.5, 1, 2 and 5 A g^{-1}) in a potential window of 0.7 V as well. Electrochemical impedance spectroscopy (EIS) experiments were carried out at the formal potential ($E^{0\prime}$) with an amplitude of 5 mV over a frequency range of 100 kHz to 0.1 Hz. All electrochemical experiments were carried out at 25 °C at ambient condition. The $E^{0\prime}$ of the COFs were calculated by determining the average of anodic (E_{pa}) and cathodic (E_{pc}) peak potentials according to eq. 5.1.

$$E^{0'} = \frac{E_{pa} + E_{pc}}{2} \qquad (5.1)$$

Capacitance from CVs was calculated using eq. 5.2 where *C*, *I*, *E* and *v* are capacitance, current, potential window and scan rate respectively. The numerator ($\int I.dE$) of the equation was calculated by integrating the area of CVs using Origin software. Subsequently, the capacitance was obtained by dividing the area of voltammograms by scan rate and two times the potential window of CV experiments according to eq. 5.2. Finally, specific capacitances (C_{sp}, F/g) were determined by dividing the calculated specific capacitances (C) by the weight of COF deposited on each electrode (m).

$$C = \frac{\int \mathrm{I.dE}}{2\mathrm{E}\nu} \qquad (5.2)$$

$$C_{SP} = \frac{C}{m} \qquad (5.3)$$

For galvanostatic charge/discharge experiments, capacitances were calculated using eq. 5.4. In this equation, *t* in the time taken to complete charging/discharging process and *I* was the applied current density. Similar to the CV experiments, specific capacitance (C_{sp}, F/g) was calculated by dividing the obtained capacitances by the weight of the deposited materials (eq. 5.3).

$$C = \frac{I.t}{2E} \tag{5.4}$$

The energy density and power density were calculated using eq. 5.5 and eq. 5.6 respectively where C, E, and t are capacitance, potential window and discharging time respectively

$$\text{Energy Density} = \frac{1}{2}CE^2 \tag{5.5}$$

$$\text{Power Density} = \text{Energy Density}/t \tag{5.6}$$

5.5.6 Two-electrode electrochemical experiment for TpPa-(OH)$_2$

For two electrode experiments, both Pt electrodes were used as current collectors and Whatman no.1 filter paper was used as a separator. In 1 mL of N-methyl-2-pyrrolidone (NMP), 10 mg **TpPa-(OH)$_2$**, 2 mg binder poly(vinylidene fluoride) (PVDF), and 1.3 mg acetylene black were added. Thereafter, the mixture was stirred for 20 h at room temperature to form a uniform and homogeneous blend. 100 µL of this homogenous mixture was taken out and spread on 1 cm^2 area of clean and dry Pt electrode. Subsequently, the electrode was dried in an oven at 65 ^{0}C for 12 h. The weight ratio of TpPa(OH)$_2$: acetylene black: PVDF was 7.5: 1.0: 1.5. The mass of material deposited on each electrode was 1.33 mg. The calculations of specific capacitance (C_{sp}, F/g) values were done following Eq. 5.7 and 5.8, where m is the weight of active material on each electrode and a factor of 2 was multiplied as both electrodes were connected in series. Other terms have a similar meaning as described above.

$$C_{SP} = 2 * \frac{\int I.dE}{2.m.E.\nu} \tag{5.7}$$

$$C_{SP} = 2 * \frac{I.t}{2.m.E} \tag{5.8}$$

5.5.7 *General methods for characterization*

All reagents were commercially available and used as received. Microscopy images of these hollow fibers were taken in Zeiss SteREO Discovery V20.

a) ***Wide-angle X-Ray Diffraction (WAXD)*:** The wide-angle X-Ray Diffraction (WAXD) analysis of MOFs and the composite membranes were carried on a Rigaku SmartLab X-ray diffractometer in reflection mode using CuKα radiation (λ = 1.54 Å). The 2θ range from 5° to 40° was scanned with a scan rate of 3° min^{-1}. The instrument was previously calibrated using a silicon standard.

b) ***FT-IR spectroscopy*:** The Fourier transform infrared spectra (FT-IR) were taken on a Bruker Optics ALPHA-E spectrometer with a universal Zn-Se ATR (attenuated total reflection) accessory in the 600-4000 cm^{-1} region or using a Diamond ATR (Golden Gate). The spectra were measured over the range of 4000-400 cm^{-1}.

c) ***Scanning Electron Microscopy*:** Scanning Electron Microscopy (SEM) was performed on an FEI Quanta 200 3D ESEM (dual beam) instrument with a field emitter as an electron source and an FEI Nova Nano SEM 650 Scanning Electron Microscope. SEM images of membrane cross section were taken after freeze cut off membranes in LN_2. Samples for SEM were gold sputtered before analyses.

d) Fractional atomic coordinates for COFs

Table 5.11: Fractional atomic coordinates for the unit cell of **TpPa-(OH)$_2$**.

	TpPa-(OH)$_2$ **Triclinic; P 1** **a =22.4124 Å; b = 22.3715 Å; c = 6.7244 Å** **α = 90.7617; β = 90.3839; γ = 119.3119**		
Atom list	x	y	z
C1	0.91715	0.9264	0.06107
C2	0.94948	0.8857	0.04858
C3	0.0198	0.91677	0.00671
C4	0.06006	0.98846	0.97735
C5	0.02785	0.02928	0.99221
C6	0.95737	0.9982	0.03363
H1	0.92023	0.83008	0.0709
H2	0.05723	0.08495	0.97103
N1	0.12956	0.0141	0.93759
C7	0.17802	0.07985	0.90616
H3	0.16225	0.11958	0.90252
C8	0.24705	0.09921	0.8822
C9	0.27144	0.0489	0.89758

C10	0.29568	0.17324	0.86069
C11	0.34611	0.07483	0.91552
C12	0.36997	0.19665	0.86853
C13	0.39618	0.14823	0.89496
O1	0.23075	0.98581	0.9005
O2	0.27346	0.21432	0.84001
O3	0.45949	0.16941	0.90209
H4	0.14824	0.97908	0.93831
C14	0.41913	0.26602	0.87032
H5	0.47376	0.27989	0.88521
C15	0.36649	0.02755	0.96822
H6	0.3266	0.97351	0.98715
N2	0.40318	0.31661	0.85871
C16	0.4485	0.38659	0.88462
C17	0.51994	0.41473	0.91338
C18	0.42005	0.43112	0.88675
C19	0.56152	0.4852	0.95076
H7	0.54442	0.38258	0.91027
C20	0.46107	0.50132	0.9264
C21	0.53256	0.52935	0.96161
H8	0.43739	0.53429	0.92945
N3	0.43286	0.04483	0.00077
O4	0.05313	0.87824	0.99235
O5	0.35051	0.40231	0.84807
H9	0.33657	0.43751	0.85292
H10	0.35063	0.30095	0.84531
H11	0.46861	0.09685	0.97938
H12	0.02071	0.82988	0.01768
N4	0.84716	0.89973	0.09788
C22	0.79834	0.83326	0.09488
C23	0.72858	0.81217	0.11533
H13	0.81393	0.79397	0.06961
C24	0.70422	0.86223	0.1396
C25	0.68019	0.7386	0.09029
C26	0.62961	0.83686	0.1438
O6	0.74521	0.92515	0.15546
C27	0.60602	0.71549	0.08437
O7	0.70238	0.69682	0.0709
C28	0.60937	0.88664	0.15193
C29	0.57955	0.76345	0.12324

C30	0.55737	0.64752	0.04087
N5	0.54306	0.87128	0.15059
H14	0.64969	0.94107	0.1566
O8	0.51619	0.74106	0.13717
H15	0.50245	0.63317	0.03414
N6	0.57531	0.59895	0.00689
H16	0.50714	0.81877	0.15012
H17	0.62855	0.61769	0.02073
O9	0.92383	0.03607	0.04986
H18	0.95541	0.08459	0.02449
O10	0.63088	0.50823	0.97941
H19	0.65748	0.55804	0.99723
C31	0.51808	0.91687	0.12649
C32	0.56054	0.98812	0.09937
C33	0.44567	0.88911	0.12247
C34	0.53047	0.02918	0.06316
H20	0.61682	0.01176	0.10405
C35	0.41558	0.93004	0.08467
C36	0.45804	0.00088	0.05035
H21	0.35929	0.90643	0.07984
O11	0.40584	0.81943	0.15591
H22	0.35694	0.80557	0.14535
O12	0.57005	0.09911	0.03434
H23	0.61899	0.11327	0.04649
H24	0.82875	0.93475	0.11523
C37	0.97768	0.04046	0.52448
C38	0.00997	0.99969	0.50796
C39	0.08022	0.03077	0.46409
C40	0.12033	0.10252	0.43357
C41	0.08801	0.14314	0.44973
C42	0.01792	0.11211	0.49567
H25	0.98081	0.94406	0.53054
H26	0.11719	0.1988	0.42837
N7	0.18987	0.12883	0.39247
C43	0.23807	0.19523	0.37073
H27	0.22167	0.23445	0.37033
C44	0.30783	0.21621	0.35475
C45	0.333	0.16646	0.36619
C46	0.35589	0.29073	0.34771
C47	0.40763	0.19236	0.38098

C48	0.43026	0.31471	0.36647
C49	0.45726	0.26623	0.37812
O13	0.29261	0.10322	0.36762
O14	0.33412	0.33229	0.33063
O15	0.52056	0.28847	0.38975
H28	0.20899	0.09412	0.39198
C50	0.4784	0.38377	0.39091
H29	0.53284	0.39758	0.41157
C51	0.42814	0.14377	0.41574
H30	0.38821	0.08927	0.42315
N8	0.46208	0.43445	0.3951
C52	0.50691	0.50363	0.43811
C53	0.57817	0.5309	0.47054
C54	0.47918	0.54862	0.45087
C55	0.61996	0.60052	0.51881
H31	0.60237	0.49857	0.46047
C56	0.52037	0.618	0.50106
C57	0.59165	0.64509	0.53694
H32	0.49713	0.65131	0.50804
N9	0.49429	0.16052	0.44516
O16	0.11373	0.99281	0.4476
O17	0.4093	0.52149	0.41204
H33	0.39776	0.5585	0.41355
H34	0.40979	0.41881	0.37487
H35	0.52982	0.21305	0.43564
H36	0.08239	0.94449	0.4762
N10	0.90832	0.01477	0.56898
C58	0.85931	0.94874	0.58807
C59	0.79078	0.92937	0.62584
H37	0.87388	0.90839	0.56929
C60	0.76744	0.98052	0.64401
C61	0.74171	0.85535	0.62652
C62	0.69278	0.95585	0.64999
O18	0.80906	0.04339	0.64997
C63	0.66768	0.83258	0.63597
O19	0.76358	0.8132	0.61538
C64	0.67227	0.00518	0.63324
C65	0.64228	0.88217	0.65163
C66	0.61794	0.76387	0.61072
N11	0.60571	0.98957	0.62467

H38	0.71231	0.05953	0.62262
O20	0.57912	0.86145	0.66158
H39	0.56314	0.74998	0.61009
N12	0.63504	0.71433	0.58408
H40	0.56987	0.93713	0.63674
H41	0.68844	0.73311	0.58986
O21	0.98493	0.15082	0.51486
H42	0.01755	0.19929	0.4919
O22	0.6889	0.62239	0.55158
H43	0.71582	0.67217	0.57052
C67	0.58016	0.03416	0.58653
C68	0.62223	0.10545	0.55793
C69	0.50776	0.00555	0.57328
C70	0.59182	0.14568	0.51402
H44	0.67849	0.1297	0.56884
C71	0.47732	0.04578	0.52888
C72	0.51939	0.11668	0.49554
H45	0.42105	0.02147	0.51867
O23	0.46827	0.93568	0.60511
H46	0.41933	0.9216	0.59362
O24	0.63109	0.21539	0.48253
H47	0.67982	0.23084	0.50723
H48	0.89063	0.05036	0.58495

Table 5.12: Fractional atomic coordinates for the unit cell of **TpPa-(OMe)$_2$**.

	TpPa-(OMe)$_2$ **Triclinic: *P* 1;** ***a* = 22.3857 Å; *b* = 22.5758 Å; *c* = 6.791 Å;** **α = 89.6424; β = 90.0665; γ = 119.1296**		
Atom list	x	y	z
C1	0.92078	0.93357	0.05748
C2	0.95292	0.89328	0.03333
C3	0.02374	0.9256	0.99762
C4	0.0637	0.99784	0.9844
C5	0.03143	0.03824	0.00753
C6	0.96054	0.00597	0.04441
H1	0.92241	0.83748	0.0425
H2	0.06191	0.09406	0.99753
N1	0.13388	0.02444	0.95124

C7	0.18247	0.09008	0.9229
H3	0.16684	0.12986	0.91805
C8	0.25172	0.1094	0.90119
C9	0.27644	0.05939	0.91542
C10	0.29993	0.18317	0.87847
C11	0.35141	0.08534	0.92374
C12	0.37429	0.20663	0.87913
C13	0.40107	0.15851	0.89976
O1	0.23588	0.99642	0.92336
O2	0.27726	0.22414	0.86187
O3	0.46456	0.17983	0.89948
H4	0.15263	0.98952	0.95191
C14	0.42304	0.2758	0.879
H5	0.4779	0.28993	0.88829
C15	0.37297	0.03815	0.96794
H6	0.33329	0.98419	0.98943
N2	0.40612	0.32573	0.87191
C16	0.45079	0.39545	0.89644
C17	0.52249	0.42316	0.92078
C18	0.4214	0.43912	0.90295
C19	0.56341	0.49313	0.95743
H7	0.54526	0.3896	0.91506
C20	0.46244	0.50915	0.93936
C21	0.534	0.53661	0.96872
H8	0.43973	0.54278	0.94505
N3	0.43977	0.05517	0.98907
O4	0.06135	0.89078	0.96959
O5	0.35054	0.40636	0.86978
H9	0.35317	0.30924	0.86321
H10	0.47525	0.10721	0.96723
N4	0.85059	0.90585	0.09229
C22	0.80196	0.83949	0.08747
C23	0.73223	0.81844	0.10769
H11	0.81763	0.80049	0.06161
C24	0.70783	0.86829	0.1294
C25	0.68386	0.74488	0.08664
C26	0.63314	0.84318	0.12846
O6	0.74852	0.93095	0.14631
C27	0.60953	0.72211	0.0795
O7	0.70576	0.70323	0.07295

C28	0.61333	0.89314	0.13049
C29	0.58297	0.77008	0.11035
C30	0.5611	0.65447	0.03999
N5	0.54715	0.87834	0.12281
H12	0.65399	0.94726	0.13555
O8	0.51945	0.74819	0.11951
H13	0.50621	0.64049	0.0328
N6	0.57828	0.60544	0.00975
H14	0.51093	0.82608	0.12127
H15	0.6312	0.62172	0.02085
O9	0.92245	0.03948	0.07407
O10	0.63495	0.52587	0.98829
C31	0.52284	0.92447	0.09811
C32	0.56643	0.99571	0.07744
C33	0.45051	0.89714	0.08826
C34	0.53773	0.03827	0.04436
H16	0.62236	0.01714	0.08559
C35	0.4218	0.93966	0.05686
C36	0.46532	0.01073	0.03109
H17	0.36583	0.91807	0.04823
O11	0.41195	0.826	0.11524
O12	0.57628	0.10937	0.01936
H18	0.83188	0.9404	0.11223
C37	0.95566	0.11278	0.05014
H19	0.0001	0.13937	0.15139
H20	0.97295	0.1285	0.8963
H21	0.91683	0.12771	0.08692
C38	0.02646	0.81784	0.00051
H22	0.00566	0.80382	0.15271
H23	0.98439	0.79068	0.89186
H24	0.06523	0.80146	0.97949
C39	0.33843	0.79363	0.08904
H25	0.31387	0.8107	0.20099
H26	0.32432	0.80273	0.93868
H27	0.3185	0.73835	0.10867
C40	0.65033	0.14129	0.03472
H28	0.66693	0.13285	0.18196
H29	0.67253	0.12296	0.91973
H30	0.67024	0.19648	0.0135
C41	0.31579	0.44583	0.89047

H31	0.32157	0.46656	0.04201
H32	0.33427	0.48816	0.78106
H33	0.26084	0.41067	0.8622
C42	0.6679	0.48422	0.98306
H34	0.7229	0.51863	0.01363
H35	0.64721	0.44367	0.09787
H36	0.66307	0.46107	0.83534
C43	0.98595	0.05477	0.5386
C44	0.01796	0.01419	0.51375
C45	0.08855	0.04611	0.4722
C46	0.12832	0.1184	0.45406
C47	0.09667	0.15893	0.48282
C48	0.02627	0.12699	0.52489
H37	0.98754	0.95842	0.52626
H38	0.12727	0.21468	0.47208
N7	0.19803	0.14578	0.41198
C49	0.24578	0.21226	0.39473
H39	0.22924	0.25126	0.40181
C50	0.31559	0.23371	0.37383
C51	0.34115	0.18433	0.37706
C52	0.36315	0.30798	0.36915
C53	0.416	0.21053	0.38616
C54	0.43775	0.33213	0.38024
C55	0.46533	0.28417	0.38413
O13	0.30118	0.1212	0.37649
O14	0.34066	0.34922	0.35987
O15	0.52897	0.30657	0.38906
H40	0.21729	0.11131	0.40398
C56	0.48548	0.401	0.40313
H41	0.54032	0.41533	0.41775
C57	0.43664	0.16169	0.41399
H42	0.39646	0.10739	0.42053
N8	0.46824	0.45078	0.41173
C58	0.51259	0.51981	0.45143
C59	0.58416	0.54692	0.47939
C60	0.48389	0.5639	0.46441
C61	0.62537	0.61637	0.52269
H43	0.60707	0.51358	0.46773
C62	0.5247	0.63292	0.51394
C63	0.59609	0.65976	0.54348

H44	0.50212	0.66655	0.52486
N9	0.50281	0.17772	0.43804
O16	0.12611	0.01215	0.44002
O17	0.41274	0.53278	0.42644
H45	0.41548	0.43436	0.39671
H46	0.53864	0.23002	0.43034
N10	0.916	0.02852	0.57586
C64	0.86636	0.96263	0.59009
C65	0.79739	0.94364	0.61765
H47	0.88083	0.92218	0.57741
C66	0.77372	0.99451	0.62754
C67	0.74832	0.86961	0.61954
C68	0.69885	0.96976	0.62798
O18	0.81515	0.05729	0.63209
C69	0.67415	0.84699	0.62485
O19	0.77019	0.82783	0.61391
C70	0.67792	0.01866	0.60821
C71	0.64846	0.89622	0.63221
C72	0.62469	0.77844	0.6043
N11	0.61119	0.00284	0.59692
H48	0.71788	0.073	0.5982
O20	0.58512	0.87554	0.6382
H49	0.56995	0.76504	0.60053
N12	0.64092	0.72834	0.58527
H50	0.5755	0.95038	0.60827
H51	0.69376	0.74401	0.59214
O21	0.98934	0.16225	0.55733
O22	0.69637	0.64807	0.55455
C73	0.5856	0.04769	0.56191
C74	0.62871	0.11897	0.5394
C75	0.51315	0.01983	0.54758
C76	0.59963	0.16093	0.50249
H52	0.68467	0.14105	0.55184
C77	0.48417	0.06175	0.50764
C78	0.52743	0.13283	0.48199
H53	0.42829	0.03977	0.49469
O23	0.4748	0.94884	0.57515
O24	0.63793	0.23206	0.47439
H54	0.89819	0.06398	0.58833
C79	0.02565	0.23567	0.53828

H55	0.06782	0.25994	0.64826
H56	0.04662	0.25227	0.38714
H57	0.98778	0.25271	0.56663
C80	0.09363	0.93937	0.47463
H58	0.07975	0.92653	0.63185
H59	0.0471	0.91089	0.38197
H60	0.13167	0.92379	0.43389
C81	0.40065	0.91697	0.56525
H61	0.37973	0.93744	0.67779
H62	0.38265	0.92298	0.41736
H63	0.38075	0.86218	0.59453
C82	0.71047	0.26565	0.51876
H64	0.72039	0.25583	0.67321
H65	0.73904	0.25025	0.41572
H66	0.72977	0.32087	0.50034
C83	0.38386	0.57748	0.39478
H67	0.38223	0.60263	0.53383
H68	0.41242	0.61666	0.28052
H69	0.33059	0.54492	0.34315
C84	0.73256	0.61499	0.47521
H70	0.78787	0.65167	0.48931
H71	0.72144	0.56815	0.56017
H72	0.72000	0.60219	0.31724

Table 5.13: Fractional atomic coordinates for the unit cell of **TpBD-(OH)$_2$**.

	TpBD-(OH)$_2$ **Triclinic; *P* 1;** ***a* = 29.6712 Å; *b* = 30.7116 Å; *c* = 6.7694 Å;** **α = 89.6435; β = 90.5336; γ = 119.3597**		
Atom list	x	y	z
C1	0.02545	0.01125	0.99437
C2	0.05019	0.9816	0.99655
C3	0.10324	0.00468	0.99963
C4	0.13443	0.05841	0.00072
C5	0.10995	0.08795	0.99774
C6	0.05689	0.0647	0.99466
C7	0.96923	0.98688	0.9923
C8	0.93849	0.93333	0.99146
C9	0.88541	0.90925	0.9898

C10	0.8602	0.93804	0.98893
C11	0.89063	0.99194	0.98998
C12	0.94382	0.01589	0.99159
H1	0.02844	0.93976	0.99614
H2	0.13227	0.12969	0.99797
H3	0.04016	0.08984	0.99247
H4	0.95571	0.90861	0.99199
H5	0.86368	0.86748	0.98916
H6	0.9652	0.05773	0.99241
N1	0.18702	0.0783	0.005
N2	0.80743	0.91687	0.98681
C13	0.77248	0.86689	0.98724
H7	0.78584	0.83875	0.9902
C14	0.22287	0.12803	0.00659
H8	0.21029	0.15683	0.00439
C15	0.27476	0.14459	0.01018
C16	0.29464	0.10857	0.01105
C17	0.30901	0.20026	0.00973
C18	0.35049	0.12963	0.00653
C19	0.36441	0.21962	0.00937
C20	0.38588	0.18497	0.00786
C21	0.72029	0.84933	0.98452
C22	0.69999	0.8849	0.9809
C23	0.68626	0.79368	0.98707
C24	0.64428	0.86389	0.97808
C25	0.63067	0.77413	0.98573
C26	0.60887	0.80863	0.979
O1	0.26555	0.06158	0.0143
O2	0.29083	0.22958	0.00957
O3	0.43308	0.20257	0.00748
O4	0.56171	0.79065	0.97454
O5	0.72872	0.93206	0.9802
O6	0.70401	0.764	0.99055
H9	0.20127	0.05271	0.00722
H10	0.79244	0.9419	0.98479
C27	0.39927	0.27149	0.00837
H11	0.44025	0.28334	0.00793
C28	0.36813	0.0949	0.99814
H12	0.33987	0.05388	0.99684
C29	0.62726	0.89918	0.97622

H13	0.65603	0.94005	0.97656
C30	0.59591	0.72232	0.99102
H14	0.5549	0.71039	0.9896
N3	0.38545	0.30774	0.00781
N4	0.57753	0.88591	0.97458
C31	0.41829	0.36015	0.00752
C32	0.47179	0.3831	0.00867
C33	0.39652	0.39255	0.0062
C34	0.50204	0.43602	0.00899
H15	0.49052	0.35977	0.00933
C35	0.42703	0.44551	0.00667
C36	0.48094	0.46875	0.00823
H16	0.54349	0.45148	0.00992
H17	0.40787	0.4685	0.00556
C37	0.51358	0.52476	0.00798
C38	0.49268	0.55766	0.00699
C39	0.56744	0.54787	0.00798
C40	0.52309	0.61053	0.00424
H18	0.45122	0.54231	0.00817
C41	0.598	0.60075	0.00541
H19	0.58655	0.52483	0.00956
C42	0.5766	0.6334	0.00252
H20	0.50448	0.63398	0.00337
C43	0.5576	0.91888	0.97415
C44	0.58722	0.97237	0.97401
C45	0.5038	0.89736	0.97401
C46	0.56415	0.00275	0.97336
H21	0.62901	0.99106	0.97444
C47	0.48088	0.92789	0.97351
C48	0.51066	0.98181	0.97294
H22	0.58949	0.04414	0.97306
H23	0.43901	0.90867	0.97391
C49	0.48658	0.01435	0.97334
C50	0.43306	0.99304	0.97058
C51	0.51601	0.06821	0.97741
C52	0.40954	0.02297	0.97517
H24	0.4079	0.95161	0.965
C53	0.49265	0.09835	0.98132
H25	0.55786	0.0876	0.97838
C54	0.4388	0.07642	0.98229

H26	0.36775	0.00398	0.97329
N5	0.60953	0.68585	0.99772
N6	0.41813	0.10881	0.99068
O7	0.12764	0.97582	0.002
H27	0.1024	0.9395	0.00039
O8	0.86517	0.01953	0.98936
H28	0.88943	0.05611	0.99044
O9	0.47493	0.8448	0.97468
H29	0.43858	0.83424	0.97491
O10	0.52114	0.15092	0.98546
H30	0.55751	0.16153	0.98436
O11	0.34414	0.36952	0.0043
H31	0.3333	0.39523	0.00252
O12	0.65077	0.6233	0.00504
H32	0.66058	0.59679	0.00809
H33	0.34606	0.29458	0.0078
H34	0.55191	0.84658	0.97443
H35	0.44339	0.14829	0.99375
H36	0.64894	0.69913	0.99797
C55	0.0648	0.08463	0.49487
C56	0.09016	0.05557	0.49739
C57	0.14334	0.07946	0.50045
C58	0.17381	0.13336	0.50135
C59	0.14866	0.16219	0.4978
C60	0.09558	0.13817	0.49458
C61	0.00858	0.06027	0.49303
C62	0.97717	0.00681	0.49233
C63	0.92411	0.98352	0.49105
C64	0.89959	0.01303	0.49035
C65	0.93074	0.06676	0.49116
C66	0.9838	0.08989	0.49248
H37	0.06874	0.01373	0.49718
H38	0.17043	0.20396	0.49763
H39	0.0784	0.16292	0.49187
H40	0.99393	0.9817	0.4927
H41	0.90183	0.94178	0.49059
H42	0.00554	0.13172	0.49311
N7	0.22657	0.15444	0.50573
N8	0.84698	0.99306	0.48866
C67	0.81123	0.9433	0.48693

H43	0.8239	0.91458	0.48786
C68	0.2616	0.20441	0.5059
H44	0.24831	0.23261	0.50239
C69	0.31377	0.22186	0.50927
C70	0.33395	0.18619	0.51182
C71	0.3479	0.2775	0.5079
C72	0.38964	0.20707	0.5084
C73	0.40346	0.29692	0.50791
C74	0.42515	0.2623	0.50697
C75	0.75931	0.9266	0.48396
C76	0.73928	0.9625	0.48237
C77	0.72519	0.87092	0.48325
C78	0.6834	0.94129	0.47871
C79	0.66977	0.8514	0.48034
C80	0.64815	0.88592	0.47682
O13	0.30514	0.13906	0.5156
O14	0.33024	0.30726	0.50669
O15	0.4723	0.28019	0.5049
O16	0.60094	0.86821	0.47304
O17	0.76827	0.00952	0.48389
O18	0.74349	0.8417	0.48533
H45	0.24148	0.12935	0.50868
H46	0.83264	0.01858	0.48803
C81	0.43833	0.34872	0.50753
H47	0.47932	0.36053	0.50729
C82	0.40656	0.17171	0.50398
H48	0.37775	0.13084	0.5053
C83	0.66561	0.97594	0.47809
H49	0.69381	0.01697	0.48053
C84	0.63503	0.7995	0.48293
H50	0.59402	0.78751	0.48134
N9	0.42485	0.38531	0.50745
N10	0.61557	0.96198	0.47501
C85	0.45789	0.43775	0.50785
C86	0.5114	0.46055	0.50901
C87	0.43658	0.47048	0.50719
C88	0.54189	0.51341	0.50882
H51	0.52994	0.43703	0.50986
C89	0.46721	0.52335	0.50717
C90	0.52107	0.54639	0.50754

H52	0.58335	0.52871	0.50958
H53	0.44816	0.54644	0.5066
C91	0.55373	0.60239	0.505
C92	0.53257	0.63507	0.50146
C93	0.60764	0.62568	0.50465
C94	0.56276	0.68796	0.49593
H54	0.49112	0.61958	0.5026
C95	0.6381	0.67863	0.49938
H55	0.62683	0.60272	0.50846
C96	0.61626	0.71096	0.49398
H56	0.54398	0.71125	0.49321
C97	0.59485	0.99438	0.47445
C98	0.6241	0.04786	0.47463
C99	0.541	0.97245	0.47371
C100	0.60058	0.0778	0.47485
H57	0.6659	0.06688	0.47494
C101	0.51763	0.00259	0.47384
C102	0.54705	0.05646	0.47493
H58	0.62574	0.11926	0.47523
H59	0.47578	0.98319	0.47356
C103	0.52298	0.08901	0.47769
C104	0.4695	0.06809	0.47863
C105	0.55279	0.14292	0.48076
C106	0.44646	0.09848	0.48428
H60	0.44414	0.02671	0.47487
C107	0.52991	0.17346	0.48635
H61	0.59466	0.16213	0.47917
C108	0.47612	0.15196	0.48946
H62	0.40467	0.07982	0.48483
N11	0.649	0.76337	0.48796
N12	0.45624	0.18493	0.49717
O19	0.16873	0.05181	0.50291
H63	0.14443	0.01524	0.50095
O20	0.90629	0.09558	0.49058
H64	0.93151	0.13191	0.49131
O21	0.51252	0.91986	0.47337
H65	0.47615	0.90925	0.47325
O22	0.55881	0.226	0.48988
H66	0.59514	0.23656	0.48574
O23	0.38382	0.44802	0.50636

H67	0.37408	0.47459	0.50529
O24	0.69048	0.70172	0.49881
H68	0.70138	0.67608	0.50531
H69	0.38546	0.37214	0.50699
H70	0.59037	0.92248	0.47351
H71	0.48188	0.22425	0.4969
H72	0.68842	0.77664	0.48867

Table 5.14: Fractional atomic coordinates for the unit cell of **TpBD-(OMe)$_2$**.

	TpBD-(OMe)$_2$ **Triclinic: *P* 1;** ***a* = 30.0891Å; *b* = 30.2535 Å; *c* = 6.7237 Å;** **α = 89.6736; β = 89.9639; γ = 118.4402**		
Atom list	x	y	z
C1	0.02561	0.0134	0.99466
C2	0.05137	0.98449	0.99719
C3	0.10435	0.0082	0.0005
C4	0.13443	0.06204	0.00162
C5	0.10897	0.09086	0.99925
C6	0.05587	0.06686	0.99584
C7	0.96931	0.98767	0.99144
C8	0.94012	0.93408	0.98981
C9	0.88703	0.90887	0.98758
C10	0.86063	0.93666	0.98682
C11	0.88945	0.99071	0.98791
C12	0.94262	0.01568	0.99024
H1	0.02972	0.94287	0.9967
H2	0.1305	0.13258	0.99999
H3	0.03824	0.09138	0.99399
H4	0.95846	0.91019	0.9903
H5	0.86633	0.86713	0.98648
H6	0.96367	0.05735	0.99131
N1	0.18706	0.08228	0.00475
N2	0.80788	0.91486	0.98498
C13	0.773	0.86511	0.98663
H7	0.78614	0.83665	0.98963
C14	0.22297	0.13177	0.00684
H8	0.21064	0.1609	0.00723
C15	0.27479	0.14753	0.00824

C16	0.29435	0.11103	0.00609
C17	0.30943	0.20294	0.00993
C18	0.35008	0.13121	0.00245
C19	0.36466	0.22148	0.00933
C20	0.38566	0.18631	0.00567
C21	0.72091	0.84856	0.98502
C22	0.70146	0.88502	0.98126
C23	0.68609	0.79326	0.98823
C24	0.64602	0.86534	0.97902
C25	0.63072	0.77497	0.98757
C26	0.60991	0.81049	0.98149
O1	0.26501	0.06412	0.00664
O2	0.29162	0.23281	0.01179
O3	0.43285	0.20344	0.00508
O4	0.56284	0.7936	0.97856
O5	0.73056	0.93205	0.97979
O6	0.70316	0.76277	0.99156
H9	0.20142	0.05662	0.00477
H10	0.79268	0.9399	0.98291
C27	0.39991	0.27314	0.01037
H11	0.44078	0.28442	0.00945
C28	0.36762	0.09612	0.99435
H12	0.33941	0.05521	0.99181
C29	0.63007	0.90169	0.97536
H13	0.65934	0.94224	0.97434
C30	0.59529	0.72343	0.992
H14	0.55446	0.71235	0.99101
N3	0.38634	0.30966	0.01213
N4	0.58065	0.88941	0.97333
C31	0.41896	0.36197	0.01202
C32	0.47236	0.38464	0.01314
C33	0.39662	0.39415	0.01025
C34	0.50229	0.43747	0.0121
H15	0.49124	0.36126	0.01479
C35	0.42689	0.44701	0.00938
C36	0.48075	0.47002	0.01005
H16	0.54373	0.4529	0.01301
H17	0.40847	0.47076	0.00797
C37	0.51297	0.526	0.00801
C38	0.49175	0.55882	0.00605

C39	0.56679	0.54881	0.00742
C40	0.52197	0.61161	0.00267
H18	0.4503	0.54357	0.00692
C41	0.59721	0.60156	0.0044
H19	0.58505	0.52493	0.00902
C42	0.57539	0.63413	0.00139
H20	0.5033	0.6352	0.00101
C43	0.56074	0.92255	0.9715
C44	0.59011	0.97591	0.96823
C45	0.50691	0.90071	0.97338
C46	0.56661	0.00614	0.96754
H21	0.63187	0.99455	0.96595
C47	0.48369	0.93115	0.97319
C48	0.51314	0.98493	0.97041
H22	0.59152	0.0475	0.96411
H23	0.442	0.91282	0.97609
C49	0.48808	0.01682	0.97141
C50	0.43455	0.99501	0.96547
C51	0.51692	0.07055	0.97918
C52	0.41039	0.02458	0.97077
H24	0.40994	0.95363	0.95653
C53	0.49305	0.10044	0.9829
H25	0.55856	0.0891	0.98363
C54	0.43904	0.07788	0.98104
H26	0.36862	0.00541	0.96657
N5	0.60832	0.68642	0.99727
N6	0.41761	0.10983	0.9891
O7	0.13252	0.98203	0.00342
O8	0.85971	0.01472	0.98658
O9	0.48048	0.84746	0.97605
O10	0.51894	0.15356	0.98987
O11	0.34363	0.36837	0.00952
O12	0.6507	0.62697	0.00352
H27	0.34697	0.29682	0.01226
H28	0.55483	0.85024	0.97474
H29	0.44259	0.14927	0.99334
H30	0.64765	0.69914	0.99749
C55	0.42566	0.82202	0.97561
H31	0.41028	0.83139	0.11059
H32	0.41049	0.83119	0.83971

H33	0.4127	0.78093	0.97625
C56	0.57392	0.17932	0.98616
H34	0.58981	0.16998	0.11895
H35	0.58869	0.17013	0.84951
H36	0.5866	0.22036	0.9873
C57	0.88466	0.0696	0.98827
H37	0.90806	0.08555	0.12412
H38	0.90906	0.08611	0.85504
H39	0.85426	0.07998	0.9869
C58	0.10495	0.9272	0.99923
H40	0.0801	0.91126	0.1324
H41	0.08173	0.91259	0.86146
H42	0.13371	0.91451	0.00066
C59	0.31762	0.39785	0.00111
H43	0.32589	0.42257	0.13457
H44	0.32756	0.42139	0.86366
H45	0.27659	0.37047	0.99859
C60	0.67574	0.59652	0.01086
H46	0.66585	0.57315	0.14888
H47	0.66665	0.5715	0.87786
H48	0.71699	0.62323	0.01149
C61	0.07425	0.10321	0.49605
C62	0.10091	0.07517	0.49943
C63	0.15407	0.10011	0.50286
C64	0.18292	0.15415	0.50333
C65	0.15657	0.18198	0.49922
C66	0.10348	0.1568	0.49558
C67	0.01795	0.07749	0.49324
C68	0.98772	0.02402	0.49188
C69	0.93462	0.99999	0.48963
C70	0.90913	0.02878	0.4885
C71	0.93918	0.08262	0.48958
C72	0.99217	0.10637	0.49202
H49	0.07983	0.0335	0.49978
H50	0.1773	0.22372	0.49873
H51	0.08517	0.1807	0.49224
H52	0.00538	0.99952	0.49246
H53	0.91312	0.95827	0.48863
H54	0.01379	0.14799	0.49311
N7	0.23566	0.17588	0.50734

N8	0.85649	0.00846	0.48608
C73	0.82066	0.95894	0.48558
H55	0.8331	0.92989	0.48791
C74	0.27063	0.2256	0.50891
H56	0.25759	0.25415	0.50823
C75	0.32269	0.24201	0.51088
C76	0.34199	0.20541	0.51029
C77	0.35764	0.29728	0.51181
C78	0.3974	0.22494	0.50801
C79	0.41298	0.31542	0.51142
C80	0.43364	0.27976	0.50894
C81	0.76882	0.94303	0.48237
C82	0.74911	0.9794	0.47884
C83	0.73432	0.88759	0.48321
C84	0.69336	0.95906	0.47533
C85	0.67906	0.86888	0.48077
C86	0.6579	0.90393	0.47653
O13	0.31279	0.1584	0.51092
O14	0.34069	0.32789	0.51273
O15	0.4807	0.29653	0.50723
O16	0.6107	0.88667	0.47439
O17	0.77834	0.02633	0.47878
O18	0.75226	0.85784	0.48619
H57	0.25077	0.15076	0.50842
H58	0.84205	0.03406	0.48428
C87	0.44853	0.36694	0.51148
H59	0.48934	0.3779	0.51081
C88	0.41322	0.18849	0.50316
H60	0.3839	0.14796	0.50237
C89	0.67568	0.99407	0.47195
H61	0.70382	0.035	0.47202
C90	0.64395	0.81719	0.48346
H62	0.60305	0.80578	0.48202
N9	0.43564	0.40406	0.51187
N10	0.62566	0.98029	0.46885
C91	0.46865	0.45634	0.51053
C92	0.52207	0.47881	0.51062
C93	0.44689	0.48896	0.50852
C94	0.55235	0.5316	0.5084
H63	0.54069	0.45517	0.51223

C95	0.47736	0.5417	0.50669
C96	0.53118	0.56447	0.50629
H64	0.59379	0.54681	0.50833
H65	0.45914	0.56562	0.50544
C97	0.56341	0.62043	0.50286
C98	0.54183	0.65295	0.49948
C99	0.61727	0.64348	0.50211
C100	0.57171	0.70576	0.49443
H66	0.50038	0.63751	0.50055
C101	0.6475	0.69634	0.49735
H67	0.63571	0.61976	0.50494
C102	0.62511	0.72847	0.49279
H68	0.55279	0.7291	0.49214
C103	0.60418	0.01223	0.46838
C104	0.63283	0.0656	0.46668
C105	0.55017	0.98965	0.4705
C106	0.60867	0.09518	0.46913
H69	0.67461	0.08483	0.46381
C107	0.5263	0.01954	0.47319
C108	0.55513	0.07331	0.4737
H70	0.6333	0.13662	0.46764
H71	0.48464	0.00094	0.47608
C109	0.53006	0.10518	0.47927
C110	0.47659	0.08398	0.47952
C111	0.55952	0.15895	0.48494
C112	0.45309	0.11419	0.48573
H72	0.45166	0.04263	0.47456
C113	0.53631	0.18937	0.49033
H73	0.60122	0.17729	0.48521
C114	0.48248	0.16754	0.49177
H74	0.41133	0.09557	0.48578
N11	0.65766	0.78078	0.48803
N12	0.46262	0.20069	0.49882
O19	0.18376	0.07605	0.50676
O20	0.91096	0.10875	0.48811
O21	0.52429	0.9365	0.47074
O22	0.56275	0.24261	0.49624
O23	0.3934	0.46362	0.50852
O24	0.70049	0.72215	0.49559
H75	0.39632	0.39143	0.51196

H76	0.60073	0.94081	0.46959
H77	0.48847	0.23985	0.50029
H78	0.69704	0.79371	0.48884
C115	0.46931	0.91076	0.4731
H79	0.45431	0.92002	0.60895
H80	0.45365	0.92004	0.33946
H81	0.45661	0.86972	0.47269
C116	0.61754	0.26809	0.48851
H82	0.634	0.25858	0.61956
H83	0.63162	0.25911	0.34896
H84	0.63048	0.30918	0.49129
C117	0.93851	0.16359	0.4882
H85	0.96227	0.17888	0.6243
H86	0.96282	0.17889	0.35329
H87	0.90973	0.17625	0.48701
C118	0.15878	0.02118	0.50284
H88	0.13364	0.0043	0.63393
H89	0.13615	0.00565	0.365
H90	0.18915	0.01076	0.50677
C119	0.36846	0.49415	0.50071
H91	0.37731	0.51899	0.63414
H92	0.37866	0.51771	0.36315
H93	0.32719	0.46749	0.49872
C120	0.72655	0.69282	0.51158
H94	0.71685	0.67076	0.65283
H95	0.71811	0.66671	0.38254
H96	0.76758	0.72024	0.51152

NOTE: The results of this chapter have already been published in *Chem. Mater.**2017**, 29, 2074−2080*. with the title: "*Molecular Level Control of the Capacitance of Two-Dimensional Covalent Organic Frameworks: Role of Hydrogen Bonding in Energy Storage Materials*." These publications were the results of the collaboration among the group of Prof. Rahul Banerjee and his student Suman Chandra from National Chemical Laboratory, Pune, India along with Dr. Amit Paul and his student Debarati Roy Chowdhury and Prof. Thomas Heine and his post doctorate student Dr. Matthew Addicoat from Jacobs University, Germany. Apart from computational study major works contributed by Suman Chandra.

CHAPTER 6

Summary of All Chapters and Future Directive

6.1 Summary

The first chapter of the thesis includes the introduction of different kinds of porous materials and special focus given on the porous covalent organic framework (COFs). It also describes the reticular approaches, different reversible reactions used, basic symmetry rules of combination and mechanism of formation of COFs. Further, it discussed the synthetic methods of preparation and important applications in gas uptake, gas separation, energy storage, catalysis, photoelectric, drug delivery, and proton conduction. In the last part of the thesis, we have discussed the different approaches used to improve the chemical stability of COFs.

In the second chapter, we have briefly discussed the synthetic methods used for the preparation of 2D nanomaterials and their importance. Here we have, for the first time, synthesized a library of five chemically stable covalent organic frameworks, namely **TpPa–NO_2**, **TpPa–F_4**, **TpBD–$(NO_2)_2$**, **TpBD–Me_2**, **TpBD–$(OMe)_2$** along with previously reported three (**TpPa–1, TpPa–2** and **TpBD**) using the simple Schiff base reaction. By adopting different functionalized diamines, we could construct these COFs with variable pore apertures ranging from 15 to 24 Å. These COFs are crystalline, porous and exceptionally stable in aqueous, acidic as well as in basic media. The synthesized COFs (all eight) were successfully delaminated by using a simple, safe and environmental-friendly mechanical grinding route, leading to their transformation into thin layered CONs. We believe that the stability of these COF layers is the main reason for the delamination. Since these individual layers with intrinsic chemical stability are stacked on top of each other with π–π stacking interactions, a mild mechanical force easily delaminates the layers from each other. The mechanical grinding is a scalable and energy efficient method compared to other existing methods like ultrasonication, CVD and layer growth and provides a simple approach for the preparation of novel bulk 2D CONs materials.

In the third chapter, we have for the first time reported azo and alkene functionalized COFs (**Tp-Azo** and **Tp-Stb**) as proton conducting materials. Exceptional chemical stability, low density, and high thermal stability make them advantageous over their MOF counterparts. We have demonstrated a simple impregnation strategy to load mineral acid *viz.* H_3PO_4 inside the framework. Interestingly, after the acid treated samples are washed, the COFs retain their crystallinity, porosity, and stability, which makes them attractive for proton conduction applications. While the parent COFs exhibit negligible conductivity, **PA@Tp-Azo** shows decent proton conductivity values under both hydrous and anhydrous conditions. **PA@Tp-Stb**, on the other hand, exhibits poor proton conductivity and, that too, only under hydrous conditions. Thus, minute changes in functionality lead to a drastic change in proton conducting ability, which establishes the crucial role of the proton responsive azo group in facilitating proton conduction pathways.

In the fourth chapter, we have synthesized a sulfonic acid ($-SO_3H$) functionalized COF **TpPa-SO_3H** for intrinsic anhydrous proton conduction at 120 °C. Further enhancement of conductivity was achieved by synthesizing a hybrid COF **TpPa-(SO_3H-Py)** and subsequent phytic acid loading. The combined effect of intrinsic and extrinsic proton conductivity in COFs has also been demonstrated for the first time to show anhydrous proton conductivity of 5×10^{-4} Scm^{-1} at 120 °C. We believe that such structure-conductivity relationships in COFs will provide a roadmap towards COF based anhydrous proton conductors in the near future.

In the fifth chapter, we have explored the possibility of precise integration of redox-active hydroquinone moieties (H_2Q) into a stable microporous 2D covalent organic framework for pseudocapacitor applications. In addition, molecular level control of the specific capacitance was achieved by tuning the functionality in the COF backbone. The remarkable high specific capacitance (416 F g^{-1} at 0.5 A g^{-1} current density) of **TpPa-$(OH)_2$** was due to the reversible proton-coupled electron transfer ($2H^+/2e^-$) redox chemistry of hydroquinone/benzoquinone (H_2Q/Q) along with high accessibility (43%) of redox active hydroquinone units due to crystalline nature of the COF. These findings are notable which will help to design more energy efficient pseudocapacitor and other electrochemical devices in the near future.

6.2 Future directive

Developing covalent organic frameworks for high energy and power density rechargeable batteries (lithium/sodium/magnesium ion battery)

Rechargeable batteries are playing an important role in solving global-scale energy/environmental issues. In particular, emerging applications such as electrified vehicles and utility grids have become critical along this direction, however, these large-scale applications are limited by safety concerns, environmental issues and the cost of Li-ion batteries (LIBs). Therefore, we proposed to use porous covalent organic frameworks as cathode materials for LIBs. The high surface area, tunable pore size, ordered one-dimensional pore channel and redox active units in their frameworks make COFs as promising materials for energy storage. But their low electric conductivity and electrochemical stability hinder it's used for energy storage purpose. In future, we will develop flexible, cheap, electrochemically stable, conducting high energy density organic cathode materials based on COFs which can operate at high voltages (<3 V vs Li/Li+). More importantly, these COF systems will also pave the way for the development organic sodium and/or magnesium ion batteries considering the increasing demand for Li metal.

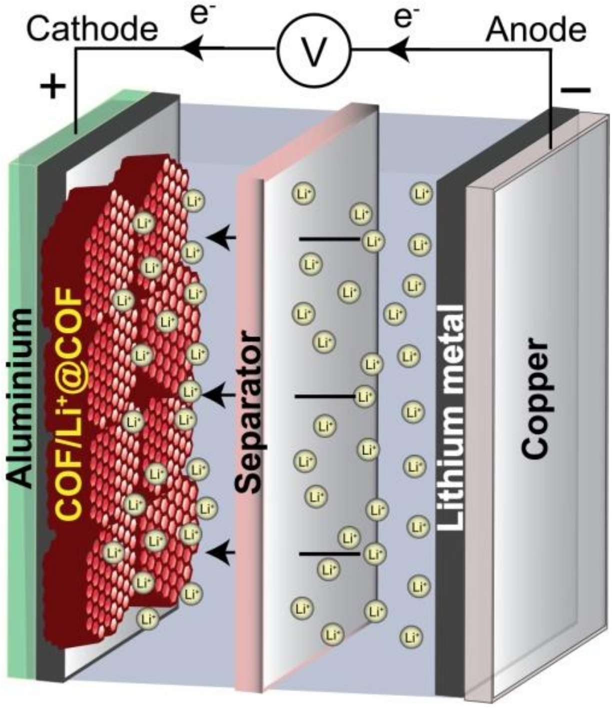

Figure 6.1: *Covalent organic frameworks for lithium ion battery applications.*

REFERENCES

CHAPTER 1

[1.1] (a) D. Ahuja, M. Tatsutani, **2008**, *Sustainable Energy for Developing Countries*, Trieste: TWAS, Academy of Sciences for the Developing World). (b) W. Hafele, W. Sassin, *Resources and Endowments, An Outline of Future Energy Systems*, P.W. Hemily, M.N. Ozdas (eds.), *Science and Future Choice,* (Oxford: Clarendon Press, **1979**). (c) P. Ramchandra, D. Boucar, **2011**, *Green Energy and Technology*. Springer, London Dordrecht Heidelberg New York. (d) Intergovernmental Panel on Climate Change (**2007**), *Climate Change 2007,* Fourth Assessment Report, http://www.ipcc.ch/ipccreports/assessments-reports.html.

[1.2] (a) J. Grigg, *Arch Dis Child,* **2002**, *86*, 79. (b) D. Lüthi, M. Le Floch, B. Bereiter, T. Blunier, J. M. Barnola, U. Siegenthaler, D. Raynaud, J. Jouzel, H. Fischer, K. Kawamura, T. F. Stocker, **2008**, *Nature, 453*, 379. (c) Health Effects of Climate Change in the UK (**2008**), UK Department of Health. (d) International Energy Outlook, (**2008**), *US Energy Information Administration*, http://www.eia.doe.gov/oiaf/ieo/highlights.html. (e) Chemical & Engineering News Archive 2012, 90, 12. (f) C. C. Tsao, J. E. Campbell, M. Mena-Carrasco, S. N. Spak, G. R. Carmichael, Y. Chen, Environ. Sci. Technol. 2012, 46, 10835-10841. (g) S. Heinhorst, G. Cannon, J. Chem. Educ. 2000, 77, 810. (h) Chemical & Engineering News Archive 2014, 92, 28. (i) M. Douziech, S. Hellweg, F. Verones, Environ. Sci. Technol. 2016, 50, 7870-7878. (j) I. J. Levy, C. H. Middlecamp, Eds., Teaching and Learning about Sustainability, Vol. 1205, Am. Chem. Soc., 2015. (k) L. Mahoney, S. Rasalingam, H. Naasz, R. T. Koodali, in Teaching and Learning about Sustainability, Vol. 1205, Am. Chem. Soc., 2015, 119-143.

[1.3] K. Ishizaki, S. Komarneni, M. Nanko. *Porous Materials: Process, technology and applications*. Kluwer Academic, **1998**.

[1.4] (a) A. Haryanto, S. Fernando, N. Murali, S. Adhikari, *Energy Fuels* **2005**, *19*, 2098. (b) R. K. Ahluwalia, T. Q. Hua, *Int. J. Hydrogen Energy*, **2011**, 37, 2891. (c) J. R.

Bartels, M. B. Pate, *Int. J. Hydrogen Energy*, 35, 8371. (d) Z. Yang, J. Zhang, M. C. W. Kintner-Meyer, X. Lu, D. Choi, J. P. Lemmon, J. Liu, Chem. Rev. 2011, 111, 3577-3613. (e) K. Liang, L. Li, Y. Yang, ACS Energy. Lett. 2017, 2, 373-390. (f) K. Sundmacher, Ind. Eng. Chem. Res. 2010, 49, 10159-10182. (g) A. Rabis, P. Rodriguez, T. J. Schmidt, ACS Catal. 2012, 2, 864-890. (h) C.-Y. Wang, Chem. Rev. 2004, 104, 4727-4766. (i) K. Lee, Economic feasibility of producing hydrogen using excess electricity from wind turbines on the Big Island of Hawaii, World renewable energy congress VIII, Denver, 3 September, 2004. http://www.sentech.org/Lee,%20K_Economic%20Feasibility%20Hawaii.pdf.

[1.5] (a) Y. Ma, W. Tong, H. Zhou, S. L Suib, *Microporous Mesoporous Mater.*, **2000**, *37*, 243, (b) S. Cavenati, C. A. Grande, A. E. Rodrigues, *J. Chem. Eng. Data*, **2004**, *49*, 1095. (c) J. Rouquerol, D. Avnir, C. W. Fairbridge, D. H. Everett, J. H. Haynes, N. Pernicone, J. D. F. Ramsay, K. S. W. Sing, K. K. Unger, *Pure and Applied Chemistry*, **1994**, *66*, 1739. (d) T. Sawaki, T. Dewa, Y. Aoyama, *J. Am. Chem. Soc*., **1998**, *120*, 8539. (e) R. E. Morris, P. S. Wheatley. *Angew. Chem., Int. Ed*. **2008**, *47*, 4966.

[1.6] (a) M. Eddaoudi, D. B. Moler, H. Li, B. Chen, T. M. Reinekee, M. O'Keeffe, O. M. Yaghi, *Acc. Chem. Res.* **2001**, *34*, 319, (b) C. Janiak, *Angew. Chem., Int. Ed.*, **1997**, *36*, 1431, (c) A. J. Blake, N. R. Champness, P. Hubberstey, W.-S. Li, M. A. Withersby, M. Schroder, *Coord. Chem. Rev.*, **1999**, *183*, 117, (d) B. Kesanli, Y. Cui, M.Smith, E. Bittner, B. Bockrath, W. Lin, *Angew. Chem., Int. Ed.*, **2005**, *44*, 72, (e) S. Kitagawa, R. Kitaura, S. -I. Noro, *Angew. Chem., Int. Ed.*, **2004**, *43*, 2334, (f) G. Ferey, *Chem. Soc. Rev.* **2008**, *37*, 191, (g) B. Chen, S. Xiang, G. Qian, *Acc. Chem. Res.*, **2010**, *43*, 1115.

[1.7] (a) P. Simon, Y. Gogotsi, *Nat. Mater.*, **2008**, *7*, 845-854. (b) Z. Wu, L. Li, J. Yan, X. Zhang, *Adv. Sci.*, **2017**, *4*, 1600382.

[1.8] F. Schuth, K. S. W. Sing, J. Weitkamp, editors. *Handbook of Porous Solids*. Wiley-VCH Verlag GmbH, **2002**.

[1.9] (a) M. Eddaoudi, D. B. Moler, H. Li, B. Chen, T. M. Reinekee, M. O'Keeffe, O. M. Yaghi, *Acc. Chem. Res.* **2001**, *34*, 319, (b) C. Janiak, *Angew. Chem., Int. Ed. Engl.*, **1997**, *36*, 1431, (c) A. J. Blake, N. R. Champness, P. Hubberstey, W.-S. Li, M. A.

Withersby, M. Schroder, *Coord. Chem. Rev.*, **1999**, *183*, 117, (d) O. M. Yaghi, G. Li, H. Li, *Nature*, **1995**, *378*, 703. (e) S. Kitagawa, R. Kitaura, S. -I. Noro, *Angew. Chem., Int. Ed.*, **2004**, *43*, 2334, (f) G. Ferey, *Chem. Soc. Rev.* **2008**, *37*, 191, (g) B. Chen, S. Xiang, G. Qian, *Acc. Chem. Res.*, **2010**, *43*, 1115, (h) L. Ma, C. Abney, W. Lin, *Chem. Soc. Rev.*, **2009**, *38*, 124, (i) Z. G. Gu, Y. P. Cai, H. C. Fang, Z. Y. Zhou, P. K. Thallapally, J. A. Tian, J. Liu, G. J. Exarhos, *Chem. Commun.*, **2010**, *46*, 5373, (j) B. Chen, M. Eddaoudi, S. T. Hyde, M. O'Keeffe, O. M. Yaghi, *Science*, **2001**, *291*, 1021, (k) P. Pachfule, Y. Chen, J. Jiang, R. Banerjee *J. Mater. Chem.*, **2011**, *21*, 17737, (l) J. W. Yoon, S. H. Jhung, Y. K. Hwang, S. M. Humphrey, P. T. Wood, J. -S. Chang, *Adv. Mater.* **2007**, *19*, 1830, (m) K. L. Mulfort, O. K. Farha, C. D. Malliakas, M. G. Kanatzidis, J. T. Hupp, *Chem. Eur. J.*, **2010**, *16*, 276, (n) H. -S. Choi, M. P. Suh, *Angew. Chem*. **2009**, *121*, 6997, (o) X. Gu, Z.-H. Lu, Q. Xu, *Chem. Commun* **2010**, *46*, 7400, (p) S. -T. Zheng, J. T. Bu, Y. Li, T. Wu, F. Zuo, P. Feng, X. Bu. *J. Am. Chem. Soc.* **2010**, *132*, 17062, (q) J. An, N. L. Rosi, *J. Am. Chem. Soc.* **2010**, *132*, 5578, (r) A. G. Wong-Foy, O. Lebel, A. J. Matzger, *J. Am. Chem. Soc.* **2007**, *129*, 15740, (s) H. Chun, D. N. Dybtsev, H. Kim, K. Kim, *Chem. Eur. J.* **2005**, *11*, 3521, (t) J. Rowsell, A. Millward, K. Park, O. Yaghi *J. Am. Chem. Soc.* **2004**, *126*, 5666.

[1.10] (a) Y. Li, R. T. Yang, *AIChE J.* **2008**, *54*, 269. (b) Z. Liang, M. Marshall, A. L. Chaffee, *Energy Fuels* **2009**, *23*, 2785. (c) F. Gul-E-Noor, B. Jee, A. Poppl, M. Hartmann, D. Himsl, M. Bertmer, *Phys. Chem. Chem. Phys*. **2011**, *13*, 7783. (d) N. C. Burtch, H. Jasuja, K. S. Walton, *Chem. Rev*., **2014**, *114*, 10575.

[1.11] (a) Y. Luo, B. Li, W. Wang, K. Wu and B. Tan, *Advanced Materials*, **2012**, *24*, 5703. (b) D. C. Wu, F. Xu, B. Sun, R. W. Fu, H. K. He, K. Matyjaszewski, *Chem. Rev.*, **2012**, *112*, 3959. (c) P. kaur, J. T. Hupp and S. T. Nguyen, *ACS Catal*., **2011**, *1*, 819. (d) Z. H. Xiang and D. P. Cao, *J. Mater. Chem. A*, **2013**, *1*, 2691.

[1.12] A. P. Cote, A. I. Benin, N. W. Ockwig, M. O'Keeffe, A. J. Matzger, O. M. Yaghi, *Science*, **2005**, *310*, 1166.

[1.13] (a) Breck, D. W., *Zeolite molecular sieves: structure, chemistry, and use*. Wiley: New York, **1974**. (b) Cundy, C. S., Cox, P. A., *Chem. Rev.* **2003**, *103 (3)*, 663.

[1.14] Wilson, S. T., Lok, B. M.,Messina, C. A., Cannan, T. R., Flanigen, E. M., *J. Am. Chem. Soc.* **1982**, *104*, 1146.

[1.15] (a) Huang, Q., Ulutagay, M., Michener, P. A., Hwu, S.-J., *J. Am. Chem. Soc*. **1999**, *121 (44)*,10323. (b) Parise, J. B., *Inorg. Chem*. **1985**, *24 (25)*, 4312. (c) Gier, T. E., Stucky, G. D., *Nature* **1991**, *349 (6309*), 508.

[1.16] (a) Wingenfelder, U., Hansen, C., Furrer, G., Schulin, R., *Environ. Sci. Technol.* **2005**, *39 (12)*, 4606. (b) Moreno, N., Querol, X., Ayora, C., Pereira, C. F., Janssen-Jurkovicová, M., *Environ. Sci. Technol*. **2001**, *35*, 3526. (c) Clearfield, *A., Chem. Rev.* **1988**, *88 (1)*, 125.

[1.17] (a) Y. Cui, H. Xu, Y. Yue, Z. Guo, J. Yu, Z. Chen, J. Gao, Y. Yang, G. Qian, B. Chen, *J. Am. Chem. Soc*. **2012**,*134*, 3979. (b) A. M. Shultz, O. K. Farha, J. T. Hupp, S. T. Nguyen, *J. Am. Chem. Soc*. **2009**, *131*, 4204. (c) V. Stavila, R. K. Bhakta, T. M. Alam, E. H. Majzoub, M. D. Allendorf, *ACS Nano* **2012**, *6*, 9807.

[1.18] (a) Y. Lee, J. Kim, W. Ahn, *Korean J. Chem. Eng*. **2013**, *30*, 1667. (b) A. Schneemann , V. Bon , I. Schwedler , I. Senkovska , S. Kaskel, R. A. Fischer *Chem. Soc. Rev*., **2014**, *43*, 6062. (c) F. X. Coudert, *Chem. Mater*., **2015**, *27 (6)*, 1905.

[1.19] (a) H. Furukawa, K. E. Cordova, M. O'Keeffe, O. M. Yaghi, *Science*, **2013**, *341*, 6149, (b) R. J. Kupplera, D. J. Timmonsb, Q. –R. Fanga, J. –R. Lia, T. A. Makala, M. D. Younga, D. Yuana, D. Zhaoa, W. Zhuanga, H .-C. Zhou. *Coord. Chem. Rev*., **2009**, **253**, 3042, (c) A. Morozan, F. Jaouen, *Energy Environ. Sci*., **2012**, *5*, 9269, (d) A. U. Czaja, N. Trukhan, U. Müller, *Chem. Soc. Rev*., **2009**, *38*, 1284, (e) U. Mueller, M. Schubert, F. Teich, H. Puetter, K. Schierle-Arndt, J. Pastré *J. Mater. Chem*., **2006**, *16*, 626.

[1.20] (a) Y. Luo, B. Li, W. Wang, K. Wu, B. Tan, *Advanced Materials*, **2012**, *24*, 5703. (b) T. Ben, S. L. Qiu, *CrystEngComm*, **2013**, *15*, 17. (c) T. Ben, H. Ren, S. Q. Ma, D. P. Cao, J. H. Lan, X. F. Jing, W. C. Wang, J. Xu, F. Deng, J. M. Simmons, S. L. Qiu, G. S. Zhu, *Angew. Chem., Int. Ed*., **2009**, *48*, 9457. (d) S. Y. Ding, W. Wang, *Chem. Soc. Rev*., **2013**, *42*, 548. (e) P. M. Budd, B. S. Ghanem, S. Makhseed, N. B. McKeown, K.

J. Msayib, C. E. Tattershall, *Chem. Commun*., **2004**, 230. (f) X. Feng, X. Ding, D. Jiang, *Chem. Soc. Rev*., **2012**, *41*, 6010.

[1.21] (a) G. Cheng, T. Hasell, A. Trewin, D. J. Adams, A. I. Cooper, *Angew. Chem., Int. Ed.*, **2012**, *51*, 12727. (b) L. Chen, Y. Honsho, S. Seki, D. Jiang, *J. Am. Chem. Soc.*, **2010**, *132*, 6742. (c) J. X. Jiang, F. B. Su, A. Trewin, C. D. Wood, N. L. Campbell, H. J. Niu, C. Dickinson, A. Y. Ganin, M. J. Rosseinsky, Y. Z. Khimyak, A. I. Cooper, *Angew. Chem., Int. Ed*., **2007**, *46*, 8574. (d) J. X. Jiang, A. Trewin, D. J. Adams, A. I. Cooper, *Chem. Sci*., **2011**, *2*, 1777. (e) Y. H. Xu, L. Chen, Z. Q. Guo, A. Nagai, D. Jiang, *J. Am. Chem. Soc*., **2011**, *133*, 17622. (f) S. W. Yuan, B. Dorney, D. White, S. Kirklin, P. Zapol, L. P. Yu, D. J. Liu, *Chem. Commun*., **2010**, *46*, 4547. (g) A. Li, R. F. Lu, Y. Wang, X. Wang, K. L. Han, W. Q. Deng, *Angew. Chem., Int. Ed.*, **2010**, *49*, 3330. (h) A. Li, H. X. Sun, D. Z. Tan, W. J. Fan, S. H. Wen, X. J. Qing, G. X. Li, S. Y. Li, W. Q. Deng, *Energy Environ. Sci*., **2011**, *4*, 2062. (i) Q. Chen, J. X. Wang, F. Yang, D. Zhou, N. Bian, X. J. Zhang, C. G. Yan, B. H. Han, J. Mater. Chem., 2011, 21, 13554. (j) Y. Kou, Y. Xu, Z. Guo, D. Jiang, *Angew. Chem., Int. Ed.*, **2011**, *50*, 8753. (k) A. I. Cooper, *Advanced Materials*, **2009**, *21*, 1291. (l) J.-X. Jiang, F. Su, A. Trewin, C. D. Wood, H. Niu, J. T. Jones, Y. Z. Khimyak, A. I. Cooper, *J. Am. Chem. Soc*., **2008**, *130*, 7710.

[1.22] (a) A. P. Cote, A. I. Benin, N. W. Ockwig, M. O’Keeffe, A. J. Matzger and O. M. Yaghi, Science, **2005**, 310, 1166–1170. (b) E. L. Spitler, W. R. Dichtel, *Nat. Chem*., **2010**, 2, 672. (c) J. X. Jiang, A. I. Cooper, *Top. Curr. Chem*., **2010**, *293*, 1. (d) P. J. Waller, F. Gandara and O. M. Yaghi, *Acc. Chem. Res*., **2015**, *48*, 3053.

[1.23] (a) H. M. El-Kaderi, J. R. Hunt, J. L. Mendoza-Cortes, A. P. Cote, R. E. Taylor, M. O’Keeffe, O. M. Yaghi, *Science*, **2007**, *316*, 268.

[1.24] C. S. Diercks, O. M. Yaghi., Science, **2017**, *355*, eaal1585.

[1.25] (a) Côté, A. P., El- Kaderi, H. M., Furukawa, H., Hunt, J. R. & Yaghi, O. M. *J. Am. Chem. Soc*. **2007**, *129*, 12914. (b) A. Nagai, Z. Guo, X. Feng, S. Jin, X. Chen, X. Ding, D. Jiang, *Nat. Commun*., **2011**, *2*, 536.

[1.26] (a) P. Kuhn, M. Antonietti, A. Thomas, *Angew. Chem., Int. Ed.*, **2008**, *47*, 3450. (b) M. J. Bojdys, J. Jeromenok, A. Thomas, M. Antonietti, *Adv. Mater.*, **2010**, *22*, 2202. (c) R. Palkovits, M. Antonietti, P. Kuhn, A. Thomas, F. Schuth, *Angew. Chem., Int. Ed.*, **2009**, *48*, 6909. (d) C. E. Chan-Thaw, A. Villa, L. Prati, A. Thomas, *Chem.–Eur. J.*, **2011**, *17*, 1052.

[1.27] (a) F. J. Uribe-Romo, J. R. Hunt, H. Furukawa, C. Klock, M. O'Keeffe, O. M. Yaghi, *J. Am. Chem. Soc.*, **2009**, *131*, 4570. (b) F. J. Uribe-Romo, C. J. Doonan, H. Furukawa, K. Oisaki, O. M. Yaghi, *J. Am. Chem. Soc*., **2011**, *133*, 11478.(c) S.-Y. Ding, J. Gao, Q. Wang, Y. Zhang, W.-G. Song, C.-Y. Su, W. Wang, *J. Am. Chem. Soc.*, **2011**, *133*, 19816. (d) S. Wan, F. Gandara, A. Asano, H. Furukawa, A. Saeki, S. K. Dey, L. Liao, M. W. Ambrogio, Y. Y. Botros, X. Duan, S. Seki, J. F. Stoddart, O. M. Yaghi, *Chem. Mater*., **2011**, *23*, 4094.

[1.28] (a) B. J. Smith and W. R. Dichtel, J. Am. Chem. Soc., 2014, 136, 8783–8789. (b) M. Calik, T. Sick, M. Dogru, M. Doblinger, S. Datz, H. Budde, A. Hartschuh, F. Auras, T. Bein, *J. Am. Chem. Soc*. **2016**, *138*, 1234. (c) S. Karak, S. Kandambeth, B. P. Biswal, H. S. Sasmal, S. Kumar, P. Pachfule, R. Banerjee, *J. Am. Chem. Soc*., **2017**, *139*, 1856–1862. (d) M. Matsumoto, R. R. Dasari, W. Ji, C. H. Feriante, T. C. Parker, S. R. Marder, W. R. Dichtel, *J. Am. Chem. Soc*. **2017**, *139*, 4999−5002. (e) S. Kandambeth, D. B. Shinde, M. K. Panda, B. Lukose, T. Heine, R. Banerjee, *Angew. Chem., Int. Ed.*, **2013**, *52*, 13052–13056. (f) V. S. Vyas, F. Haase, L. Stegbauer, G. Savasci, F. Podjaski, C. Ochsenfeld, B. V. Lotsch, *Nat. Commun.*, **2015**, *6*, 8508. (g) H. Xu, J. Gao, D. Jiang, *Nat. Chem.*, **2015**, *7*, 905–912. (h) X. Chen, M. Addicoat, S. Irle, A. Nagai, D. Jiang, *J. Am. Chem. Soc.*, **2013**, *135*, 546–549. (i) L. M. Salonen, D. D. Medina, E. Carbo-Argibay, M. G. Goesten, L. Mafra, N. Guldris, J. M. Rotter, D. G. Stroppa, C. Rodriguez-Abreu, *Chem. Commun.*, **2016**, *52*, 7986–7989. (j) L. Ascherl, T. Sick, J. T. Margraf, S. H. Lapidus, M. Calik, C. Hettstedt, K. Karaghiosoff, M. Döblinger, T. Clark, K. W. Chapman, F. Auras, T. Bein, *Nat. Chem.*, **2016**, *8*, 310–316.

[1.29] K. T. Jackson, T. E. Reich, H. M. El-Kaderi, *Chem. Commun.*, **2012**, *48*, 8823-8825.

[1.30] (a) F. J. Uribe-Romo, C. J. Doonan, H. Furukawa, K. Oisaki and O. M. Yaghi, J. Am. Chem. Soc., 2011, 133, 11478-11481. (b) D. N. Bunck, W. R. Dichtel, *J. Am. Chem. Soc*., **2013**, *135*, 14952-14955.

[1.31] S. Dalapati, S. Jin, J. Gao, Y. Xu, A. Nagai, D. Jiang, *J. Am. Chem. Soc.*, **2013**, *135*, 17310-17313.

[1.32] J. Guo, Y. Xu, S. Jin, L. Chen, T. Kaji, Y. Honsho, M. A. Addicoat, J. Kim, A. Saeki, H. Ihee, S. Seki, S. Irle, M. Hiramoto, J. Gao, D. Jiang, *Nat. Commun.*, **2013**, 4, 2736-2743.

[1.33] (a) P. Kuhn, M. Antonietti, A. Thomas, *Angew. Chem., Int. Ed*., **2008**, *47*, 3450. (b) M. J. Bojdys, J. Jeromenok, A. Thomas, M. Antonietti, *Adv. Mater.*, **2010**, *22*, 2202. (c) R. Palkovits, M. Antonietti, P. Kuhn, A. Thomas, F. Schuth, *Angew. Chem., Int. Ed.*, **2009**, *48*, 6909. (d) C. E. Chan-Thaw, A. Villa, L. Prati, A. Thomas, *Chem.–Eur. J.*, **2011**, *17*, 1052.

[1.34] D. Beaudoin, T. Maris, J. D. Wuest, *Nat. Chem*., **2013**, *5*, 830-834.

[1.35] (a) P. Kissel, D. J. Murray, W. J. Wulftange, V. J. Catalano, B. T. King, *Nat. Chem.*, **2014**, *6*, 774–778. (b) R. Bhola, P. Payamyar, D. J. Murray, B. Kumar, A. J. Teator, M. U. Schmidt, S. M. Hammer, A. Saha, J. Sakamoto, A. D. Schluter and B. T. King, *J. Am. Chem. Soc.*, **2013**, *135*, 14134-14141.

[1.36] Q. Fang, Z. Zhuang, S. Gu, R. B. Kaspar, J. Zheng, J. Wang, S. Qiu, Y. Yan, *Nat. Commun.*, **2014**, *5*, 4503-4510.

[1.37] X. Zhuang, W. Zhao, F. Zhang, Y. Cao, F. Liu, S. Bi, X. Feng, *Polym. Chem.*, **2016**, *7*, 4176-4181.

[1.38] M. R. Rao, Y. Fang, S. De Feyter, D. F. Perepichka, *J. Am. Chem. Soc.*, **2017**, *139*, 2421-2427.

[1.39] Y. Zeng, R. Zou, Z. Luo, H. Zhang, X. Yao, X. Ma, R. Zou, Y. Zhao, *J. Am. Chem. Soc.*, **2015**, *137*, 1020-1023.

[1.40] C. Qian, Q. Qi, G. Jiang, F. Cui, Y. Tian, X. Zhao, *J. Am. Chem. Soc.*, **2017**, *139*, 6736−6743.

[1.41] W. Y. Dai, F. Shao, J. Szczerbinski, R. McCaffrey, R. Zenobi, Y. H. Jin, A. D. Schluter, W. Zhang, *Angew. Chem., Int. Ed.*, **2016**, *55*, 213–217.

[1.42] D. J. Murray, D. D. Patterson, P. Payamyar, R. Bhola, W. T. Song, M. Lackinger, A. D. Schlîter, B. T. King, *J. Am. Chem. Soc.*, **2015**, *137*, 3450 – 3453.

[1.43] Y. Peng, W. K. Wong, Z. Hu, Y. Cheng, D. Yuan, S. A. Khan, D. Zhao, *Chem. Mater.*, **2016**, *28*, 5095–5101.

[1.44] (a) (a) N. L. Campbell, R. Clowes, L. K. Ritchie, A. I. Cooper, *Chem. Mater.*, **2009**, *21*, 204. (b) M. Dogru, A. Sonnauer, A. Gavryushin, P. Knochel, T. Bein, *Chem. Commun.*, **2011**, *47*, 1707.

[1.45] (a) P. Kuhn, M. Antonietti, A. Thomas, *Angew. Chem., Int. Ed.*, **2008**, *47*, 3450. (b) M. J. Bojdys, J. Jeromenok, A. Thomas, M. Antonietti, *Adv. Mater.*, **2010**, *22*, 2202. (c) R. Palkovits, M. Antonietti, P. Kuhn, A. Thomas, F. Schuth, *Angew. Chem., Int. Ed.*, **2009**, *48*, 6909. (d) C. E. Chan-Thaw, A. Villa, L. Prati, A. Thomas, *Chem.–Eur. J.*, **2011**, *17*, 1052.

[1.46] B. P. Biswal, S. Chandra, S. Kandambeth, B. Lukose, T. Heine, R. Banerjee, *J. Am. Chem. Soc.*, **2013**, *135*, 5328.

[1.47] M .Matsumoto, R. R. Dasari, W. Ji, C. H. Feriante, T. C. Parker, S. R. Marder, W. R. Dichtel, *J. Am. Chem. Soc.*, **2017**, *139*, 4999−5002.

[1.48] Y. Peng, W. K. Wong, Z. Hu, Y. Cheng, D. Yuan, S. A. Khan, D. Zhao, *Chem. Mater.*, **2016**, *28*, 5095−5101.

[1.49] (a) N. A. A. Zwaneveld, R. Pawlak, M. Abel, D. Catalin, D. Gigmes, D. Bertin, L. Porte, *J. Am. Chem. Soc.*, **2008**, *130*, 6678. (b) J. W. Colson, A. R. Woll, A. Mukherjee, M. P. Levendorf, E. L. Spitler, V. B. Shields, M. G. Spencer, J. Park, W. R. Dichtel, *Science*, **2011**, *332*, 228.(c) X. H. Liu, C. Z. Guan, S. Y. Ding, W. Wang, H. J. Yan, D. Wang, L. J. Wan, *J. Am. Chem. Soc.*, **2013**, *135*, 10470.

[1.50] (a) H. M. El-Kaderi, J. R. Hunt, J. L. Mendoza-Cortes, A. P. Cote, R. E. Taylor, M. O'Keeffe, O. M. Yaghi, *Science*, **2007**, *316*, 268. (b) H. Furukawa, O. M. Yaghi, *J. Am. Chem. Soc.*, **2009**, *131*, 8875.

[1.51] (a) E. Klontzas, E. Tylianakis, G. E. Froudakis, *J. Phys. Chem. C*, **2009**, *113*, 21253. (b) F. Li, J. Zhao, B. Johansson, L. Sun, *Int. J. Hydrogen Energy*, **2010**, *35*, 266.

[1.52] H. Furukawa, O. M. Yaghi, *J. Am. Chem. Soc*., **2009**, *131*, 8875.

[1.53] Y. J. Choi, J. H. Choi, K. M. Choi, J. K. Kang, *J. Mater. Chem*., **2011**, *21*, 1073.

[1.54] P. Kuhn, M. Antonietti, A. Thomas, *Angew. Chem. Int. Ed.*, **2008**, *47*, 3450–3453.

[1.55] (a) N. Huang, X. Chen, R. Krishna, D. Jiang, *Angew. Chem. Int. Ed.*, **2015**, 54, 2986–2990. (b) N. Huang, R. Krishna, D. Jiang, *J. Am. Chem. Soc.*, 2015, *137*, 7079–7082.

[1.56] C. J. Doonan, D. J. Tranchemontagne, T. G. Glover, J. R. Hunt, O. M. Yaghi, *Nat. Chem*., **2010**, *2*, 235.

[1.57] (a) S. Y. Ding, J. Gao, Q. Wang, Y. Zhang,W. G. Song, C. Y. Su, W. Wang, *J. Am. Chem. Soc*., **2011**, *133*, 19816. (b) Y. Hou, X. Zhang, J. Sun, S. Lin, D. Qi, R. Hong, D. Li, X. Xiao, J. Jiang, *Microporous Mesoporous Mater.*, **2015**, *214,* 108–114. (c) P. Pachfule, S. Kandmabeth, A. Mallick, R. Banerjee, *Chem. Commun*., **2015**, *51*, 11717. (d) P. Pachfule, S. Kandambeth, D. Diaz Diaz, R. Banerjee, *Chem. Commun*., **2014**, *50*, 3169. (e) D. B. Shinde, S. Kandambeth, P. Pachfule, R. R. Kumar, R. Banerjee, *Chem. Commun.*, **2015**, *51*, 310–313. (f) Q. Fang, S. Gu, J. Zheng, Z. Zhuang, S. Qiu, Y. Yan, *Angew. Chem., Int. Ed.*, **2014**, *53*, 2878–2882. (g) N. Huang, R. Krishna, D. L. Jiang, *J. Am. Chem. Soc.*, **2015**,*137*, 7079–7082. (h) H. Xu, J. Gao, D. L. Jiang, *Nat. Chem.*, **2015**,*7*, 905–912.

[1.58] (a) S. Wan, J. Guo, J. Kim, H. Ihee, D. Jiang, *Angew. Chem.,Int. Ed*., **2009**, *48*, 5439. (b) S. Wan, J. Guo, J. Kim, H. Ihee, D. Jiang, *Angew. Chem.,Int. Ed*., **2008**, *47*, 8826. (c) X. Feng, L. Liu, Y. Honsho, A. Saeki, S. Seki, S. Irle, Y. Dong, A. Nagai, D. Jiang, *Angew. Chem., Int. Ed*., **2012**, *51*, 2618. (d) D. D. Medina, V. Werner, F. Auras, R. Tautz, M. Dogru, J. Schuster, S. Linke, M. Dçblinger, J. Feldmann, P. Knochel, T. Bein, *ACS Nano*, **2014**, *8*, 4042–4052. (e) X. Ding, L. Chen, Y. Honsho, X. Feng, O. Saengsawang, J. Guo, A. Saeki, S. Seki, S. Irle, S. Nagase, V. Parasuk, D. Jiang, *J. Am. Chem. Soc.*, **2011**, 133, 14510–14513.

[1.59] (a) C. R. DeBlase, K. E. Silberstein, T. T. Truong, H. D. Abruna,W. R. Dichtel, *J. Am. Chem. Soc*., **2013**, *135*, 16821. (b) C. R. DeBlase, K. Hernandez-Burgos, K. E.

Silberstein, G. G. Rodriguez-Calero, R. P. Bisbey, H. D. Abruna, W. R. Dichtel, *ACS Nano*, **2015**, *9*, 3178. (c) C. R. Mulzer, L. Shen, R. P. Bisbey, J. R. McKone, N. Zhang, H. D. Abruna, W. R. Dichtel, *ACS Cent. Sci.*, **2016**, 2, 667. (d) Z. Zha, L. Xu, Z. Wang, X. Li, Q. Pan, P. Hu, S. Lei, *ACS Appl. Mater. Interfaces*, **2015**, *7*, 17837–17843. (e) A. M. Khattak, Z. A. Ghazi, B. Liang, N. A. Khan, A. Iqbal, L. Li, Z. Tang, *J. Mater. Chem. A*, **2016**, *4*, 16312–16317. (f) X. Chen, M. Addicoat, E. Jin, L. Zhai, H. Xu, N. Huang, Z. Guo, L. Liu, S. Irle, D. Jiang, *J. Am. Chem. Soc.*, **2015**, 137, 3241–3247.

[1.60] (a) S. Chandra, T. Kundu, S. Kandambeth, R. BabaRao, Y. Marathe, S. M. Kunjir, R. Banerjee, *J. Am. Chem. Soc.*, **2014**, *136*, 6570–6573. (b) S. Chandra, T. Kundu, K. Dey, M. Addicoat, T. Heine, R. Banerjee, *Chem. Mater.*, **2016**, *28*, 1489–1494. (c) D. B. Shinde, H. B. Aiyapp, M. Bhadra, B. P. Biswal, P. Wadge, S. Kandambeth, B. Garai, T. Kundu, S. Kurungot, R. Banerjee, *J. Mater. Chem. A*, **2016**, *4*, 2682-2690. (d) H. Xu, S. Tao, D. Jiang, *Nat. Mater.*, **2016**, *15*, 722-726.

[1.61] (a) H. Lu, C. Wang, J. Chen, R. Ge, W. Leng, B. Dong, J. Huang, Y. Gao, *Chem. Commun*. **2015**, *51*, 15562. (b) B. P. Biswal, H. D. Chaudhari, R. Banerjee, U. K. Kharul, *Chem. Eur. J.*, **2016**, *22*, 4695. (c) S. Kandambeth, B. P. Biswal, H. D. Chaudhari, K. C. Rout, S. H. Kunjattu, S. Mitra, S. Karak, A. Das, R. Mukherjee, U. K. Kharul, R. Banerjee, *Adv. Mater.*, **2017**, *29*, 1603945.

[1.62] (a) Q. Fang, J. Wang, S. Gu, R. B. Kaspar, Z. Zhuang, J. Zheng, H. Guo, S. Qiu, Y. Yan, *J. Am. Chem. Soc*., **2015**, *137*, 8352. (b) L. Bai, S. Z. F. Phua, W. Q. Lim, A. Jana, Z. Luo, H. P. Tham, L. Zhao, Q. Gao, Y. Zhao, *Chem. Commun.*, **2016**, *52*, 4128–4131.

[1.63] (a) L. M. Lanni, R. W. Tilford, M. Bharathy, J. J. Lavigne, *J. Am. Chem. Soc*., **2011**, *133*, 13975. (b) Y. Du, K. Mao, P. Kamakoti, P. Ravikovitch, C. Paur, S. Cundy, Q. Li, D. Calabro, *Chem. Commun*. **2012**, *48*, 4606. (c) S. Kandambeth, D. B. Shinde, M. K. Panda, B. Lukose, T. Heine, R. Banerjee, *Angew. Chem., Int. Ed.*, **2013**, *52*, 13052–13056. (d) P. J. Waller, S. Lyle, T. Osborn Popp, C. S. Diercks, J. A. Reimer, O. M. Yaghi, *J. Am. Chem. Soc.*, **2016**, *138*, 15519–15522. (e) S. Kandambeth, A.

Mallick, B. Lukose, M. V. Mane, T. Heine, R. Banerjee, *J. Am. Chem. Soc.*, **2012**, *134*, 19524–19527.

CHAPTER 2

[2.1] (a) G. A. Ozin, A. C. Arsenault, *Nanochemistry*, 2005, RSC Publishing, Cambridge, UK. (b) Springer Handbook of Nanotechnology (Ed. B. Bhushan), Springer-Verlag, Berlin, **2004**. (c) K. S. Novoselov, A. K. Geim, S. V. Morozov, D. Jiang, Y. Zhang, S. V. Dubonos, I. V. Grigorieva, A. A. Firsov, *Science*, **2004**, *306*, 666. (d) S. Park, R. S. Ruoff, *Nat. Nanotechnol.,* **2009**, *4*, 217.

[2.2] (a) C. L. Tan, H. Zhang, *Chem. Soc. Rev.,* **2015**, *44*, 2713−2731. (b) M. Chhowalla, H. S. Shin, G. Eda, L. J. Li, K. Loh, H. Zhang, *Nat. Chem.*, **2013**, *5*, 263−275. (c) X. Huang, Z. Y. Zeng, H. Zhang, *Chem. Soc. Rev.*, **2013**, *42*, 1934−1946. (d) R. Lv, J. A. Robinson, R. E. Schaak, D. Sun, Y. Sun, T. E. Mallouk, M. Terrones, *Acc. Chem. Res.,* **2015**, *48*,56−64. (e) M. Osadaab, T. Sasaki, *J. Mater. Chem.*, **2009**, *19*, 2503−2511. (f) R. Ma, T. Sasaki, *Acc. Chem. Res.,* **2015**, 48, 136−143. (g) Q. Wang, D. O'Hare, *Chem. Rev.,* **2012**, *112*, 4124−4155. (h) Y. Lin, T. V. Williams, J. W. Connell, *J. Phys. Chem. Lett.,* **2010**, *1*, 277−283. (i) Q. Weng, X. Wang, Y. Bando, D. Golberg, *Chem. Soc. Rev.,* **2016**, *45*, 3989−4012. (j) L. H. Li, Y. Chen, *Adv. Funct. Mater.*, **2016**, *26*, 2594−2608.

[2.3] A. P. Cote, A. I. Benin, N. W. Ockwig, M. O'Keeffe, A. J. Matzger, O. M. Yaghi, *Science,* **2005**, *310,* 1166.

[2.4] (a) I. Berlanga, M. L. Ruiz-González, J. M. González-Calbet, J. L. G. Fierro, R. Mas-Ballesté, F. Zamora, *Small,* **2011**, *7*, 1207−1211. (b) D. N. Bunck, W. R. Dichtel, *J. Am. Chem. Soc.*, **2013**, *135*, 14952–14955.

[2.5] (a) C. J. Doonan, D. J. Tranchemontagne, T. G. Glover, J. R. Hunt, O. M. Yaghi, *Nat. Chem.,* **2010**, *2*, 235−238. (b) H. Furukawa, O. M. Yaghi, *J. Am. Chem. Soc.,* **2009**, *131*, 8875−8883. (c) S .Y. Ding, J. Gao, Q. Wang, Y. Zhang, W. G. Song, C. Y. Su, W. Wang, *J. Am. Chem. Soc.* **2011**, *133*, 19816−19822. (d) S. Wan, J. Guo, J. Kim, H. Ihee, D. L. Jiang, *Angew. Chem., Int. Ed.,* **2009**, *48*, 5439−5442. (e) J. E. Anthony, *Chem. Rev.*, **2006**, *106*, 5028−5048.

[2.6] A. K. Geim, K. S. Novoselov, *Nat. Mater.*, **2007**, *6*, 183−191.

[2.7] (a) G. Fiori, F. Bonaccorso, G. Iannaccone, T. Palacios, D. Neumaier, A. Seabaugh, S. K. Banerjee, L. Colombo, *Nat. Nanotechnol.*, **2014**, 7, 768−779. (b) M. Chhowalla, D. Jena, H. Zhang, *Nat. Rev. Mater.*, **2016**, 1, 16052.

[2.8] (a) M. D. Stoller, S. Park, Y. Zhu, J. An, R. S. Ruoff, *Nano Lett.* **2008**, *8*, 3498−3502. (b) D. Deng, K. S. Novoselov, Q. Fu, N. Zheng, Z. Tian, X. Bao, *Nat. Nanotechnol.*, **2016**, *11*, 218−230. (c) F. Bonaccorso, L. Colombo, G. Yu, M. Stoller, V. Tozzini, A. C. Ferrari, R. S. Ruoff, V. Pellegrini, *Science*, **2015**, *347*,41−50.

[2.9] (a) B. Mendoza-Sá nchez, Y. Gogotsi, *Adv. Mater.* **2016**, *28*, 6104−6135. (b) C. L. Tan, Z. D. Liu,; W. Huang, H. Zhang, *Chem. Soc. Rev.* **2015**, *44*, 2615−2628.

[2.10] S. Kandambeth, A. Mallick, B. Lukose, V. M. Mane, T. Heine, R. Banerjee, *J. Am. Chem. Soc.*, **2012**, *134*, 19524−19527.

[2.11] B. P. Biswal, S. Chandra, S. Kandambeth, B. Lukose, V. M. Mane, T. Heine, R. Banerjee, *J. Am. Chem. Soc.* **2013**, *135*, 5328−5331.

[2.12] J. W. Colson, A. R. Woll, A. Mukherjee, M. P. Levendorf, E. L. Spitler, V. B. Shields, M. G. Spencer, J. Park, W. R. Dichtel, *Science*., **2011**, *332*, 228−231.

[2.13] J. C. Tan, P. J. Saines, E. G. Bithell, A. K. Cheetham, *ACS Nano*. **2012**, *6*, 615−621.

[2.14] I.-Y. Jeon, H.-J. Choi, S.-M. Jung, J.-M. Seo, M.-J. Kim, L. Dai, J.-B. Baek, *J. Am. Chem. Soc.* **2013**, *135*, 1386−1393.

[2.15] L. M. Lanni, R. W. Tilford, M. Bharathy, J. J. Lavigne, *J. Am. Chem. Soc.* **2011**, *130*, 13975−13983.

[2.16] T. Heine, M. Rapacioli, S. Patchkovskii, J. Frenzel, A. M. Koester, P. Calaminici, S. Escalante, H. A. Duarte, R. Flores, G. Geudtner, A. Goursot, J. U. Reveles, A. Vela, Salahub, D. R. deMon-nano; Jacobs University Bremen: Bremen, Germany, **2009**.

[2.17] Accelrys, Material Studio Release Notes, Release 4.2, Accelrys Software, San Diego **2006**.

[2.18] B. Lukose, A. Kuc, T. Heine, *Chem.Eur. J.*, **2011**, 17, 2388.

[2.19] J. H. Chong, M. Sauer, B. O. Patrick, M. MacLachlan, *J. Org. Lett.*, **2003**, *5*, 3823.

CHAPTER 3

[3.1] (a) U.S. Department of Energy, U.S. Energy Information Administration: International Energy Outlook 2013 (Report: DOE/EIA-0484(2013)), **2013**. (b) D. Larcher, J. M. Tarascon, *Nat Chem*., **2015**, 7,19–29. (c) K. M. Abraham, *J. Phys. Chem. Lett.*, **2015**, 6, 830-844. (d) C. Turner, *J. Chem. Educ.*, **2015**, 92, 601-602. (e) C. A. Jones, J. J. Leonard, J. A. Sofranko, *Energy & Fuels*, **1987**, *1*, 12-16. (f) F. T. Wagner, B. Lakshmanan, M. F. Mathias, *J. Phys. Chem. Lett.* **2010**, *1*, 2204-2219.

[3.2] (a) *Chemical & Engineering News Archive,* **2014**, *92*, 28. (b) M. Douziech, S. Hellweg, F. Verones, *Environ. Sci. Technol.* **2016**, *50*, 7870-7878. (c) I. J. Levy, C. H. Middlecamp, Eds., Teaching and Learning about Sustainability, Vol. 1205, *Am. Chem. Soc.*, **2015**. (d) L. Mahoney, S. Rasalingam, H. Naasz, R. T. Koodali, in *Teaching and Learning about Sustainability*, Vol. 1205, *Am. Chem. Soc.*, **2015**, 119-143. (e) Boyle, Godfrey. *Renewable energy*. OXFORD university press, 2004. (f) Johansson, Thomas B., and Laurie Burnham, eds. *Renewable energy: sources for fuels and electricity*. Island Press, **1993**.

[3.3] S. Banerjee, J. A. Tiarks, M. Lukawski, S.-C. Kong, R. C. Brown, *Energy & Fuels*, **2013**, *27*, 1381-1390.

[3.4] (a) Z. Yang, J. Zhang, M. C. W. Kintner-Meyer, X. Lu, D. Choi, J. P. Lemmon, J. Liu, *Chem. Rev.* **2011**, *111*, 3577-3613. (b) K. Liang, L. Li, Y. Yang, *ACS Energ. Lett.* **2017**, 2, 373-390.

[3.5] (a) G. W. Crabtree, M. S. Dresselhaus, *MRSBull*. 2008, **33**, 421. (b) S. Hamrock and M. Yandrasits, *Polym. Rev*., 2006, **46**, 219. (c) K. Sundmacher, *Ind. Eng. Chem. Res.*, **2010**, *49*, 10159-10182. (d) A. Rabis, P. Rodriguez, T. J. Schmidt, *ACS Catal.*, **2012**, *2*, 864-890. (e) C.-Y. Wang, *Chem. Rev.*, **2004**, *104*, 4727-4766.

[3.6] (a) K. -D. Kreuer, *Chem. Mater.*, 1996, **8**, 610; (b) K. -D. Kreuer, *J. Membr. Sci.*, 2001, **185**, 29; (c) K. D. Kreuer, S. J. Paddison, E. Spohr, M. Schuster, *Chem. Rev*. 2004, **104**, 4637; (c) B., Atilla. *Int. J. Hydrogen Energ*, 2005, **30**, 1181. (d) Y. Shao, G. Yin, Z. Wang, Y. Gao, *J. Power Sources*, 2007, **167**, 235. (e) H. Zhang, P. K. Shen, *Chem. Rev.* **2012**, *112*, 2780-2832.

[3.7] (a) K. A. Mauritz, R. B. Moore, *Chem. Rev.*, 2004, **104**, 4535. (b) G. Alberti, R. Narducci, M. Sganappa, *J. Power Source*, 2008, **178**, 575. (c) G. Alberti, R. Narducci, *Fuel Cells*, 2009, **9**, 410. (d) K. A. Mauritz and R. B. Moore, *Chem. Rev.* 2004, **104**, 4535.

[3.8] (a) A. Shigematsu, T. Yamada, H. Kitagawa, *J. Am. Chem. Soc.* 2011, **133**, 2034. (b) J. M. Taylor, R. K. Mah, I. L. Moudrakovski, C. I. Ratcliffe, R. Vaidhyanathan, G. K. H. Shimizu, *J. Am. Chem. Soc*. 2010, **132**, 14055. (c) T. Yamada, M. Sadakiyo, H. Kitagawa, *J. Am. Chem. Soc*. 2009, **131**, 3144. (d) M. Yoon, K. Suh, H. Kim, Y. Kim, N. Selvapalam, K. Kim, *Angew. Chem. Int. Ed.* 2011, **50**, 7870. (e) S. Bureekaew, S. Horike, M. Higuchi, M. Mizuno, T. Kawamura, D. Tanaka, N. Yanai, S. Kitagawa, *Nat. Mater*. 2009, **8**, 831. (f) V. G. Ponomareva, K. A. Kovalenko, A. P. Chupakhin, D. N. Dybtsev, E. S. Shutova, V. P. Fedin, *J. Am. Chem. Soc*. 2012, **134**, 15640. (g) J. A. Hurd, R. Vaidhyanathan, V. Thangadurai, C. I. Ratcliffe, I. L. Moudrakovski, G. K. Shimizu, *Nat. Chem*. 2009, **1**, 705. (h) T. Yamada, S. Morikawa, H. Kitagawa, *Bull. Chem. Soc. Jpn*. 2010, **83**, 42. (i) S. Kim, K. W. Dawson, B. S. Gelfand, J. M. Taylor, G. K. H. Shimizu, *J. Am. Chem. Soc.* 2013, **135**, 963. (j) S. C. Sahoo, T. Kundu, R. Banerjee. *J. Am. Chem. Soc.* 2011, **133**, 17950. (k) S. Sen, N. N. Nair, T. Yamada, H. Kitagawa, P. K. Bharadwaj, *J. Am. Chem. Soc.* 2012, **134**, 19432. (l) C. Dey, T. Kundu, R. Banerjee. *Chem. Commun.*, 2012, **48**, 266. (m) H. Okawa, A. Shigematsu, M. Sadakiyo, T. Miyagawa, K. Yoneda, M. Obha, H. Kitagawa, *J. Am. Chem. Soc*. 2009, **131**, 13516. (n) E. Pardo, C. Train, G. Gontard, K. Boubekeur, O. Fabelo, H. Liu, B. Dkhil, F. Lloret, K. Nakagawa, H. Tokoro, S. Ohkoshi, M. Verdaguer, *J. Am. Chem. Soc*. 2011, **133**, 15328. (o) B. M. Wiers, M. -L. Foo, N. P. Balsara, J. R. Long, *J. Am. Chem. Soc.* 2011, **133**, 14522. (p) M. Sadakiyo, H. Okawa, A. Shigematsu, M. Ohba, T. Yamada, H. Kitagawa, *J. Am. Chem. Soc*. 2012, **134**, 5472. (q) C. Serre, F. Millange, C. Thouvenot, M. Nogus, G. Marsolier, D. Lour, G. Frey, *J. Am. Chem. Soc*. 2002, **124**, 13519. (r) A. Shigematsu, T. Yamada, H. Kitagawa, *J. Am. Chem. Soc.* 2011, **133**, 2034. (s) T. Kundu, S. C. Sahoo, R. Banerjee. *Chem. Commun.*, 2012, **48**, 4998. (t) V. G. Ponomareva, K. A. Kovalenko, A. P. Chupakhin, D. N. Dybtsev, E. S. Shutova, V. P. Fedin, *J. Am. Chem. Soc.* 2012, **134**, 15640. (u) M. Sadakiyo, T. Yamada, H. Kitagawa, *J. Am. Chem. Soc.*

2009, **131**, 9906. (v) S. Kanda, K. Yamashita, K. Ohkawa, *Bull. Chem. Soc. Jpn*. 1979, **52**, 3296. (w) D. Umeyama, S. Horike, M. Inukai, Y. Hijikata, S. Kitagawa, *Angew. Chem., Int. Ed.* 2011, **50**, 11706. (x) S. Horike, D. Umeyama, M. Inukai, T. Itakura, S. Kitagawa, *J. Am. Chem. Soc*. 2012, **134**, 7612. (y) D. Umeyama, S. Horike, M. Inukai, T. Itakura, S. Kitagawa, *J. Am. Chem. Soc*. 2012, **134**, 12780.

[3.9] (a) X. Feng, X. Ding, D. Jiang, *Chem. Soc. Rev.*,**2012**, *41*, 6010−6022. (b) J. W.vColson, W. R. Dichtel, *Nat. Chem.*, **2013**, *5*, 453−465. (c) S.-Y. Ding, W. Wang, *Chem. Soc. Rev.*, **2013**, 42, 548−568. (d) A. P. Côté , A. I. Benin, N. W. Ockwig, M. O'Keeffe, A. J. Matzger, O. M. Yaghi, *Science*, **2005**, *310*, 1166−1170.

[3.10] S. Chandra, T. Kundu, S. Kandambeth, R. BabaRao, Y. Marathe, S. M. Kunjir, R. Banerjee, *J. Am. Chem. Soc.*, **2014**, 136, 6570−6573.

[3.11] S. Wan, J. Guo, J. Kim, H. Ihee, D. Jiang, *Angew. Chem.*, *Int. Ed.*, **2008**, *120*, 8958.

[3.12] (a) M. Dogru, M. Handloser, F. Auras, T. Kunz, D. Medina, A. Hartschuh, P. Knochel, T. Bein, *Angew. Chem.*, **2013**, *52*, 2920. (b) D. Gopalakrishnan, W. R. Dichtel, *J. Am. Chem. Soc.*, **2013**, *135*, 8357.

[3.13] S. S. Han, H. Furukawa, O. M. Yaghi, W. A. Goddard, *J. Am. Chem. Soc.*, **2008**, *130*, 11580.

[3.14] (a) K. A. Mauritz, R. B. Moore, *Chem. Rev.*, **2004**, *104*, 4535. (b) M. Hickner, H. Ghassemi, Y. S. Kim, B. R. Einsla, J. E. McGrath, *Chem. Rev.*, **2004**, 104, 4587. (c) S. Paddison, *J. Annu. Rev. Mater. Res.*, **2003**, *33*, 289.

[3.15] L. M. Lanni, R. W. Tilford, M. Bharathy, J. J. Lavigne, *J. Am. Chem. Soc.*, **2011**, 130, 11872.

[3.16] (a) S. Kandambeth, A. Mallick, B. Lukose, V. M. Mane, T. Heine, R. Banerjee, *J. Am. Chem. Soc.* **2012**, 134, 19524. (b) B. P. Biswal, S. Chandra, S. Kandambeth, B. Lukose, V. M. Mane, T. Heine, R. Banerjee, *J. Am. Chem. Soc.*, **2013**, 135, 5328. (c) S. Chandra, S. Kandambeth, B. P. Biswal, B. Lukose, S. M. Kunjir, M.Chaudhary, R. Babarao, T. Heine, R. Banerjee, *J. Am. Chem. Soc.*, **2013**, 135, 17853.

[3.17] J. A. Asensio, E. M. Sanchez, P. Gomez-Romero, *Chem. Soc. Rev.*, **2010**, 39, 3210.

[3.18] (a) I. Halasz, K. Lukic, H. Vancik, *Acta Crystallogr.*, **2007**, C63, o61. (b) A. M. Sanchez, M. Barra, R. H. de Rossi, *J. Org. Chem.*, **1999**, 64, 1604.

[3.19] R. Dovesi, V. R. Saunders, C. Roetti, R. Orlando, C. M. ZicovichWilson, F. Pascale, B. Civalleri, K. Doll, N. M. Harrison, I. J. Bush, P. D. Arco, M. Llunell, *Crystal1.0.2 ed*.

[3.20] B. Lukose, A. Kuc, T. Heine, *Chem. Eur. J.*, **2011**, 17, 2388.

[3.21] Accelrys, Material Studio Release Notes, Release 4.2, *Accelrys Software*, San Diego **2006**.

[3.22] D. Beaudoin, T. Maris, J. D. Wuest, *Nat. Chem.*, **2013**, 5, 830.

[3.23] J. H. Chong, M. Sauer, B. O. Patrick, M. MacLachlan, *J. Org. Lett.*, **2003**, *5*, 3823.

CHAPTER 4

[4.1] N. Garland, J. P. Kopasz, *J. Power Sources*, **2007**, *172*, 94−99.

[4.2] Q. Li, R. He, J. O. Jensen, N. J. Bjerrum, *Chem. Mater.*, **2003**, 15, 4896−4915.

[4.3] K. A. Mauritz, R. B. Moore, *Chem. Rev.*, **2004**, *104*, 4535−4585.

[4.4] J. S. Wainright, J. T. Wang, D. Weng, R. F. Savinell, M. Litt, *J. Electrochem. Soc.*,**1995**, *142*, L121−L123.

[4.5] T. Higashihara, K. Matsumoto, M. Ueda, *Polymer*, **2009**, *50*, 5341−5357.

[4.6] M. Sadakiyo, T. Yamada, H. Kitagawa, *J. Am. Chem. Soc.*, **2009**, *131*, 9906−9907.

[4.7] S. Horike, D. Umeyama, S. Kitagawa, *Acc. Chem. Res.*, **2013**, *46*, 2376−2384.

[4.8] M. Yoon, K. Suh, S. Natarajan, K. Kim, *Angew. Chem., Int. Ed.*, **2013**, *52*, 2688−2700.

[4.9] G. K. H. Shimizu, J. M. Taylor, S. R. Kim, *Science*, **2013**, 341, 354−355.

[4.10] P. Ramaswamy, N. E. Wong, G. K. H. Shimizu, *Chem. Soc. Rev.* **2014**, *43*, 5913−5932.

[4.11] W. J. Phang, H. Jo, W. R. Lee, J. H. Song, K. Yoo, B. Kim, C. S. Hong, *Angew. Chem., Int. Ed.*, **2015**, *54*, 5142−5146.

[4.12] Y. Peng, Z. Hu, Y. Gao, D. Yuan, Z. Kang, Y. Qian, N. Yan, D. Zhao, *ChemSusChem*, **2015**, *8*, 3208−3212.

[4.13] S. Bureekaew, S. Horike, M. Higuchi, M. Mizuno, T. Kawamura, D. Tanaka, N. Yanai, S. Kitagawa, *Nat. Mater.*, **2009**, *8*, 831−836.

[4.14] D. Umeyama, S. Horike, M. Inukai, Y. Hijikata, S. Kitagawa, *Angew. Chem., Int. Ed.*, **2011**, *50*, 11706−11709.

[4.15] V. G. Ponomareva, K. A. Kovalenko, A. P. Chupakhin, D. N. Dybtsev, E. S. Shutova, V. P. Fedin, *J. Am. Chem. Soc.*, **2012**, *134*, 15640−15643.

[4.16] Z. Li, G. He, B. Zhang, Y. Cao, H. Wu, Z. Jiang, Z. Tiantian, *ACS Appl. Mater. Interfaces*, **2014**, 6, 9799−9807.

[4.17] S. C. Sahoo, T. Kundu, R. Banerjee, *J. Am. Chem. Soc.* **2011**, *133*, 17950−17958.

[4.18] J. A. Hurd, R. Vaidhyanathan, V. Thangadurai, C. I. Ratcliffe, I. L. Moudrakovski, G. K. H. Shimizu, *Nat. Chem.*, **2009**, *1*, 705−710.

[4.19] S. Horike, D. Umeyama, M. Inukai, T. Itakura, S. Kitagawa, *J. Am. Chem. Soc.*, **2012**, *134*, 7612−7615.

[4.20] D. Umeyama, S. Horike, M. Inukai, S. Kitagawa, *J. Am. Chem. Soc.*, **2013**, *135*, 11345−11350.

[4.21] S. Chandra, T. Kundu, S. Kandambeth, R. Babarao, Y. Marathe, S. M. Kunjir, R. Banerjee, *J.Am. Chem. Soc.*, **2014**, *136*, 6570−6573.

[4.22] Y. Ye, L. Zhang, Q. Peng, G. E. Wang, Y. Shen, Z. Li, L. Wang, X. Ma, Q. H. Chen, Z. Zhang, S. Xiang, *J. Am. Chem. Soc.*, **2015**, *137*, 913−918.

[4.23] D. N. Dybtsev, V. G. Ponomareva, S. B. Aliev, A. P. Chupakhin, M. R. Gallyamov, N. K. Moroz, B. A. Kolesov, K. A. Kovalenko, E. S. Shutova, V. P. Fedin, *ACS Appl. Mater. Interfaces*, **2014**, *6*, 5161−5167.

[4.24] D. Hoel, E. Grunwald, *J. Phys. Chem.*, 1977, 81, 2135−2136.

[4.25] S. M. Haile, D. A. Boysen, C. R. I. Chisholm, R. B. Merle, *Nature*, **2001**, 410, 910−913.

[4.26] H. Steininger, M. Schuster, K. D. Kreuer, A. Kaltbeitzel, B. Bingol, W. H. Meyer, S. Schauff, G. Brunklaus, J. Maier, H. W. Spiess, *Phys. Chem. Chem. Phys.,* **2007**, *9*, 1764−1773.

[4.27] G. K. H. Shimizu, R. Vaidhyanathan, J. M. Taylor, *Chem. Soc. Rev.*, **2009**, *38*, 1430−1449.

[4.28] D. Umeyama, S. Horike, M. Inukai, T. Itakura, S. Kitagawa, *J. Am. Chem. Soc.*, **2012**, *134*, 12780−12785.

[4.29] S. Tominaka, A. K. Cheetham, *RSC Adv.*, 2014, 4, 54382−54387.

[4.30] P. Ramaswamy, R. Matsuda, W. Kosaka, G. Akiyama, H. J. Jeon, S. Kitagawa, *Chem. Commun.*, **2014**, *50*, 1144−1146.

[4.31] A. P. Côté, A. I. Benin, N. W. Ockwig, A. J. Matzger, M. O'Keeffe, O. M. Yaghi, *Science*, **2005**, *310*, 1166−1170.

[4.32] J. W. Colson, W. R. Dichtel, *Nat.Chem.,* **2013**, *5*, 453−465.

[4.33] N. Huang, X. Chen, R. Krishna, D. Jiang, *Angew. Chem., Int. Ed.*, **2015**, *54*, 2986−2990.

[4.34] Ding, S. Y.; Gao, J.; Wang, Q.; Zhang, Y.; Song, W.; Su, C.; Wang, W. *J. Am. Chem. Soc.*, **2011**, 133, 19816−19822.

[4.35] M. Dogru, M. Handloser, F. Auras, T. Kunz, D. Medina, A. Hartschuh, P. Knochel, T. Bein, *Angew. Chem., Int. Ed.*, **2013**, *52*, 2920−2924.

[4.36] S. Kandambeth, A. Mallick, B. Lukose, V. M. Mane, T. Heine, R. Banerjee, *J. Am. Chem. Soc.*, **2012**, *134*, 19524−19527.

[4.37] C. R. DeBlase, K. E. Silberstein, T.-T. Truong, H. D. Abruña, W. R. Dichtel, *J. Am. Chem. Soc.*, **2013**, *135*, 16821−16824.

[4.38] M. L. Foo, S. Horike, T. Fukushima, Y. Hijikata, Y. Kubota, M. Takata, S. Kitagawa, *Dalton Trans.,* **2012**, 41, 13791−13794.

[4.39] X. Chen, M. Addicoat, S. Irle, A. Nagai, D. Jiang, *J. Am. Chem. Soc.*, **2013**, 135, 546−549.

[4.40] D. A. G. Gualdron, P. Z. Moghadam, J. T. Hupp, O. K. Farha, R. Q. Snurr, *J. Am. Chem. Soc.,* **2016**, *138*, 215−224.

[4.41] L. Sarkisov, A. Harrison, *Molecular Simulation.*, **2011**, *37*, 1248–1257.

[4.42] J. H. Chong, M. Sauer, B. O. Patrick, M. MacLachlan, *J. Org. Lett.*, **2003**, *5*, 3823.

CHAPTER 5

[5.1] S. Chu, A. Majumdar, *Nature*, **2012**, *488*, 294.

[5.2] A. S. Arico, P. Bruce, B. Scrosati, J. M. Tarascon, W. Van Schalkwijk, *Nat. Mater.* **2005**, 4, 366.

[5.3] G. Wang, L. Zhang, J. Zhang, *Chem. Soc. Rev.*, **2012**, *41*, 797.

[5.4] D. G. Nocera, *Chem. Soc. Rev.,* **2009**, *38*, 13.

[5.5] P. Simon, Y. Gogotsi, *Nat. Mater.*, **2008**, *7*, 845.

[5.6] B. Luo, B. Wang, X. L. Li, Y. Y. Jia, M. H. Liang, L. J. Zhi, *Adv. Mater.*, **2012**, *24*, 3538.

[5.7] X. Xiao, X. Liu, H. Zhao, D. Chen, F. Liu, J. Xiang, Z. Hu, Y. Li, *Adv. Mater.*, **2012**, *24*, 5762.

[5.8] H.-C. Chien, W.-Y. Cheng, Y.-H. Wang, S.-Y. Lu, *Adv. Funct. Mater.,* **2012**, *22*, 5038.

[5.9] Y. Zhai, Y. Dou, D. Zhao, P. F. Fulvio, R. T. Mayes, S. Dai, *Adv. Mater.*, **2011**, *23*, 4828.

[5.10] J. R. Miller, P. Simon, *Science,* **2008**, *321*, 651.

[5.11] L. L. Zhang, X. S. Zhao, *Chem. Soc. Rev.,* **2009**, *28*, 2520.

[5.12] B. E. Conway, Electrochemical supercapacitors: Scientific fundamentals and technological applications, *Kluwer Academic/Plenum, New York* **1999**.

[5.13] Y. Wang, Y. Song, Y. Xia, *Chem. Soc. Rev.,* **2016**, *45*, 5925-5950.

[5.14] A. M. Österholm, J. F. Ponder, J. A. Kerszulis, J. R. Reynolds, *ACS Appl. Mater. Interfaces*, **2016**, *8*, 13492–13498.

[5.15] H. Ma, J. He, D.-B. Xiong, J. Wu, Q. Li, V. Dravid, Y. Zhao, *ACS Appl. Mater. Interfaces*, **2016**, *8*, 1992-2000.

[5.16] P. Du, H. C. Liu, C. Yi, K. Wang, X. Gong, *ACS Appl. Mater. Inter.* **2015**, *7*, 3263–3271.

[5.17] M. F. El-Kady, V. Strong, S. Dubin, R. B. Kaner, *Science*, **2012**, *335*, 1326-1330.

[5.18] P. Tamailarasan, S. Ramaprabhu, *J. Phys. Chem. C*, **2012**, *116*, 14179-14187.

[5.19] D. J. Bozym, S. Korkut, M. A. Pope, I. A. Aksay, *ACS Sust. Chem. & Eng.*, **2016**, 4,

7167-7174.

[5.20] P. C. Chen, G. Z. Shen, Y. Shi, H. T. Chen, C. W. Zhou, *ACS Nano*, **2010**, *4*, 4403.

[5.21] J. Yan, Z. Fan, W. Sun, G. Ning, T. Wei, Q. Zhang, R. Zhang, L. Zhi, F. Wei, *Adv. Funct. Mater.* **2012**, *22*, 2632.

[5.22] Z. Tang, C.-h. Tang, H. Gong, *Adv. Funct. Mater.*, **2012**, *22*, 1272.

[5.23] Z. Chen, V. Augustyn, J. Wen, Y. W. Zhang, M. Q. Shen, B. Dunn, Y. F. Lu, *Adv. Mater.* **2011**, *23*, 791.

[5.24] A. Izadi-Najafabadi, S. Yasuda, K. Kobashi, T. Yamada, D. N. Futaba, H. Hatori, M. Yumura, S. Iijima, K. Hata, *Adv. Mater.*, **2010**, *22*, E235.

[5.25] S. J. Guo, S. J. Dong, *Chem. Soc. Rev.*, **2011**, *40*, 2644.

[5.26] M. D. Stoller, S. Park, Y. Zhu, J. An, R. S. Ruoff, *Nano Lett.*, **2008**, *8*, 3498.

[5.27] Z. Yu, L. Tetard, L. Zhai, J. Thomas, *Energy Environ. Sci.* **2015**, *8*, 702.

[5.28] S. Z. Butler, S. M. Hollen, L. Cao, Y. Cui, J. A. Gupta, H. R. Gutiérrez, T. F. Heinz, S. S. Hong, J. Huang, A. F. Ismach, E. Johnston-Halperin, M. Kuno, V. V. Plashnitsa, R. D. Robinson, R. S. Ruoff, S. Salahuddin, J. Shan, L. Shi, M. G. Spencer, M. Terrones, W. Windl, J. E. Goldberger, *ACS Nano*, **2013**, 7, 2898.

[5.29] X. Peng, L. Peng, C. Wu, Y. Xie, *Chem. Soc. Rev.*, **2014**, *43*, 3303.

[5.30] M. Chhowalla, H. S. Shin, G. Eda, L.-J. Li, K. P. Loh, H. Zhang, *Nat. Chem.*, **2013**, *5*, 263.

[5.31] M. Naguib, O. Mashtalir, J. Carle, V. Presser, J. Lu, L. Hultman, Y. Gogotsi, M. W. Barsoum, *ACS Nano*, **2012**, *6*, 1322.

[5.32] M. Naguib, G. W. Bentzel, J. Shah, J. Halim, E. N. Caspi, J. Lu, L. Hultman, M. W. Barsoum, *Mater. Res. Lett.*, **2014**, *2*, 233.

[5.33] M. Naguib, M. Kurtoglu, V. Presser, J. Lu, J. Niu, M. Heon, L. Hultman, Y. Gogotsi, M. W. Barsoum, *Adv. Mater.,* **2011**, *23*, 4248.

[5.34] M. Naguib, V. N. Mochalin, M. W. Barsoum, Y. Gogotsi, *Adv. Mater.,* **2014**, *26*, 992.

[5.35] M. R. Lukatskaya, O. Mashtalir, C. E. Ren, Y. Dall'Agnese, P. Rozier, P. L. Taberna, M. Naguib, P. Simon, M. W. Barsoum, Y. Gogotsi, *Science*, **2013**, *341*, 1502.

[5.36] M. D. Levi, M. R. Lukatskaya, S. Sigalov, M. Beidaghi, N. Shpigel, L. Daikhin, D. Aurbach, M. W. Barsoum, Y. Gogotsi, *Adv. Energy Mater.*, **2015**, *5*, 1400815.

[5.37] M. Beidaghi, Y. Gogotsi, *Energy Environ. Sci*. **2014**, *7*, 867.

[5.38] X. Feng, X. S. Ding, D.Jiang, *Chem. Soc. Rev*., **2012**, *41*, 6010−6022.

[5.39] S. Y. Ding, W. Wang, *Chem. Soc. Rev.,* **2013**, *42*, 548−568.

[5.40] C. Portet, G. Yushin, Y. Gogotsi, *Carbon*, **2007**, *45*, 2511−2518.

[5.41] Z. S. Wu, Y. Sun, Y. Z. Tan, S. Yang, X. Feng, K. Müllen, *J. Am. Chem. Soc*. **2012**, *134*, 19532−19535.

[5.42] L. Hao, J. Ning, B. Luo, B. Wang, Y. Zhang, Z. Tang, J. Yang, A. Thomas, L. Zhi, *J. Am. Chem. Soc.,* **2015**, *137*, 219−225.

[5.43] S. Kandambeth, A. Mallick, B. Lukose, M. V. Mane, T. Heine, R. Banerjee, *J. Am. Chem. Soc.,* **2012**, *134*, 19524−19527.

[5.44] P. Pachfule, S. Kandambeth, D. D. Diaz, R. Banerjee, *Chem. Commun.,* **2014**, *50*, 3169−3172.

[5.45] S. Chandra, T. Kundu, S. Kandambeth, R. BabaRao, Y. Marathe, S. M. Kunjir, R. Banerjee, *J.Am. Chem. Soc.,* **2014**, *136*, 6570−6573.

[5.46] C. R. DeBlase, K. E. Silberstein, T. T. Truong, H. D. Abruna, W. R. Dichtel, *J. Am. Chem. Soc.*, **2013**, *135*, 16821−16824.

[5.47] C. R. DeBlase, K. Hernandez-Burgos, K. E. Silberstein, G. G. Rodriguez-Calero, R. P. Bisbey, H. D. Abruna, W. R. Dichtel, *ACS Nano*, **2015**, *9*, 3178−3183.

[5.48] Z. Zha, L. Xu, Z. Wang, X. Li, Q. Pan, P. Hu, S. Lei, *ACS Appl. Mater. Interfaces*, **2015**, *7*, 17837−17843.

[5.49] C. R. Mulzer, L. Shen, R. P. Bisbey, J. R. McKone, N. Zhang, H. D. Abruña, W. R. Dichtel, *ACS Cent. Sci.,* **2016**, *2*, 667−673.

[5.50] A. M. Khattak, Z. A. Ghazi, B. Liang, N. A. Khan, A. Iqbal, L. Li, Z. Tang, *J. Mater. Chem. A*, **2016**, *4*, 16312−16317.

[5.51] C. Singh, A. Paul, *J. Phys. Chem. C*, **2015**, *119*, 11382−11390.

[5.52] S. Roldán, C. Blanco, M. Granda, R. Menéndez, R. Santamaría, *Angew. Chem., Int. Ed.* **2011**, *50*, 1699−1701.

[5.53] A.Vlad, K. Arnould, B. Ernould, L. Sieuw, J. Rolland, J.- F. Gohy, *J. Mater. Chem. A*, **2015**, *3*, 11189−11193.

[5.54] C. Karlsson, H. Huang, M. Strømme, A. Gogoll, M. Sjödin, *J.Phys. Chem. C*, **2013**, *117*, 23558−23567.

[5.55] S.-K. Kim, J. Cho, J. S. Moore, H. S. Park, P. V. Braun, *Adv. Funct. Mater.*, 2016, 26, 903−910.

[5.56] G. Milczarek, O.Inganäs, *Science*, **2012**, 335, 1468−1471.

[5.57] Y. Xu, Z. Lin, X. Huang, Y. Wang, Y. Huang, X. Duan, *Adv. Mater.*, **2013**, 25, 5779−5784.

[5.58] D. Puthusseri, V. Aravindan, S. Madhavi, S. B. Ogale, *Energy Environ. Sci.*, **2014**, *7*, 728−735.

[5.59] M. Pourbaix, Atlas of Electrochemical Equilibria in Aqueous Solutions; *National Association of Corrosion Engineers: New York*, **1974**; p 379.

[5.60] D. R. Weinberg, C. J. Gagliardi, J. F. Hull, C. F. Murphy, C. A. Kent, B. C. Westlake, A. Paul, D. H. Ess, D. G. McCafferty, T. J. Meyer, *Chem. Rev.*, **2012**, *112*, 4016−4093.

[5.61] K. Brezesinski, J. Wang, J. Haetge, C. Reitz, S. O. Steinmueller, S. H. Tolbert, B. M. Smarsly, B. Dunn, T. Brezesinski, *J. Am. Chem. Soc.*, **2010**, *132*, 6982−6990.

[5.62] W. Sugimoto, H. Iwata, K. Yokoshima, Y. Murakami, Y. Takasu, *J. Phys. Chem. B*, **2005**, *109*, 7330−7338.

[5.63] C. Costentin, C. Louault, M. Robert, J.-M. Savéant, *Proc. Natl. Acad. Sci. USA*, **2009**, *106*, 18143–18148.

[5.64] C. Li, M. Z. Hoffman, *J. Phys. Chem. B*, **1999**, *103*, 6653−6656.

[5.65] N. Song, C. J. Gagliardi, R. A. Binstead, M.-T. Zhang, H. Thorp, T. J. Meyer, *J. Am. Chem. Soc.*, **2012**, *134*, 18538−18541.

[5.66] F. Thomas, O. Jarjayes, H. Jamet, Hamman, S.; Saint-Aman, E.; Duboc, C.; Pierre, J.-L. *Angew. Chem.*, *2004*, 116, 604−607;*Angew. Chem., Int. Ed.*, **2004**, 43, 594−597.

[5.67] R. Wang, T. E. Keyes, R. Hage, R. H. Schmehl, J. G. Vos, *J. Chem. Soc., Chem. Commun.*, **1993**, 1652−1654.

[5.68] T. M. Alligrant, J. C. Hackett, J. C. Alvarez, *Electrochim. Acta*, **2010**, 55, 6507−6516.

[5.69] P. D. Astudillo, J. Tiburcio, F. J. González, *J. Electroanal. Chem.*, **2007**, *604*, 57−64.

[5.70] N. Gupta, H. Linschitz, *J. Am. Chem. Soc.*, **1997**, *119*, 6384−6391.

[5.71] P. He, R. M. Crooks, L. R. Faulkner, *J. Phys. Chem.*, **1990**, *94*, 1135−1141.

[5.72] G. R. Desiraju, *Acc. Chem. Res.*, **2002**, *35*, 565−573.

[5.73] G. R. Desiraju, T. Steiner, The Weak Hydrogen Bond; *Oxford University Press: New York*, **1999**.

[5.74] G. R. Desiraju, *Angew. Chem., Int. Ed. Engl.*, **1995**, 34, 2311−2327.

[5.75] T. Steiner, *Angew. Chem., Int. Ed.*, **2002**, *41*,48−76.

[5.76] M. D. Stoller, R. S. Ruoff, *Energy Environ. Sci.*, **2010**, *3*, 1294−1301.

ABOUT THE AUTHOR

Mr. Suman Chandra, son of Gourinath Chandra and Asha Chandra, was born in Jhalda village of Purulia district, West Bengal, India, in 1987. He did his schooling (2002) and higher secondary (2004) from Jhalda Satyabhama Vidyapith, Jhalda. He has completed his B.Sc. (Chemistry) from Jagannath Kishore (J.K) College, Purulia (2007). Then he moved to Department of Applied Chemistry, Indian Institute of Technology (Indian School of Mines), Dhanbad to pursue his M.Sc. (Chemistry). After qualifying all India Graduate Aptitude Test (GATE) examination, he joined Chemistry Department, Indian Institute of Technology (IIT), Roorkee, India as MHRD research fellow in July 2009 under the guidance of Prof. Uday Pratap Singh. Again, after qualifying all India CSIR-UGC National Eligibility Test (NET-JRF) examination, he moved to Physical and Materials Chemistry Division, CSIR-National Chemical Laboratory, Pune, India to pursue his Ph.D. degree in July 2012 under the guidance of Prof. Dr. Rahul Banerjee. He has received the research fellowship (JRF and SRF) from University Grants Commission (UGC), New Delhi, India for the period of July 2012 - June 2017 to carry out the Ph.D. thesis work.

LIST OF PUBLICATIONS

1. **Suman Chandra**, Debarati Roy Chowdhury, Matthew Addicoat, Thomas Heine, Amit Paul, and Rahul Banerjee*, *"Molecular Level Control on the Capacitance of Two-Dimensional Covalent Organic Frameworks: The Role of H-bonding in Energy Storage Materials."*

   ***Chem. Mater., 2017,** 29, 2074-2080.*

   [Most read article for February 2017 and front cover page of March 2017]

2. **Suman Chandra**, Tanay Kundu, Kaushik Dey, Matthew Addicoat, Thomas Heine, Rahul Banerjee*, *"Interplaying Intrinsic and Extrinsic Proton Conductivities in Covalent Organic Frameworks."*

   ***Chem. Mater., 2016,** 28, 1489–1494.*

   [Most read article for February 2016]

3. **Suman Chandra**, Tanay Kundu, Sharath Kandambeth, Ravichandar BabaRao, Yogesh Marathe, Shrikant M. Kunjir and Rahul Banerjee*, *"Phosphoric acid Loaded Azo (-N=N-) based Covalent Organic Framework for Proton Conduction."*

   ***J. Am. Chem. Soc., 2014,** 136, 6570–6573.*

   [*Highlighted in Nature Chemistry, News and Views*]

4. **Suman Chandra**, Sharath Kandambeth, Bishnu P. Biswal, Binit Lukose, Shrikant M. Kunjir, Minakshi Chaudhary, Ravichandar Babarao, Thomas Heine and Rahul Banerjee*, *"Chemically Stable Multi-layered Covalent Organic Nanosheets from Covalent Organic Frameworks via Mechanical Delamination".*

   ***J. Am. Chem. Soc., 2013,** 135, 17853–17861.*

5. Bishnu P. Biswal, **Suman Chandra**, Sharath Kandambeth, Binit Lukose, Thomas Heine and Rahul Banerjee* *"Mechanochemical Synthesis of Chemically Stable Isoreticular Covalent Organic Frameworks".*

   ***J. Am. Chem. Soc., 2013,** 135, 5328–5331.*

[B.P.B., S.C., and S.K. contributed equally.]

6. Bishnu P. Biswal, Sharath Kandambeth, **Suman Chandra**, Digambar Balaji Shinde, Saibal Bera, Suvendu Karak, Bikash Garai, Ulhas K. Kharul, Rahul Banerjee*. *" Pore Surface Engineering in Porous, Chemically Stable Covalent Organic Frameworks for Water Adsorption.*
   J. Mater Chem. A, 2015, *3, 23664-23669.*

LIST OF PATENTS

1. Rahul Banerjee, Sharath Kandambeth, **Suman Chandra**, "*Chemically stable porous crystalline framework for gas purification and bio-application"* Publication number: **EP2906565 A1** (Also published as **US20150266885**, **WO2014057504A1**).
2. Rahul Banerjee, **Suman Chandra**, Tanay Kundu, Sharath Kandambeth "*Phosphoric Acid Loaded Covalent Organic Framework And A Process For The Preparation Thereof*" Publication number: **US20150299147 A1**.

CONFERENCES AND PRESENTATIONS

1. Presented poster in "*Modern Trends in Inorganic Chemistry-XV (MTIC-XV)*" **2013,** Indian Institute of Technology, Roorkee.
2. Presented poster in *International Conference on* "*Structural Chemistry of Molecules and Materials (SCOMM)*" **2014**, Kolkata.